NASA
Technical
Paper
2213

January 1985

Laminar Heat-Transfer Distributions on Biconics at Incidence in Hypersonic-Hypervelocity Flows

Charles G. Miller III,
John R. Micol,
and Peter A. Gnoffo

NASA

NASA Technical Paper 2213

1985

Laminar Heat-Transfer Distributions on Biconics at Incidence in Hypersonic-Hypervelocity Flows

Charles G. Miller III,
John R. Micol,
and Peter A. Gnoffo

Langley Research Center
Hampton, Virginia

National Aeronautics and Space Administration

Scientific and Technical Information Branch

CONTENTS

SUMMARY

Laminar heating distributions at hypersonic-hypervelocity flow conditions have been measured on spherically blunted, 12.84°/7° straight and bent-nose (fore-cone axis bent 7° upward relative to aft-cone axis) biconics in the Langley Expansion Tube. The bent-nose biconic represented a 1.9-percent-scale model of an aeroassisted vehicle proposed for missions to a number of planets. Test gases used were helium, nitrogen, air, and carbon dioxide. The free-stream Mach numbers ranged from 6.0 to 9.0, and velocities ranged from 4.5 to 6.9 km/sec. Helium behaved as an ideal gas, with a normal-shock density ratio of 3.7. Calculated thermochemical equilibrium values of density ratios for nitrogen and air were about 11 and for carbon dioxide were about 19. The model surface was essentially noncatalytic. Angles of attack, referenced to the axis of the aft-cone, varied from 0° to 20°. The effects of nose bend (i.e., comparison of bent-nose biconic with straight biconic), angle of attack, and test gas on heating distributions were examined and measurements in helium and air are compared with prediction from a code which solves the three-dimensional "parabolized" Navier-Stokes (PNS) equations.

The 7° nose bend naturally caused an increase in windward heating to the fore-cone at a given angle of attack; however, this increase was only 10 to 20 percent at the design trim angle of attack of 20° for the bent-nose biconic. Perhaps more important to the designer is the fact that this nose bend caused a decrease in windward heating to the aft-cone, which represents approximately 60 percent of the vehicle surface. Aft-cone windward heating was more sensitive to angle of attack than fore-cone heating, increasing for the bent-nose biconic by a factor of three to four as the angle of attack was increased from 0° to 20°; windward heating increased by a factor of two on the fore-cone. Heating along the most leeward ray initially decreased but then increased with increasing angle of attack. This trend was attributed to cross-flow separation on the leeward side when the fore-cone angle of attack exceeded the fore-cone half angle. (The flow separation resulted in the formation of longitudinal, counterrotating primary vortices that reattached along the most leeward ray, thereby augmenting the heat-transfer rate.) Although Mach number, Reynolds number, ratio of wall temperature to total temperature, and normal-shock density ratio (shock strength) varied for the four test gases, windward heating was correlated reasonably well for all the test gases (except CO_2) in terms of the density ratio, the Stanton number, and a form of the viscous-interaction parameter. Expressed in terms of these parameters, the CO_2 results were consistently lower than the other three gases. Contrary to results for the other three test gases, the aft-cone heating in CO_2 increased in the direction of the base; this trend was attributed to the lower ratio of specific heats within the shock layer for CO_2. Heating distributions along the most windward and most leeward rays on both biconics in helium and on the straight biconic in air were generally underpredicted with the PNS code.

INTRODUCTION

Recent advances in navigation and the knowledge of planetary atmospheres (refs. 1 to 3), along with the need for Earth orbital transfer vehicles (OTV's) (refs. 4 to 6), have rekindled interest in aerobraking and aerocapture techniques for proposed Earth and planetary missions. A vehicle configuration proposed for missions to a number of planets (refs. 2 and 3) is a spherically blunted biconic with the

fore-cone section bent upward relative to the aft-cone section to provide self-trim capability. This type of vehicle is also a viable candidate as a moderate lift-drag OTV (refs. 4 to 6) and offers many advantages as a reentry vehicle (ref. 7). Because of the scarcity of experimental data for bent-nose biconics, a study was initiated at the Langley Research Center to establish a comprehensive data base. To date, aerodynamic coefficients, pressure distributions, oil-flow patterns, and shock shapes have been measured and reported on 2.9-percent-scale models of the proposed configuration and this configuration without a bent nose (straight biconic). (See refs. 8 to 10.) These measurements have been made in three conventional-type hypersonic wind tunnels, namely, the Langley 20-Inch Mach 6 Tunnel, the Langley 31-Inch Mach 10 Tunnel (formerly known as the Langley Continuous-Flow Hypersonic Tunnel), and the Langley Hypersonic CF_4 Tunnel, thereby providing a range of Mach numbers, Reynolds numbers, and ratios of specific heats.

As a continuation of this establishment of an experimental data base, heat-transfer distributions and shock shapes were measured on a 1.9-percent-scale model of the proposed configuration (bent-nose biconic) and on the straight biconic in the Langley Expansion Tube[1], which is described in references 11 to 14. This facility is capable of generating a range of hypersonic-hypervelocity flow conditions in arbitrary test gases about stationary models, thereby allowing real-gas effects (results of vibrational excitation, dissociation, and ionization) on the flow about various configurations to be examined in gases corresponding to planetary atmospheres. Test gases chosen in the present study were: (1) carbon dioxide (CO_2), the primary constituent of Mars and Venus atmospheres; (2) nitrogen (N_2), the primary constituent of the Titan atmosphere; (3) air, the Earth atmosphere (corresponding to a density altitude of 67 km for the present scale model); and (4) helium (He), which behaves as an ideal gas over a wide range of flow conditions (ref. 14). The corresponding range of calculated equilibrium normal shock density ratios for the four test gases was 4 to 19 for free-stream Mach numbers from 6.0 to 9.0 and free-stream velocities from 4.5 to 6.9 km/sec. Thus, the biconic models were tested in ideal-gas and real-gas flow environments in the same facility, thereby reducing uncertainties associated with testing in several facilities having different flow characteristics, instrumentation, and data-acquisition systems.

The purposes of this report are: (1) to examine the effects of nose bend and angle of attack on heating distributions for the biconics, (2) to examine the effects of different test gases having a range of calculated equilibrium post-shock ratios of specific heats from 1.13 to 1.67, and (3) to compare measurements with predictions from a three-dimensional parabolized Navier-Stokes (PNS) code (refs. 15 to 17). Because heat-transfer measurements for bent-nose biconics are particularly scarce in the open literature, the present data represent a step toward filling this void. Hopefully, the data base established in references 8 to 10 and in the present study will provide an improved understanding of the flow characteristics about biconics at hypersonic conditions and will also provide the opportunity for comparisons with flow-field computer codes.

---

[1]Operation of the Langley Expansion Tube was terminated at the completion of the present study in December 1982. The facility was placed on standby for approximately 18 months and then disassembled and removed from its original site in late 1984.

APPARATUS AND TESTS

Facility

The Langley Expansion Tube (refs. 11 and 12) is basically a 15.24-cm-diameter tube divided into three sections by two diaphragms; thus, this facility may be viewed as two shock tubes in tandem. The upstream section is the driver, or high-pressure, section and is pressurized at ambient temperature with a gas having a high speed of sound. (Greater operation efficiency is realized as driver-gas speed of sound increases.) The intermediate section, sometimes referred to as the driven section, is evacuated and filled with the desired test gas at ambient temperature. The driver and driven sections are separated by thick steel diaphragms (double-diaphragm apparatus). The downstream section is referred to as the acceleration, or expansion, section. A weak, low-pressure diaphragm (secondary diaphragm) separates the intermediate and acceleration sections. The isentropic, unsteady expansion resulting from the rupture of this thin Mylar[2] film diaphragm generates hypersonic and hypervelocity flow at the acceleration section exit from the low Mach number shock-tube flow which encounters the secondary diaphragm. Test models are positioned at the exit of the acceleration section. Flow through this section exhausts into a dump tank; hence, models are tested in an open jet. The operating sequence of the expansion tube is shown schematically in figure 1 and discussed in detail in reference 18.

Models

Sketches and dimensions of the biconic models are shown in figure 2, and a photograph of the bent-nose biconic model installed in the test section of the expansion tube is shown in figure 3. The bent-nose-biconic model represented a 1.9-percent-scale model of the proposed Mars sample-return, single-mission vehicle (ref. 2). The models were fabricated from stainless steel except for the nose tips, which were fabricated from MACOR[3] machinable glass-ceramic (ref. 19). Each model contained five slots for instrumented inserts (MACOR glass-ceramic substrates), the surfaces of which were contoured to the conic section. (See fig. 4.) Two slots were machined along the most windward ray (ϕ = 180°), two along the most leeward ray (ϕ = 0°) (one on the fore-cone and one on the aft-cone), and one along the ray 90° from the most leeward ray of the aft-cone (ϕ = 90°).

Instrumentation

Heat transfer.- Thin-film resistance gages (refs. 20 and 21) were used to measure heat-transfer rates during the 250-μsec test period of the expansion tube. Eight palladium gages, each approximately 120 nm thick, were deposited along the polished surface of each MACOR glass-ceramic substrate; a single thin-film gage was deposited at the spherical nose tip. Each gage was in the form of a serpentine pattern (as shown in ref. 20) and provided nearly a point measurement since the sensing surface was 1.02 mm by 1.27 mm. (It should be noted that the serpentine palladium sensing element covered a region within 10° of the stagnation point of the nose tip at zero incidence; thus, the heating rates inferred from this element are

---

[2]Mylar is a registered trademark of E. I. du Pont de Nemours & Co., Inc.
[3]MACOR is a registered trademark of Corning Glass Works.

slightly lower than the stagnation-point heat-transfer rate.) Gages were covered with Al_2O_3 approximately 500 nm thick to prevent the gage from becoming electrically shorted because of the ionized flow over the model. The MACOR glass-ceramic substrates were 5.1 mm thick and 6.4 mm wide; thus, the serpentine sensing element was 2.5 mm from the edges of the substrate. This relatively large thickness and width ensured the substrates behaved as semi-infinite media during the 250-μsec test time, thereby satisfying the basic assumption of the data reduction procedure used for thin-film gages (refs. 20 to 23). Each gage was calibrated in a well-stirred oil bath for temperatures of 297 K to 380 K, thereby covering the range of surface temperatures experienced during most tests with the exception of the gage at the tip of the spherical nose, where surface temperatures were much higher. A constant current of 2 mA was maintained through each gage, which is sufficiently low to avoid ohmic heating effects (ref. 20).

Heat-transfer rates were determined by using two methods: (1) numerical integration of the surface temperature change as a function of time (refs. 20, 22, and 23), and (2) use of the analog circuit described in reference 21. The first method accounts for the variation of substrate thermal properties with temperature (refs. 20 and 23), but requires considerable time on the desktop computer used to reduce the data. The analog circuit method requires little computer time and was used for gages experiencing low surface temperatures during the run. Heat-transfer rates on the nose, on the windward ray of the fore-cone, and on alternate gages on the windward ray of the aft-cone were determined from numerical integration; heat-transfer rates for the remaining gages were obtained with the analog circuits.

Signals from the thin-film gage on the spherical nose and from the 32 gages located along the most windward and most leeward rays were recorded at 400 kHz (2.5 μsec between data samples) with a transient-waveform recording system. Digital data from this analog-to-digital system was retrieved with a Hewlett-Packard 9845T computer and reduced to time histories of the heating rate. Output signals for the eight thin-film gages located along the 90° ray were recorded from an oscilloscope with a camera. Sample time histories are shown in figure 5 for a windward gage and for a leeward gage on the straight biconic in air. The heating rate for the windward gage was determined numerically, whereas that for the leeward gage was obtained with the analog circuit.

Flow visualization.- Shock detachment distance was obtained by using a single-pass schlieren system with a xenon arc lamp as a light source. This point light source, having a duration of approximately 150 nsec, was discharged just prior to termination of the useful test period. (See fig. 5(b).) Representative schlieren photographs are shown in figure 6 for the bent-nose biconic model in CO_2.

Facility flow quantities.- Incident shock velocity at the tube exit (test section) was determined by applying a least-squares curve fit to the average shock velocity between successive instrumented stations (ref. 24). The time required for the shock to travel between stations was obtained from counter-timer readings of the "stop" signals supplied by pressure transducers and heat-transfer gages mounted flush with the tube wall. Tube wall pressures and pitot pressures were measured with piezoelectric (quartz) transducers in conjunction with charge amplifiers. (It should be noted that pitot pressures were measured during calibration tests performed prior to this study (see appendix A) but were not measured for tests with the biconic models, as discussed subsequently.) Free-stream static pressures were inferred from measurements from a transducer located 1.7 m upstream of the tube exit; the variation in static pressure between this station and the tube exit is expected to be small (within experimental uncertainty).

Test Conditions

The driver gas was unheated hydrogen at a nominal pressure of 4.14 Pa, and the double-diaphragm mode of operation (refs. 11 to 14) was used to reduce randomness in the pressure ratio across the primary diaphragm at the time of rupture. Test gases were He, N_2, dry air, and CO_2. For a given test, the acceleration gas was the same as the test gas but at a lower initial pressure. (See appendix A and ref. 12.) Flow conditions for this study correspond to the optimum flow obtained with each test gas (ref. 12), and no attempt was made to operate the facility at off-optimum conditions for any of the test gases in order to match Mach numbers or Reynolds numbers or both. Representative values of the quiescent-test-gas pressure and of the acceleration-gas pressure for the various test gases are presented in the figures of appendix A.

Free-stream and post-normal-shock flow conditions were determined by using the thermochemical equilibrium program of reference 25 modified to include He. Based on the findings of references 26 and 27, the free-stream flows for He, air, and CO_2 were believed to be in thermochemical equilibrium; free-stream flow for N_2 was assumed to be in thermochemical equilibrium. The program of reference 25 accepts free-stream static pressure, free-stream velocity, and pitot pressure as inputs. The free-stream static pressure was assumed to be equal to the measured tube wall pressure near the tube exit, free-stream velocity was assumed to be equal to the incident shock velocity at the tube exit (refs. 14 and 26), and pitot pressure corresponded to a mean value across the inviscid test core as inferred from tests with a pitot-pressure survey rake performed prior to the present study. Nominal values of the measured inputs to the program of reference 25 are presented in table 1, and the corresponding free-stream and post-normal-shock flow conditions are given in table 2. Because of the relatively small values of free-stream Reynolds number and the small model size, flow over the models was probably laminar for all test gases.

The models were tested at angles of attack α from 0° to 20° referenced to the axis of the aft-cone section. Both biconic models were tested in 4° increments in air; for the other three test gases, the biconics were tested at α = 0°, 4°, 12°, and 20°. The straight biconic was rolled at α = 12° in air to provide a more detailed circumferential heating distribution. At α = 0°, the spherical nose tip of the straight biconic was located 1.27 cm downstream of the tube exit. Based on the calibration results of appendix A and on other unpublished calibration results, the models were located within the inviscid test core and in a region of uniform axial flow for all angles of attack. However, the shock layer about the models was not always within the test core, particularly on the leeward side and at the higher angles of attack.

Data Reduction and Uncertainty

Heat transfer.- The numerical method used to compute heat-transfer rates from the output of the thin-film resistance gages is discussed in reference 20, and the analog circuit method is discussed in reference 21. Also included in reference 20 is a discussion of the calibration procedure used to determine the temperature coefficient of resistance of each gage and the contributors to the uncertainty in the heat-transfer rate inferred from thin-film gages. Primary contributors for the present study are believed to be the uncertainty in the thermal properties of MACOR glass-ceramic, the changes that occurred in gage properties for gages that were used in successive tests without recalibration, and the poor signal-to-noise ratio experienced during a number of tests.

The heat-transfer rate inferred from a thin-film gage is directly proportional to the thermal product of the substrate $\beta_s = (\rho_s c_s k_s)^{1/2}$. Because of the acknowledged uncertainty in β_s for MACOR glass-ceramic (ref. 20), a study was performed in which thin-film gages with MACOR glass-ceramic, quartz, and Pyrex 7740[4] glass substrates were tested simultaneously in two conventional hypersonic wind tunnels at Langley. By comparing the heat-transfer rates for the MACOR glass-ceramic substrates with those for the other two substrates (for which β_s is more accurately known), a determination of β_s for MACOR glass-ceramic is possible. The results of these tests are discussed in appendix B. The tests were performed after the present biconic tests in the expansion tube. Based on the findings presented in appendix B, the values of heat-transfer rate $\dot{q}$ originally inferred for the biconic models are corrected for the error in β_s by simply multiplying $\dot{q}$ by 1.13. That is, the values of $\dot{q}$ presented herein correspond to $\beta_s = 1996$ W-sec$^{1/2}$/m^2-K at $T = 298$ K instead of the value of 1766 W-sec$^{1/2}$/m^2-K from reference 20.

The maximum increase in substrate surface temperature experienced during the 250 μsec test period (other than at the spherical nose tip) was about 100 K. This increase, which occurred on the windward ray of the bent-nose biconic fore-cone section, corresponds to a 6-percent correction in the heat-transfer rate to account for variation in substrate thermal properties (ref. 20 and appendix B). The surface temperature change on the leeward ray ($\phi = 0°$) was roughly a factor of 10 smaller, and no correction was made to the substrate thermal properties.

In an effort to minimize the uncertainty associated with the data-acquisition system (i.e., the constant-current circuit, amplifier, cables, and analog-to-digital waveform recorder), the thin-film-gage circuits and the analog-to-digital recording system were calibrated as a unit. An accurately known voltage was placed into each circuit and compared with the value retrieved by the computer. A correction factor was obtained for each channel; when applied to the value retrieved by the computer, this factor brought the value into exact agreement with the input voltage. In general, this correction factor was within 4 percent of unity. Calibrations were performed prior to, during, and immediately after the test series. Correction factors for 30 of the 33 channels varied less than 2 percent over the course of the test series, and the remaining channels were within 6 percent.

Values of heat-transfer rate presented herein were obtained from second-order least-squares curve fits of the time histories of the measured heating rates. These curve fits were performed for the time interval of relatively constant heat-transfer rate between the post-flow establishment period and either the flow breakdown or the disturbance caused by the schlieren spark. (See fig. 5.) The present data correspond to a time of 200 μsec.

In previous tests, all thin-film gages used in models that faced into the expansion tube flow were destroyed. However, even though the models were sandblasted during the post-run period (see fig. 4(b)), a surprising number of gages survived in the present study at the lower angles of attack. At the higher angles of attack, most gages on the windward ray were destroyed, but those shielded from the flow on the leeward ray survived. This survival allowed substrates to be used for more than one test, but often at a sacrifice in resolution and accuracy. The loss of accuracy is a result of sandblasting and possible annealing of the gage (ref. 20). Time

[4]Pyrex 7740 is a trademark of Corning Glass Works.

constraints prohibited the substrates from being removed, recalibrated, and reinstalled. In the case of a substrate being tested twice, only data for gages having a relatively small change in resistance (less than 10 percent) are presented. Previous experience (ref. 20) has shown that although the gage resistance may change significantly between runs, the change in the temperature coefficient of resistance is usually small and generally may be neglected.

When the flow over the thin-film gage is ionized and the gage is not adequately protected from electrons, shorting of the gage can occur (ref. 28). The present thin-film gages were covered with a layer of Al_2O_3 to shield the palladium element from electrons, but it is difficult to provide an impermeable cover without introducing significant thermal lag because of the cover thickness. No gage shorting was experienced for the He flow, nor was shorting experienced for CO_2. However, most of the thin-film gages experienced a negative output signal upon arrival of the acceleration gas for the air (fig. 5) and N_2 tests. The output of the thin-film gages for air and N_2 tests fully recovered from the initial negative deflection shortly after arrival of the test gas. Gage shorting is believed to have been restricted to the acceleration gas phase of the expansion tube flow, and the test flow period was free of shorting.

From the probable sources of errors discussed in reference 20, the maximum uncertainty in measured heat-transfer rate along the most windward ray is believed to be less than 10 percent, and the rate along the most leeward ray is believed to be less than 15 percent. This larger uncertainty on the leeward ray is due to the lower values of heating on this ray when the model is at incidence, resulting in lower gage output and larger signal-to-noise ratio. Also, relatively large oscillations in the heat-transfer rate time histories were observed on the leeward side, particularly at the higher angles of attack, and were attributed to the flow establishment process and possible unsteady nature of the vortex system resulting from cross-flow separation. Other factors that may contribute to the overall uncertainty in the present heat-transfer data are discussed in appendix C.

Shock shape.- The shock detachment distance from the model surface was read manually from the schlieren photographs using a digitizing system having a sensitivity of 100 counts per 2.54 mm. The maximum uncertainty in measured shock detachment distance is probably less than 5 percent.

Flow conditions.- Uncertainties in the measured and calculated nominal free-stream and post-normal-shock flow conditions for the four test gases depend primarily on: (1) the precision associated with the measurement of the tube wall static pressure p_w, incident shock velocity $U_{s,10}$, and pitot pressure $p_{t,2}$; (2) the run-to-run repeatability of these quantities, always a primary concern with impulse-type facilities; and (3) the validity of the assumptions made concerning the use of these measurements.

Careful and frequent calibrations of the pressure transducers demonstrated that measured values of p_w and $p_{t,2}$ were accurate to within 10 and 6 percent. Shock velocity $U_{s,10}$ is believed to have been accurate to within 2.5 percent (ref. 26). Nominal values of measured p_w and $U_{s,10}$ for each test gas were obtained from calibration tests with a pitot-pressure survey rake performed prior to this study (appendix A) and from tests with the biconic models. Because the diameter of the inviscid test core was only 7.5 to 10.0 cm (refs. 12 and 14 and appendix A), the relatively large models prohibited installation of a pitot-pressure probe in the inviscid test core without disturbing the model flow field. Thus, the nominal value

of pitot pressure presented in table 1 for each test gas was inferred from pitot-pressure surveys measured with nearly the same H_2 driver conditions and the same initial pressures in the intermediate section and the acceleration section as for the tests with the biconic models. (See appendix A.) This procedure for determining flow conditions is the same as that used in reference 26 for the He driver.

Data scatter between the various calibration runs and runs with the biconic models was small (less than 8 percent for p_w and $p_{t,2}$ and 3.5 percent for $U_{s,10}$) primarily because of the double-diaphragm mode of operation. (See appendix A.) Based on unpublished pressure distributions measured on a sharp-leading-edge flat plate for the four test gases, the assumption that $p_\infty = p_w$ is believed valid. As mentioned previously, the present flow conditions for each test gas corresponded to the optimum flow quality obtainable for that gas. One criterion for the determination of the optimum flow condition was that the pitot pressure be essentially constant with run time. As observed in reference 29, the variation in flow velocity during the test period is small relative to the variation in pitot pressure. This implies the flow velocity U_∞ was constant with run time for the present study. The assumption that $U_\infty = U_{s,10}$ is believed reasonable for the present flow conditions, based on the findings of references 14 and 26. The sensitivity of calculated free-stream and post-normal-shock flow conditions (including stagnation-point heat-transfer rate of a sphere $\dot{q}_{sph}$) to these uncertainties in measured inputs are presented in table 3 and discussed in reference 26. (The sign (positive or negative) of the uncertainty in the three inputs was selected to yield the maximum corresponding uncertainty in calculated free-stream Mach number and Reynolds number. From table 3, the maximum uncertainty in $\dot{q}_{sph}$ is 8 percent, which is about the experimental uncertainty.)

Calculated stagnation-point heat-transfer rate of a sphere.- Heating distributions on the biconics are presented herein in terms of the free-stream Stanton number $N_{St,\infty}$ and as the ratio of surface heat-transfer rate to predicted stagnation-point heat-transfer rate of a sphere with radius equal to the biconic nose radius $\dot{q}/\dot{q}_{sph}$. The wall enthalpy h_w required to compute $N_{St,\infty}$ corresponds to a wall temperature equal to 300 K. Values of $\dot{q}_{sph}$ for the four test gases were obtained from the thermochemical equilibrium calculations of reference 30, in which $\dot{q}_{sph}$ was correlated to provide the simple expression

$$\dot{q}_{sph} = K\left(\frac{p_{t,2}}{r_n}\right)^{1/2}(h_{t,2} - h_w) \qquad (1)$$

Values of $\dot{q}_{sph}$ obtained from this equation and presented in table 2 correspond to nominal values of $p_{t,2}$ and $h_{t,2}$, the biconic nose radius r_n of 3.835 mm, and h_w evaluated at $T_w = 300$ K. Values of the proportionality constant K used are given in the following table:

Gas	K, kg/sec-m$^{3/2}$-atm$^{1/2}$
He	0.0797
N_2	.1112
Air	.1113
CO_2	.1210

Comparison of $\dot{q}_{sph}$ predicted with equation (1) for air to that predicted with the generally accepted theory of Fay and Riddell (ref. 31) shows that the Fay-Riddell value is approximately 8 percent higher than equation (1). There is also an indication that $\dot{q}_{sph}$ predicted with equation (1) for N_2 and CO_2 will be less than that obtained from other studies (refs. 32 and 33). Because reference 30 includes correlations for all four test gases, it was decided to use just this one source for $\dot{q}_{sph}$ so the procedure for obtaining $\dot{q}_{sph}$ for all four test gases was the same.

PREDICTION METHOD

Heating distributions were computed with a computer code that solves the steady, three-dimensional "parabolized" Navier-Stokes (PNS) equations (refs. 15 and 16). This code, obtained from the late John V. Rakich of the NASA Ames Research Center, requires supersonic flow above the boundary layer in the downstream marching direction from the starting plane of data at or in front of the sphere-cone junction. (This starting plane of data is determined from the Navier-Stokes solution over a sphere by using the finite-volume, adaptive-grid algorithm described in ref. 34.) The bow shock is treated as a discontinuity by using the Rankine-Hugoniot relations. A total of 50 points are taken between the shock and the surface along an axis-normal coordinate, and the number of points in the boundary layer is varied with angle of attack to account for the thinning of the boundary layer.

The PNS code has been modified to include the straight-biconic and bent-nose-biconic geometries, and increased circumferential resolution was added (ref. 17). Also added was the capability of computing real-gas effects of C, H, He, O, and N systems by coupling the vectorized chemical equilibrium code of reference 35 with a variable-effective-gamma (VEG) capability within the PNS code. This VEG option utilizes the underlying perfect-gas code structure to perform equilibrium-gas calculations; the program is described in reference 17. Gamma is defined in the VEG option as the ratio of enthalpy to the internal energy of the gas mixture referenced to 0 K. This PNS code was applied to the straight biconic and to the bent-nose biconic in He and to the straight biconic in air over the present range of angles of attack. The nominal flow conditions for He and air tabulated in table 2 were used as input to the PNS code.

RESULTS AND DISCUSSION

Because the data provide the opportunity to compare measurement with prediction from various perfect-gas and real-gas flow-field computer codes and because it is difficult to extract data from figures, the measured heat-transfer rates for both biconic models in all four test gases are presented in tables 4 to 11. Appendix D contains discussions about flow establishment over the models, model surface conditions (catalytic or noncatalytic), flow chemistry (equilibrium or nonequilibrium), and viscous effects.

Effect of Nose Bend

Bending the fore-cone section upward relative to the aft-cone section provides aerodynamic advantages (refs. 2 and 3) because of the asymmetry, but at an expected penalty of higher heating rates on the fore-cone section. To examine the effect of this nose bend, heating distributions for the bent-nose biconic are compared with

those for the straight biconic in figures 7 to 9 for various angles of attack. Longitudinal heating distributions along the most windward and most leeward rays are shown for He in figure 7 and for air in figure 8. The ratio of windward heat-transfer coefficient for the bent-nose biconic to that for the straight biconic is shown in figure 9 for all four test gases.

Naturally, at zero incidence (figs. 7(a) and 8(a)), higher heating occurs along the most windward ray ($\phi = 180°$) of the fore-cone and lower heating occurs along the most leeward ray ($\phi = 0°$) because of the nose bend. The nose bend causes a decrease in the windward aft-cone heating for air (fig. 8(a)), indicating qualitative agreement with the pressure distributions of reference 8 for Mach 6 ideal air. (The nose bend resulted in a reduction of surface pressure along the most windward ray of the aft-cone by 10 to 15 percent at zero incidence in reference 8.) This decrease in windward aft-cone heating for air is attributed to the larger expansion at the junction of the fore-cone and aft-cone for the bent-nose biconic. However, such a decrease in aft-cone heating is not observed for He (fig. 7(a)). The decrease in windward heating due to this expansion at the fore-cone/aft-cone junction corresponds roughly with the surface inclination change; that is, between the last gage on the fore-cone and the first gage on the aft-cone, $N_{St,\infty}$ decreases about 1.3 to 1.5 for the straight biconic (surface inclination change of 5.8°) and approximately twice this for the bent-nose biconic (change of 12.8°, or roughly twice that of the straight biconic) for all four test gases.

At zero incidence (figs. 7(a) and 8(a)), the nose bend causes a larger variation in heating with z/L on the most leeward ray of the fore-cone, a smaller variation on the aft-cone, and a decrease in leeward heating level by a factor of two to three for all test gases. When α is increased to 4° (not shown), corresponding to the leeward side of the bent-nose biconic being nearly shielded from the free-stream flow, the leeward heating distributions for the two biconics begin to converge with increasing distance from the nose tip. At $\alpha = 12°$ (figs. 7(b) and 8(b)), corresponding to the leeward side of the straight biconic being almost shielded from the free-stream flow and the bent-nose biconic being fully shielded, leeward heating still decreases with increasing x/L for the straight biconic but increases with z/L for the bent-nose biconic. These trends cause the leeward heating distributions for the two biconics to cross at about 40 percent of the body length. At $\alpha = 20°$, the leeward heating along the fore-cone and the aft-cone of the bent-nose biconic exceeds that for the straight biconic in air and, for the most part, in He. Similar trends were observed for the other gases and are consistent with leeward cross-flow separation (e.g., refs. 8 to 10 and 36 to 38), as discussed in the next section.

As shown in figure 9, where the windward heating for the bent-nose biconic nondimensionalized by that for the straight biconic is plotted as a function of distance from the nose tip, the penalty, or increase, in windward fore-cone heating because of the nose bend diminishes rapidly with increasing angle of attack. For example, the increase in windward fore-cone heating because of the nose bend is about a factor of 1.7 to 2.0 at $\alpha = 0°$ for the four test gases (fig. 9(a)); however, this factor is only about 1.1 to 1.2 at $\alpha = 20°$ (fig. 9(c)), which is the design trim angle of attack for the bent-nose biconic (refs. 2 and 3). This relatively modest penalty in windward fore-cone heating at the design trim angle of attack should be of interest to the designer of this type or similar types of biconic vehicles. Another point of interest to the designer sizing the thermal protection system for such a biconic vehicle is the decrease in windward aft-cone heating caused by the nose bend, since the aft-cone surface area represents roughly 60 percent of the total surface area. Thus, the penalty in thermal protection system weight because of the increase in windward fore-cone heating resulting from the nose bend is partially offset by a

reduction in windward aft-cone heating. At $\alpha = 0°$ (fig. 9(a)), the nose bend causes a decrease in windward aft-cone heating for air, N_2, and CO_2, whereas the heating for He is essentially unaffected by the bend. This departure of windward aft-cone heating in He from the other test gases may be primarily due to the lower values of the ratio of specific heat γ within the shock layer for these gases as compared with He. A lower value of γ is expected to cause a larger expansion at the junction and, hence, a lower aft-cone surface pressure (ref. 10) and heat transfer. At $\alpha = 12°$ and $20°$ (figs. 9(b) and 9(c)), windward heating on the aft-cone of the bent-nose biconic is less than the straight biconic for all test gases. In general, the difference in windward aft-cone heating between the two biconics at a given angle of attack is less than 10 percent for He. This relative independence of windward aft-cone heating to nose bend in He ($\gamma = 1.67$) is in qualitative agreement with the perfect air ($\gamma = 1.40$) pressure distributions presented in references 8 and 9.

Effect of Angle of Attack

The effect of angle of attack on heating for the biconics in air is presented in figures 10 and 11. Heating on the windward ray increases orderly with angle of attack for both biconics and all test gases (as expected), but the relative effect of α on heating decreases with increasing α (figs. 10(a) and 11(a)). For the present range of α ($0° \leq \alpha \leq 20°$), the windward heating for the bent-nose biconic increases roughly by a factor of two on the fore-cone and by a factor of three to four on the aft-cone (fig. 12). Heating along the midmeridian ray ($\phi = 90°$) on the aft-cone of the straight biconic is nearly constant over $0° \leq \alpha \leq 20°$ for air test gas (fig. 13). This trend is in agreement with the pressure distributions measured along this ray at Mach 6 in ideal air (refs. 8 and 9) and with heat-transfer measurements on cones (e.g., ref. 39). The sensitivity of windward heating, for a given value of x/L or z/L, to angle of attack for both biconics in air is shown in figure 14(a) in terms of the fore-cone angle of attack α_f and aft-cone angle of attack α_a. ($\alpha_f = \alpha$ for straight biconic and $\alpha_f = \alpha + \eta$ for bent-nose biconic; the aft-cone angle of attack $\alpha_a = \alpha$ for both biconics.) Reasonably good agreement in windward heating is observed for the fore-cone of the two biconics, as expected, and the variation of heating with angle of attack is nearly linear. The aft-cone heating varies linearly with angle of attack for both biconics, but the heating is less for the bent-nose biconic because of the larger flow expansion at the junction.

The effect of angle of attack on leeward heating is not nearly as orderly as on the windward side (figs. 10(b) and 11(b)). Leeward heating initially decreases as α is increased from 0° but reaches a point where it then increases with increasing α. This trend, which was observed for all test gases, is illustrated in figure 14(b) for both biconics in air. When presented in this manner, the angle of attack at which a change in the trend occurs for a given x/L or z/L becomes more apparent. For example, the leeward heating on the aft-cone ($x/L \approx 0.78$) of the straight biconic decreases with increasing α up to $\alpha = 12°$ but then increases for $\alpha > 12°$. This increase in leeward heating with increasing α is probably due to cross-flow separation and the formation of longitudinal vortices. The oil-flow patterns of references 9 and 10 show that a "stagnation-line" type of flow is created on the most leeward ray by the mutual action of counterrotating longitudinal vortices that reattach on this ray. For the low Reynolds numbers of this study, the leeward separated flow should be free of any secondary vortices (refs. 10 and 40). The reattachment of the primary vortex results in the heating on the most leeward ray being higher than just off this ray, as is evident from the circumferential heating distribution shown in figure 15 for the straight biconic at $\alpha = 12°$ and from the

data of reference 41. From figure 14(b), the variation of leeward heating on the fore-cone is similar for the two biconics, with the heating increasing for $\alpha_f \geq 15°$. However, the nose bend causes leeward cross-flow separation to occur at a lower angle of attack on the aft-cone, thereby resulting in higher leeward heating for the bent-nose biconic at $\alpha > 10°$. The variation of the ratio of windward heating to leeward heating with angle of attack is relatively small for the bent-nose biconic once the leeward flow separates (fig. 11(c)). For this case ($\alpha \geq 4°$) in air, the fore-cone windward heating is 10 to 15 times the leeward heating, but on the aft-cone the windward heating is only 3 to 5 times that of the leeward heating. This ratio for the straight biconic (fig. 10(c)) is essentially constant along the length of the model as long as the flow remains attached (i.e., $\alpha \leq 8°$).

The effect of angle of attack on measured shock shape is shown in figure 16 for the bent-nose biconic in CO_2. Shock detachment distance on the windward side of the fore-cone is quite small, relatively insensitive to angle of attack for $4° \leq \alpha \leq 20°$, and free of any inflections that might result from the overexpansion of the flow from the spherical nose to the fore-cone. (Close inspection of the schlieren photographs for both biconics shows that a slight inflection may occur at x/L or z/L of about 0.14 for CO_2 and $\alpha_f < 11°$.) The leeward detachment distance is more sensitive to angle of attack and increases with increasing α. Downstream of the inflection in the windward shock due to the flow expansion at the fore-cone/aft-cone junction, the detachment distance decreases with increasing α. At $\alpha = 12°$, the windward shock is nearly parallel to the aft-cone surface, whereas at $\alpha = 20°$, the shock slants inward toward the surface. This inward slant implies a departure from cone-like flow characteristics over the aft-cone and was observed previously in tests performed in a conventional wind tunnel with a test gas having a low value of γ (ref. 10).

Effect of Test Gas

Measured shock shapes for the four test gases are presented in figure 17 for the bent-nose biconic at $\alpha = 4°$. The fact that the shock detachment distance for blunt bodies in continuum (i.e., high Reynolds number regime) hypersonic flows correlates in terms of a single parameter ρ_2/ρ_∞ is well known (e.g., see ref. 26). For this type of flow, the detachment distance decreases with increasing density ratio. This decrease in shock detachment distance with increasing ρ_2/ρ_∞ (or decreasing γ_{eff} (ref. 26) or decreasing γ within the shock layer) also occurs for the relatively slender biconic models (fig. 17), as expected. The effect of density ratio (or of γ_{eff}) on the shock detachment distance diminishes with increasing angle of attack on the windward and leeward sides; that is, a lesser effect of ρ_2/ρ_∞ on windward shock detachment distance occurs as the effective body ($\theta + \alpha$) becomes blunter. The trend on the leeward side is due to the shock inclination downstream of the nose region becoming more dependent on Mach number at the higher α (ref. 8).

Shock shapes measured on the bent-nose biconic in real-air are compared in figure 18 with those measured on a larger scale model at Mach 6.0 in ideal air (refs. 8 and 9) and at Mach 6.3 in CF_4 (ref. 10). The density ratio for CF_4 is close to that for the present real-air results ($\rho_2/\rho_\infty \approx 11.8$ in CF_4 and 11.1 in air), whereas the density ratio for the Mach 6.0 ideal-air flow is 5.3. It should be noted that γ is constant throughout the shock layer for the ideal-air results of references 8 and 9 and is nearly constant for the CF_4 results of reference 10. The equilibrium value of γ varies within the shock layer for real air and is higher than the value of γ for CF_4. (Typically, the equilibrium value of γ in air is 1.16 on the windward side of the fore-cone and 1.19 on the windward side of the aft-cone; γ for CF_4 is

1.12 on the windward side of the fore-cone and 1.13 on the windward side of the aft-cone.) At $\alpha = 0°$ (fig. 18(a)), the detachment distance for real air and for CF_4 are in good agreement over the fore-cone (windward and leeward), but the detachment distance for CF_4 is somewhat less than that for real air downstream of the junction. In the region over the aft-cone, the real-air shock tends to converge toward the ideal-air shock. This trend is expected because of the lower γ for CF_4 in this region but may also be in part due to possible nonequilibrium flow downstream of the junction in air. Similar trends are observed at $\alpha = 20°$ (fig. 18(b)). At this higher α, the windward shock over the aft-cone is essentially parallel to the surface for both real air and CF_4.

Measured heating on the spherical nose tip of the straight biconic at $\alpha = 0°$ is discussed before presenting the effect of test gas on the heating distributions along the conic sections. The measured stagnation-point heat-transfer coefficient was constant to within 6 percent over the time interval 100 to 200 μsec for all test gases, and the surface temperature T_w at $t = 200$ μsec ranged from 425 K for CO_2 to 540 K for air. As discussed previously, these values of surface temperature exceed the range for which the gages were calibrated; however, the calibrations are believed valid for extrapolation to at least 505 K (ref. 20), which covers the range of T_w for all test gases except air. Comparisons of the measured results with predictions based on classic boundary-layer theory (refs. 30 and 31), on the solution of the Navier-Stokes equations (ref. 34), and on an empirical expression (ref. 33) are presented in the following table:

Test gas	t, μsec	T_w, K	$\dot{q}_{t,2,m}$, MW/m^2	Predicted values based on -			
				Classic boundary-layer theory		Navier-Stokes equations	Empirical expression
				$\frac{\dot{q}_{t,2,m}}{\dot{q}_{t,2}}$ (a)	$\frac{\dot{q}_{t,2,m}}{\dot{q}_{t,2}}$ (b)	$\frac{\dot{q}_{t,2,m}}{\dot{q}_{t,2}}$ (c)	$\frac{\dot{q}_{t,2,m}}{\dot{q}_{t,2}}$ (d)
He	160	468	29.3	1.16		1.07	
Air	120	471	38.5	1.22	1.11	1.01	1.10
N_2	140	476	33.5	1.20	1.12		1.16
CO_2	160	408	18.2	.84			.74

[a] $\dot{q}_{t,2}$ from reference 30.
[b] $\dot{q}_{t,2}$ from reference 31.
[c] $\dot{q}_{t,2}$ from reference 34.
[d] $\dot{q}_{t,2}$ from reference 33.

The inputs required for these predictions correspond to the values of T_w tabulated above and to the nominal flow conditions presented in table 2, which are based on the assumption of thermochemical equilibrium. With the exception of CO_2, measurement exceeds prediction from classic boundary-layer theory by 10 to 20 percent. These differences are attributed primarily to the effects of vorticity and viscosity. As

discussed in appendix D, boundary-layer theories underpredict stagnation-point heating for the present range of $R_{2,r_n}/(\rho_2/\rho_\infty)^2$ because shock-induced external vorticity and the interaction of the boundary layer and the outer inviscid flow are significant. The relatively good agreement between measured stagnation-point heating and values predicted with a code that accounts for viscous interaction effects (Navier-Stokes code of ref. 34) also implies that viscous effects are the primary cause of the differences. Other phenomena that may influence the present comparisons are nonequilibrium flow effects and surface catalytic efficiency. Neither of these phenomena are of concern for He but may be for the other test gases, particularly CO_2. MACOR glass-ceramic is expected to have a very low catalytic efficiency, and since each nose tip was tested only one time, the surface was uncontaminated. Thus, surface catalytic efficiency should not be a significant contributor to the observed differences in stagnation-point heating. The results of reference 26 show that the flow in the stagnation region for air, N_2, and CO_2 test gases will be in nonequilibrium or possibly frozen, which will lower the heating. The comparisons for air and N_2 imply that any effect of nonequilibrium flow on stagnation-point heating is small for the present test conditions. This may not be the case, however, for CO_2. The above comparisons for CO_2 may indicate that the effects of flow chemistry dominate over viscous effects.

In examining the effects of nose bend and angle of attack on heating distributions, differences in Mach number, Reynolds number, density ratio (or γ), and wall-temperature ratio $T_w/T_{t,2}$ are not considered explicitly. However, because the expansion tube was operated to yield the highest quality flow for each test gas and M_∞ and R_∞ were not matched for the four gases (see table 2), these four quantities must be considered in any attempt to deduce the effect of test gas on heating. For example, although values of R_∞ for He, air, and CO_2 are relatively close, R_∞ for N_2 is only half as large.

Heating distributions for the four test gases are presented in two forms. As is commonly used in the presentation of distributions, the measured heat-transfer rate is nondimensionalized by the calculated (ref. 30) thermochemical equilibrium stagnation-point heat-transfer rate of a sphere having a radius equal to the spherical nose; that is, heating distributions are presented as $\dot{q}/\dot{q}_{sph}$. (Values of $\dot{q}_{sph}$ are presented in table 2 for the four test gases.) Because laminar heating rates for blunt cones have been correlated reasonably well over a range of Mach numbers and Reynolds numbers by using a viscous-interaction parameter $\bar{v}^*$ (e.g., refs. 42 and 43), this form is also used. The viscous-interaction parameter is defined as $M_\infty\left(C^*/R_{\infty,L}\right)^{1/2}$, where $C^* \equiv \mu^* T_\infty/\mu_\infty T^*$ and the reference temperature T^* used herein is that suggested by Cheng (ref. 44) for blunt cones, $T^* = (T_{t,2}/6)[1 + 3T_w/T_{t,2}]$. As discussed in reference 42, correlation of heating results in terms of $\bar{v}^*$ is limited by cone half-angle, Mach number, and γ. Because the ratio $N_{St,\infty}/\bar{v}^*$ tends to account for the effects of Mach number (e.g., the heating distribution for blunt cones was observed in ref. 42 to be independent of Mach number when expressed in terms of $\bar{v}^*$), Reynolds number, and wall-temperature ratio on heating, it is used for the four test gases. To account for differences in the density ratios between the various test gases, $N_{St,\infty}/\bar{v}^*$ is multiplied by the density ratio ρ_2/ρ_∞ raised to a power.

Heating distributions $\dot{q}/\dot{q}_{sph}$ for the four test gases are presented in figure 19 for the straight biconic and in figure 20 for the bent-nose biconic. As expected, differences occur between the heating distributions for the various gases. For example, $\dot{q}/\dot{q}_{sph}$ on the fore-cone of the straight biconic at $\alpha = 0°$

(fig. 19(a)) is nearly the same for air, N_2, and CO_2 but is lower for He. As the flow expands at the fore-cone/aft-cone junction, the decrease in heating to the aft-cone for CO_2 is greater than that for the other two gases, and $\dot{q}/\dot{q}_{sph}$ for CO_2 approaches that for He. This larger expansion for CO_2 is probably primarily due to γ effects, although nonequilibrium flow effects may also contribute to the lower heating on the aft-cone. The same trends in windward $\dot{q}/\dot{q}_{sph}$ are observed at $\alpha = 12°$ and at $\alpha = 20°$, but the differences in $\dot{q}/\dot{q}_{sph}$ between test gases decrease with increasing α, especially on the fore-cone. Heating distributions on the leeward side exhibit the same trend as those observed on the windward side at $\alpha = 12°$, but the heating ratio for CO_2 is less than for the other gases at $\alpha = 20°$. Basically, the same trends in $\dot{q}/\dot{q}_{sph}$ are observed for the bent-nose biconic (fig. 20) as are observed for the straight biconic. One notable exception is that $\dot{q}/\dot{q}_{sph}$ for CO_2 is lower than for the other gases on the windward and leeward sides of the aft-cone for all angles of attack. As with the straight biconic, $\dot{q}/\dot{q}_{sph}$ on the leeward side of the bent-nose biconic for air and for N_2 either agrees with or exceeds values for He. An interesting feature for CO_2 is that the windward aft-cone heating distributions at the higher angles of attack decrease monotonically immediately downstream of the junction, but then increase in the direction of the base. Schlieren photographs of the bent-nose biconic in CO_2 (fig. 6) revealed that the shock over the aft-cone on the windward side slanted back toward the model surface in the region of the base. This minimum in heating on the windward side of the aft-cone is believed to be characteristic of flows with low γ because it is observed in pressure distributions measured at Mach 6 in CF_4 ($\gamma_{eff} = 1.13$) but not at Mach 6 in air ($\gamma = 1.40$) (ref. 10). The minimum in pressure on the aft-cone was also predicted for CF_4 from a perfect-gas, inviscid flow-field code with γ_{eff} as the input, as discussed in reference 10, and a minimum in aft-cone heating was predicted in reference 3 for CO_2 at Mach 30.

Another observation from figures 19 and 20 concerns the possible effect of free-stream Reynolds number on heating. Although values of free-stream Mach number, free-stream ratio of specific heats, and normal-shock density ratio for air and for N_2 are close (within 7 percent), the free-stream Reynolds number of air is 75 percent greater than that of N_2. The windward heating in air and in N_2 is generally in good agreement for the present range of angles of attack (figs. 19 and 20); however, differences occur in the leeward heating. These results imply an absence of significant Reynolds number effects on windward heating but an increase in leeward heating with increasing Reynolds number at the higher angles of attack. This finding is in qualitative agreement with reference 39. Because the present study was not controlled to explicitly examine the effects of Reynolds number, the implication of a dependence of leeward heating on Reynolds number must be viewed as a conjecture. It should be noted, however, that a strong influence of Reynolds number on leeward surface oil-flow patterns was observed on the larger scale models of these biconics at angles of attack sufficient to cause cross-flow separation (ref. 10). As discussed in reference 45, vortex-induced heating is extremely sensitive to Reynolds number. Thus, it is not surprising to find a corresponding Reynolds number effect on the leeward heating.

Windward heating rates for the four test gases are shown in figures 21 and 22 for the straight biconic and bent-nose biconic in terms of $(\rho_2/\rho_\infty)^{1/4} N_{St,\infty}/\bar{v}^*$ as a function of x/L or z/L. With few exceptions, the air, N_2, and He results are in fairly good agreement for both biconics and $0° \leq \alpha \leq 20°$, particularly on the aft-cone. This good agreement between air and N_2 is expected (provided Reynolds number effects are properly accounted for) because of the similarities in γ within

the shock layer, in Mach number, and in wall-temperature ratio for these two gases. Although the agreement between these two gases and He is encouraging, the parameter $(\rho_2/\rho_\infty)^{1/4} N_{St,\infty}/\bar{v}^*$ does not encompass all the physics and chemistry of the present flow conditions, as indicated by the differences between CO_2 and the other three test gases. The results for CO_2 are consistently lower than for the other gases, suggesting that (1) Mach number effects are not properly accounted for, (2) a greater sensitivity of heat transfer to γ exists at the low values of γ for CO_2, and (3) large nonequilibrium flow effects exist for CO_2.

An engineering method sometimes used to predict windward heat transfer is the effective cone method. With this method, surface-flow properties along the most windward ray of a cone at incidence are approximated with another cone of the same bluntness having an effective cone angle θ_{eff} equal to $\theta + \alpha$. This method does not properly account for three-dimensional effects, which are often quite strong for laminar boundary layers, and tends to underpredict the windward heating (e.g., refs. 46 and 47). Nevertheless, this concept of θ_{eff} is used for the present air results shown in figure 23, in which the parameter $(\rho_2/\rho_\infty)^{1/4} N_{St,\infty}/\bar{v}^*$ is divided by $\sin \theta_{eff}$ and plotted as a function of x/L. This form was selected because previous studies (e.g., 48) have shown that when cone data are expressed as $N_{St,\infty}/\sin \theta$, the data exhibit a relatively small dependence on θ. Results for the straight biconic are shown in figure 23(a) and the effective cone angle θ_{eff} is equal to $\theta_f + \alpha$ for the fore-cone and $\theta_a + \alpha$ for the aft-cone. For $\alpha > 4°$, the fore-cone data correlate reasonably well, as do the aft-cone data for $\alpha > 4°$. The following curve fit expression for the present data

$$N_{St,\infty} = \left[\bar{v}^* \sin \theta_{eff}/(\rho_2/\rho_\infty)^{1/4}\right] [4.355 - 5.970(x/L) + 3.128(x/L)^2] \qquad (2)$$

predicts the windward heating for air, N_2, and He to within 10 percent on both the fore-cone and aft-cone of the straight biconic (fig. 23(a)). This expression also predicts windward heating on the fore-cone of the bent-nose biconic in air, He, and N_2 for $0° < \alpha < 20°$, where $\theta_{eff} = \theta_f + \alpha + \eta$; however, it tends to overpredict windward heating on the aft-cone (fig. 23(b)). A corresponding approximation of windward aft-cone heating for this bent-nose biconic for $\alpha > 0°$ is given by the expression

$$N_{St,\infty} = \left[\bar{v}^* \sin \theta_{eff}/(\rho_2/\rho_\infty)^{1/4}\right] [4.252 - 6.832(z/L) + 3.958(z/L)^2] \qquad (3)$$

It must be emphasized that these expressions (eqs. (2) and (3)) are limited to the present hypervelocity flow conditions, which involve high wall cooling and, because of the small model size, possible viscous effects and nonequilibrium flow effects. These expressions are also limited to the present model geometries because they are based on free-stream flow conditions instead of flow conditions within the shock layer (i.e., local flow conditions). For these reasons, equations (2) and (3) must be used with caution.

There are no established engineering methods for predicting heat transfer on the leeward ray of cones or biconics at angles of attack (refs. 3 and 46). An attempt to correlate leeward heating for cones was made in reference 46, in which $\dot{q}_\alpha/\dot{q}_{\alpha=0}$ was

plotted as a function of α/θ. Although reasonable correlation existed for $\alpha/\theta < 1$, corresponding to attached leeward flow, a wide divergence in $\dot{q}_\alpha/\dot{q}_{\alpha=0}$ was observed as the leeward flow separated for $\alpha/\theta > 1$. With this approach, leeward heating rates for both biconics in air test gas are shown in figure 24, in which $\dot{q}_\alpha/\dot{q}_{\alpha=0,\text{straight}}$ is plotted as a function of α_{eff}/θ. For the straight biconic and for the aft-cone of the bent-nose biconic, $\alpha_{eff} = \alpha$; for the fore-cone of the bent-nose biconic, $\alpha_{eff} = \alpha + \eta$. Good agreement with the correlation of reference 46 is observed for $\alpha_{eff}/\theta < 1$. The agreement worsens for $\alpha_{eff}/\theta > 1$; however, the fore-cone and aft-cone leeward heating for the straight biconic and the fore-cone heating for the bent-nose biconic correlate reasonably well.

Comparison With Prediction

The parabolized Navier-Stokes code described in the section entitled "Prediction Method" was used to provide comparisons with measured shock shapes and heating distributions in He and air. Measured and predicted windward shock detachment distances are presented in figure 25 for the straight biconic in He at $\alpha = 12°$, and the agreement is excellent over the fore-cone. Measured and predicted heating distributions in He are presented in figure 26 for the straight biconic and in figure 27 for the bent-nose biconic. Although the qualitative agreement between measurement and prediction for He is generally good, the quantitative agreement is relatively poor. For example, there is a 10- to 15-percent difference in heating for the straight biconic at $\alpha = 0°$ (fig. 26(a)), and this disparity increases to 20 to 35 percent at $\alpha = 20°$ (fig. 26(d)). Comparisons of heating distributions for the straight biconic in air (fig. 28) show better agreement than observed for He (fig. 26), except for leeward heating at $\alpha = 12°$. The PNS code was run with a constant wall temperature of 324 K in He and 312 K in air. (Measured wall temperatures are shown in tables 4, 6, 8, and 10.) One case was repeated in air for $\alpha = 20°$ using a wall temperature of 360 K, which is more representative of the measured wall temperature on the windward ray of the fore-cone. As can be inferred from figure 28(d), this wall temperature of 360 K is high enough to keep the effect of the measured variation in wall temperature on predicted windward heating to within 2 percent.

The PNS code used does not have the capability for performing nonequilibrium flow calculations. However, as discussed previously, nonequilibrium flow is expected in the nose region and may possibly persist over the conic sections. A limiting case can be performed with the PNS code by assuming the free-stream flow properties are frozen across the bow shock; that is, γ and the molecular weight of the mixture are constant within the shock layer and equal to the free-stream values. The case of the straight biconic in air at $\alpha = 20°$ was repeated with this assumption of frozen flow, and the effects on heating are shown in figure 28(d) and the effects on shock detachment distance are shown in figure 29. The equilibrium and frozen flow calculations bound the shock shape data and most of the windward heating data. The windward heating distribution on the aft-cone follows the trend of the frozen flow calculation more closely than that of the equilibrium flow calculation (fig. 28(d)). Measured shock detachment distance is closer to the frozen flow calculation just downstream of the nose and asymptotically approaches the equilibrium flow value up to the fore-cone/aft-cone junction (fig. 29). The expansion at this junction affects the shock at $x/L = 0.6$, and the measured shock detachment distance folds down more slowly than the equilibrium flow prediction. Although the trends of figures 28(d) and 29 suggest the presence of nonequilibrium flow effects, the experimental uncertainties preclude any definite conclusion on this point.

In reviewing the heat-transfer comparisons of figures 26 to 28, it is disturbing to see that the agreement between measurement and prediction for He, which behaves as an ideal gas for the present conditions, is not as good as that for air. The PNS code has accurately predicted windward heating (within 10 percent) on these same biconic models tested in a conventional wind tunnel at Mach 10 in air (ref. 49), and excellent agreement was obtained with the heating data of reference 50. The poorer agreement obtained herein is believed to be due to experimental errors uniquely associated with the expansion tube or due to the inability of the PNS code to accurately model the flow field for the present low Reynolds number flow conditions or due to both. Potential sources of error in the experimental technique and in the computational method are discussed in appendix C.

CONCLUDING REMARKS

Laminar heating distributions have been measured in the Langley Expansion Tube at hypersonic-hypervelocity flow conditions on a 1.9-percent-scale model of a proposed aeroassisted planetary vehicle. This vehicle is a spherically blunted, 12.84°/7° biconic with the fore-cone bent upward 7° relative to the aft-cone; also tested was a straight biconic (i.e., 12.84°/7° biconic with no nose bend). These tests were performed at free-stream velocities from 4.5 to 6.9 km/sec and Mach numbers from 6.0 to 9.0 with He, N_2, air, and CO_2 test gases. Angle of attack was referenced to the axis of the aft-cone of both biconics and was varied from 0° to 20°. The effects of nose bend, angle of attack, and test gas on heating distributions were examined along with comparisons of measurements in He and air with predictions from a code which solved the three-dimensional "parabolized" Navier-Stokes (PNS) equations.

As expected, the 7° nose bend caused an increase in heating to the windward side of the fore-cone at a given angle of attack as observed from comparisons of the heating distributions on the straight and bent-nose biconics; however, this increase was only 10 to 20 percent at the design trim angle of attack of 20° for the bent-nose biconic. Also important to the designer is the fact that this nose bend caused a decrease in windward heating to the aft-cone. (The aft-cone section represents approximately 60 percent of the vehicle surface.) Aft-cone windward heating was more sensitive to angle of attack than was fore-cone heating, increasing for the bent-nose biconic by a factor of three to four as the angle of attack was increased from 0° to 20° compared with a factor of two for the fore-cone. Leeward heating initially decreased but then increased with increasing angle of attack. This trend was attributed to cross-flow separation on the leeward side when the fore-cone angle of attack exceeds the fore-cone half-angle. (The flow separation resulted in the formation of longitudinal, counterrotating primary vortices that reattached along the most leeward ray, thereby causing an increase in the heat-transfer rate.) The nose bend caused leeward cross-flow separation to occur at a lower angle of attack, diminishing the effect of angle of attack on the ratio of windward heating to leeward heating for the bent-nose biconic. Once the flow separated, windward heating was 10 to 15 times higher than leeward heating on the fore-cone but only 3 to 5 times higher on the aft-cone. The ratio of windward heating to leeward heating for the straight biconic was essentially constant along the length of the model when the leeward flow was attached.

Although Mach number, Reynolds number, ratio of wall temperature to total temperature, and normal-shock density ratio (shock strength) varied for the test gases, windward heating was correlated reasonably well for all the test gases (except CO_2) in terms of the density ratio, the Stanton number, and a form of the viscous-

interaction parameter. Expressed in terms of these parameters, the CO_2 heating levels were consistently lower than the other three gases. Unlike the other three test gases, the aft-cone heating in CO_2 increased in the direction of the base; this trend was attributed to the lower value of γ within the shock layer for CO_2.

Heat-transfer rates measured at the stagnation point of the small spherical nose (radius of 3.835 mm) in He (which behaved as an ideal gas) and in air were within 10 percent (experimental uncertainty) of rates predicted with a code that solves the Navier-Stokes equations. Stagnation-point heat-transfer rates measured in He, air, and N_2 exceeded equilibrium, classic boundary-layer predictions by 10 to 20 percent, and these differences were attributed primarily to the effects of shock-induced external vorticity and to the interaction of the boundary layer and the outer inviscid flow. Predicted stagnation-point heating, however, exceeded measurement by about 20 percent for CO_2, which may indicate that nonequilibrium flow chemistry effects outweigh the effects of vorticity and viscous interaction. (The results of NASA TN D-7800 show the flow in the nose region for air, N_2, and CO_2 test gases was in nonequilibrium and may have possibly been frozen. Also, the assumption was made that the substrates were essentially noncatalytic.) The PNS code underpredicted heating along the most windward ray of both biconics in He for the present range of angles of attack; leeward heating was also underpredicted at the lower angles of attack, but the code tended to underpredict fore-cone heating and to overpredict aft-cone heating at higher angles of attack. Basically, the same trends between measurement and prediction were observed in air. Measured shock detachment distance for the straight biconic in air fell between equilibrium and frozen flow calculations, implying the shock layer flow may have been in nonequilibrium.

Langley Research Center
National Aeronautics and Space Administration
Hampton, VA 23665
September 24, 1984

APPENDIX A

EXPANSION-TUBE FLOW CHARACTERISTICS WITH A HYDROGEN DRIVER GAS

A basic difference between this study and previously reported studies conducted in the Langley Expansion Tube, from a facility operation viewpoint, was the use of hydrogen (H_2) as the driver gas. Although designed for H_2 operation, unheated He was used as the driver gas for facility shakedown, and its use continued until recently. Several factors prompted use of an unheated H_2 driver gas, even in the face of the very stringent safety requirements that accompany its use. The major advantage offered by H_2 was a substantial reduction in the high-pressure pulse that models are subjected to following the 250- to 300-μsec test flow period (ref. 12). Nominal operation with a He driver corresponded to driver-gas pressures of approximately 33 MPa; thus, models were subjected to a 14- to 17-MPa pulse lasting several milliseconds (ref. 12). This pulse often caused extensive damage to the model and to the instrumentation. Now, the introduction of very small, fragile, fast-response-semiconductor pressure transducers (e.g., refs. 51 and 52) brought about the need to drastically reduce the magnitude of this pulse. A reduction by a factor of about 15 was achieved (with no appreciable sacrifice in performance) by using a H_2 driver gas at a nominal pressure of 4.1 MPa. Cost benefits were also realized with H_2, since a smaller quantity of driver gas was required, H_2 was less expensive than He, and thinner steel diaphragms were required for H_2. Naturally, the facility was recalibrated when hydrogen was introduced as the driver gas for the existing test gases and for N_2 test gas as well. The purpose of this appendix is to present a sample of the results of this calibration.

Pitot-Pressure Profiles

Vertical pitot-pressure profiles measured 5.6 cm downstream of the tube exit for He, air, N_2, and CO_2 are shown in figure 30 for a test time t of 200 μsec. These profiles were obtained with the survey rake illustrated in reference 26 and the pitot-pressure probe illustrated in reference 14. Test repeatability (always a primary concern with impulse-type facilities), indicated by centerline pitot pressures, was good (within 5 percent) for He, air, and N_2 and was somewhat less satisfactory (within 8 percent) for CO_2. This poorer repeatability for CO_2 may have been in part due to the difficulty of repeating and maintaining the lower value of quiescent acceleration gas pressure required for the CO_2 tests. The test core was defined as the relatively flat section of the vertical pitot-pressure profile about the tube centerline, for which the pitot pressure was within 10 percent of the average of the three center probes. The boundaries of the test core were uncertain in several instances because of the nature of the pitot-pressure distributions and the relatively large survey-rake probe spacing of 1.91 cm. The test core for all four test gases was approximately half the expansion-tube diameter (7.62 cm). For air, N_2, and CO_2, the product $R_{2,d}(\rho_2/\rho_\infty)^{1/2}$ (where $R_{2,d}$ is the Reynolds number behind a normal shock based on the outside diameter of the flat-faced pitot-pressure probe) was greater than 3000; hence, pitot-pressure measurements in the test core should have been free from viscous effects (ref. 53). Although this product for He was much smaller than for the other gases ($R_{2,d}(\rho_2/\rho_\infty)^{1/2} = 1270$ for He), the results of reference 53 imply that measured pitot pressure in He should also have been essentially free of viscous effects.

APPENDIX A

Tests were performed with the survey rake located 3.1 and 18.3 cm downstream of the tube exit, thus covering the axial region in which the models were located. Sample radial pitot-pressure profiles for the two axial stations are shown in figure 31 for air. These profiles show the flow between these two axial stations was free of any significant axial gradients. A radially and axially uniform test core was found to exist for each of the present test gases over the region occupied by the models.

Heat-Transfer Profiles

Complementary vertical profiles of the heat-transfer rate measured at the center of 6.35-mm-diameter flat-faced quartz cylinders are shown in figure 32 for all four test gases. These profiles were measured at the same two axial stations as the pitot-pressure profiles (x = 3.1 and 18.3 cm) and correspond to a run time of 200 μsec. A complete vertical survey across the entire tube exit (from top to bottom) was not obtained because several shakedown runs were made that resulted in a limited quantity of flat-faced quartz cylinders. This is because each quartz cylinder tested was destroyed during the posttest period. Thus, only 8 cylinders were used in the 13-probe rake so that surveys could be measured for all 4 gases at both axial stations with the existing supply of cylinders. With the exception of N_2, the profiles of figure 32 show the existence of a uniform test core having a diameter approximately half the tube diameter or larger and the absence of significant axial gradients between the two axial stations. There is an indication that a decrease in test-core diameter occurred for the most downstream axial station. The high values of heat-transfer ratio $\dot{q}/\dot{q}_{CL}$ for N_2 at the most upstream station may have been due to the nature of the flow or to a large uncertainty in the heating rate measured on the tube centerline. It should be noted that a similar trend was observed for one out of the eight pitot-pressure survey tests shown in figure 30(c).

Test Repeatability

Run-to-run variation of test-gas and acceleration-gas interface velocity at the tube exit $U_{s,10}$, tube wall static pressure p_w measured 1.7 m upstream of the tube exit, and ratio of tube wall static pressure to pitot pressure $p_w/p_{t,2}$ are shown in figure 33 for a number of expansion-tube runs in N_2. (Similar plots for He, air, and CO_2 test gases are shown in ref. 26 for a He driver gas.) These results were obtained during calibration tests and tests with the biconic models. Values of pitot pressure correspond to the average of the center three pitot-pressure probes of the survey rake used in the calibration tests. The tube wall static pressure and the pitot pressure correspond to a run time of 200 μsec. Data scatter in all three measured flow quantities for N_2 is small. This small degree of data scatter is attributed primarily to the double-diaphragm mode of operation used in this study, the small leakage of the facility while under vacuum, and the conscientious effort to accurately repeat the initial pressures in the intermediate section and in the acceleration section. From figure 33 for N_2 and similar plots for the other three test gases, nominal values of p_w, $p_{t,2}$, and $U_{s,10}$ were obtained and used to calculate test-section flow conditions. These nominal values are presented in table 1, in which the run-to-run variations about the nominal values are also presented. Data scatter for all four test gases is quite small for an impulse facility, and these results demonstrate that flow conditions for this facility may be accurately inferred from tests performed without a measurement of the pitot pressure,

such as in the present study. (See the section entitled "Data Reduction and Uncertainty" in this report.)

The results of this appendix show the existence of an axially and radially uniform test core for He, air, N_2, and CO_2 test gases in the Langley Expansion Tube with a H_2 driver gas. The diameter of this test core was approximately 7.6 cm for He, 8.9 cm for air and N_2, and 10.2 cm for CO_2. Test repeatability was good for all test gases. Comparison of flow conditions obtained with the H_2 driver gas with those of reference 26 for a He driver gas at eight times the pressure of the H_2 driver gas shows no loss in facility performance occurred with the lower pressure H_2 driver gas.

APPENDIX B

COMPARISON OF THIN-FILM RESISTANCE HEAT-TRANSFER GAGES CONSISTING OF QUARTZ, PYREX GLASS, AND MACOR GLASS-CERAMIC SUBSTRATES

Various factors that may contribute to the uncertainty in the inferred heat-transfer rate from thin-film resistance gages are discussed in reference 20. One of the more significant factors is the uncertainty in the thermal properties of the substrate material, and this factor is of particular concern for a MACOR glass-ceramic substrate. The reason for this concern is the heat-transfer rate is directly proportional to the thermal product of the substrate β_s (where $\beta_s = (\rho_s c_s k_s)^{1/2}$), and, as discussed in reference 20, the uncertainty in β_s for MACOR glass-ceramic may be as high as 15 percent, as compared with 2 to 3 percent for quartz. After completion of the tests in the expansion tube with the two biconic models and following the reduction of the heat-transfer data, new information on the thermal properties of MACOR became available. The purpose of this appendix is to present this new information and to discuss its application to the biconic heat-transfer data presented in this report.

Tests were performed in two conventional-type hypersonic wind tunnels, the Langley 31-Inch Mach 10 Tunnel (formerly known as the Langley Continuous-Flow Hypersonic Tunnel) (ref. 20) and the Langley Hypersonic CF_4 Tunnel (ref. 20), a Mach 6 facility that uses Freon 14[5] gas to generate a normal-shock density ratio of approximately 12. Thin-film gages deposited on substrates of different materials were simultaneously exposed to the same hypersonic flow conditions; that is, the high-quality flow of a conventional-type wind tunnel with accurately known flow conditions was used to evaluate certain aspects of the data reduction procedure (ref. 20) for thin-film gages designed for impulse facilities. These tests were designed to make the substrate material the only variable. Small hemispheres (4.1 mm radius) of quartz, Pyrex 7740 glass, and MACOR glass-ceramic, each with a thin-film gage deposited over the stagnation region, were tested. The sensing element for these hemispheres was the same as that used for the biconic models - palladium sputtered onto the surface in a serpentine pattern. The radius of each hemisphere was examined with an optical comparator at a magnification of 20 and measured to within 0.025 mm. (It should be noted that the sensing element covered a region of the nose tip within 9° of the geometric stagnation point; hence, the heat-transfer rate inferred from this element was slightly lower (approximately 1.5 percent) than the actual stagnation-point heat-transfer rate.) Five hemispheres (two MACOR glass-ceramic, two quartz, and one Pyrex glass) were mounted in a survey rake having a probe spacing of 5.1 cm that was injected into the flow such that all five hemispheres were subjected to the same flow conditions at the same time. The primary reason for testing such small hemispheres was to allow several hemispheres to be tested simultaneously without tunnel blockage. Another reason was to obtain heating rates and surface temperatures indicative of the maximum values expected in these facilities.

The excitation current for the five thin-film gages was supplied by a recently fabricated 100-channel system of circuits interfaced to an analog-to-digital Hewlett-Packard 6940B Multiprogrammer and Hewlett-Packard 9826 desktop computer. Each

---

[5]Freon 14 is a registered trademark of E. I. du Pont de Nemours & Co., Inc.

channel supplied a constant current of 1 mA to the gage and contained an amplifier with a maximum gain of 100. This low excitation current ensured negligible ohmic heating effects and is the same current for which the gages were calibrated. The constant-current circuits used for the five hemispheres were calibrated before and immediately after each run and remained unchanged. Each channel was sampled at 50 samples per second.

Two sources of error determined in reference 20 were reduced by the following changes in the fabrication procedure for the thin-film gages: (1) the problem of the resistance of the leads between the sensing element and the wire not being negligible compared with the resistance of the sensing element was corrected by thickening the leads to significantly lower their resistance, and (2) the problem of the thin-film sensing element changing properties from run to run was minimized by an improved annealing procedure for the gages. All gages were calibrated before and after the test series in a well-stirred oil bath with temperature increments of 13.9 K over the temperature range $297 \leq T \leq 380$ K. These calibrations revealed the resistance of four of the five gages remained constant to within 1 percent and the other remained constant to within 3 percent. The temperature coefficient of resistance α_R was determined by applying a linear fit to the variation of resistance with temperature for discrete temperature ranges; thus α_R was a function of temperature, but the variation of α_R was relatively small (less than 3 percent for $297 \leq T \leq 380$ K). This method of determining α_R represents a refinement to that presented in reference 20, and the resulting overall uncertainty in α_R is believed to be less than 2 percent. (The heat-transfer rate is inversely proportional to α_R.) The temperature coefficient of resistance increased 0.9 to 1.4 percent for all five hemispheres between the pretest and posttest calibrations. Characteristics of the five hemispheres prior to the first test in the Mach 10 tunnel are given in the following table:

Hemisphere probe location	Substrate material	Nose radius, mm	$\bar{\alpha}_R$, 1/K	R at 297°K, Ω	I, mA
Top	MACOR glass-ceramic	4.064	2.2430×10^{-3}	78.6	0.999
Next	MACOR glass-ceramic	4.064	2.1715	90.7	.966
Middle	Pyrex glass	4.140	2.0196	134.5	.918
Next	Quartz	4.064	2.0873	108.6	1.005
Bottom	Quartz	4.013	2.1317	111.9	.994

Four runs were made in the Mach 10 tunnel with the five-probe rake, the last run being a repeat of the first, and two runs were made in the CF_4 tunnel. Test conditions were as presented in the following table:

APPENDIX B

Facility	Run	$p_{t,1}$, MPa	$T_{t,1}$, K	M_∞	$p_{t,2}$, kPa
Mach 10	13	2.35	945	9.86	7.46
	14	5.12	974	10.03	15.10
	15	10.96	980	10.16	30.97
	16	2.36	973	9.86	7.46
CF_4	1072	8.02	594	6.41	10.26
	1073	5.76	597	6.38	7.33

As mentioned previously, these tests were designed so the substrate material was the only intended variable; that is, the same geometry and type of thin-film sensing element were tested at the same flow conditions and with the same circuitry and analog-to-digital data-acquisition system. Values of the heat-transfer rate were determined for each hemisphere by using the data reduction procedure of reference 20; thus, the only difference in the method (software) used to compute heat-transfer rate was the different expressions for the thermal properties of the various substrates. Hence, these tests allowed a direct comparison between values of $\dot{q}$ for the MACOR glass-ceramic hemisphere with those for quartz and Pyrex glass to be made. (The comparison with quartz was especially meaningful since the thermal product β_s for this material is accurately known (ref. 23).) To account for the small variation in radii between the hemispheres, the results are presented in the form $C_T/(p_{t,2}/r_n)^{1/2}$, where $C_T = \dot{q}/(T_{t,2} - T_w)$. These data are shown in figure 34 and, for convenience, are tabulated as follows:

Facility	Run	$C_T/(p_{t,2}/r_n)^{1/2}$, $(W/m^2 - K)/(Pa/m)^{1/2}$, and (T_w, K) for -				
		MACOR no. 1	MACOR no. 2	Pyrex	Quartz no. 1	Quartz no. 2
Mach 10	13	0.3424 (399)	0.3285 (397)	0.3709 (403)	0.3742 (417)	0.3655 (413)
	14	.3250 (435)	.3136 (427)	.3758 (437)	.3698 (455)	.3604 (448)
	15	.3171 (480)	.2932 (460)	.3625 (467)	.3505 (482)	.3410 (482)
	16	.3304 (397)	.3121 (396)	.3766 (410)	.3699 (411)	.3650 (422)
CF_4	1072	0.3762 (364)	0.3460 (360)	0.3901 (368)	0.4268 (376)	0.4044 (374)
	1073	.3782 (356)	.3443 (353)	.3887 (360)	.4222 (368)	.3984 (366)

The measured (i.e., inferred) values of $\dot{q}$ and T_w used to compute the above values of C_T correspond to a time of 0.6 sec. ($t = 0$ is defined as the time at which the thin-film gage began its movement into the flow from its sheltered position outside the tunnel nozzle wall.) The heat-transfer coefficient C_T for the hemispheres initially increased rapidly with time (as expected) and began to level off approximately 0.4 sec following the start of the insertion of the survey rake into the flow. These time histories and the output from a switch mounted on the insertion mechanism revealed the hemispheres were well within the inviscid test core of the tunnels by $t \approx 0.5$ sec.

APPENDIX B

As acknowledged in reference 20, the procedure used to account for the variation of β_s with temperature (T_w increases with time) was approximate. The results from the five hemispheres not only provided the opportunity to determine the value of β_s for MACOR glass-ceramic, but also provided the opportunity to evaluate the procedure for accounting for $\beta_s(T)$, since C_T should have remained essentially constant with time. Surface temperature changes up to 270 K were experienced during the present tests over the time interval $0 \leq t \leq 1.4$ sec. For this time interval, the maximum correction to the heat-transfer rate required to account for the change in β_s with temperature was quite large, being 16 percent for MACOR glass-ceramic, 33 percent for quartz, and 59 percent ofr Pyrex glass. Also, T_w at $t = 0.6$ sec exceeded the upper value of temperature for which the gages were calibrated. However, even with the large values of T_w experienced, the variation of C_T over the time interval $0.6 \leq t \leq 1.4$ sec in the Mach 10 tunnel was only ±2 percent for the quartz and MACOR glass-ceramic hemispheres and was ±5 percent for the Pyrex glass hemisphere. These small variations of C_T with time lend credibility to the procedure of reference 20 to account for the variation of substrate thermal properties with temperature.

The heat-transfer coefficient is plotted in figure 34 as a function of the velocity gradient term $(p_{t,2}/r_n)^{1/2}$. As mentioned previously, the substrate material is assumed to be the only variable for a given run. Possible viscous or vibrational relaxation effects, or both, within the shock layer of the hemispheres are assumed to be the same magnitude for each hemisphere for a given run. The average value of $C_T/(p_{t,2}/r_n)^{1/2}$ for the two quartz hemispheres ranged from 1.100 to 1.150 times the average for the two MACOR glass-ceramic hemispheres for the six runs; the average of this range for these runs in both facilities was 1.135 and was 1.133 for the ratio of Pyrex to MACOR. Because the thermal properties for quartz and Pyrex are believed to be accurately known, the present results demonstrate that values of $\dot{q}$ determined with the method of reference 20 for thin-film gages with MACOR substrates will be too small by approximately 13 percent. (Note that $\dot{q} \propto \beta_{s,o}$.) Based on these findings, the following simple expression is recommended to determine $\beta_{s,o}$ for a MACOR substrate at ambient, or prerun, conditions:

$$\beta_{s,o} = 1816.6 + 0.6303T_o \qquad (294 \leq T_o \leq 312 \text{ K}) \qquad \text{(B1)}$$

where the effect of the variation in β with T is accounted for by using the expression

$$\dot{q}(t)_{\beta_s(T)} = \dot{q}(t)_{\beta_{s,o}} \left[1 + (6.38 \times 10^{-4})\ \Delta T_s(t)\right] \qquad (T_s < 450 \text{ K}) \qquad \text{(B2)}$$

The value of $\beta_{s,o}$ from equation (B1) is within 1 percent of the value determined experimentally at Calspan Corp., Advanced Technology Center, Buffalo, New York (2008 W-sec$^{1/2}$/m^2-K at $T = 298$ K). (See ref. 20.) Unfortunately, this Calspan measurement was discarded in reference 20 in favor of properties furnished by the manufacturer of MACOR and inferred from several other sources. Equation (B1) is also within 1.0 percent of the more recent measurements of reference 54 (1979 W-sec$^{1/2}$/m^2-K at $T = 298$ K) and within 3.5 percent of the typical value given for MACOR in reference 55 (2050 W-sec$^{1/2}$/m^2-K at $T = 298$ K). Thus, the initial values of heat-transfer rate for the biconics were simply multiplied by 1.13 to

correct for the error in β_s for MACOR glass-ceramic. Although uncertainties in the heat-transfer rate inferred for a MACOR glass-ceramic substrate still exist (e.g., a ±5 percent uncertainty in β_s between different samples for MACOR glass-ceramic was observed in the tests at Calspan), the application of the findings from these hemispheres to the biconic heating data is believed to substantially reduce this uncertainty.

APPENDIX C

POSSIBLE CONTRIBUTING FACTORS TO DIFFERENCES BETWEEN MEASURED AND PREDICTED HEATING FOR BICONICS

An important phase in most aerothermodynamic studies, experimental or analytical, is the comparison of measurement and prediction. Now, duplication of the flow environment for a full-size reentry vehicle is not possible in existing ground-based facilities; thus, the designer of such a vehicle must rely heavily on flow-field codes that are often verified by data obtained in conventional-type hypersonic wind tunnels. These facilities have relatively low velocities (low enthalpy) and, at best, simulate a portion of the entry corridor. Because the expansion tube generates hypervelocity (high enthalpy) and hypersonic flow over models, this flow being more representative of flight than that obtained in wind tunnels, the present comparisons take on added significance. As discussed previously, the agreement between the present data and the predictions with the parabolized Navier-Stokes (PNS) code for He and air were disappointing. A discussion of factors that may contribute to the observed differences is believed to be beneficial to both experimentalists and operators of similar flow-field codes.

Impulse facilities such as the expansion tube provide a needed capability by generating hypersonic-hypervelocity flow, but often at a sacrifice in the knowledge of the flow conditions and in data accuracy compared with a conventional-type hypersonic wind tunnel. The loss of data accuracy is primarily because of the extremely short test times of impulse facilities, requiring fast-response, high-frequency instrumentation; also, the rather hostile test environment generated in an impulse facility cannot be controlled on a run-to-run basis with the same precision of a conventional tunnel. The purpose of this appendix is to list and briefly discuss factors that may contribute to the differences observed between measured and predicted heating in figures 26 to 28.

Experimental Uncertainties

The primary factors that may contribute to uncertainties in the experimental data are as follows:

1. Uncertainties in the flow conditions.- Such uncertainties stem from (1) the uncertainty in the measurements of p_w, $U_{s,10}$, and $p_{t,2}$, (2) the assumptions that $p_\infty = p_w$ and $U_\infty = U_{s,10}$, (3) the assumption that U_∞ is constant with time, and (4) a lack of definitive knowledge of the free-stream chemical state (thermochemical equilibrium, nonequilibrium, or nonreacting). This last uncertainty is not a concern for He test gas. These assumptions and uncertainties were discussed previously. One uncertainty not discussed previously is the selection of the value of tube wall pressure p_w to be used as input to the program of reference 25 for calculation of the free-stream and post-normal-shock flow conditions. Although pitot pressure was essentially constant over the time interval $100 \leq t \leq 250$ μsec, the tube wall pressure was not constant, as shown by the time histories in figure 35 for air and He test gases. These time histories show that p_w varied 15 to 18 percent over the time interval $100 \leq t \leq 250$ μsec. The value of p_w used as an input corresponds to $t = 200$ μsec and is usually close to the minimum value that occurred over

$100 \leq t \leq 250$ μsec. Thus, this time variation in p_w introduces another uncertainty. However, an indication that the flow conditions for He are known to within reasonable limits is the good agreement obtained between measured stagnation-point heat-transfer rate and that calculated with a Navier-Stokes code (ref. 34).

2. Assumption that flow about the model was fully established.- Time histories of the heat-transfer rate on the windward side implied the flow was steady for at least half of the 250-μsec test time. This was not always the case on the leeward side, and there is some question as to whether sufficient test time was available to establish the detailed structure of the separated leeward flow at the higher angles of attack.

3. Data reduction procedure for MACOR glass-ceramic substrate.- This subject, which also includes uncertainties in the measurement of gage characteristics such as initial voltage and voltage change during a run, is discussed in appendix B and in reference 20. One point that should be noted is that a large number of substrates were used in the present study, thereby involving different pieces of MACOR glass-ceramic. As noted in reference 20, some variation in MACOR glass-ceramic thermal properties was observed between different batches at Calspan, and variation in substrate properties between different batches may have contributed to the uncertainties.

4. Possible contamination of the test gas.- The probable source of contamination would be leaks in the vacuum system and outgassing products. Periodic leak checks were performed throughout the test series; the leak rates for the intermediate section and for the acceleration section were low and remained the same for the present tests. Test gas contamination would be especially detrimental to the flow quality of He, since a relatively small amount of air and water vapor may cause large differences in gas properties. Because care was taken to minimize flow contamination and photomultiplier tubes positioned along the length of the expansion tube did not detect any light during the He tests, the He and the air are believed to have been relatively free of contaminants.

5. Question of the model experiencing uniform flow.- Accurate determination of flow uniformity is extremely important for all facilities and particularly for the expansion tube, since the tube wall boundary-layer thickness is half the tube radius and models are tested in a free jet. Several calibrations of the expansion tube (refs. 11 to 14), including that presented in appendix A, revealed the flow was radially and axially uniform in the region occupied by the biconic models at low angles of attack. The good agreement between heating distributions measured on the leeward ray ($\phi = 0°$) and on the windward ray ($\phi = 180°$) of the straight biconic at $\alpha = 0°$ supported this finding that the flow was uniform. However, at $\alpha = 20°$, the bent-nose biconic occupied a vertical height of 7.6 cm; thus, the bow shock over the entire length of the biconic would not lie within the inviscid test core for any of the test gases. Schlieren photographs revealed that the bow shock at the base plane ($x/L = 1.0$) of the straight biconic at $\alpha = 12°$ was just barely out of the test core for air and N_2 test gases; the bow shock at the base plane for the bent-nose biconic was definitely out of the test core at $\alpha = 12°$. This means that the bow shock for the straight and bent-nose biconics at $\alpha > 12°$ would be out of the test core in He, since the core diameter was smaller for He (see appendix A) and the shock detachment distance was larger. It is doubtful that the bow shock over the entire length of the biconics in He was entirely within the test core for any angle of attack tested. The effect on the surface heating distributions of the shock layer about the biconics encountering the tube boundary layer for x/L or $z/L < 1.0$ is not known. It is

expected to be small at the lower angles of attack and on the windward side of the fore-cone. These biconic models are not expected to produce any blockage phenomena.

6. Model surface effects.- These include mismatches in thermal properties and catalyticity between the steel models and the MACOR glass-ceramic substrates. Although the magnitude of any of the effects resulting from the mismatch in thermal properties is unknown, it is expected to be significant only on the most windward ray at $\alpha > 12°$. This is because of the low surface temperatures at low angles of attack and on the leeward ray. Tests made with and without a noncatalytic cover over the steel model showed the cover had no effect on heating. (See appendix D.) Naturally, surface catalytic efficiency is not a concern for He. Also considered in this category is the fit of the substrate (i.e., did the substrate produce rearward- or forward-facing steps). All substrates were hand-fitted to the models prior to sputtering the thin-film elements on the substrate surface. In all but a few instances, a precise fit of the substrate and the MACOR glass-ceramic nose tip was achieved. The model geometry was verified at the acceptance check and again from the schlieren photographs. The last topic considered under this section is shorting of the thin-film element during the test flow period. Although not a problem for He test gas, some shorting because the Al_2O_3 overlayer was not "pinhole free" may have occurred for air test gas. As discussed previously, there is no evidence to suggest this was a major problem.

7. Uncertainty in angle of attack.- The support system for the expansion tube is designed to vary the angle of attack in discrete increments of 4°. The angle of attack was verified from the schlieren photographs made during the run. In all cases, the measured angle of attack was within ±0.5° of the desired value. As shown in figure 3, the model was supported by a large-diameter short sting and locking nut combination. In a conventional wind tunnel, possible support interference effects may exist with this arrangement and cause the pressure in the base region to exceed that on the aft-cone. When this occurs, the pressure or heat transfer along the aft-cone section increases in the direction of the base. No such trend was observed for He, air, or N_2, and when it was observed for CO_2 it could have been attributed to the low values of γ within the flow field. It should be noted that support interference effects are usually discounted in impulse facilities with extremely short test times such as in this study.

8. Radiation heating.- Radiation contributions from the model surface to the surrounding walls of the tube and dump tank or from the walls to the model surface are believed to be small. The tube and tank walls are expected to remain near ambient temperature (typically 297 K) during the test. Except for the nose tip, the maximum model surface temperature experienced was 390 K; thus, the radiative heat transfer was less than 0.0013 MW/m^2, which is negligible compared with the convective heating contribution.

Following the present study, these same biconic models were tested in the Langley 31-Inch Mach 10 Tunnel for the same range of angle of attack (ref. 49). These data correspond to Mach 9.9 in air, $\rho_2/\rho_\infty = 5.95$, and $R_{\infty,L} \approx 2.20 \times 10^5$, compared with the present Mach number of 6.9 in real air, $\rho_2/\rho_\infty = 11.10$, and $R_{\infty,L} = 0.55 \times 10^5$. Tests in the Mach 10 tunnel circumvent several of the uncertainties associated with the expansion tube. For example, free-stream flow conditions in the Mach 10 tunnel are accurately known, and with run times of several seconds, the flow has ample time to fully establish. (C_h was constant to within a few percent for all thin-film gages over a 1-sec period.) These relatively small models were contained well within the large test core of the Mach 10 tunnel, and support

interference effects were minimized by use of a sting having a ratio of sting diameter to model-base diameter of 0.375 and a ratio of sting length to model-base diameter of 7. Uncertainties associated with reacting gases, surface catalyticity, and gage shorting are not pertinent to the Mach 10 tunnel. Also, because the model surface temperatures in the Mach 10 tunnel tests were slightly less than those in the expansion tube tests, the effects of mismatches in the model surface materials and radiation effects should be about the same between the two studies and are believed to be negligible. Further, the measured heating distributions on these biconics in the Mach 10 tunnel were compared with predictions from the same PNS code (refs. 15 to 17) used for the tests in the expansion tube. Agreement between measurement and prediction improved over that observed in the expansion tube, with windward heating generally being predicted to within 10 percent and leeward heating to within 25 percent. However, as observed in the expansion tube tests, this PNS code underpredicted windward heating at all angles of attack and leeward heating at the lower angles of attack; it still tended to overpredict leeward heating levels at the highest angle of attack.

Computational Uncertainties

The assumptions incorporated in the PNS code are the flow field is steady, planar, symmetric, can be treated as a continuum, and contains all the terms of the Navier-Stokes equations except for the viscous terms in the marching direction (assumed small) and the full pressure-gradient term in the marching direction. The streamwise pressure-gradient term is approximated by using backward differences where the flow is supersonic in the marching direction. In the subsonic portion of the boundary layer only a fraction ω of the pressure-gradient term can be stably approximated by using backward differences. The remainder of the term $(1 - \omega)$ should be approximated by using forward differences to account for downstream influences propagating upstream through the subsonic boundary layer. In general, such treatment is not possible, and in the present code this portion of the pressure-gradient term is set equal to zero. In reference 56, an iterative marching PNS code is described which accounts for upstream influence through the boundary layer by using forward differences in pressure taken from the previous pass. The study examined skin-friction predictions over a flat plate with a 1° compression corner and expansion corners up to 10° for a free-stream Mach number of 3 and a Reynolds number based on plate length of 50×10^6 by using a single-sweep PNS code (as used herein) and a multiple-sweep PNS code. The study indicated some significant differences in skin friction within $\Delta x/L = 0.001$ of the corner. It appeared that the difference in skin friction would go to zero farther downstream, but the analysis ended at $\Delta x/L = 0.004$. Further investigation revealed a 10-percent difference in skin friction due to hypersonic viscous interaction for flow over a flat plate at Mach 5, $R_{\infty,L} = 0.78 \times 10^6$, and adiabatic wall conditions. Although these test conditions do not closely duplicate the conditions of the present study and although only skin friction was considered in reference 56, it should be acknowledged that some of the differences between prediction and experiment could be caused by failure of the PNS code to properly account for the importance of the pressure-gradient term due to viscous interaction at high Mach numbers and low Reynolds numbers. However, it should also be noted that the present PNS code has yielded excellent comparisons with the heating rates measured on a 15° half-angle cone at $M_\infty = 10.6$ (data of ref. 50). In addition, as mentioned in the previous section of this appendix, reasonably good comparisons were obtained with heating distributions measured on these same biconic models in Mach 10 air.

APPENDIX D

GENERAL DISCUSSION OF FLOW ESTABLISHMENT, MODEL SURFACE EFFECTS, FLOW CHEMISTRY, AND VISCOUS EFFECTS

Flow Establishment

A major uncertainty at the outset of this study was whether the flow would fully establish (C_h become essentially constant with time) over the model within the 250-μsec test period. Previous studies in the expansion tube (refs. 26 and 57) with relatively large spheres and flat-faced cylinders revealed that, as a worst case, it took approximately 80 to 100 μsec to obtain steady flow conditions (surface pressure and heat-transfer rate). This maximum time of 100 μsec includes the time required for the test gas to replace the lower density acceleration gas, which is incident upon the model first. Although these establishment times for blunt bodies were encouraging, it was recognized that the flow over the relatively slender biconics would be more complex, particularly at high angles of attack at which cross-flow separation occurs. Unpublished results for a sharp-leading-edge flat plate with forward-facing ramps of various inclinations revealed the flow established within approximately 150 μsec. This finding was particularly encouraging since the flow over the plate had a significant viscous contribution and a relatively large region of separated flow. These results for the flat plate were also in qualitative agreement with the predictions of reference 58 and provided the confidence needed to perform the present study. They imply that the acceleration gas first incident upon the biconic models will be removed by the test gas within the 250 μsec test period and are mentioned herein because of their contribution to the study of flow establishment about models in impulse facilities.

In general, the flow established on the windward side of both biconic models within 120 μsec for all test gases at $0° \leq \alpha \leq 20°$. Flow establishment on the leeward side at $0° \leq \alpha \leq 20°$ required more time, especially at the higher angles of attack, and the outputs of the leeward gages were characterized by larger fluctuations with time. Following the arrival of the test gas, the gages along the most leeward ray experienced a decrease in heating with time at the higher angles of attack but became essentially constant within 200 μsec in most cases. This indicates the leeward flow probably achieved a fully established flow condition. The longer establishment time on the leeward side at incidence is attributed to the complexity of the flow in this region due to cross-flow separation and the larger fluctuations are attributed to the possible unsteady nature of the resulting vortex system.

Model Surface Effects

To avoid or minimize the effects on measured heat-transfer rates of surface temperature discontinuities (ref. 23), which result from differences in the thermal properties of the model surface, the thermal conductivities of the substrates and models should be matched as close as possible. Another concern at the high enthalpies of this study is the difference in surface catalyticity (e.g., refs. 59 to 61) between the MACOR glass-ceramic substrates and the stainless-steel models. Because of these concerns, the model was coated for all tests with a uniform deposit

of Parylene C[6] or sprayed with Krylon No. 1303[7], a crystal-clear acrylic, prior to installation of the substrates. As mentioned previously, windward substrates were generally destroyed and the Parylene C or Krylon acrylic cover was badly sandblasted during the post-run period (fig. 4(b)). When this occurred, the model was removed from the facility, the substrates were removed from the model, the cover was removed, a new cover was installed, and new substrates were installed.

The effect of removing the cover on measured heating distributions is shown in figure 36 for the bent-nose biconic in air. Removing the cover produced no significant effect on heating. For the short test times of this study and the correspondingly low surface temperatures on the fore-cone and aft-cone of the biconics, the effect of any surface-temperature discontinuity resulting from the use of different materials for the model and substrates is expected to be small (less than 5 percent for the worst case, i.e., the most upstream gage on windward fore-cone substrate (ref. 23)). However, removing the cover results in a higher catalytic efficiency of the model surface excluding, of course, the MACOR glass-ceramic substrates. (MACOR glass-ceramic is assumed to be essentially noncatalytic, as is the thin-film gage, which is covered with a layer of Al_2O_3.) Now, if the characteristic time required for atom recombination is much smaller than the time required for atom diffusion across the boundary layer, then an equilibrium boundary layer exists in which the recombination is completed before the atoms can diffuse to the cold surface. For this limiting case, which represents an upper limit on the heat-transfer rate, the catalyticity of the surface does not influence the heating. If the characteristic time for atom recombination is so large that no recombination can occur before the atoms have diffused to the surface, the boundary-layer flow is frozen. In the case of a partially or completely frozen boundary layer, the catalyticity of the surface affects the heating. For a fully catalytic wall, all atoms that diffuse to the surface recombine there, depositing their chemical energy on the surface and increasing the heat-transfer rate. If the surface is not fully catalytic, the heat-transfer rate will be reduced because of the decrease in surface recombination. The condition of a completely frozen boundary layer and a completely noncatalytic surface represents the lower limit on heating. Thus, one possible explanation for the good agreement between the heating for the covered and uncovered models is that the flow is in equilibrium. Alternatively, perhaps the flow is in nonequilibrium, but the effect of surface catalyticity on heating for the present conditions is relatively small (within the experimental uncertainty). Another possible explanation for the good agreement between the covered and uncovered models is that the thin-film gages were placed a sufficient distance from the steel-MACOR glass-ceramic junctions in the model surface to allow the flow to adjust locally, if necessary, to the MACOR glass-ceramic surfaces. For the sake of continuity and the fact that the cover provided excellent protection of the model surface from solid contaminants carried in the posttest flow, the model was covered for all runs. The assumption is made that the present heating data correspond to a noncatalytic surface.

---

[6]Parylene is the generic name for members of a polymer series developed by Union Carbide Corp.; because of its low permeability to moisture and corrosive gases, is commonly used to coat electronic assemblies.

[7]Krylon is a registered trademark of Borden, Inc.

APPENDIX D

Flow Chemistry

Because of the close proximity of the shock to the model surface at the higher density ratios, the flow within the shock layer may depart from equilibrium (ref. 26); that is, the relaxation length (the product of relaxation time and flow speed) for air, N_2, and CO_2 may be large compared with a characteristic length, such as the shock detachment distance. This is especially true in the nose region, where physical dimensions are small and there may not be sufficient time for reactions to occur. The results of reference 26, based on binary scaling for blunt bodies, revealed that the product of free-stream density and predicted equilibrium shock detachment distance at the stagnation point must exceed 10^{-5} kg/m^2 to avoid significant nonequilibrium flow effects. For the biconic spherical nose radius of 3.835 mm, this product is less than 1.3×10^{-6} kg/m^2 for air, N_2, and CO_2 test gases, thus well within the nonequilibrium flow regime and may be frozen. Downstream of the nose, where the physical dimensions are larger than in the nose region, the flow processed by the bow shock in the nose region may tend toward equilibrium. However, the expansion of the flow over the spherical nose and its adjustment to the conic section may also discourage equilibration. Whether nonequilibrium, or frozen, flow is restricted to the nose region or also occurs over the fore-cone and aft-cone sections and cannot be determined from the present experimental heating results alone. As discussed previously, comparison between measured and predicted (PNS code) heating distributions and shock shapes in air indicate the probable existence of nonequilibrium flow.

Viscous Effects

At sufficiently low Reynolds numbers, the shock and boundary-layer thicknesses are no longer negligible compared with the shock detachment distance, and the shock thickness can no longer be represented as a surface of discontinuity. Viscous effects may predominate over the entire flow field and, in this case, the classic approach of dividing the flow field into a viscous boundary-layer region and an outer inviscid region becomes inaccurate. A number of researchers have suggested various criteria in an effort to define regimes between what is commonly referred to as the continuum-flow regime and the free-molecular-flow regime (a collection of such criteria is presented in ref. 62), but these are recognized as approximations. Cheng's rarefaction parameter K_r^2 (ref. 63) and the parameter $R_{2,r_n}/(\rho_2/\rho_\infty)^2$ (see ref. 64) were selected to determine if viscous effects for the flow over the spherical nose tip were significant. As indicated by these parameters, with K_r^2 varying from 22 for N_2 to 53 for He and $R_{2,r_n}/(\rho_2/\rho_\infty)^2$ varying from 2.6 for CO_2 to 23.0 for He, the present flows over the nose bridge the "boundary" between the continuum-flow regime and the slip-flow regime (e.g., see refs. 3 and 65). In this region, classic boundary-layer theories initially underestimate heating as the Reynolds number is reduced and shock-induced vorticity and interaction between the boundary layer and the outer inviscid flow become significant; the theories then progressively overestimate heating as slip effects become significant. This trend is well documented in the literature (e.g., refs. 63 to 69) and is also quite sensitive to shock strength (ρ_2/ρ_∞), as illustrated by the curves in figure 37 which were taken from reference 64.

Measured heating rates at the nose tip of the straight biconic at $\alpha = 0°$ are shown in figure 37 for the four test gases used in the expansion tube. Also shown in figure 37 is the stagnation-point heating measured on the spherical nose of a model with a 45° half-angle cone, fabricated entirely from MACOR glass-ceramic, at $\alpha = 0°$ in the expansion tube with air test gas; the nose radius for this spherically blunted

cone model is 1.27 cm. Stagnation-point heat-transfer measurements on small quartz hemispheres in the Langley 31-Inch Mach 10 Tunnel and the Langley Hypersonic CF_4 Tunnel (see appendix B) are also represented in figure 37. As discussed in appendix B, each of the five hemispheres tested simultaneously in the Mach 10 tunnel revealed an effect of Reynolds number on stagnation-point heating. The quantity $C_T/(p_{t,2}/r_n)^{1/2}$ increased about 8 percent as R_{∞,r_n} decreased from 32.5×10^3 to 7.9×10^3. As shown in figure 37, the ratio of measured to predicted stagnation-point heating for the quartz hemispheres exceeded unity for Mach 10 air and Mach 6.4 CF_4. (Predicted stagnation-point heating for air was obtained from the theory of Fay and Riddell (ref. 31) and for CF_4 was obtained from boundary-layer theory and the thermodynamic properties of reference 70 for CF_4.) These results at two different normal-shock density ratios demonstrate the sensitivity of viscous effects on heating to the shock strength and qualitatively agree with the predictions of reference 64. Measured values of stagnation-point heating in the expansion tube with He, air, and N_2 test gases also exceed prediction with boundary-layer theory (fig. 37). This is in spite of probable nonequilibrium flow effects for air and N_2 reducing the heating. Collectively, the expansion tube data of figure 37 imply viscous effects are more important than the effects of flow chemistry for air and N_2, whereas the reverse may be true for CO_2. As in the case of nonequilibrium flow effects, it is not possible to determine from the present heating distributions alone if vorticity interaction effects extend throughout a major portion of the flow field or are confined to the nose region. It should be noted that the effects of vorticity were predicted to be strong in the nose region of a spherically blunted cone at low Reynolds numbers but relatively weak along the conical afterbody (ref. 71).

REFERENCES

1. Walberg, Gerald D.: A Review of Aeroassisted Orbit Transfer. AIAA-82-1378, Aug. 1982.

2. Florence, Dwight E.: Aerothermodynamic Design Feasibility of a Mars Aerocapture/Aeromaneuver Vehicle. AIAA-81-0350, Jan. 1981.

3. Florence, Dwight E.: Aerothermodynamic Design Feasibility of a Generic Planetary Aerocapture/Aeromaneuver Vehicle. AIAA-81-1127, June 1981.

4. Austin, R. E.; Cruz, M. I.; and French, J. R.: System Design Concepts and Requirements for Aeroassisted Orbital Transfer Vehicles. AIAA-82-1379, Aug. 1982.

5. Letts, W. R.; and Pelekanos, A.: Aeroassisted Orbital Transfer Mission Evaluation. AIAA-82-1380, Aug. 1982.

6. Jamison, Charles C.; and Visentine, James T.: The Utilization of Shuttle Launched Vehicles for Technical Validation of Advanced Earth and Planetary Entry Systems. AIAA-82-1383, Aug. 1982.

7. Lin, T. C.; Grabowsky, W. R.; and Yelmgren, K. E.: The Search of Optimum Configurations for Reentry Vehicles. AIAA-82-1303, Aug. 1982.

8. Miller, Charles G., III; and Gnoffo, Peter A.: Pressure Distributions and Shock Shapes for 12.84°/7° On-Axis and Bent-Nose Biconics in Air at Mach 6. NASA TM-83222, 1981.

9. Miller, C. G.; and Gnoffo, P. A.: An Experimental Investigation of Hypersonic Flow Over Biconics at Incidence and Comparison to Prediction. AIAA-82-1382, Aug. 1982.

10. Miller, C. G.; Blackstock, T. A.; Helms, V. T.; and Midden, R. E.: An Experimental Investigation of Control Surface Effectiveness and Real-Gas Simulation for Biconics. AIAA-83-0213, Jan. 1983.

11. Moore, John A.: Description and Initial Operating Performance of the Langley 6-Inch Expansion Tube Using Heated Helium Driver Gas. NASA TM X-3240, 1975.

12. Miller, Charles G.: Operational Experience in the Langley Expansion Tube With Various Test Gases. NASA TM-78637, 1977.

13. Miller, Charles G.: Flow Properties in Expansion Tube With Helium, Argon, Air, and CO_2. AIAA J., vol. 12, no. 4, Apr. 1974, pp. 564-566.

14. Shinn, Judy L.; and Miller, Charles G., III: Experimental Perfect-Gas Study of Expansion-Tube Flow Characteristics. NASA TP-1317, 1978.

15. Vigneron, Y. C.: Calculation of Supersonic Viscous Flow Over Delta Wings With Sharp Subsonic Leading Edges. AIAA Paper 78-1137, July 1978.

16. Agarwal, R.; and Rakich, J. V.: Supersonic Laminar Viscous Flow Past a Cone at Angle of Attack in Spinning and Coning Motion. AIAA J., vol. 20, no. 6, June 1982, pp. 761-768.

17. Gnoffo, Peter A.: Hypersonic Flows Over Biconics Using a Variable-Effective Gamma, Parabolized-Navier-Stokes Code. AIAA-83-1666, July 1983.

18. Miller, Charles G., III: A Program for Calculating Expansion-Tube Flow Quantities for Real-Gas Mixtures and Comparison With Experimental Results. NASA TN D-6830, 1972.

19. Grossman, David G.: Machining a Machinable Glass-Ceramic. Vacuum, vol. 28, no. 2, Feb. 1978, pp. 55-61.

20. Miller, Charles G., III: Comparison of Thin-Film Resistance Heat-Transfer Gages With Thin-Skin Transient Calorimeter Gages in Conventional-Hypersonic Wind Tunnels. NASA TM-83197, 1981.

21. Reddy, N. M.: Heating-Rate Measurements Over 30° and 40° (Half-Angle) Blunt Cones in Air and Helium in the Langley Expansion Tube Facility. NASA TM-80207, 1980.

22. Cook, W. J.: Determination of Heat-Transfer Rates From Transient Surface Temperature Measurements. AIAA J., vol. 8, no. 7, July 1970, pp. 1366-1368.

23. Schultz, D. L.; and Jones, T. V.: Heat-Transfer Measurements in Short-Duration Hypersonic Facilities. AGARD-AG-165, Feb. 1973.

24. Miller, Charles G., III; and Jones, Jim J.: Incident Shock-Wave Characteristics in Air, Argon, Carbon Dioxide, and Helium in a Shock Tube With Unheated Helium Driver. NASA TN D-8099, 1975.

25. Miller, Charles G., III: Computer Program of Data Reduction Procedures for Facilities Using CO_2-N_2-O_2-Ar Equilibrium Real-Gas Mixtures. NASA TM X-2512, 1972.

26. Miller, Charles G., III: Shock Shapes on Blunt Bodies in Hypersonic-Hypervelocity Helium, Air, and CO_2 Flows, and Calibration Results in Langley 6-Inch Expansion Tube. NASA TN D-7800, 1975.

27. Haggard, Kenneth V.: Free-Stream Temperature, Density, and Pressure Measurements in an Expansion Tube Flow. NASA TN D-7273, 1973.

28. Marrone, P. V.; and Hartunian, R. A.: The Performance of Thin-Film Thermometers in Partially Ionized Shock-Tube Flows. AFOSR TN 59-1046, AD-1118-A-5, U.S. Air Force, Nov. 1959.

29. Friesen, Wilfred J.: Investigation of an Anomalous Flow Condition of The Langley Pilot Model Expansion Tube. NASA TN D-7704, 1974.

30. Sutton, Kenneth; and Graves, Randolph A., Jr.: A General Stagnation-Point Convective-Heating Equation for Arbitrary Gas Mixtures. NASA TR R-376, 1971.

31. Fay, J. A.; and Riddell, F. R.: Theory of Stagnation Point Heat Transfer in Dissociated Air. J. Aeronaut. Sci., vol. 25, no. 2, Feb. 1958, pp. 73-85, 121.

32. Marvin, J. G.; and Deiwert, G. S.: Convective Heat Transfer in Planetary Gases. NASA TR R-224, July 1965.

33. Zoby, Ernest V.: Empirical Stagnation-Point Heat-Transfer Relation in Several Gas Mixtures at High Enthalpy Levels. NASA TN D-4799, 1968.

34. Gnoffo, P. A.: A Vectorized, Finite-Volume, Adaptive Grid Algorithm Applied to Planetary Entry Problems. AIAA-82-1018, June 1982.

35. Kumar, Ajay; Graves, Randolph A., Jr.; and Weilmuenster, K. James: User's Guide for Vectorized Code EQUIL for Calculating Equilibrium Chemistry on Control Data STAR-100 Computer. NASA TM-80193, 1980.

36. Stetson, Kenneth F.: Boundary-Layer Separation on Slender Cones at Angle of Attack. AIAA J., vol. 10, no. 5, May 1972, pp. 642-648.

37. Rainbird, William John: Turbulent Boundary-Layer Growth and Separation on a Yawed Cone. AIAA J., vol. 6, no. 12, Dec. 1968, pp. 2410-2416.

38. Rainbird, W. J.; Crabbe, R. S.; Peake, D. J.; and Meyer, R. F.: Some Examples of Separation in Three-Dimensional Flow. Canadian Aeronaut. Space J., vol. 12, no. 10, Dec. 1966, pp. 409-423.

39. Widhopf, George F.: Turbulent Heat-Transfer Measurements on a Blunt Cone at Angle of Attack. AIAA J., vol. 9, no. 8, Aug. 1971, pp. 1574-1580.

40. Rizk, Y. M.; Chaussee, D. S.; and McRae, D. S.: Computation of Hypersonic Viscous Flow Around Three-Dimensional Bodies at High Angles of Attack. AIAA-81-1261, June 1981.

41. Dearing, J. David: Laminar Heat-Transfer Distributions for a Blunted-Cone, Cone-Frustum Reentry Configuration at Mach 10. NASA TN D-5146, 1969.

42. Griffith, B. J.; and Lewis, Clark H.: Laminar Heat Transfer to Spherically Blunted Cones at Hypersonic Conditions. AIAA J., vol. 2, no. 3, Mar. 1964, pp. 438-444.

43. Boylan, D. E.: Laminar Heat Transfer on Sharp and Blunt Ten-Degree Cones in Conical and Parallel Low-Density Flow. Rep. No. AEDC-TR-73-106, U.S. Air Force, Aug. 1973. (Available from DTIC as AD 765 546.)

44. Cheng, Hsien K.: Hypersonic Flow With Combined Leading-Edge Bluntness and Boundary-Layer Displacement Effect. Rep. No. AF-1285-A-4 (Contract Nonr-2653(00)), Cornell Aeronaut. Lab., Inc., Aug. 1960.

45. Hefner, Jerry N.: Lee-Surface Heating and Flow Phenomena on Space Shuttle Orbiters at Large Angles of Attack and Hypersonic Speeds. NASA TN D-7088, 1972.

46. Nestler, D. E.: Hypersonic Laminar Heat Transfer to Cones at Angle of Attack. Heat Transfer 1978, Volume 5, Hemisphere Pub. Corp., 1978, pp. 215-220.

47. Adams, John C., Jr.: Evaluation of Windward Streamline Effective Cone Boundary-Layer Analyses. J. Spacecr. & Rockets, vol. 9, no. 9, Sept. 1972, pp. 718-720.

48. Waldron, H. F.: Viscous Hypersonic Flow Over Pointed Cones at Low Reynolds Numbers. AIAA J., vol. 5, no. 2, Feb. 1967, pp. 208-218.

49. Miller, Charles G., III: Experimental and Predicted Heating Distributions for Biconics at Incidence in Air at Mach 10. NASA TP-2334, 1984.

50. Cleary, Joseph W.: Effects of Angle of Attack and Bluntness on Laminar Heating-Rate Distributions of a 15° Cone at a Mach Number of 10.6. NASA TN D-5450, 1969.

51. Miller, Charles G.: A Critical Examination of Expansion Tunnel Performance. A Collection of Technical Papers - AIAA 10th Aerodynamic Testing Conference, Apr. 1978, pp. 14-29. (Available as AIAA Paper 78-768.)

52. Shinn, Judy L.: Comparison of Predicted and Experimental Real-Gas Pressure Distributions on Space Shuttle Orbiter Nose for Shuttle Entry Air Data System. NASA TP-1627, 1980.

53. Bailey, A. B.: Further Experiments on Impact-Pressure Probes in a Low-Density Hypervelocity Flow. AEDC-TDR-62-208, U.S. Air Force, Nov. 1962.

54. Wannenwetsch, G. D.; Ticatch, L. A.; Kidd, C. T.; and Arterbury, R. L.: Results of Wind Tunnel Tests Utilizing the Thin-Film Technique To Measure Wind Leading-Edge Heating Rates. AEDC-TR-83-50, U.S. Air Force, May 1984.

55. Ligrani, P. M.; Camci, C.; and Grady, M. S.: Thin Film Heat Transfer Gage Construction and Measurement Details. VKI-TM-33, Von Karman Inst. Fluid Dyn., Nov. 1982.

56. Rakich, John V.: Iterative PNS Method for Attached Flows With Upstream Influence. AIAA 6th Computational Fluid Dynamics Conference - A Collection of Technical Papers, July 1983, pp. 473-482. (Available as AIAA-83-1955.)

57. Miller, Charles G.; and Moore, John A.: Flow-Establishment Times for Blunt Bodies in an Expansion Tube. AIAA J., vol. 13, no. 12, Dec. 1975, pp. 1676-1678.

58. Gupta, Roop N.: An Analysis of the Relaxation of Laminar Boundary Layer on a Flat Plate After Passage of an Interface With Application to Expansion-Tube Flows. NASA TR R-397, 1972.

59. Sheldahl, Robert E.; and Winkler, Ernest L.: Effect of Discontinuities in Surface Catalytic Activity on Laminar Heat Transfer in Arc-Heated Nitrogen Streams. NASA TN D-3615, Sept. 1966.

60. Anderson, L. A.: Effect of Surface Catalytic Activity on Stagnation Heat-Transfer Rates. AIAA J., vol. 11, no. 5, May 1973, pp. 649-656.

61. Shinn, Judy L.; Moss, James N.; and Simmonds, Ann L.: Viscous-Shock-Layer Heating Analysis for the Shuttle Windward-Symmetry Plane With Surface Finite Catalytic Recombination Rates. AIAA-82-0842, June 1982.

62. Little, Herbert R.: An Experimental Investigation of Surface Conditions on Hyperboloids and Paraboloids at a Mach Number of 10. AEDC-TR-69-225, U.S. Air Force, Jan. 1970. (Available from DTIC as AD 698 755.)

63. Cheng, Hsien K.: Hypersonic Shock-Layer Theory of the Stagnation Region at Low Reynolds Number. Rep. No. AF-1285-A-7 (Contract Nonr-2653(00)), Cornell Aeronaut. Lab., Inc., Apr. 1961. (Available from DTIC as AD 256 745.)

64. Gilbert, Leon M.; and Goldberg, Leon: A Reynolds Number Scaling Theory for Hypersonic Ablation. AIAA Paper 67-155, Jan. 1967.

65. Coleman, G. T.; Metcalf, S. C.; and Berry, C. J.: Heat Transfer to Hemisphere Cylinders and Bluff Cylinders Between Continuum and Free Molecular Flow Limits. Rarefied Gas Dynamics, J. Leith Potter, ed., American Inst. Aeronaut. & Astronaut., c.1977, pp. 393-404.

66. Cheng, H. K.: The Blunt-Body Problem in Hypersonic Flow at Low Reynolds Number. IAS Paper 63-92, Jan. 1963.

67. Ferri, Antonio; and Zakkay, Victor: Measurements of Stagnation Point Heat Transfer at Low Reynolds Numbers. J. Aerosp. Sci., vol. 29, no. 7, July 1962, pp. 847-850.

68. Ferri, Antonio; Zakkay, Victor; and Ting, Lu: On Blunt-Body Heat Transfer at Hypersonic Speed and Low Reynolds Numbers. J. Aerosp. Sci., vol. 29, no. 7, July 1962, pp. 882-883.

69. Kao, Hsiao C.: Hypersonic Viscous Flow Near the Stagnation Streamline of a Blunt Body: II. Third-Order Boundary-Layer Theory and Comparison With Other Methods. AIAA J., vol. 2, no. 11, Nov. 1964, pp. 1898-1906.

70. Sutton, Kenneth: Relations for the Thermodynamic and Transport Properties in the Testing Environment of the Langley Hypersonic CF_4 Tunnel. NASA TM-83220, 1981.

71. Marchand, E. O.; Lewis, C. H.; and Davis, R. T.: Second-Order Boundary-Layer Effects on a Slender Blunt Cone at Hypersonic Conditions. AIAA Paper No. 68-54, Jan. 1968.

SYMBOLS

C^*	$= \mu^* T_\infty / \mu_\infty T^*$
C_h	heat-transfer coefficient, $\dot{q}/(h_{t,2} - h_w)$, J-sec/m^4
C_T	heat-transfer coefficient, $\dot{q}/(T_{t,2} - T_w)$, W/m^2-K
c	specific heat, J/kg-K
d	outside diameter of pitot-pressure probe, m
h	enthalpy, J/kg
I	current, A
K	proportionality constant (see eq. (1))
K_r^2	Cheng's rarefaction parameter (ref. 63), $R_{\infty,r_n}/\gamma_\infty C^* M_\infty^2$, where C^* is determined for $T^* = (T_2 + T_w)/2$
k	thermal conductivity, W/m-K
L	model length, m
M	Mach number
N_{Kn}	Knudsen number, λ/r_n
N_{St}	Stanton number, $C_h/\rho_\infty U_\infty$
p	pressure, Pa
q	dynamic pressure, Pa
$\dot{q}$	heat-transfer rate, W/m^2 (Q in computer-generated tables)
$\dot{q}_{sph}$	stagnation-point heat-transfer rate of a sphere (see eq. (1)), W/m^2
R	unit Reynolds number, m^{-1}
R_Ω	resistance, Ω
r	radius, m
T	temperature, K
T^*	reference temperature, $(T_{t,2}/6)[1 + (3T_w/T_{t,2})]$, K
t	time, sec
U	velocity, m/sec
$\bar{v}^*$	viscous-interaction parameter, $M_\infty (C^*/R_{\infty,L})^{1/2}$

$\bar{x}$	distance downstream of tube exit, m
x,y,z	model coordinates (see fig. 2), m
Z	moles of dissociated gas per moles of undissociated gas
α	angle of attack, deg
α_R	temperature coefficient of resistance, K^{-1}
β	thermal product of the substrate, $(\rho ck)^{1/2}$, $W\text{-}sec^{1/2}/m^2\text{-}K$
γ	ratio of specific heats
γ_E	isentropic exponent
δ	shock-detachment distance measured perpendicular to fore-cone axis, m
η	nose bend angle, deg
θ	cone half-angle, deg
λ	mean free path, m
μ	viscosity, $N\text{-}sec/m^2$
μ^*	viscosity evaluated at T*, $N\text{-}sec/m^2$
ρ	density, kg/m^3
ϕ	circumferential angle measured from the most leeward ray, deg

Subscripts:

a	aft-cone section
BL	boundary layer
b	base
CL	centerline
e	tube exit
eff	effective
f	fore-cone section
m	measured
n	nose
o	initial
s	substrate

s,10	incident shock into quiescent acceleration gas
t,1	reservoir stagnation conditions
t,2	stagnation conditions behind normal shock
w	expansion tube wall or model surface (not subscripted in computer-generated tables)
1	state of quiescent test gas in front of incident shock in intermediate section
2	static conditions immediately behind normal shock
4	driver gas conditions at time of primary diaphragm rupture
10	state of quiescent acceleration gas in front of incident shock in acceleration section
∞	free-stream conditions

TABLE 1.- MEASURED INPUTS USED TO DETERMINE NOMINAL FLOW CONDITIONS

[p_w, $U_{s,10}$, and $p_{t,2}$ represent mean values obtained from a number of calibration runs and runs with present biconic models; Δ represents scatter in these quantities and not data precision]

Test gas	p_w, Pa	Δp_w, percent	$U_{s,10}$, m/sec	$\Delta U_{s,10}$, percent	$p_{t,2}$, kPa	$\Delta p_{t,2}$, percent
He	1300	±3.0	6900	±1.4	72.6	±7.0
N_2	1635	±4.0	5515	±1.5	85.6	±3.0
Air	2180	±8.0	5325	±2.0	130.35	±3.0
CO_2	1030	±8.0	4535	±3.5	103.0	±8.0

TABLE 2.- NOMINAL FLOW CONDITIONS

[$Z_\infty = 1$ for all test gases; $r_n = 3.835$ mm; $L = 12.2$ cm]

(a) Free-stream flow

Test gas	p_∞, Pa	ρ_∞, kg/m^3	T_∞, K	$\gamma_{E,\infty}$	U_∞, m/sec	M_∞	R_∞, m^{-1}	$\bar{v}^*$ (a)	N_{Kn,∞,r_n} (b)
He	1300	1.72×10^{-3}	364	1.667	6900	6.15	4.87×10^5	0.0218	5.33×10^{-3}
N_2	1635	2.88	1913	1.302	5515	6.41	2.62	.0388	9.12
Air	2182	4.73	1604	1.296	5326	6.89	4.50	.0313	5.70
CO_2	1030	5.09	1070	1.179	4535	9.29	5.64	.0377	5.85

(b) Post-normal-shock flow

Test gas	$p_{t,2}$, kPa	$\rho_{t,2}$, kg/m^3	$T_{t,2}$, K	$\gamma_{E,t,2}$	$Z_{t,2}$	$h_{t,2}$, MJ/kg	R_2, m^{-1}	h_w, MJ/kg (c)	$\frac{\rho_2}{\rho_\infty}$	$\dot{q}_{sph}$, MW/m^2 (d)
He	72.60	0.71×10^{-2}	4948	1.667	1.00	25.69	0.82×10^5	1.56	3.71	26.28
N_2	85.60	3.55	6471	1.127	1.26	17.41	1.11	.31	11.83	28.22
Air	130.35	5.49	6162	1.143	1.34	15.96	1.58	.30	11.13	31.92
CO_2	103.00	9.83	3531	1.132	1.57	2.41	2.43	-8.72	18.83	21.92

[a] $a_{\bar{v}^*} = M_\infty \left(C^*/R_{\infty,L}\right)^{1/2}$

[b] $b_{N_{Kn,\infty,r_n}} = M_\infty \left(\pi\gamma_{E,\infty}/2\right)^{1/2}/R_{\infty,r_n}$

[c] h_w evaluated at $T_w = 300$ K.

[d] Obtained from expression derived in reference 30.

TABLE 3.- UNCERTAINTY IN COMPUTED FLOW CONDITIONS

[Uncertainties correspond to -10 percent in p_∞, -5 percent in U_∞, and 10 percent in $p_{t,2}$]

Test gas	Ratio of flow quantity in error to flow quantity corresponding to nominal flow values of measured inputs for -						
	ρ_∞	T_∞	M_∞	R_∞	ρ_2/ρ_∞	$T_{t,2}$	$\dot{q}_{sph}$ (a)
He	1.220	0.738	1.106	1.435	1.014	0.891	0.927
N_2	1.226	.734	1.102	1.427	.957	.979	.919
Air	1.225	.735	1.097	1.410	.968	.960	.922
CO_2	1.220	.737	1.099	1.420	.999	.961	.922

[a]Based on expression derived in reference 30 for $\dot{q}_{sph}$.

TABLE 4.- MEASURED HEATING RATES FOR STRAIGHT BICONIC IN HELIUM

		$\alpha=0$		$\alpha=4$	
x/L	Φ, deg	Tw, K	Q, MW/m^2	Tw, K	Q, MW/m^2
.247	180	312.6	1.981	320.2	3.051
.287	180	--	--	--	--
.328	180	312.6	1.968	319.0	2.946
.368	180	311.7	1.833	318.1	2.788
.408	180	311.4	1.820	316.9	2.661
.449	180	310.8	1.749	316.5	2.578
.489	180	310.2	1.679	316.8	2.581
.530	180	310.3	1.649	315.8	2.510
.613	180	--	1.176	--	1.765
.654	180	305.5	1.046	309.0	1.540
.695	180	--	.956	--	1.416
.737	180	304.6	.907	307.4	1.365
.778	180	--	.909	--	1.323
.819	180	303.7	.802	306.9	1.235
.860	180	--	.788	--	1.205
.901	180	--	--	306.4	1.207
.247	0	--	2.049	--	1.377
.287	0	--	1.945	--	1.229
.328	0	--	1.913	--	1.167
.368	0	--	1.851	--	1.095
.408	0	--	1.783	--	1.050
.449	0	--	1.866	--	1.040
.489	0	--	1.802	--	--
.530	0	--	1.755	--	.932
.613	0	--	1.190	--	.729
.654	0	--	1.060	--	.633
.695	0	--	.985	--	.585
.737	0	--	.895	--	.549
.778	0	--	.864	--	.520
.819	0	--	.797	--	.497
.860	0	--	.805	--	.452
.901	0	--	.805	--	.434

TABLE 4.- Concluded

		α=12		α=20	
x/L	Φ, deg	Tw, K	Q, MW/m^2	Tw, K	Q, MW/m^2
.247	180	335.6	5.615	--	--
.287	180	--	--	--	--
.328	180	332.4	5.129	340.4	6.950
.368	180	329.4	4.642	--	--
.408	180	328.2	4.510	337.4	6.464
.449	180	327.0	4.334	333.2	6.044
.489	180	325.9	4.166	332.4	5.975
.530	180	324.7	3.990	331.0	5.716
.613	180	--	2.726	--	3.814
.654	180	313.5	2.439	317.5	3.713
.695	180	--	2.336	--	3.478
.737	180	312.7	2.309	315.2	3.397
.778	180	--	2.276	--	3.352
.819	180	312.0	2.217	313.9	3.210
.860	180	--	2.155	--	3.059
.901	180	--	--	313.1	3.103
.247	0	--	.660	--	.472
.287	0	--	.539	--	.417
.328	0	--	.506	--	.463
.368	0	--	--	--	.494
.408	0	--	.419	--	--
.449	0	--	.414	--	--
.489	0	--	.397	--	.450
.530	0	--	.355	--	.452
.613	0	--	.271	--	.385
.654	0	--	.246	--	.357
.695	0	--	.240	--	.355
.737	0	--	.224	--	.339
.778	0	--	.225	--	.331
.819	0	--	.223	--	.318
.860	0	--	.212	--	.315
.901	0	--	.215	--	.298

TABLE 5.- MEASURED HEATING RATES FOR STRAIGHT BICONIC IN NITROGEN

		$\alpha=0$		$\alpha=4$	
x/L	Φ, deg	Tw, K	Q, MW/m^2	Tw, K	Q, MW/m^2
.247	180	315.4	2.787	329.3	4.155
.287	180	--	--	--	--
.328	180	315.0	2.645	328.8	4.103
.368	180	314.1	2.531	328.2	4.016
.408	180	313.7	2.502	327.6	3.927
.449	180	312.8	2.418	326.5	3.748
.489	180	312.3	2.347	326.9	3.769
.530	180	312.6	2.333	325.6	3.587
.613	180	--	1.744	--	2.312
.654	180	306.0	1.537	314.2	2.075
.695	180	--	1.342	--	1.901
.737	180	304.6	1.303	312.8	1.845
.778	180	--	--	--	1.807
.819	180	303.6	1.157	312.1	1.738
.860	180	--	1.163	--	1.706
.901	180	303.3	1.109	311.8	1.702
.247	0	--	2.796	--	1.788
.287	0	--	2.657	--	--
.328	0	--	2.538	--	1.614
.368	0	--	2.535	--	1.521
.408	0	--	2.465	--	1.483
.449	0	--	2.465	--	1.484
.489	0	--	2.370	--	1.431
.530	0	--	2.285	--	--
.613	0	--	1.690	--	1.063
.654	0	--	1.480	--	.937
.695	0	--	1.390	--	.875
.737	0	--	1.305	--	.826
.778	0	--	1.234	--	.790
.819	0	--	1.162	--	.724
.860	0	--	1.158	--	.731
.901	0	--	1.113	--	.722

TABLE 5.- Concluded

		α=12		α=20	
x/L	Φ, deg	Tw, K	Q, MW/m^2	Tw, K	Q, MW/m^2
.247	180	353.7	7.762	374.1	10.829
.287	180	--	--	--	--
.328	180	341.0	6.216	--	--
.368	180	339.4	5.893	355.6	8.074
.408	180	338.6	5.823	352.0	7.493
.449	180	336.8	5.497	350.2	7.277
.489	180	335.8	5.413	--	--
.530	180	334.0	5.126	352.3	6.824
.613	180	--	--	--	--
.654	180	320.8	3.352	332.0	5.137
.695	180	--	3.082	--	4.633
.737	180	317.8	3.024	330.8	4.539
.778	180	--	--	--	4.365
.819	180	318.4	2.857	328.1	4.197
.860	180	--	2.692	--	4.015
.901	180	316.6	2.747	--	--
.247	0	--	.800	--	.565
.287	0	--	--	--	.504
.328	0	--	.598	--	--
.368	0	--	.564	--	--
.408	0	--	.521	--	--
.449	0	--	.499	--	.575
.489	0	--	.460	--	.546
.530	0	--	.416	--	.555
.613	0	--	.340	--	.469
.654	0	--	.324	--	.490
.695	0	--	.306	--	.449
.737	0	--	.295	--	.431
.778	0	--	--	--	.432
.819	0	--	.281	--	.403
.860	0	--	.279	--	.416
.901	0	--	.275	--	.418

TABLE 6.- MEASURED HEATING RATES FOR STRAIGHT BICONIC IN AIR

		$\alpha=0$		$\alpha=4$	
x/L	Φ, deg	Tw, K	Q, MW/m^2	Tw, K	Q, MW/m^2
.247	180	323.1	3.180	332.2	4.688
.287	180	--	--	330.6	4.509
.328	180	321.9	3.042	329.8	4.466
.368	180	321.3	2.929	328.4	4.262
.408	180	321.1	2.970	328.6	4.294
.449	180	321.1	2.984	328.6	4.328
.489	180	321.0	2.976	327.7	4.271
.530	180	320.8	2.944	327.4	4.140
.613	180	--	2.140	--	2.686
.654	180	312.4	1.860	314.9	2.399
.695	180	--	1.679	--	2.260
.737	180	310.5	1.602	312.9	2.170
.778	180	--	1.577	--	2.089
.819	180	309.4	1.435	312.1	1.940
.860	180	--	1.443	--	1.954
.901	180	308.8	1.390	312.3	1.961
.247	0	--	3.105	--	1.902
.287	0	--	3.111	--	1.878
.328	0	--	2.897	--	1.788
.368	0	--	3.035	--	1.704
.408	0	--	2.907	--	1.639
.449	0	--	2.945	--	1.599
.489	0	--	2.918	--	1.626
.530	0	--	--	--	1.487
.613	0	--	2.232	--	1.207
.654	0	--	1.915	--	1.059
.695	0	--	1.741	--	.971
.737	0	--	1.664	--	.928
.778	0	--	1.557	--	.849
.819	0	--	1.492	--	.818
.860	0	--	1.468	--	.784
.901	0	--	1.380	--	.748

TABLE 6.- Concluded

		α=12		α=20	
x/L	Φ,deg	Tw,K	Q,MW/m^2	Tw,K	Q,MW/m^2
.247	180	359.6	8.720	382.3	11.639
.287	180	353.9	7.652	--	--
.328	180	346.6	7.153	369.8	9.829
.368	180	344.5	6.651	363.0	8.804
.408	180	343.5	6.413	361.6	8.512
.449	180	341.9	6.194	359.3	8.126
.489	180	339.1	5.871	357.0	7.814
.530	180	338.0	5.753	--	--
.613	180	--	4.134	--	5.151
.654	180	--	3.748	339.8	5.277
.695	180	--	3.723	--	4.880
.737	180	--	3.717	338.3	5.016
.778	180	--	3.592	--	4.728
.819	180	--	--	336.0	4.662
.860	180	--	3.450	--	4.512
.901	180	--	3.289	335.9	4.619
.247	0	--	.912	--	.673
.287	0	--	.840	--	.655
.328	0	--	.749	--	.646
.368	0	--	.678	--	.649
.408	0	--	.628	--	.647
.449	0	--	.622	--	.705
.489	0	--	.573	--	.692
.530	0	--	.546	--	--
.613	0	--	.487	--	.634
.654	0	--	.449	--	.594
.695	0	--	.432	--	.576
.737	0	--	.403	--	.567
.778	0	--	.420	--	.549
.819	0	--	.402	--	.564
.860	0	--	.393	--	.557
.901	0	--	.398	--	.540

TABLE 7.- MEASURED HEATING RATES FOR STRAIGHT BICONIC IN CARBON DIOXIDE

		$\alpha=0$		$\alpha=4$	
x/L	Φ, deg	Tw, K	Q, MW/m^2	Tw, K	Q, MW/m^2
.247	180	311.6	1.945	320.2	3.343
.287	180	--	--	--	--
.328	180	312.4	2.033	318.3	3.068
.368	180	311.9	1.974	316.8	2.894
.408	180	311.3	1.897	316.9	2.877
.449	180	--	--	314.6	2.600
.489	180	310.7	1.854	313.9	2.512
.530	180	311.2	1.855	313.3	2.417
.613	180	--	1.201	--	1.573
.654	180	304.3	.991	305.2	1.271
.695	180	--	.835	--	1.109
.737	180	302.9	.788	303.7	1.063
.778	180	--	.763	--	1.053
.819	180	302.3	.695	303.2	.984
.860	180	--	.685	--	.972
.901	180	302.3	.683	303.2	.974
.247	0	--	2.086	--	1.079
.287	0	--	1.976	--	.976
.328	0	--	1.991	--	.936
.368	0	--	1.945	--	.938
.408	0	--	1.842	--	--
.449	0	--	1.903	--	.889
.489	0	--	--	--	.852
.530	0	--	1.762	--	.838
.613	0	--	1.224	--	.619
.654	0	--	.988	--	.529
.695	0	--	.868	--	.480
.737	0	--	.825	--	.417
.778	0	--	.763	--	.409
.819	0	--	.736	--	.386
.860	0	--	.705	--	.398
.901	0	--	.713	--	.397

TABLE 7.- Concluded

x/L	Φ, deg	α=12 Tw, K	α=12 Q, MW/m^2	α=20 Tw, K	α=20 Q, MW/m^2
.247	180	335.5	5.509	355.1	8.075
.287	180	--	--	350.0	7.108
.328	180	330.5	4.819	346.3	6.700
.368	180	327.5	4.379	342.3	5.949
.408	180	327.4	4.378	339.5	5.630
.449	180	323.6	3.917	337.9	5.456
.489	180	322.9	3.822	335.1	5.247
.530	180	321.9	3.671	334.6	5.154
.613	180	--	2.461	--	4.170
.654	180	311.2	2.133	321.1	3.176
.695	180	--	1.945	--	2.987
.737	180	309.6	1.910	320.1	2.966
.778	180	--	1.863	--	2.931
.819	180	308.5	1.749	322.1	3.120
.860	180	--	1.756	--	3.189
.901	180	--	--	323.4	3.381
.247	0	--	--	--	.276
.287	0	--	--	--	.270
.328	0	--	--	--	.299
.368	0	--	--	--	.279
.408	0	--	--	--	.303
.449	0	--	--	--	.287
.489	0	--	--	--	.303
.530	0	--	--	--	.310
.613	0	--	--	--	.247
.654	0	--	--	--	.232
.695	0	--	.164	--	.219
.737	0	--	.156	--	.202
.778	0	--	.154	--	.198
.819	0	--	.160	--	.191
.860	0	--	.162	--	.193
.901	0	--	.155	--	.194

TABLE 8.- MEASURED HEATING RATES FOR BENT-NOSE BICONIC IN HELIUM

		$\alpha=0$		$\alpha=4$	
z/L	Φ, deg	Tw, K	Q, MW/m^2	Tw, K	Q, MW/m^2
.256	180	325.2	3.852	330.1	4.921
.296	180	--	--	--	--
.337	180	324.3	3.704	328.8	4.606
.377	180	323.1	3.580	326.1	4.303
.418	180	322.6	3.457	325.1	4.155
.459	180	321.4	3.336	323.8	3.931
.499	180	320.8	3.249	322.5	3.790
.540	180	320.2	3.176	321.6	3.641
.634	180	--	1.176	--	1.361
.676	180	305.1	1.018	305.0	1.286
.717	180	--	.903	--	1.149
.759	180	303.9	.835	303.8	1.121
.800	180	--	.826	--	1.119
.842	180	303.4	.767	303.7	1.087
.884	180	--	.748	--	1.050
.925	180	303.2	.748	303.5	1.068
.256	0	--	1.096	--	.699
.296	0	--	.939	--	.573
.337	0	--	.878	--	.548
.377	0	--	.809	--	.507
.418	0	--	.746	--	.443
.459	0	--	.645	--	.389
.499	0	--	.637	--	--
.540	0	--	.612	--	.351
.636	0	--	.550	--	.346
.679	0	--	.549	--	.315
.721	0	--	.540	--	.337
.764	0	--	.559	--	.333
.806	0	--	.531	--	.306
.849	0	--	.548	--	--
.892	0	--	.533	--	.298
.935	0	--	.529	--	.304

TABLE 8.- Concluded

z/L	Φ, deg	α=12		α=20	
		Tw, K	Q, MW/m^2	Tw, K	Q, MW/m^2
.256	180	343.9	6.895	--	--
.296	180	--	--	--	--
.337	180	339.6	6.285	--	--
.377	180	337.1	5.900	348.8	7.124
.418	180	336.1	5.693	348.0	7.018
.459	180	334.4	5.469	349.3	7.038
.499	180	333.2	5.256	344.5	6.427
.540	180	332.4	5.172	344.3	6.379
.634	180	--	2.184	--	--
.676	180	311.3	2.155	321.7	3.277
.717	180	--	2.032	--	3.103
.759	180	310.4	2.027	320.4	3.109
.800	180	--	1.979	--	3.007
.842	180	309.8	1.955	319.8	2.917
.884	180	--	1.938	--	2.869
.925	180	309.9	1.972	319.2	2.910
.256	0	--	.475	--	.520
.296	0	--	--	--	.442
.337	0	--	.408	--	.481
.377	0	--	.373	--	.468
.418	0	--	.418	--	.487
.459	0	--	.363	--	.411
.499	0	--	.399	--	--
.540	0	--	.416	--	.442
.636	0	--	.445	--	.462
.679	0	--	.453	--	.458
.721	0	--	.473	--	.441
.764	0	--	.479	--	.452
.806	0	--	.503	--	.444
.849	0	--	.519	--	.446
.892	0	--	.519	--	.451
.935	0	--	.532	--	.432

TABLE 9.- MEASURED HEATING RATES FOR BENT-NOSE BICONIC IN NITROGEN

		$\alpha=0$		$\alpha=4$	
z/L	Φ, deg	Tw, K	Q, MW/m^2	Tw, K	Q, MW/m^2
.256	180	336.2	5.290	344.2	6.656
.296	180	--	--	--	--
.337	180	334.2	4.949	337.3	5.754
.377	180	331.4	4.634	335.8	5.456
.418	180	332.2	4.622	335.3	5.361
.459	180	329.4	4.375	332.8	5.097
.499	180	326.3	4.032	332.0	4.951
.540	180	326.2	3.926	331.7	4.864
.634	180	--	1.522	--	1.887
.676	180	307.7	1.318	308.7	1.703
.717	180	--	1.130	--	1.518
.759	180	306.1	1.089	307.2	1.460
.800	180	--	1.048	--	1.427
.842	180	305.4	.985	306.8	1.376
.884	180	--	.956	--	1.340
.925	180	305.6	.983	306.6	1.366
.256	0	--	1.422	--	.846
.296	0	--	1.226	--	.794
.337	0	--	1.202	--	.659
.377	0	--	1.095	--	.635
.418	0	--	1.019	--	.586
.459	0	--	.985	--	.532
.499	0	--	.925	--	.531
.540	0	--	.868	--	.493
.636	0	--	.836	--	.501
.679	0	--	.834	--	.486
.721	0	--	.876	--	.485
.764	0	--	.859	--	.452
.806	0	--	.861	--	.467
.849	0	--	.840	--	.441
.892	0	--	.820	--	.460
.935	0	--	.826	--	--

TABLE 9.- Concluded

z/L	Φ, deg	α=12		α=20	
		Tw, K	Q, MW/m^2	Tw, K	Q, MW/m^2
.256	180	366.4	9.782	386.6	12.554
.296	180	--	--	--	--
.337	180	353.9	7.981	368.8	10.026
.377	180	351.4	7.599	362.4	8.985
.418	180	347.5	6.992	358.3	8.306
.459	180	345.5	6.718	355.3	7.990
.499	180	345.0	6.235	354.1	7.766
.540	180	332.4	5.073	352.8	7.557
.634	180	--	--	--	--
.676	180	315.6	2.479	324.7	3.683
.717	180	--	2.313	--	3.498
.759	180	314.2	2.330	323.6	3.492
.800	180	--	2.319	--	3.582
.842	180	314.0	2.204	324.7	3.596
.884	180	--	2.187	--	3.518
.925	180	314.8	2.320	324.4	3.611
.256	0	--	--	--	.554
.296	0	--	.503	--	.562
.337	0	--	.486	--	.541
.377	0	--	.490	--	.538
.418	0	--	.504	--	.564
.459	0	--	.488	--	.571
.499	0	--	.493	--	.553
.540	0	--	.486	--	.532
.636	0	--	.516	--	.528
.679	0	--	.546	--	.567
.721	0	--	.551	--	.571
.764	0	--	.583	--	.550
.806	0	--	.577	--	.544
.849	0	--	--	--	.545
.892	0	--	.609	--	.558
.935	0	--	--	--	.562

TABLE 10.- MEASURED HEATING RATES FOR BENT-NOSE BICONIC IN AIR

		$\alpha=0$		$\alpha=4$	
z/L	Φ, deg	Tw, K	Q, MW/m^2	Tw, K	Q, MW/m^2
.256	180	342.0	6.252	354.1	7.928
.296	180	--	--	--	--
.337	180	337.5	5.681	348.8	7.099
.377	180	334.2	5.181	343.4	6.277
.418	180	334.1	5.147	343.0	6.204
.459	180	334.0	5.100	341.4	6.013
.499	180	333.5	5.073	340.8	6.031
.540	180	331.6	4.842	339.6	5.781
.634	180	--	1.610	--	1.928
.676	180	306.1	1.422	310.8	1.781
.717	180	--	1.248	--	1.712
.759	180	305.0	1.248	310.4	1.706
.800	180	--	1.220	--	--
.842	180	304.3	1.199	310.1	1.701
.884	180	--	1.179	--	1.677
.925	180	304.6	1.153	310.5	1.722
.256	0	--	--	--	--
.296	0	--	1.336	--	.844
.337	0	--	1.168	--	.724
.377	0	--	1.133	--	.707
.418	0	--	1.089	--	.629
.459	0	--	.970	--	.575
.499	0	--	.936	--	.566
.540	0	--	.851	--	.524
.636	0	--	.881	--	.505
.679	0	--	.887	--	.472
.721	0	--	.844	--	.476
.764	0	--	.855	--	.476
.806	0	--	.854	--	.464
.849	0	--	.871	--	--
.892	0	--	.846	--	.472
.935	0	--	.815	--	.445

TABLE 10.- Concluded

z/L	Φ, deg	α=12		α=20	
		Tw, K	Q, MW/m^2	Tw, K	Q, MW/m^2
.256	180	371.9	10.580	389.9	12.995
.296	180	--	--	381.6	12.068
.337	180	363.1	9.243	376.5	11.311
.377	180	357.7	8.409	371.4	10.364
.418	180	356.6	8.205	370.3	10.067
.459	180	353.2	7.761	366.2	9.497
.499	180	351.9	7.390	--	--
.540	180	350.6	7.281	362.8	8.958
.634	180	--	3.181	--	4.323
.676	180	320.8	3.256	332.0	4.614
.717	180	--	3.035	--	4.121
.759	180	319.4	2.918	329.6	4.118
.800	180	--	3.002	--	4.215
.842	180	318.6	2.800	330.3	4.192
.884	180	--	2.814	--	4.026
.925	180	319.3	2.849	330.7	4.273
.256	0	--	--	--	.872
.296	0	--	.565	--	.852
.337	0	--	.618	--	.877
.377	0	--	.618	--	.935
.418	0	--	.650	--	.825
.459	0	--	.677	--	.834
.499	0	--	.732	--	.791
.540	0	--	.695	--	.826
.636	0	--	.736	--	.866
.679	0	--	.774	--	.860
.721	0	--	.815	--	.887
.764	0	--	.843	--	.866
.806	0	--	.875	--	.836
.849	0	--	--	--	--
.892	0	--	.883	--	.868
.935	0	--	.893	--	.878

TABLE 11.- MEASURED HEATING RATES FOR BENT-NOSE BICONIC IN CARBON DIOXIDE

		$\alpha=0$		$\alpha=4$	
z/L	Φ, deg	Tw, K	Q, MW/m^2	Tw, K	Q, MW/m^2
.256	180	326.0	3.728	329.9	4.485
.296	180	--	--	--	--
.337	180	325.6	3.691	329.0	4.415
.377	180	324.1	3.440	328.4	4.225
.418	180	323.8	3.452	326.0	3.955
.459	180	322.7	3.287	324.2	3.721
.499	180	321.9	3.152	323.7	3.595
.540	180	320.7	2.965	323.0	3.476
.634	180	--	--	--	--
.676	180	303.2	.652	303.0	.961
.717	180	--	--	--	.850
.759	180	--	--	302.1	.799
.800	180	--	.495	--	.767
.842	180	302.0	.464	301.5	.759
.884	180	--	.461	--	.705
.925	180	302.0	.444	301.5	.673
.256	0	--	.695	--	--
.296	0	--	--	--	--
.337	0	--	.516	--	--
.377	0	--	.431	--	--
.418	0	--	.441	--	--
.459	0	--	--	--	--
.499	0	--	.374	--	--
.540	0	--	.398	--	--
.636	0	--	.384	--	--
.679	0	--	.398	--	--
.721	0	--	.407	--	--
.764	0	--	.381	--	--
.806	0	--	.381	--	--
.849	0	--	--	--	--
.892	0	--	.391	--	--
.935	0	--	.402	--	--

TABLE 11.- Concluded

z/L	Φ, deg	α=12 Tw, K	α=12 Q, MW/m^2	α=20 Tw, K	α=20 Q, MW/m^2
.256	180	350.5	7.191	368.2	9.348
.296	180	--	--	358.8	8.360
.337	180	344.5	6.386	352.7	7.482
.377	180	338.7	5.523	350.1	6.936
.418	180	336.1	5.236	346.9	6.536
.459	180	334.7	5.000	344.7	6.288
.499	180	333.3	4.664	343.9	6.108
.540	180	328.7	4.189	342.7	5.920
.634	180	--	1.445	--	2.251
.676	180	309.0	1.437	315.1	2.159
.717	180	--	1.337	--	2.022
.759	180	307.5	1.259	313.6	1.997
.800	180	--	1.218	--	2.259
.842	180	307.2	1.200	317.8	2.564
.884	180	--	1.248	--	2.372
.925	180	308.3	1.392	318.7	2.538
.256	0	--	.225	--	.286
.296	0	--	--	--	.262
.337	0	--	.210	--	.285
.377	0	--	.215	--	.275
.418	0	--	.240	--	.297
.459	0	--	--	--	.303
.499	0	--	.229	--	.288
.540	0	--	.260	--	.269
.636	0	--	.272	--	.292
.679	0	--	.262	--	.301
.721	0	--	.270	--	.315
.764	0	--	.252	--	.297
.806	0	--	.276	--	.288
.849	0	--	.288	--	.280
.892	0	--	.281	--	.268
.935	0	--	.280	--	.278

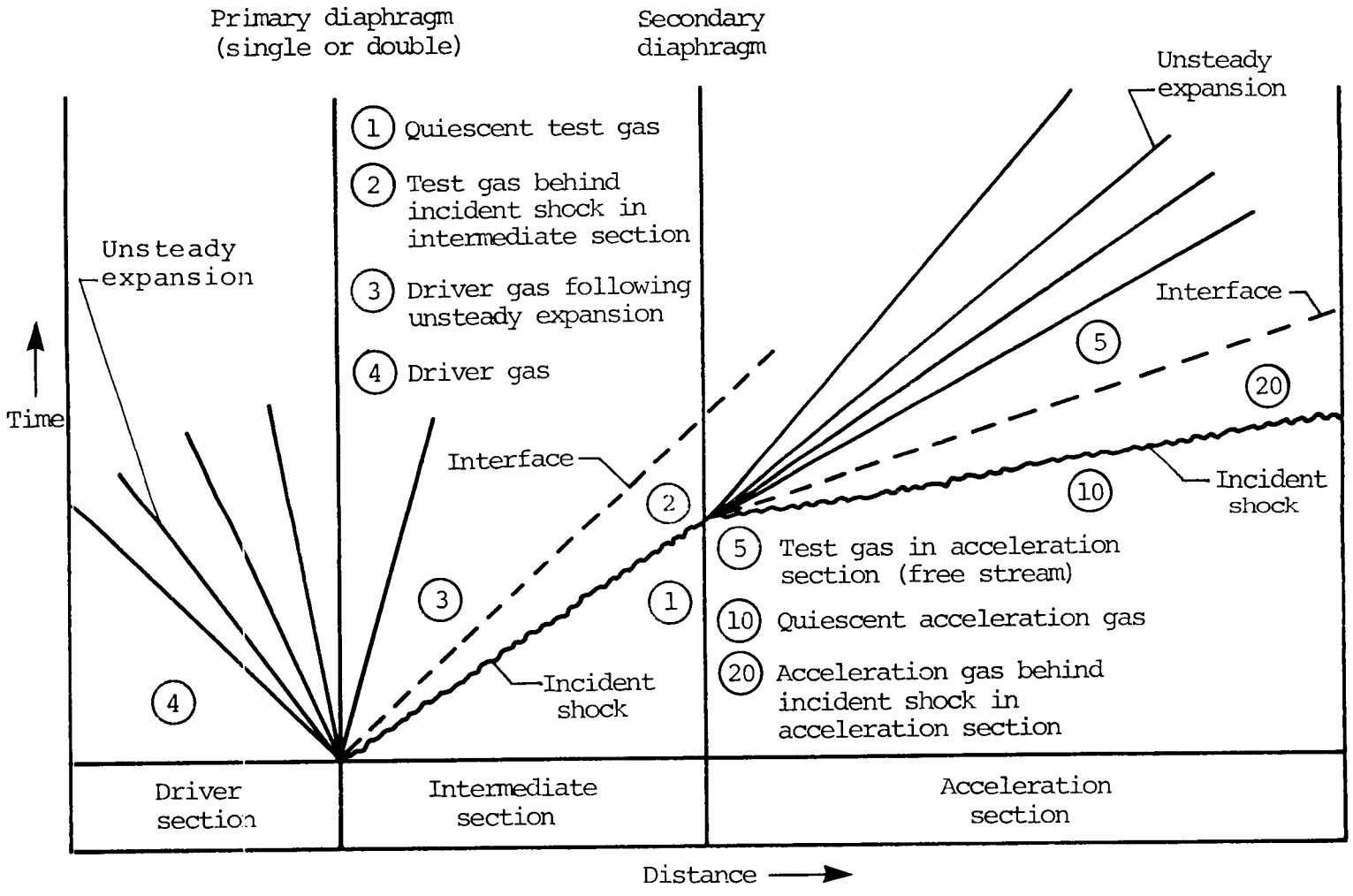

Figure 1.- Schematic diagram of expansion-tube flow sequence.

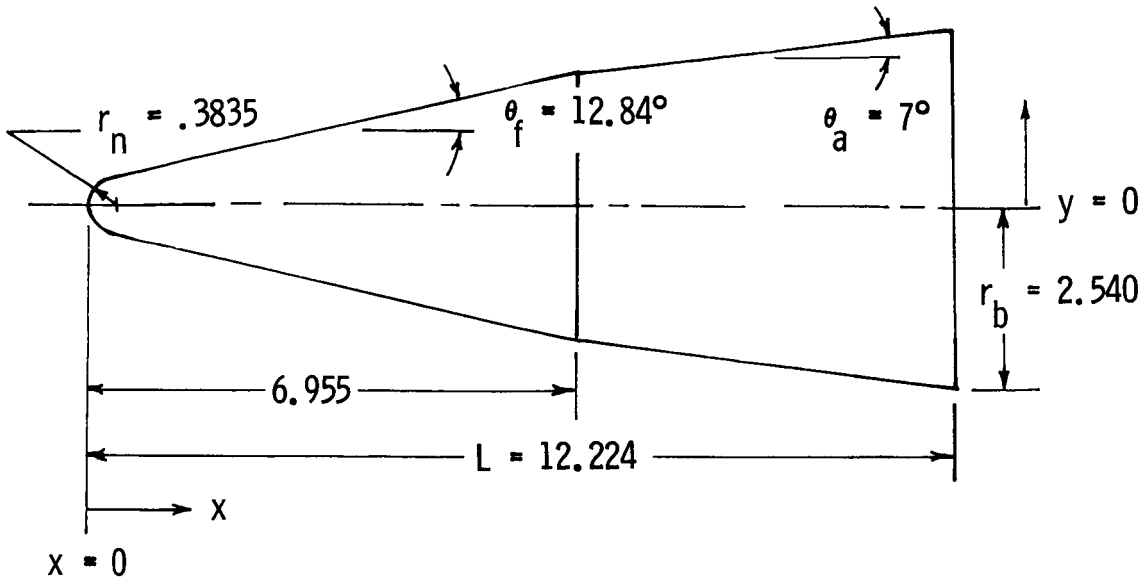

(a) Straight biconic.

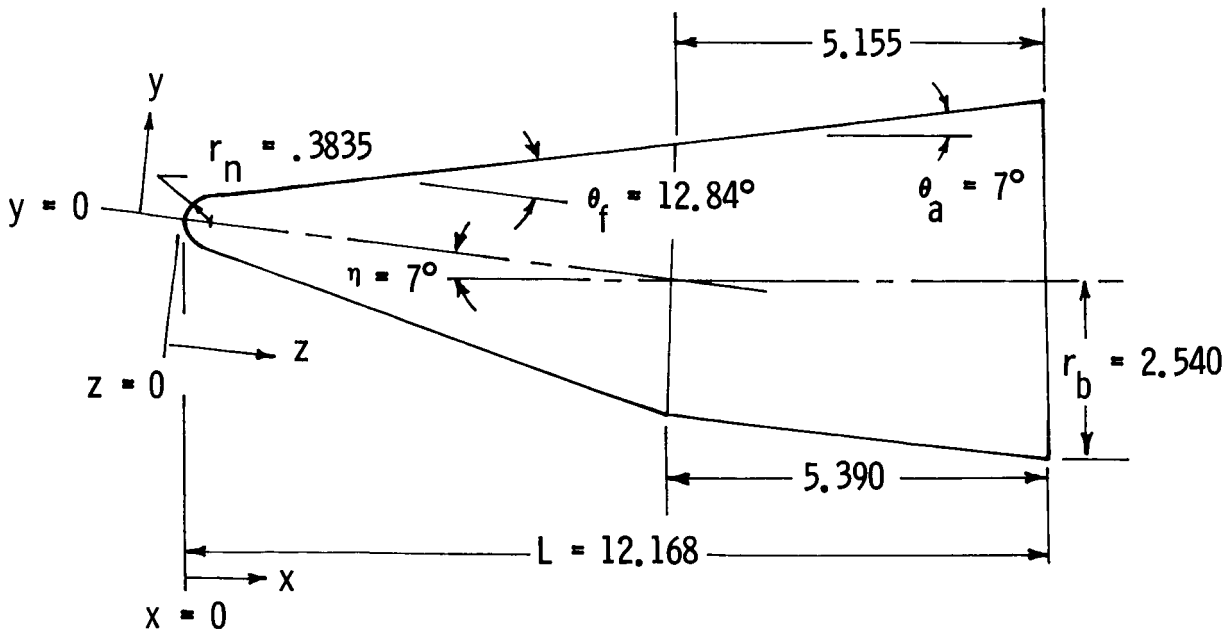

(b) Bent-nose biconic.

Figure 2.- Sketch and dimensions of models. All dimensions in centimeters.

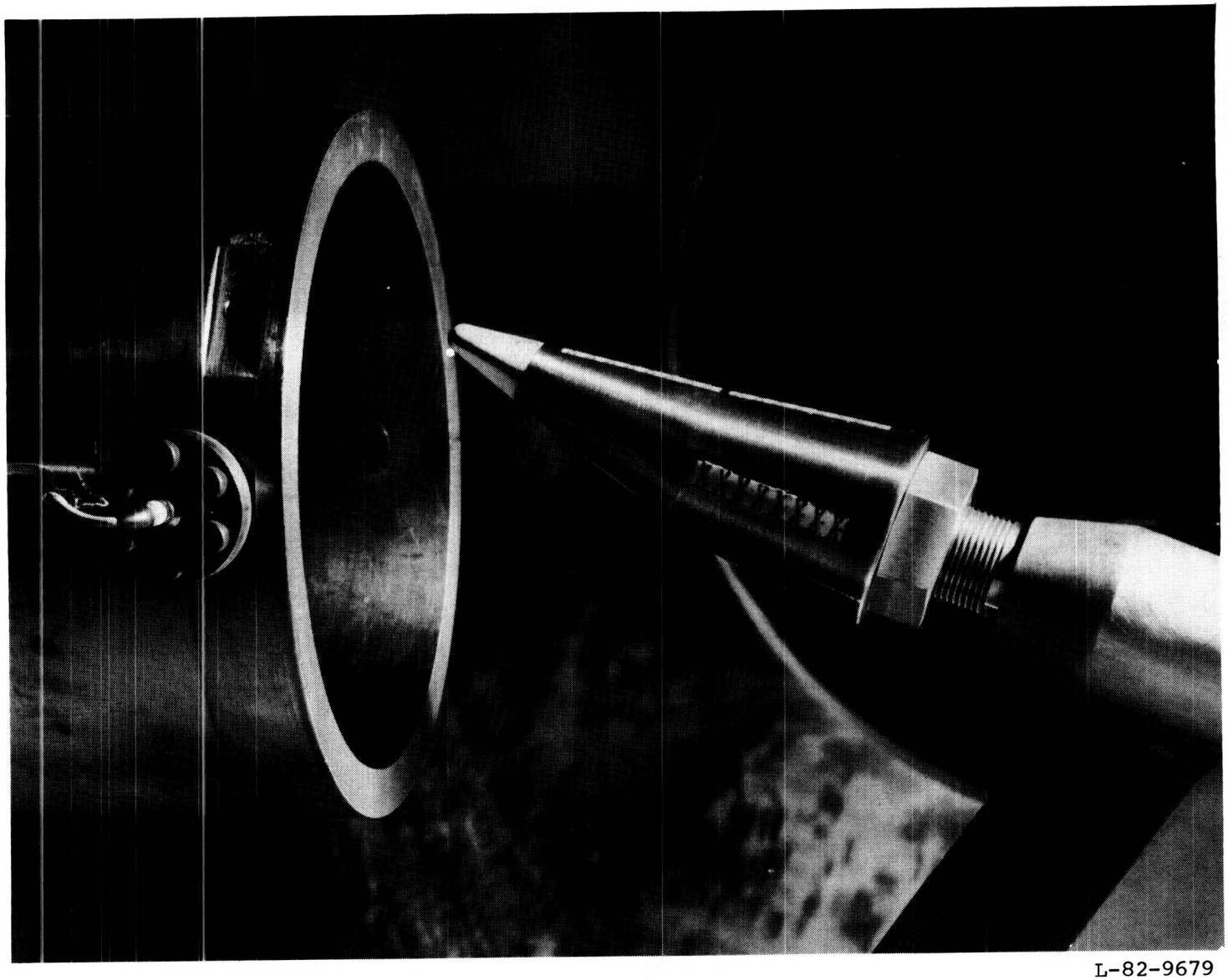

L-82-9679

Figure 3.- Bent-nose-biconic model in test section.

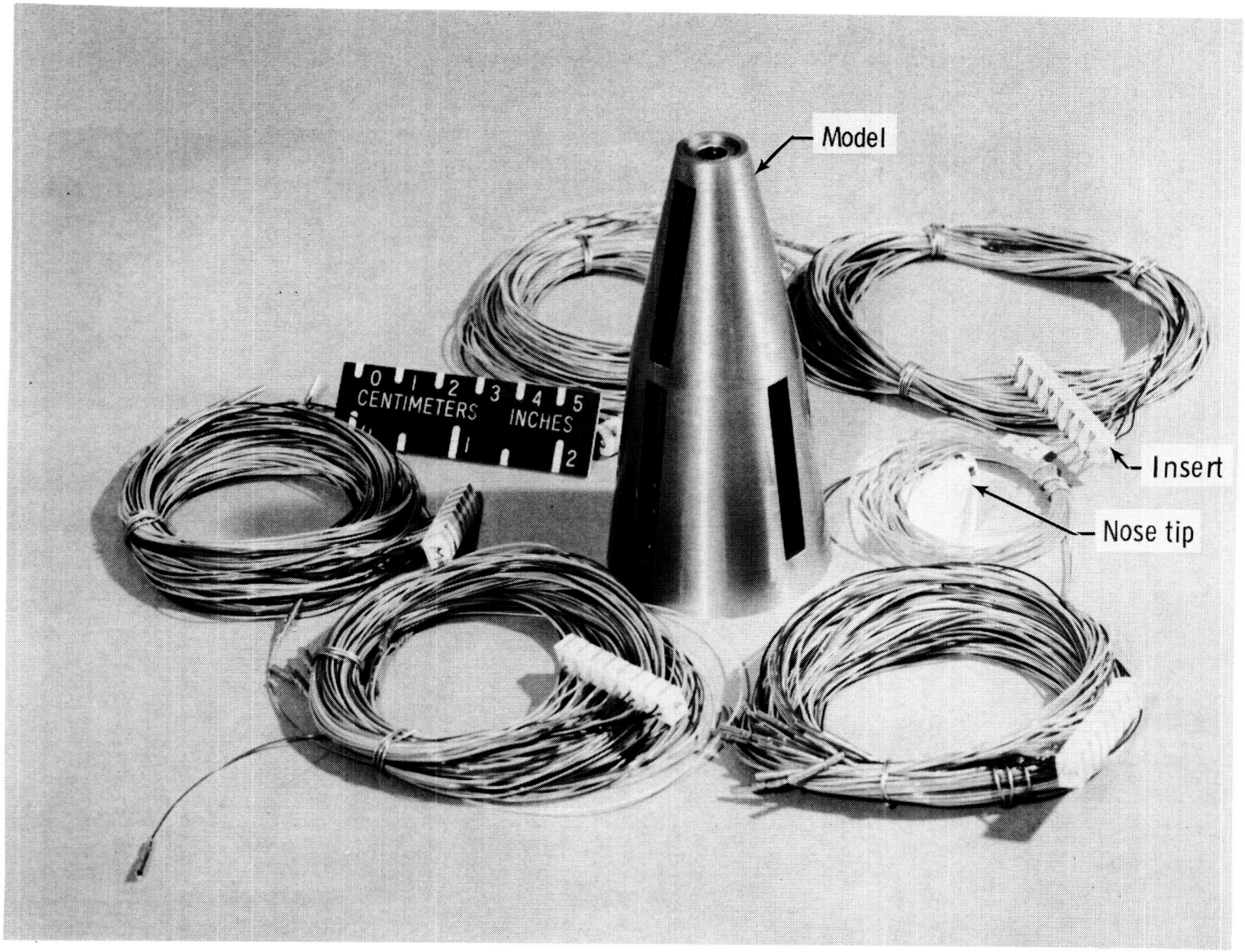

L-82-7297

(a) Unassembled.

Figure 4.- Unassembled and assembled model.

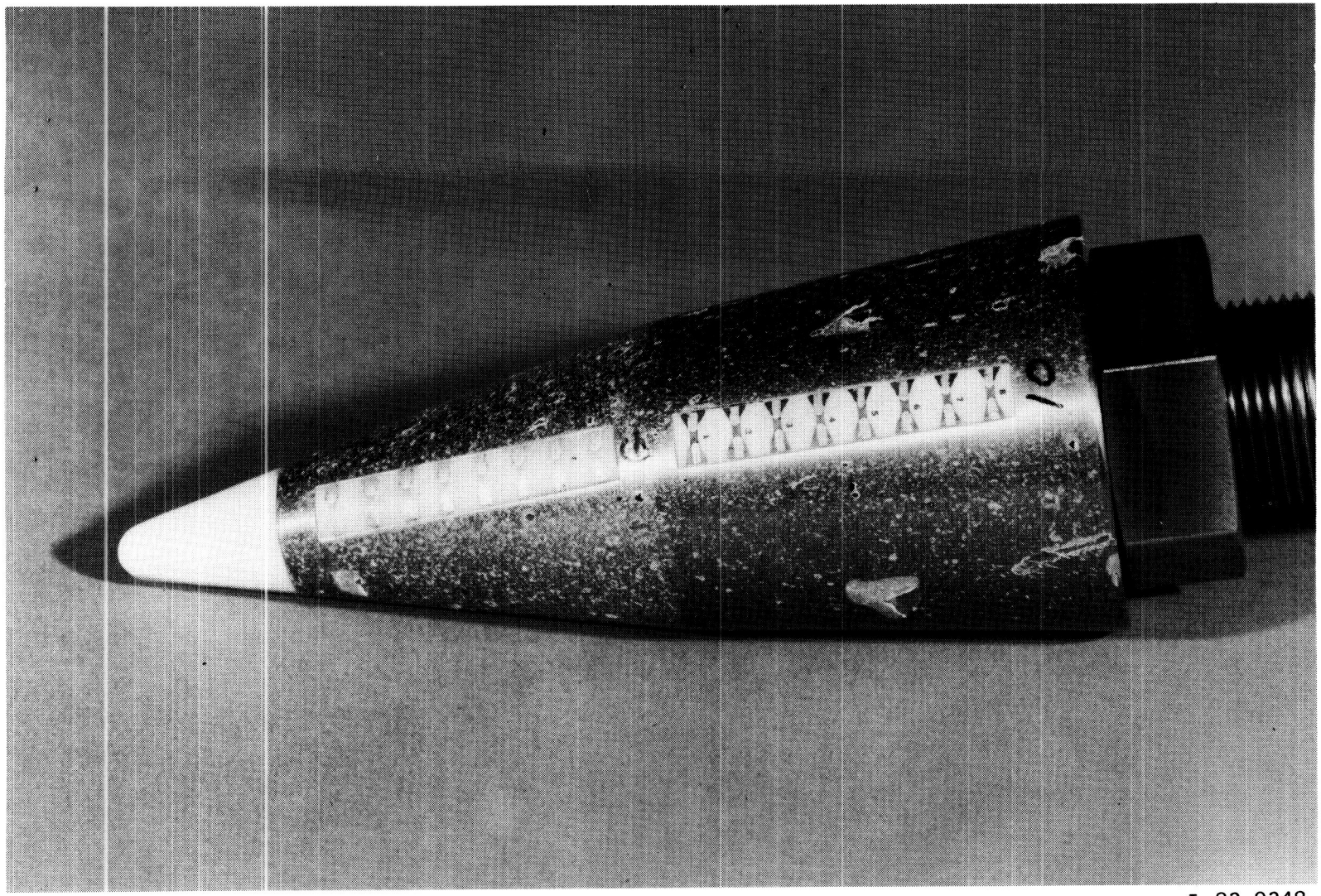

L-82-9248

(b) Assembled (post run).

Figure 4.- Concluded.

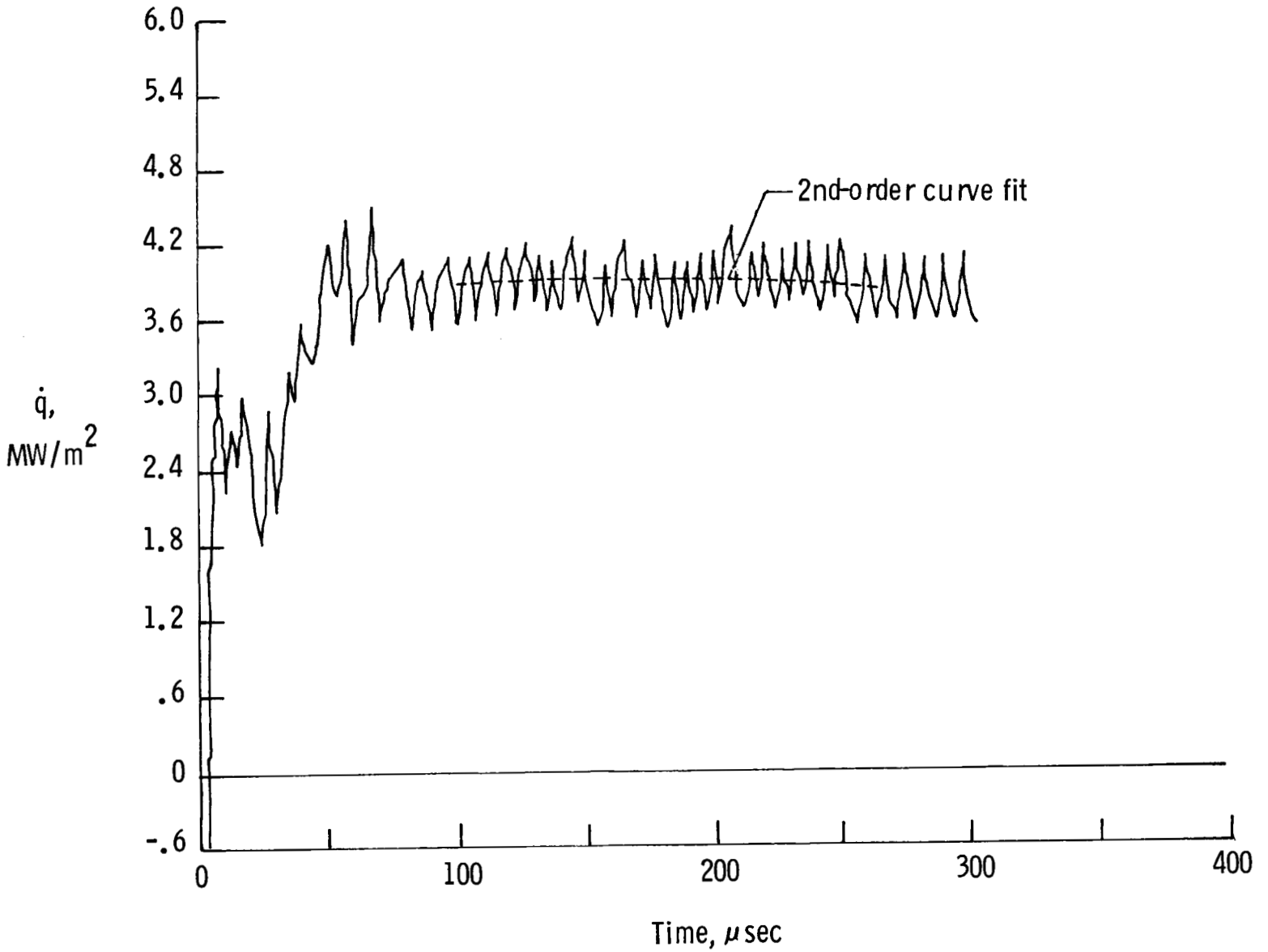

(a) Windward ray (ϕ = 180°); x/L = 0.45; $\dot{q}$ obtained by numerical method (ref. 20).

Figure 5.- Sample time histories of heat-transfer rate measured on straight biconic in air at α = 4°.

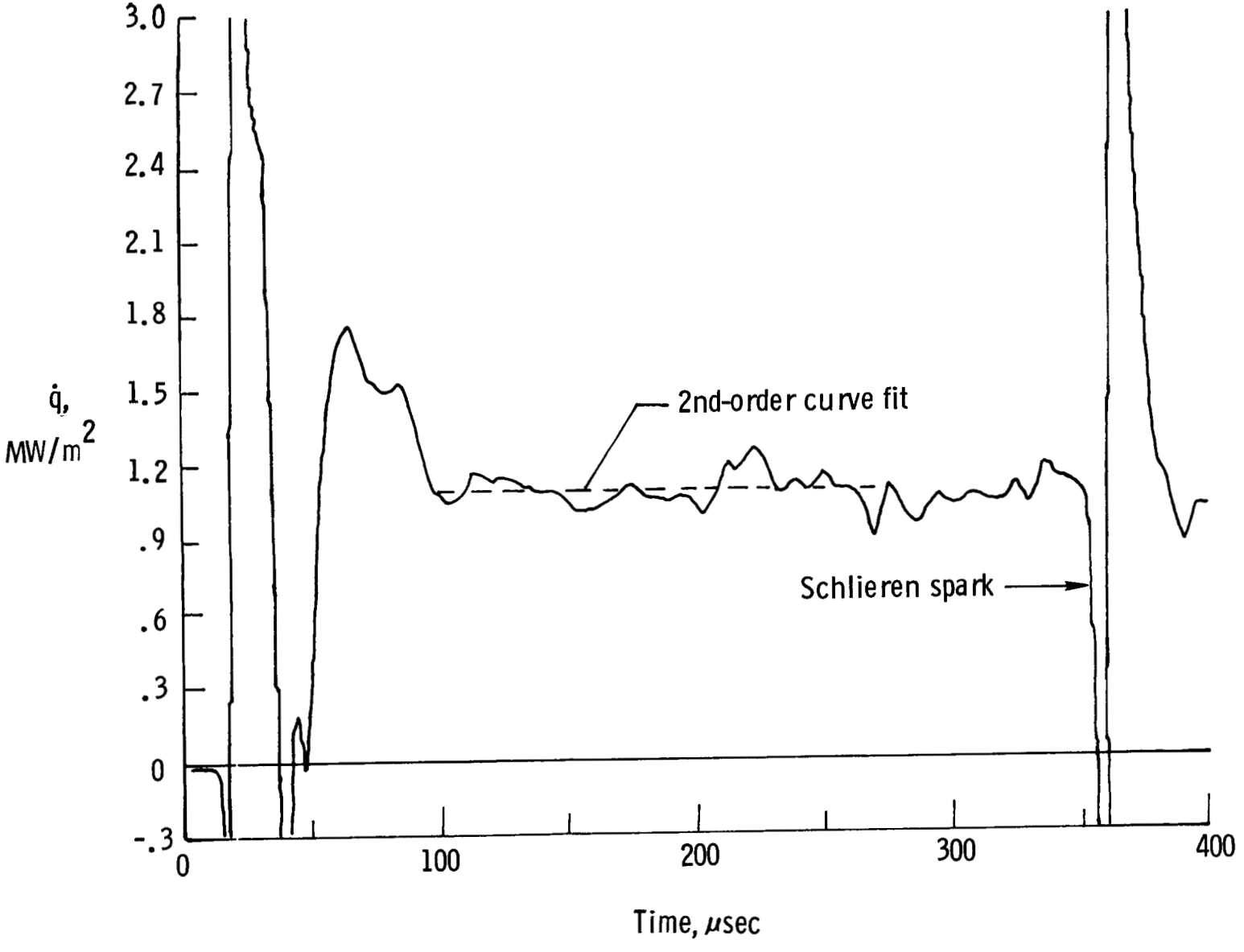

(b) Leeward ray (ϕ = 0°); x/L = 0.61; $\dot{q}$ obtained with analog circuit (ref. 21).

Figure 5.- Concluded.

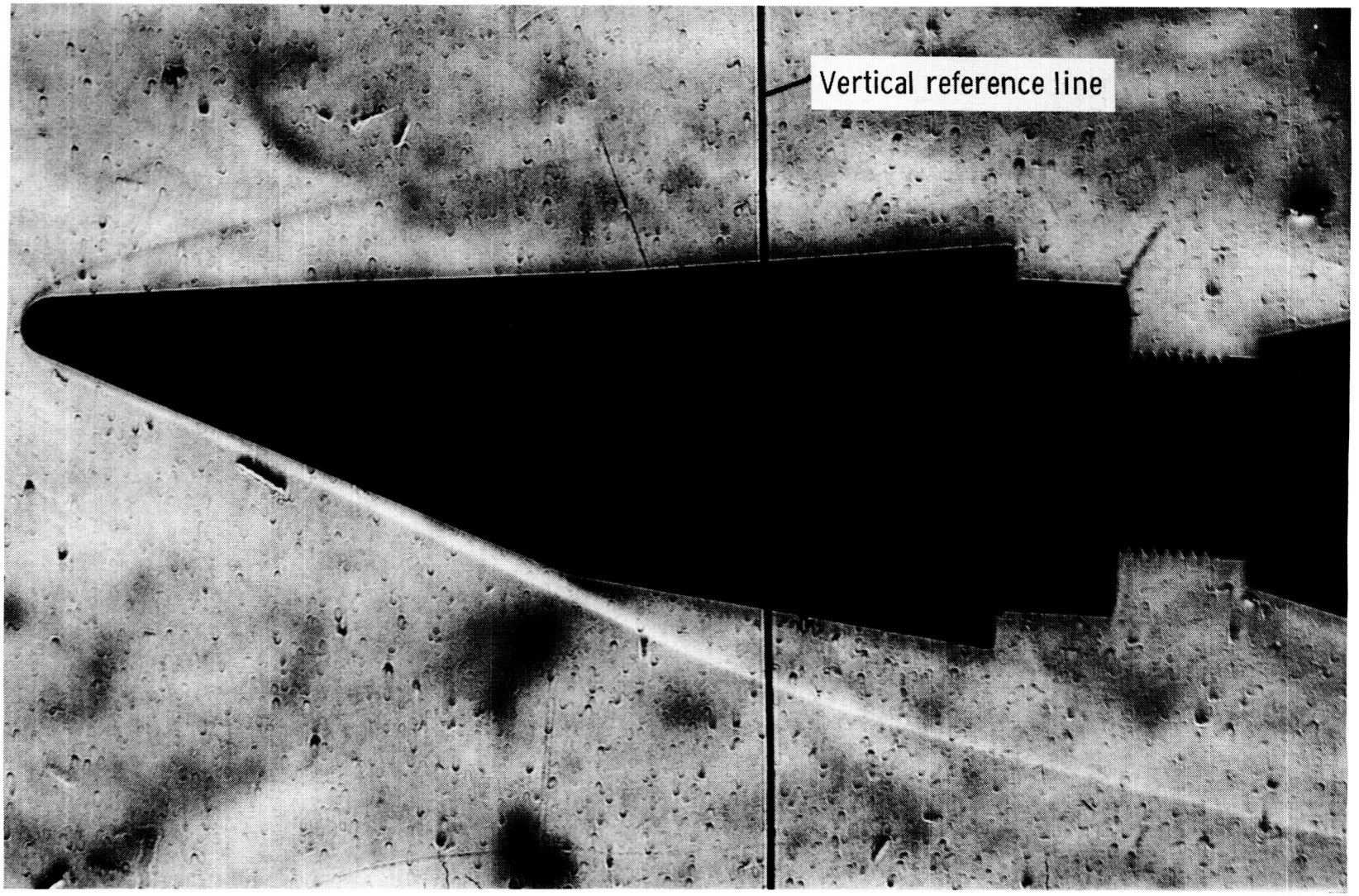

L-84-131

(a) $\alpha = 4°$.

Figure 6.- Representative schlieren photographs of bent-nose biconic in CO_2 test gas.

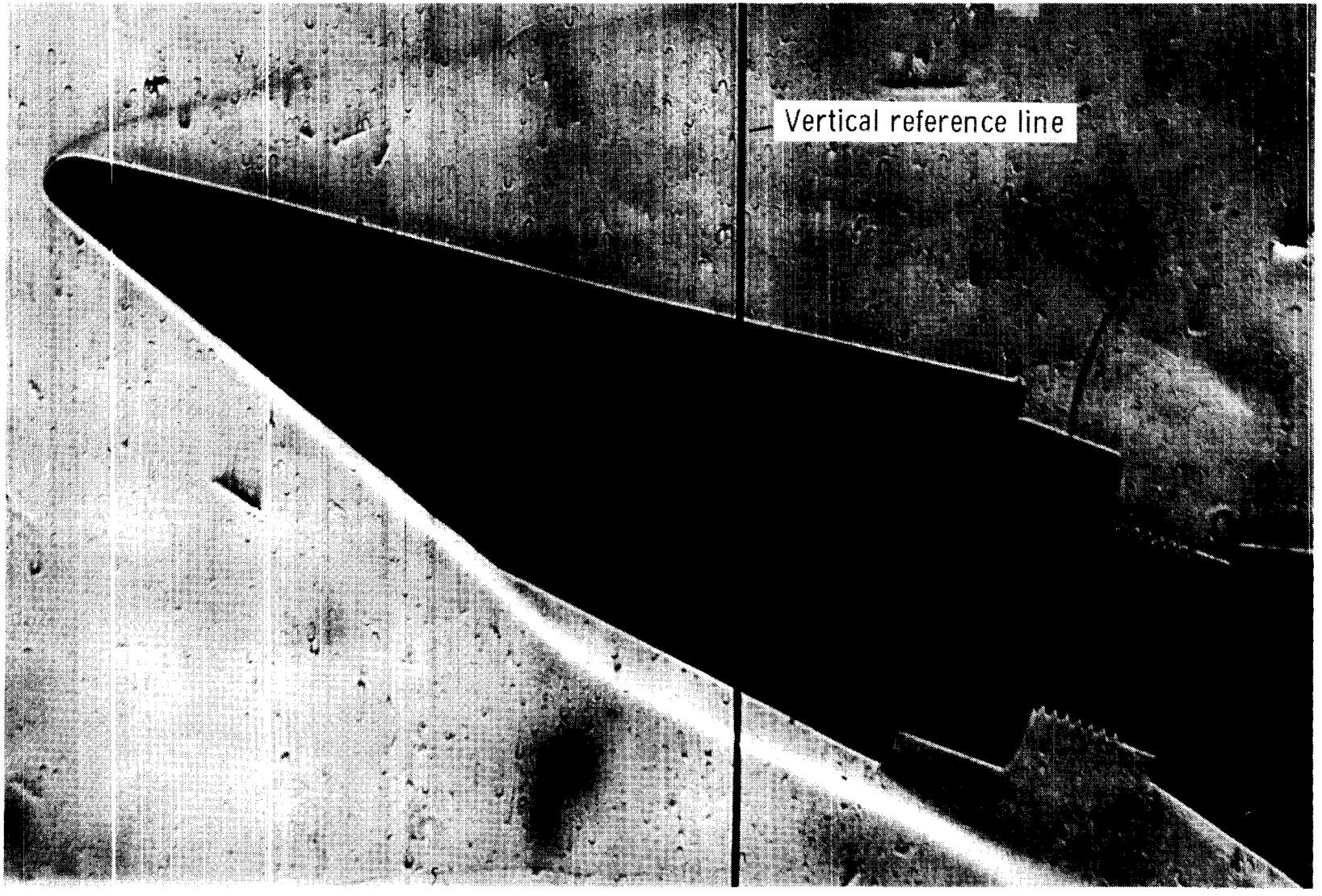

L-84-132

(b) $\alpha = 20°$.

Figure 6.- Concluded.

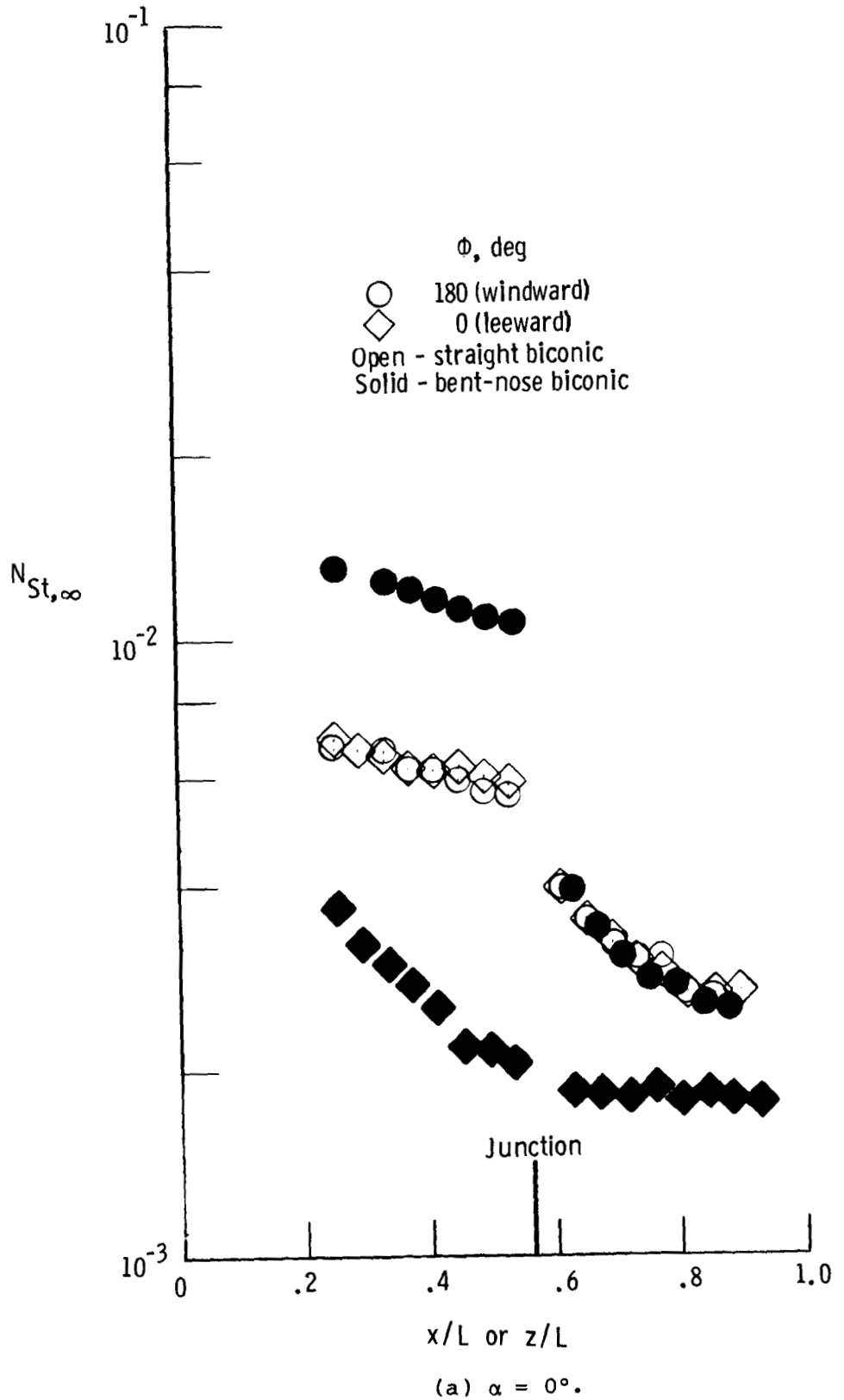

(a) $\alpha = 0°$.

Figure 7.- Effect of nose bend on heating in helium.

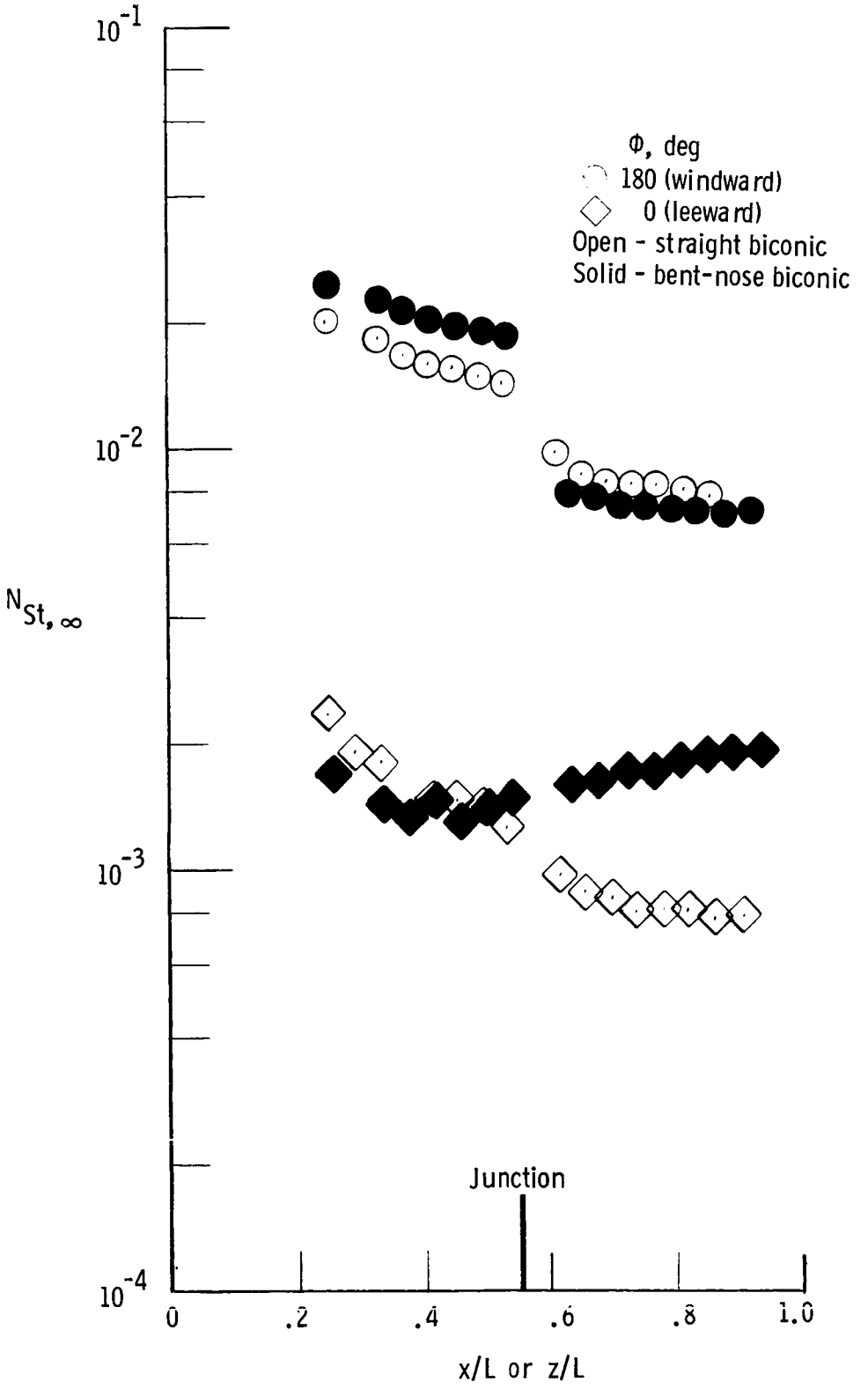

(b) $\alpha = 12°$.

Figure 7.- Continued.

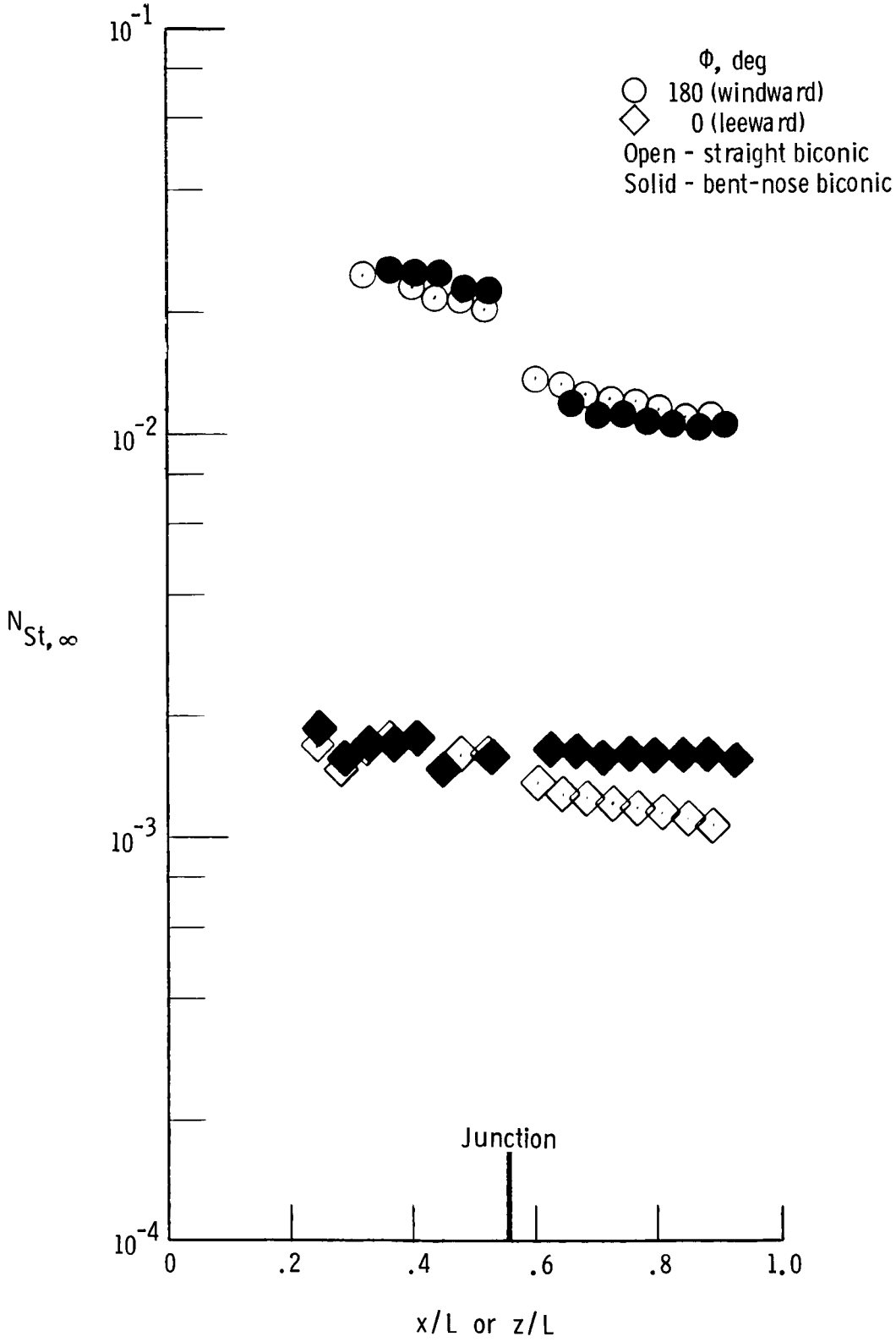

(c) $\alpha = 20°$.

Figure 7.- Concluded.

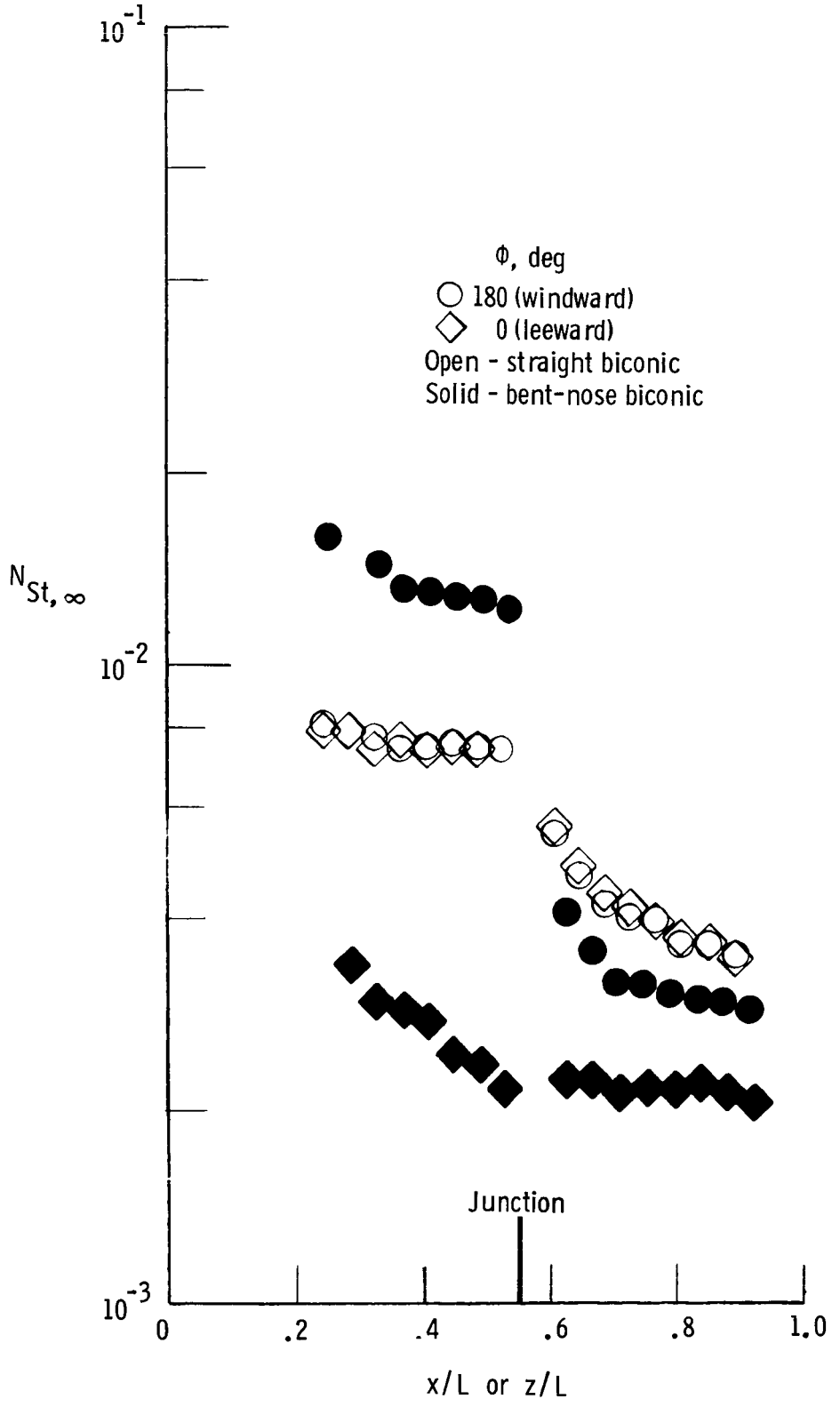

(a) $\alpha = 0°$.

Figure 8.- Effect of nose bend on heating in air.

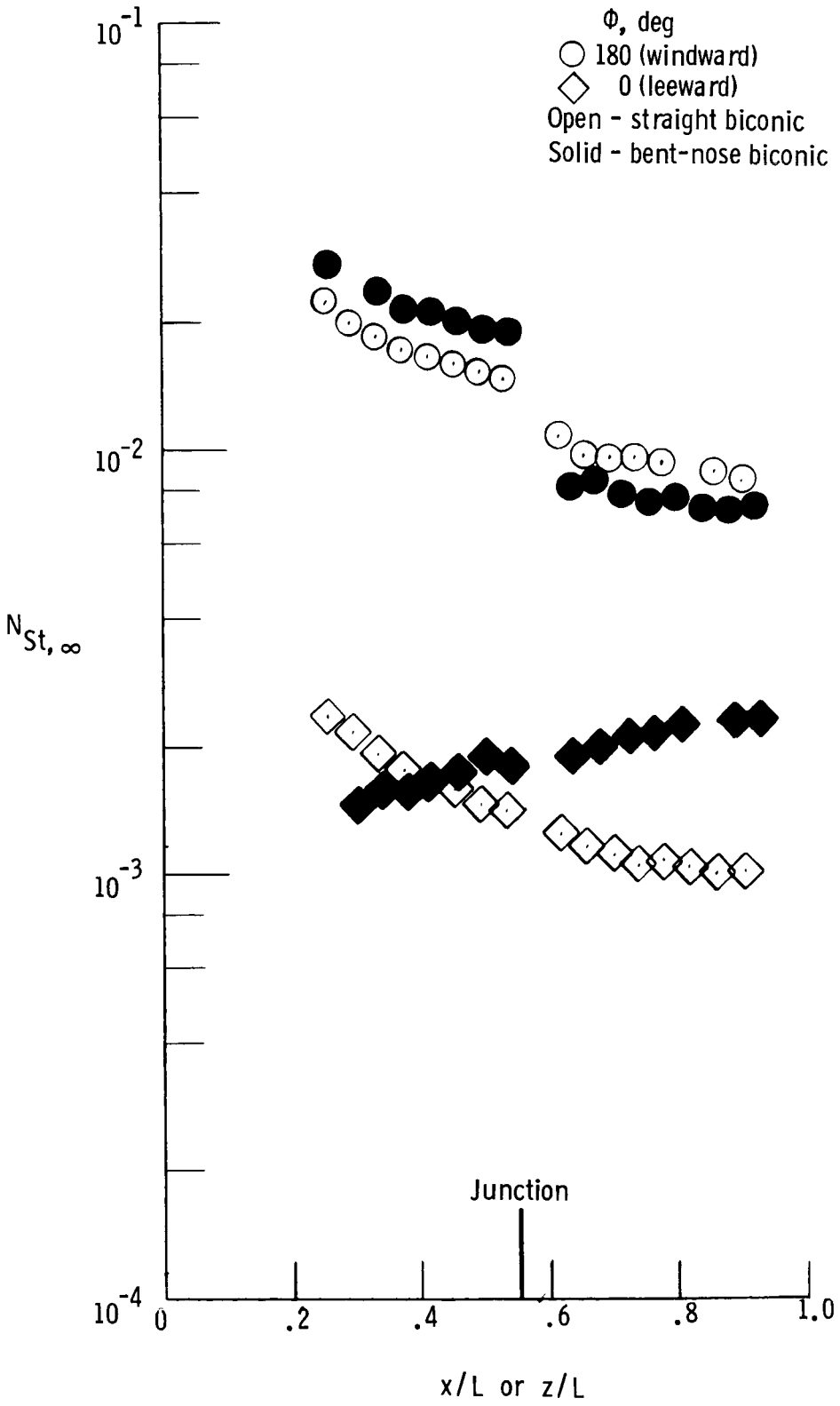

(b) $\alpha = 12°$.

Figure 8.- Continued.

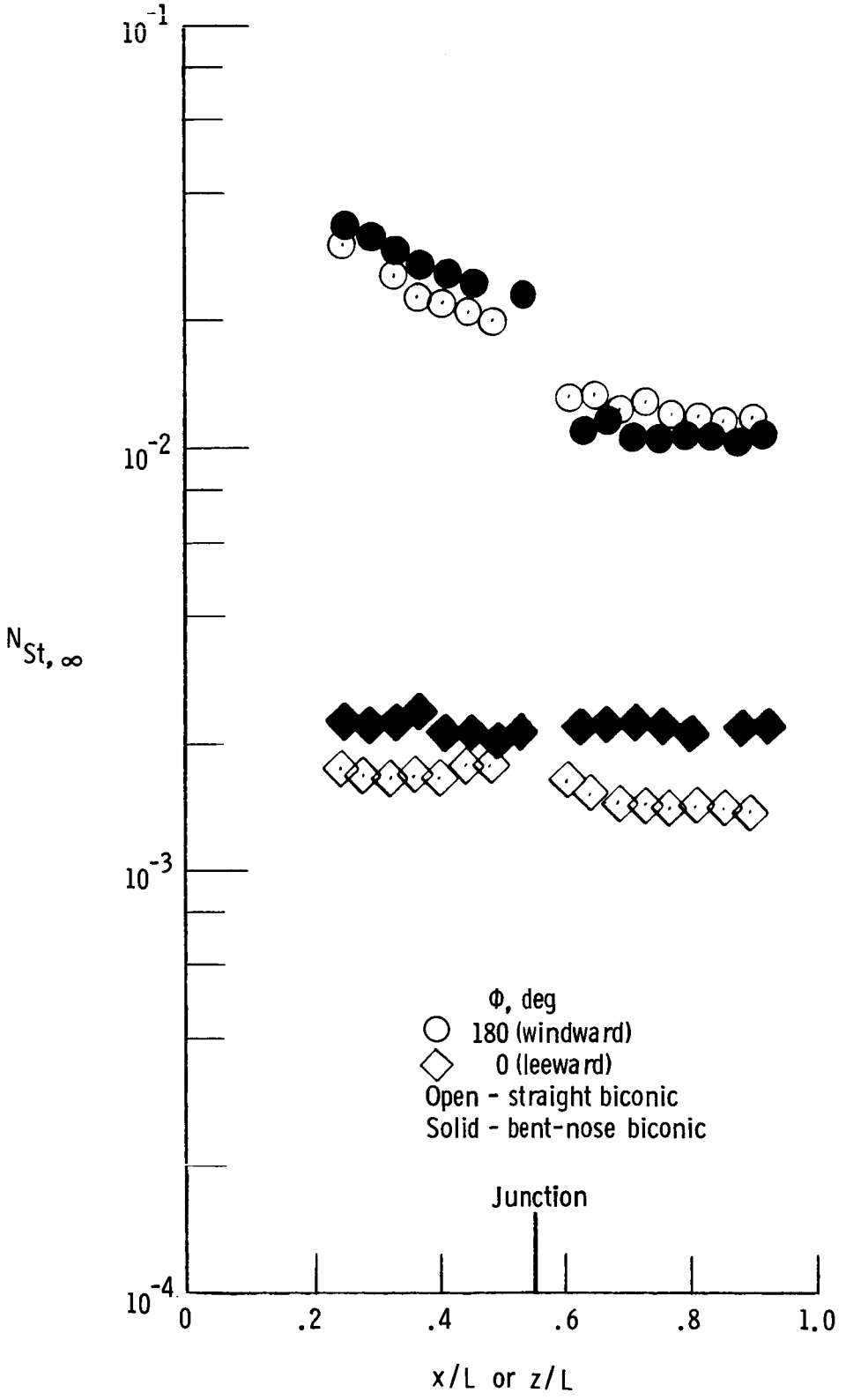

(c) $\alpha = 20°$.

Figure 8.- Concluded.

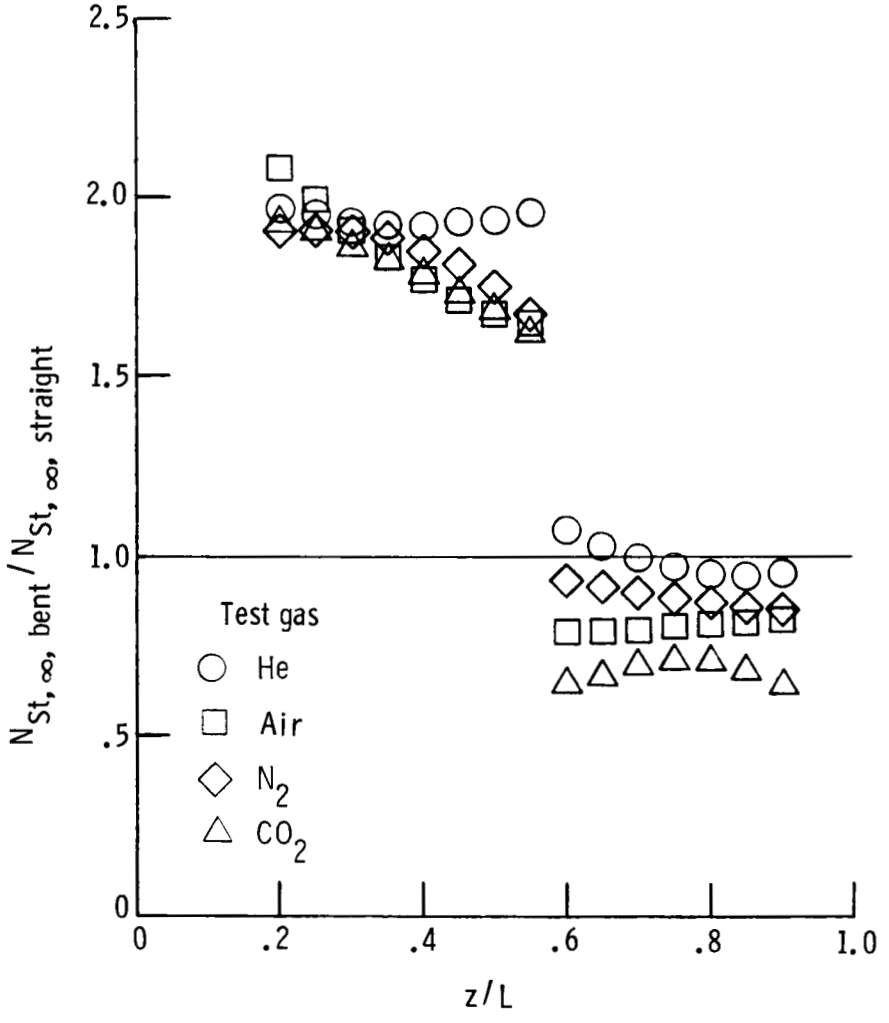

(a) $\alpha = 0°$.

Figure 9.- Ratio of bent-nose-biconic to straight-biconic windward heating for present test gases.

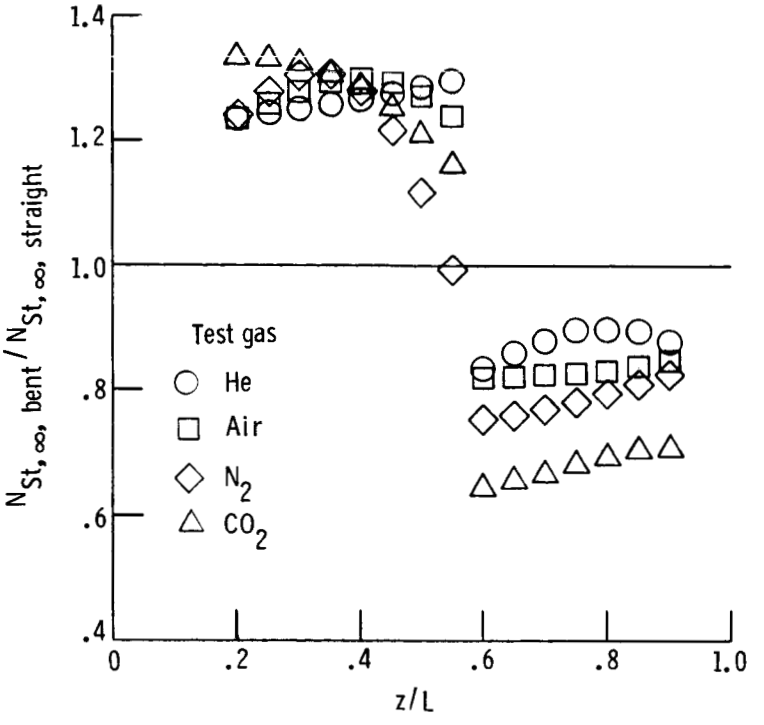

(b) $\alpha = 12°$.

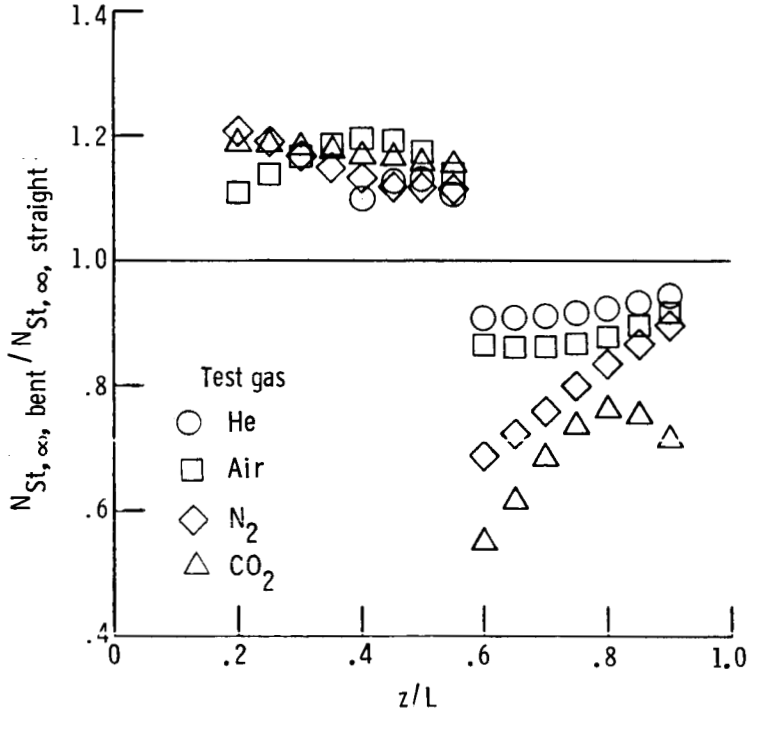

(c) $\alpha = 20°$.

Figure 9.- Concluded.

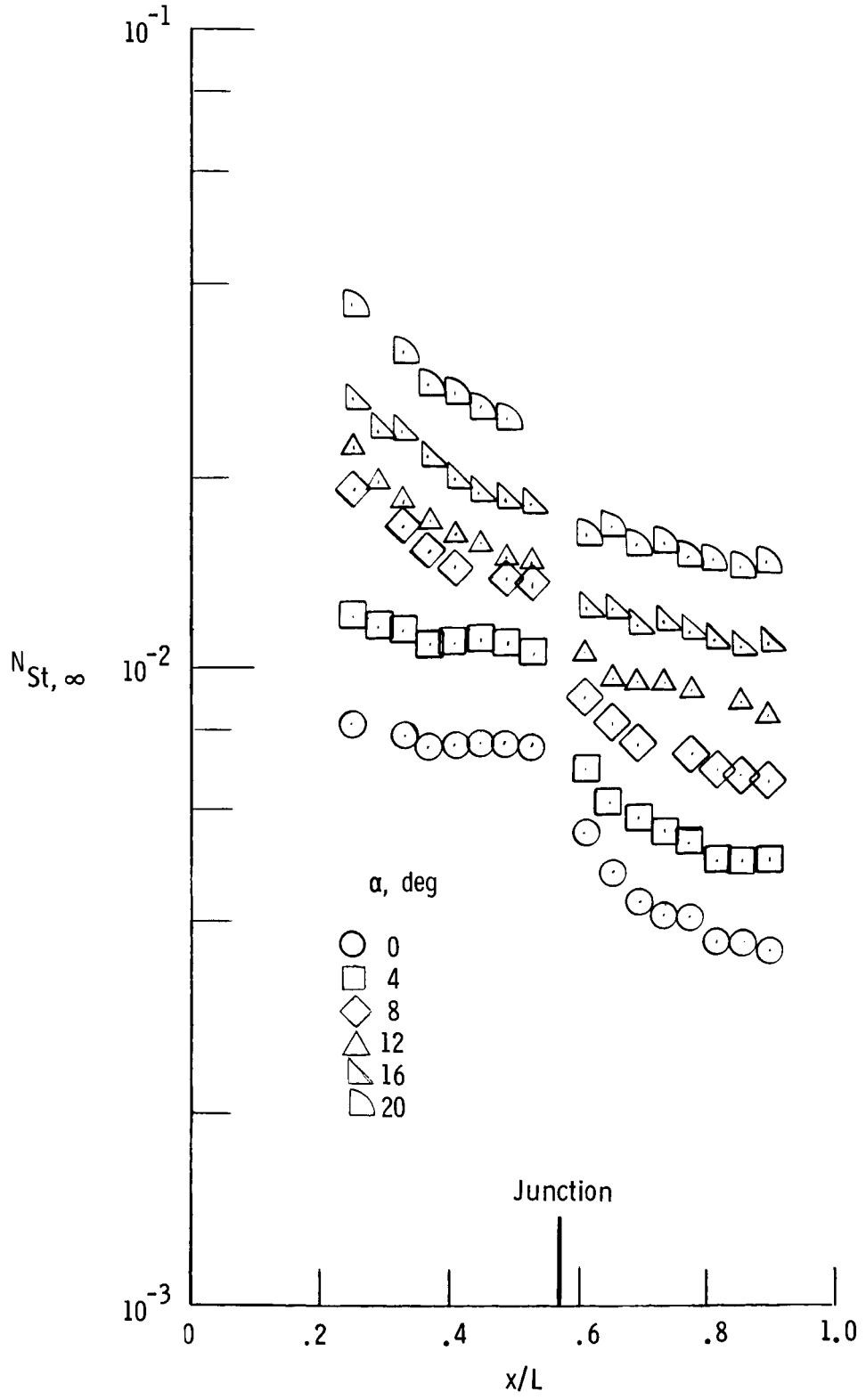

(a) Windward ray (ϕ = 180°).

Figure 10.- Effect of angle of attack on heating of straight biconic in air.

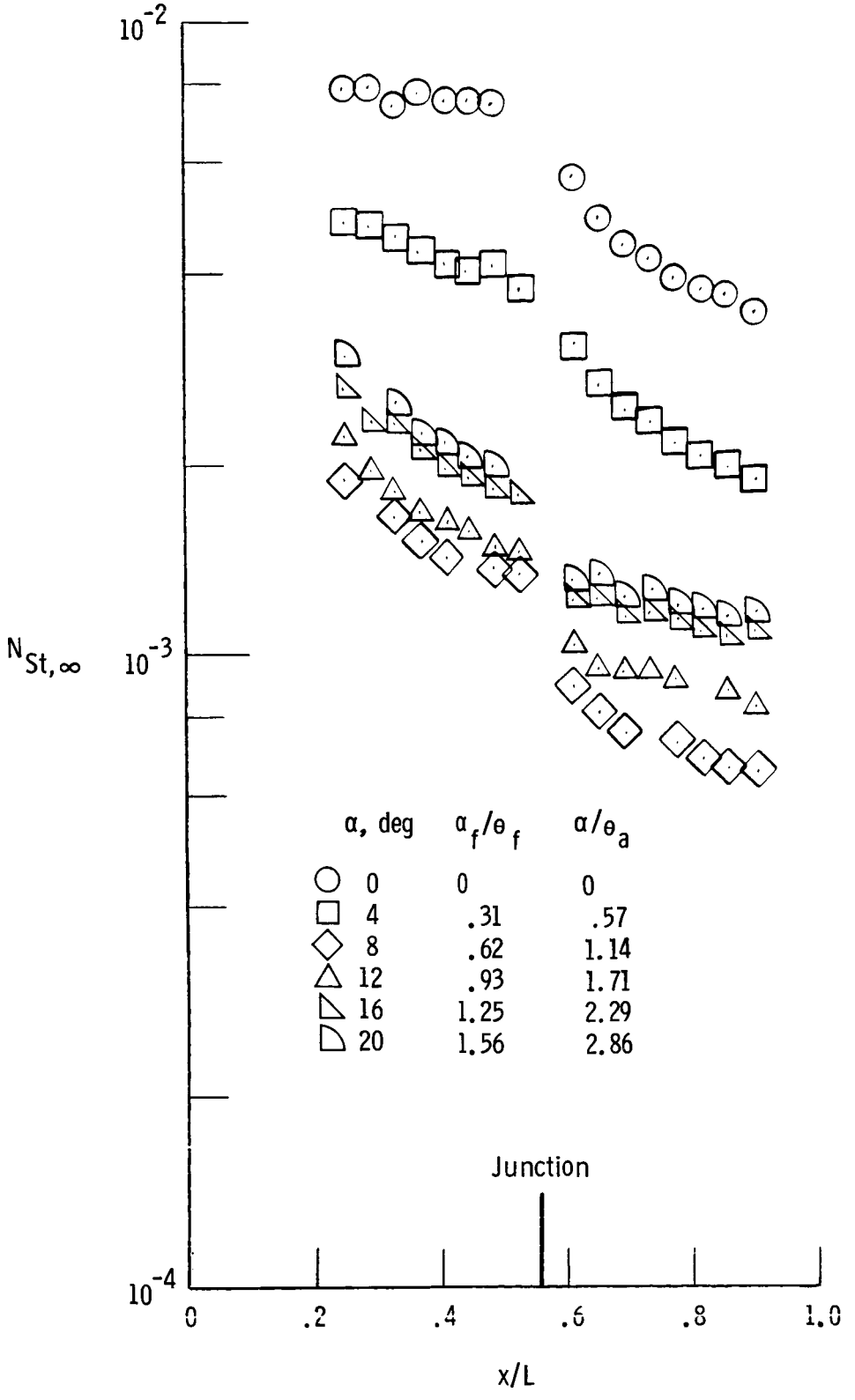

(b) Leeward ray (ϕ = 0°).

Figure 10.- Continued.

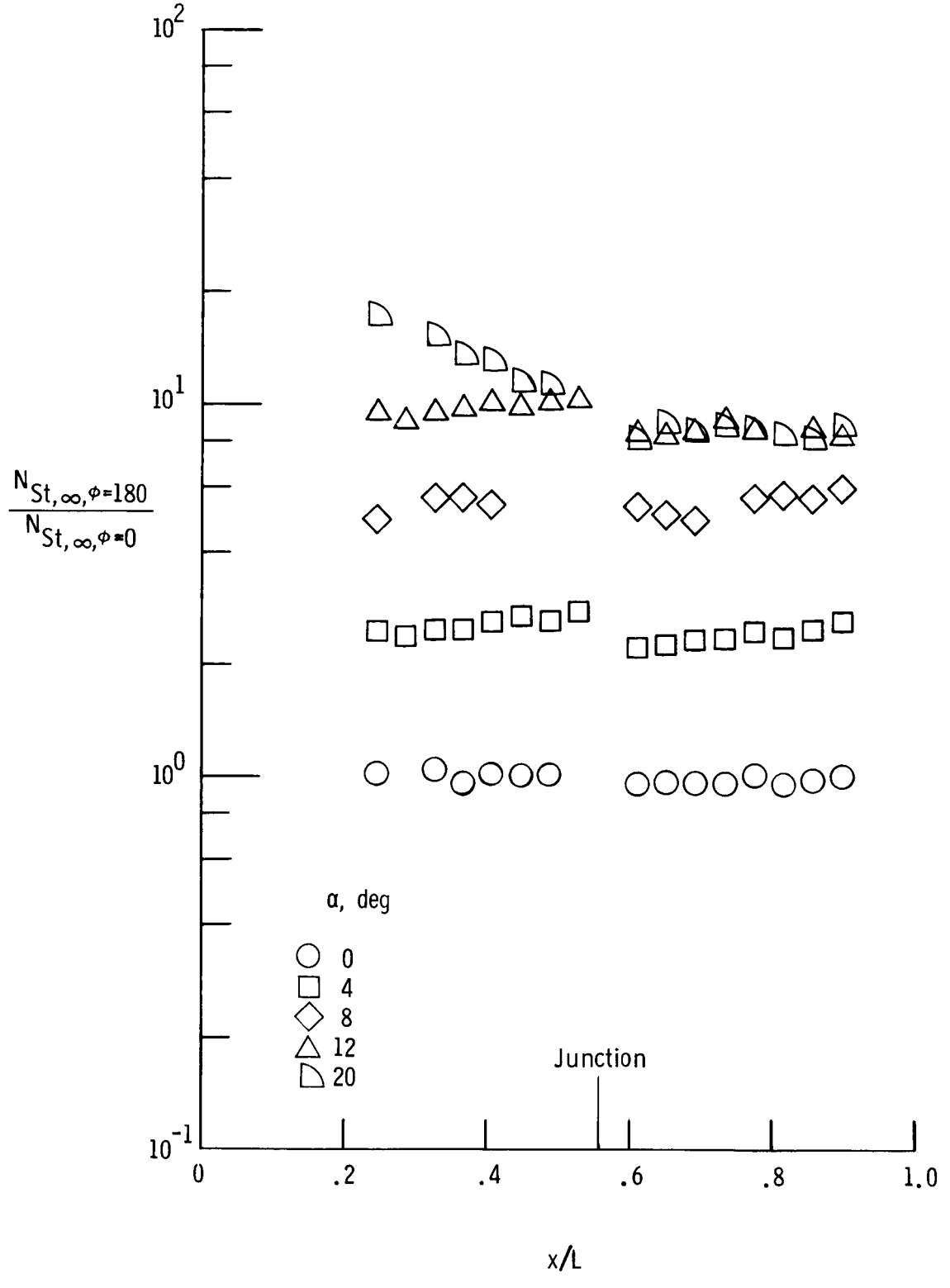

(c) Ratio of windward to leeward.

Figure 10.- Concluded.

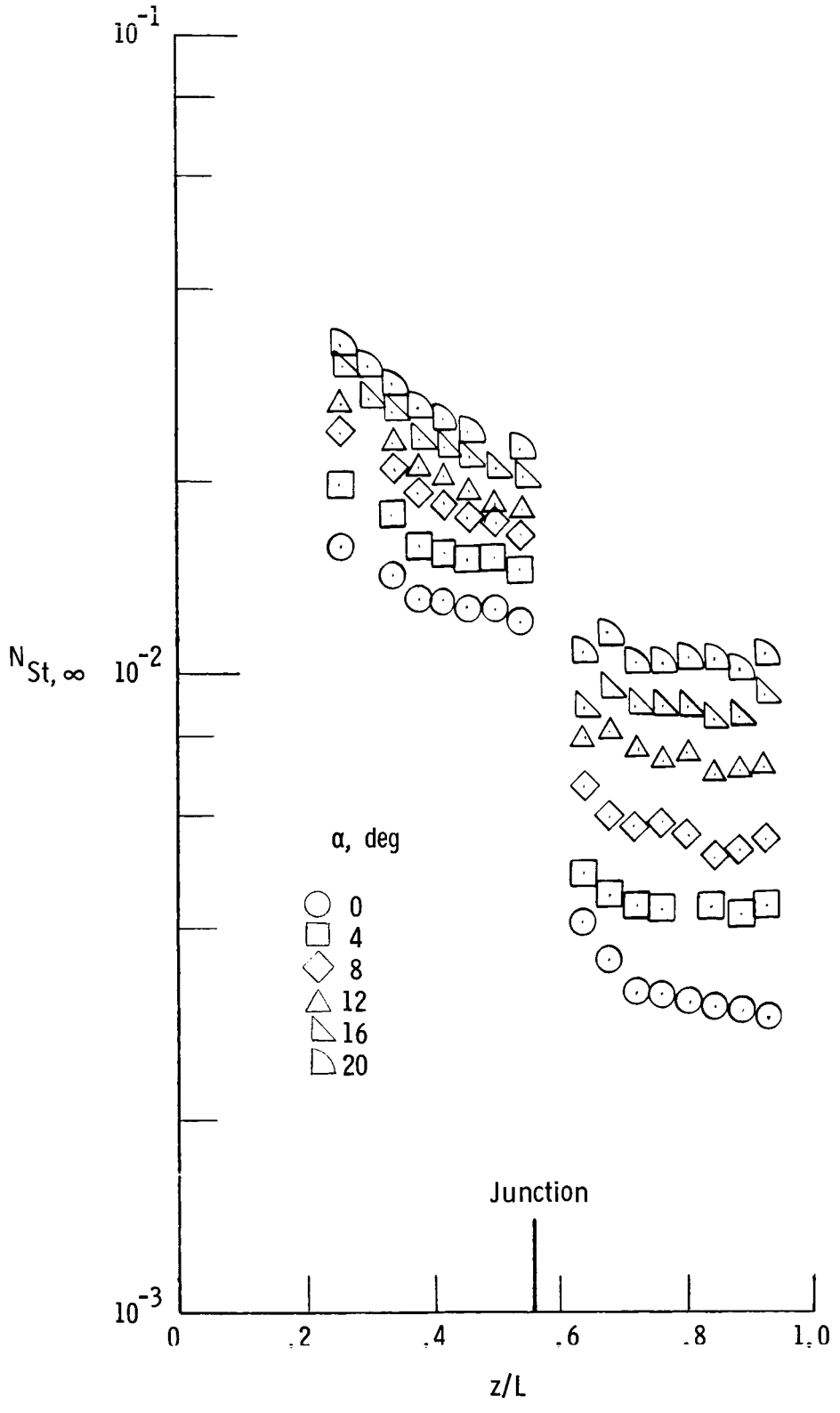

(a) Windward ray (ϕ = 180°).

Figure 11.- Effect of angle of attack on heating of bent-nose biconic in air.

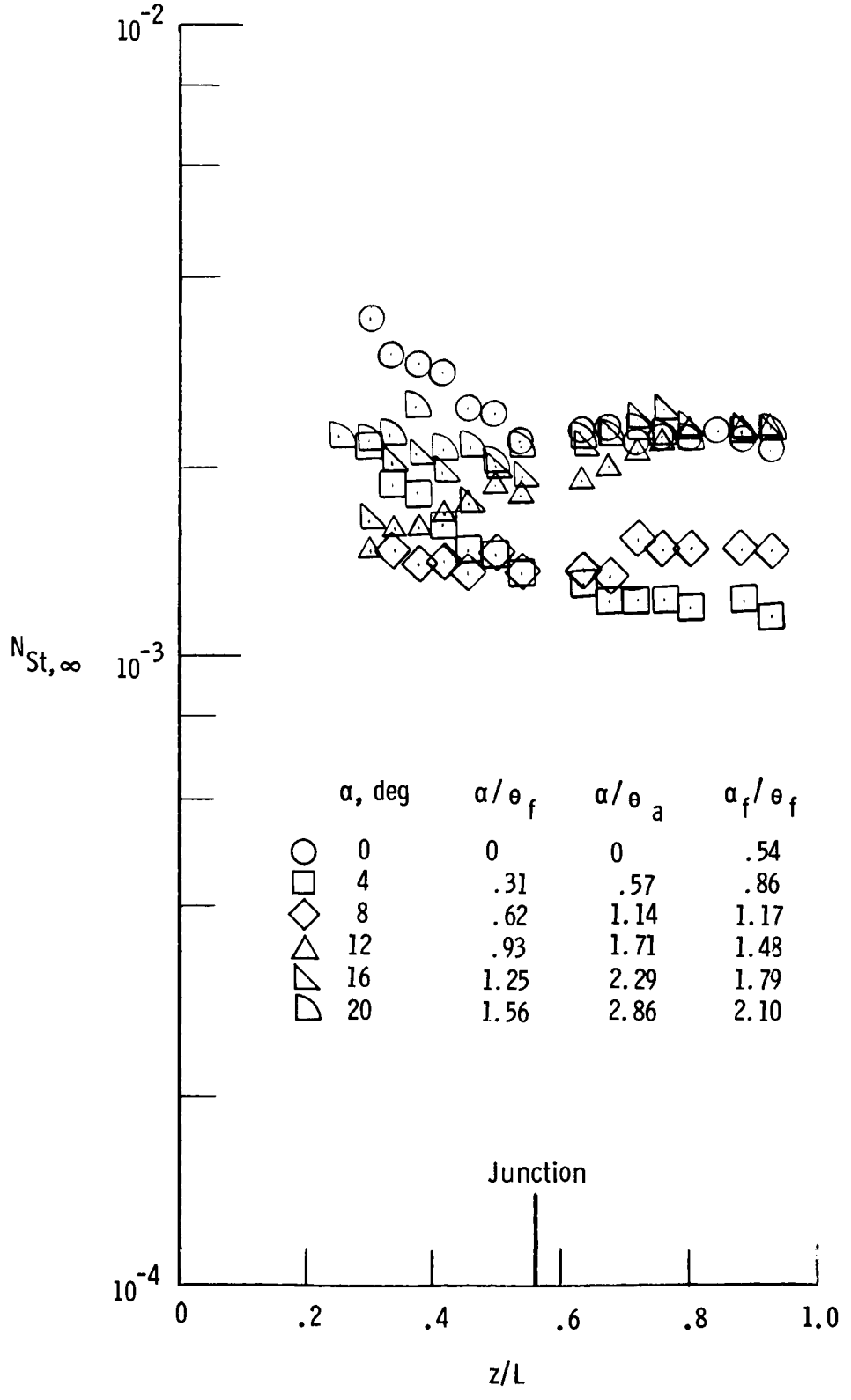

(b) Leeward ray (ϕ = 0°).

Figure 11.- Continued.

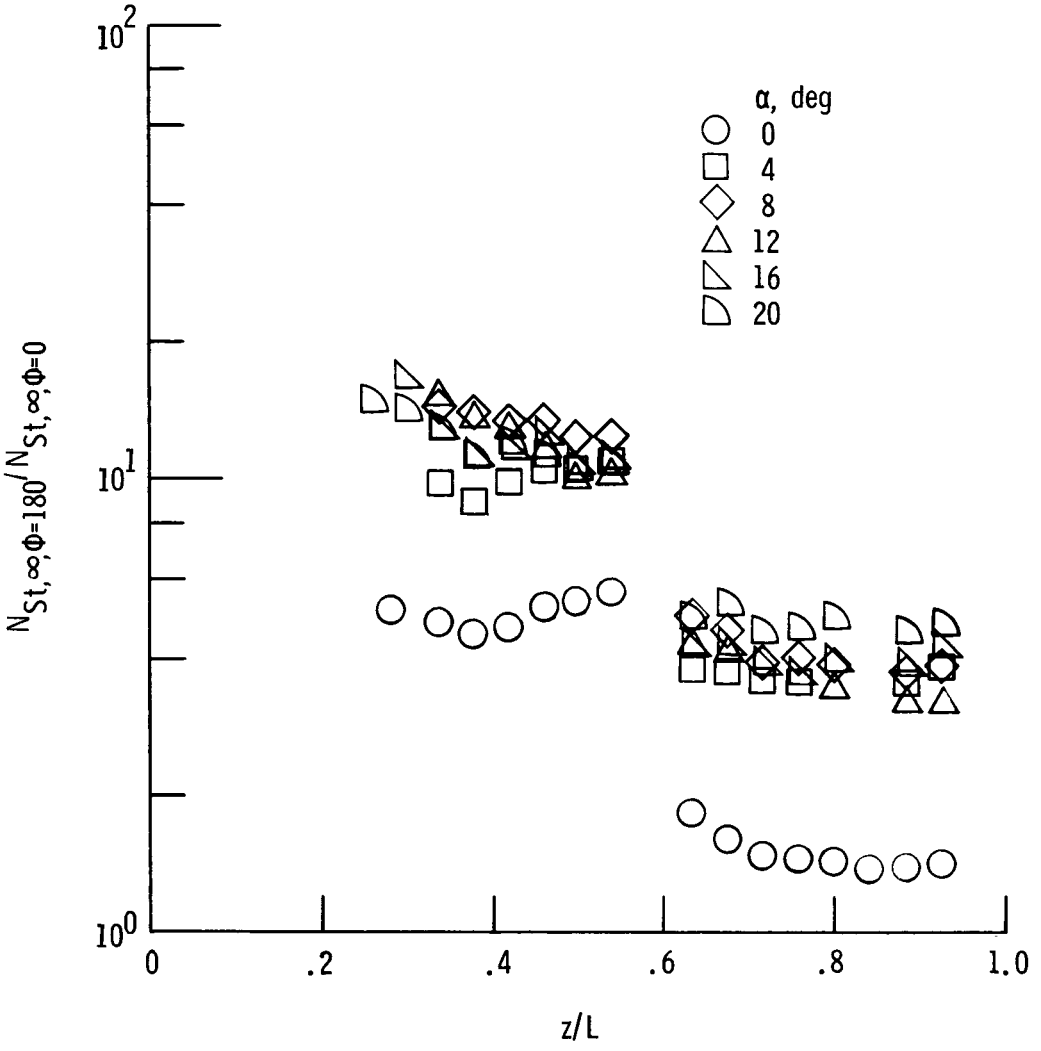

(c) Ratio of windward to leeward.

Figure 11.- Concluded.

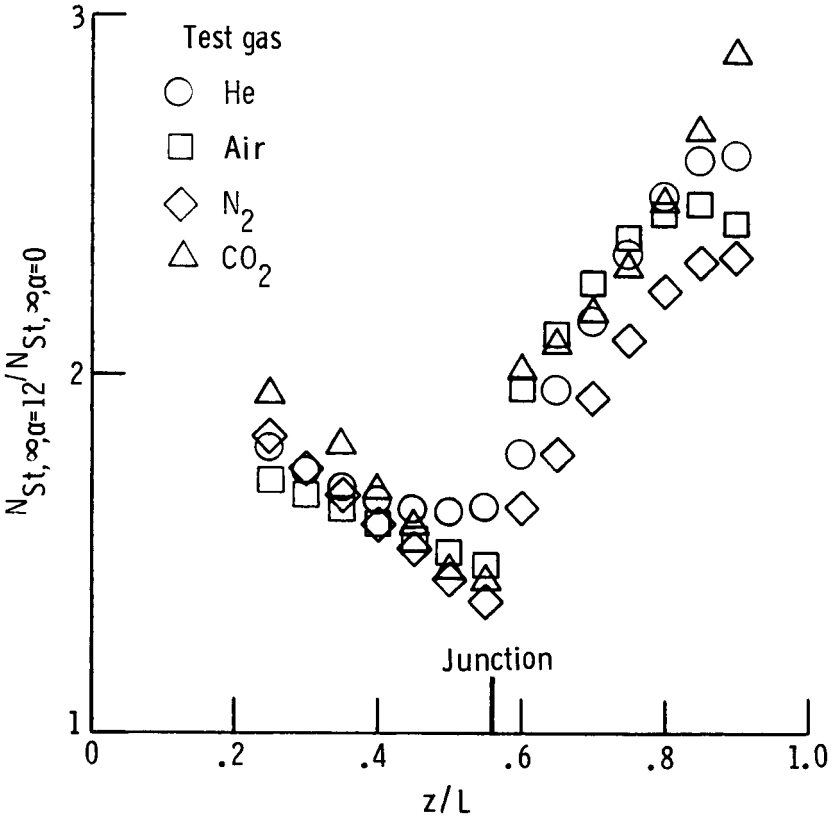

(a) $\alpha = 12°$.

Figure 12.- Ratio of bent-nose-biconic windward heating at incidence ($\alpha = 12°$ and $20°$) to windward heating at $\alpha = 0°$ for present test gases.

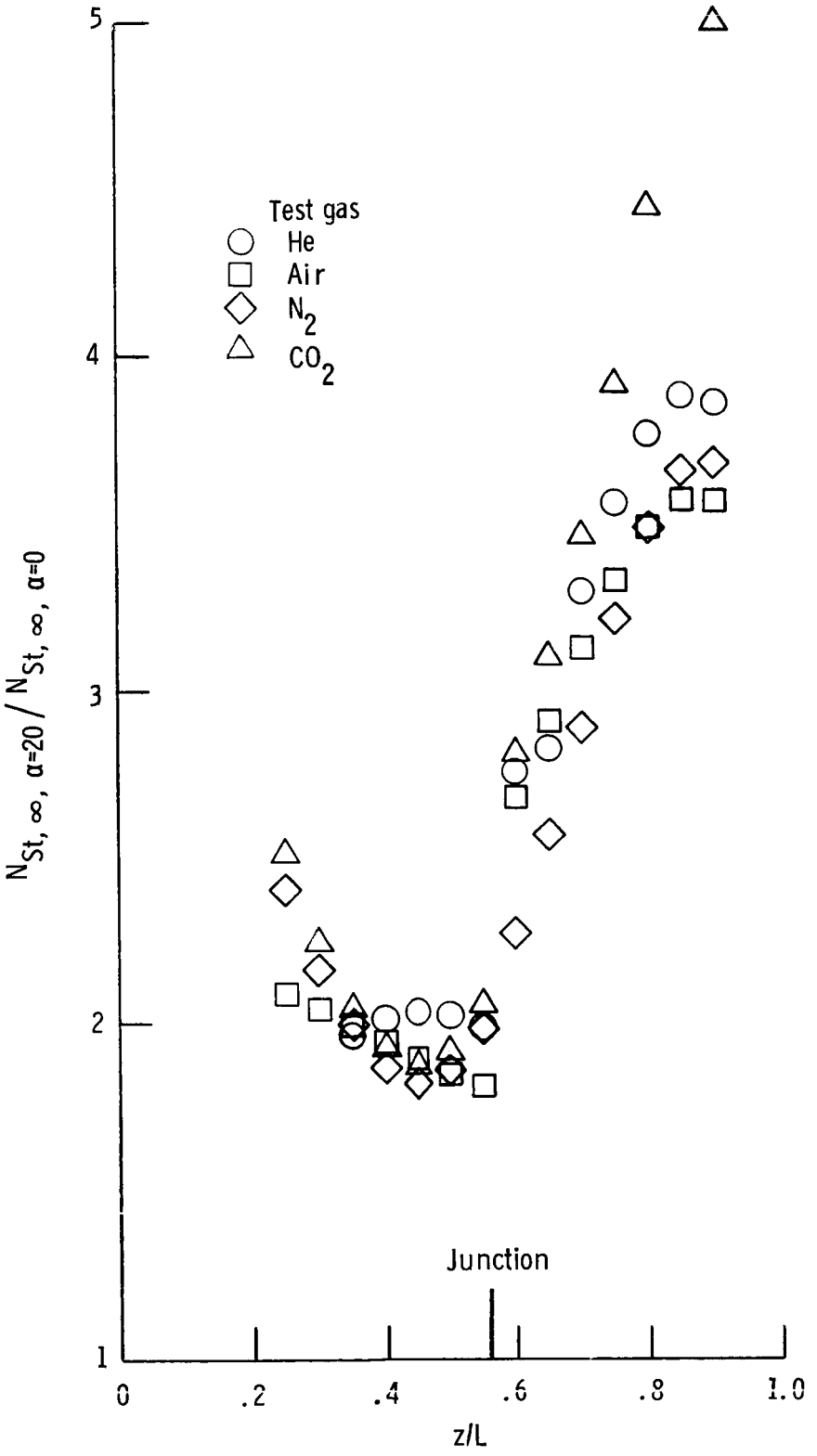

(b) $\alpha = 20°$.

Figure 12.- Concluded.

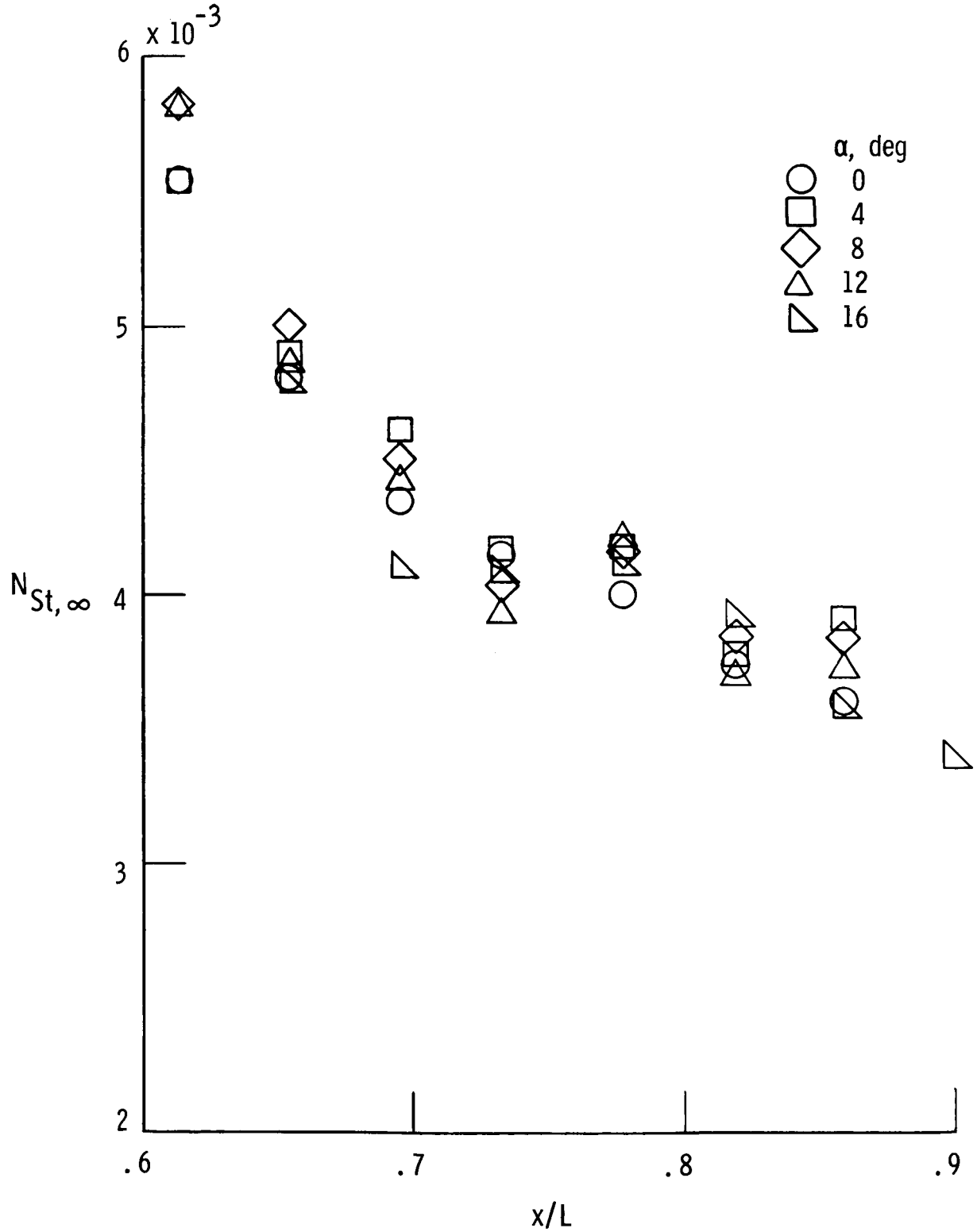

Figure 13.- Effect of angle of attack on heating along midmeridian ray (ϕ = 90°) of straight biconic in air.

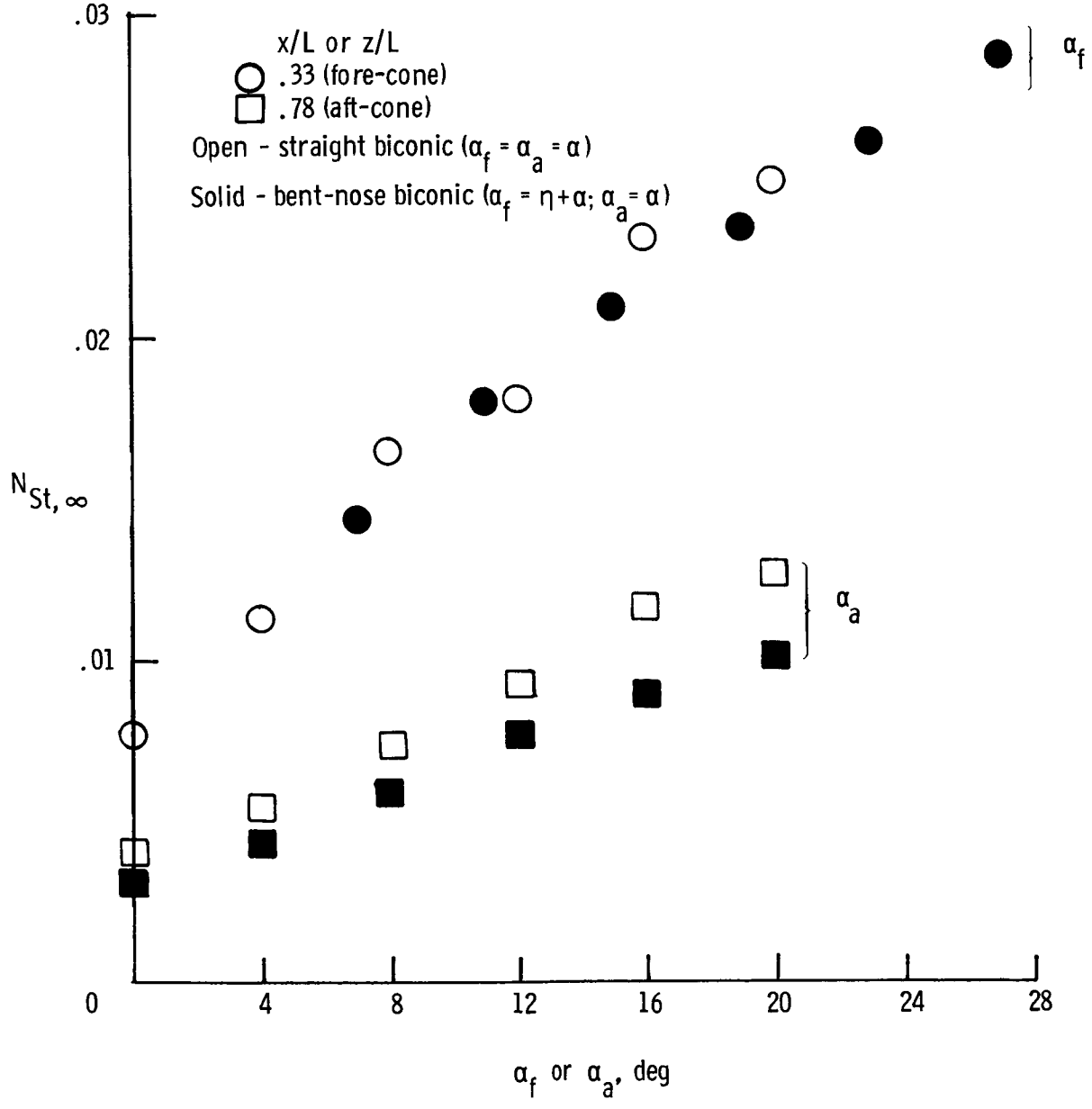

(a) Windward (ϕ = 180°).

Figure 14.- Effect of angle of attack on windward and leeward heating in air.

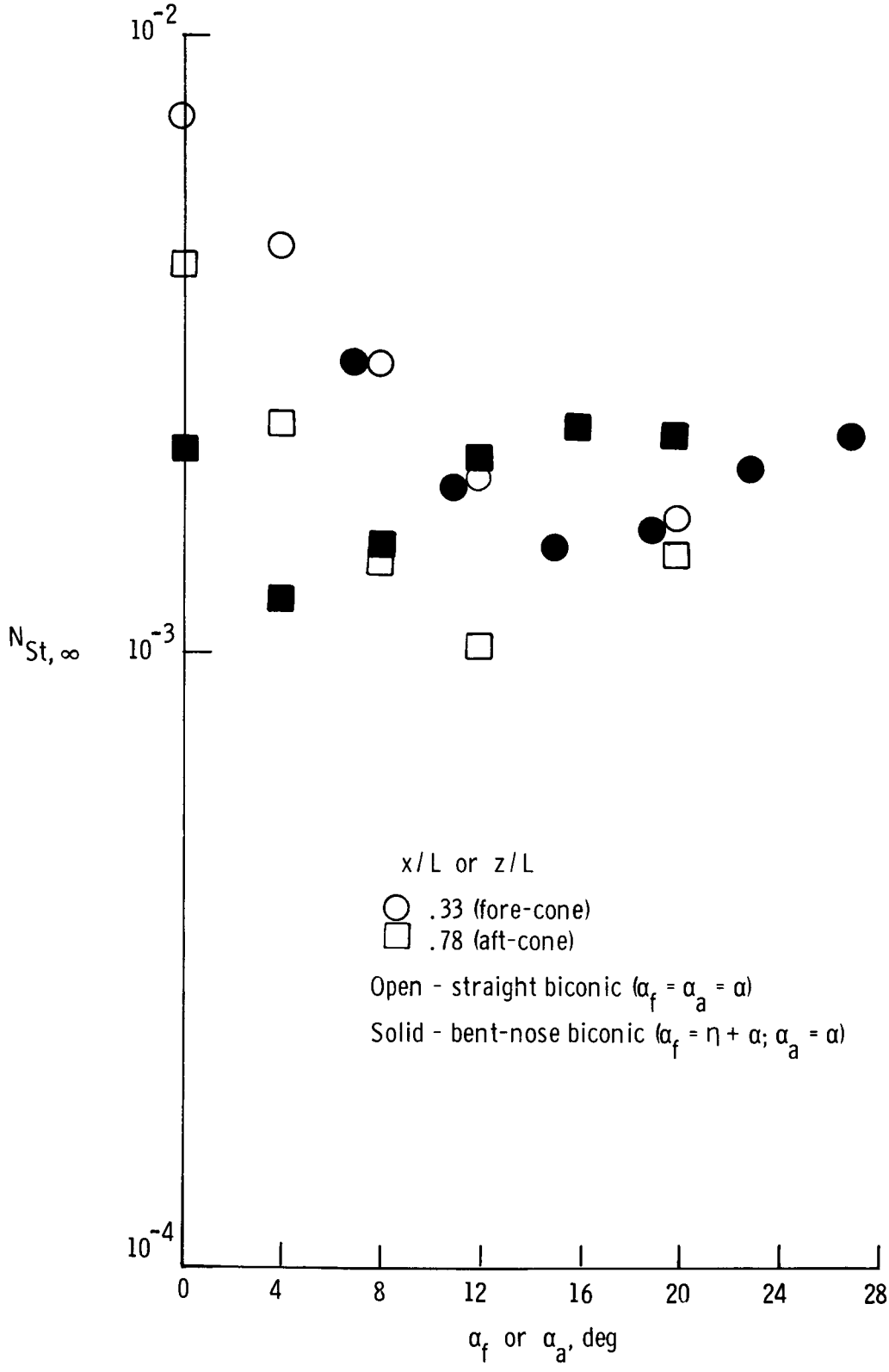

(b) Leeward (ϕ = 0°).

Figure 14.- Concluded.

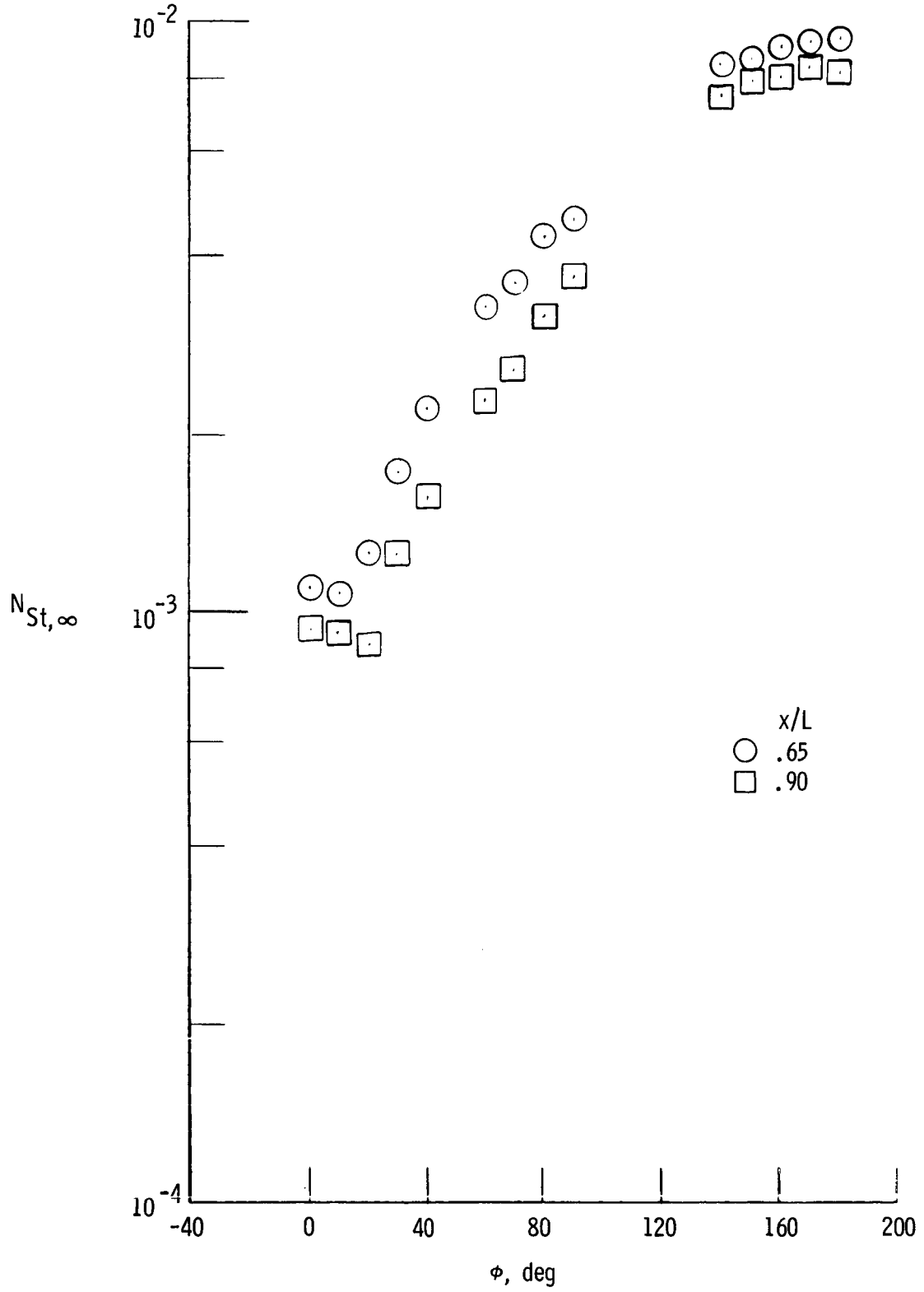

Figure 15.- Circumferential heating distribution on aft cone of straight biconic in air at $\alpha = 12°$.

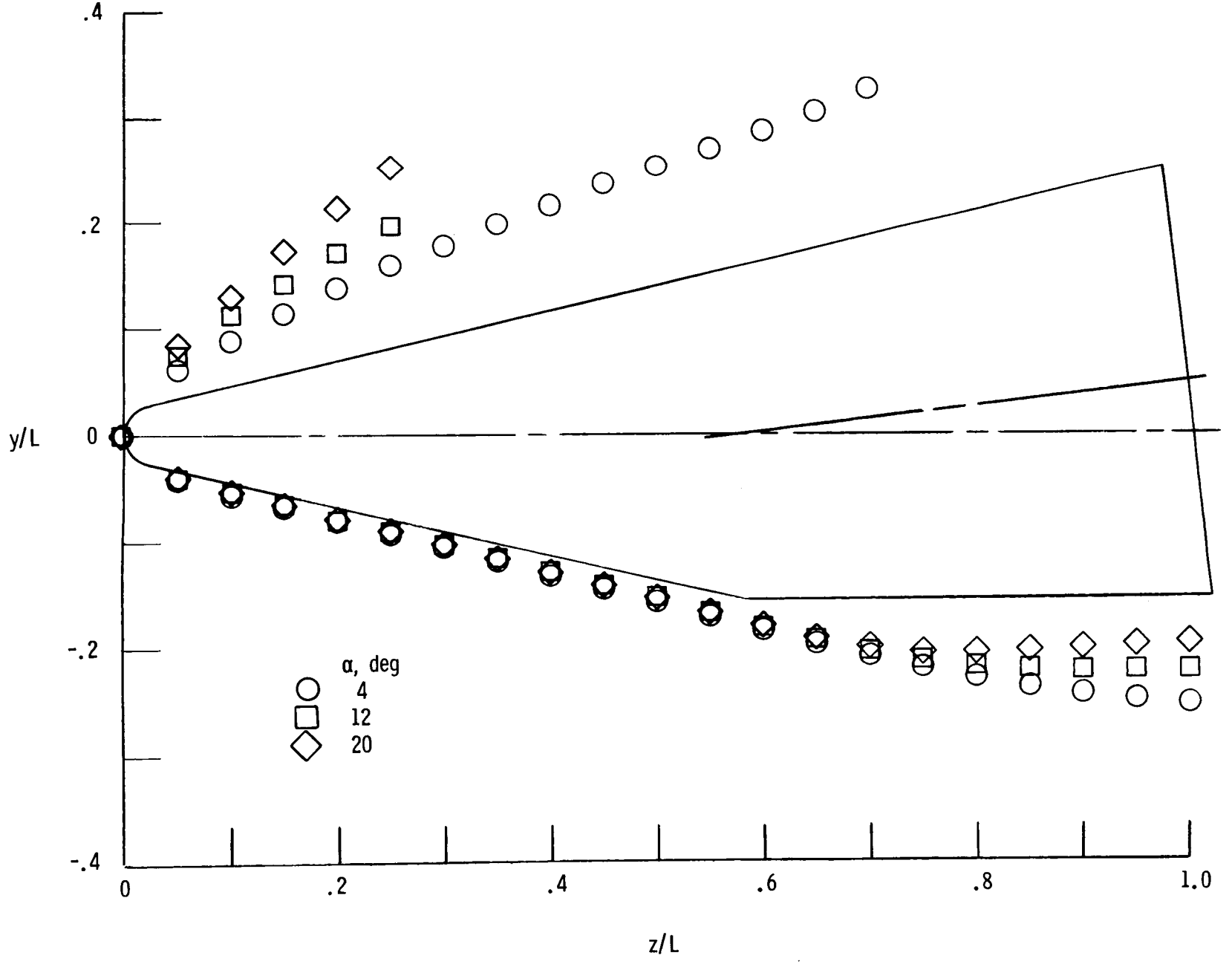

Figure 16.- Effect of angle of attack on measured shock shape for bent-nose biconic in CO_2.

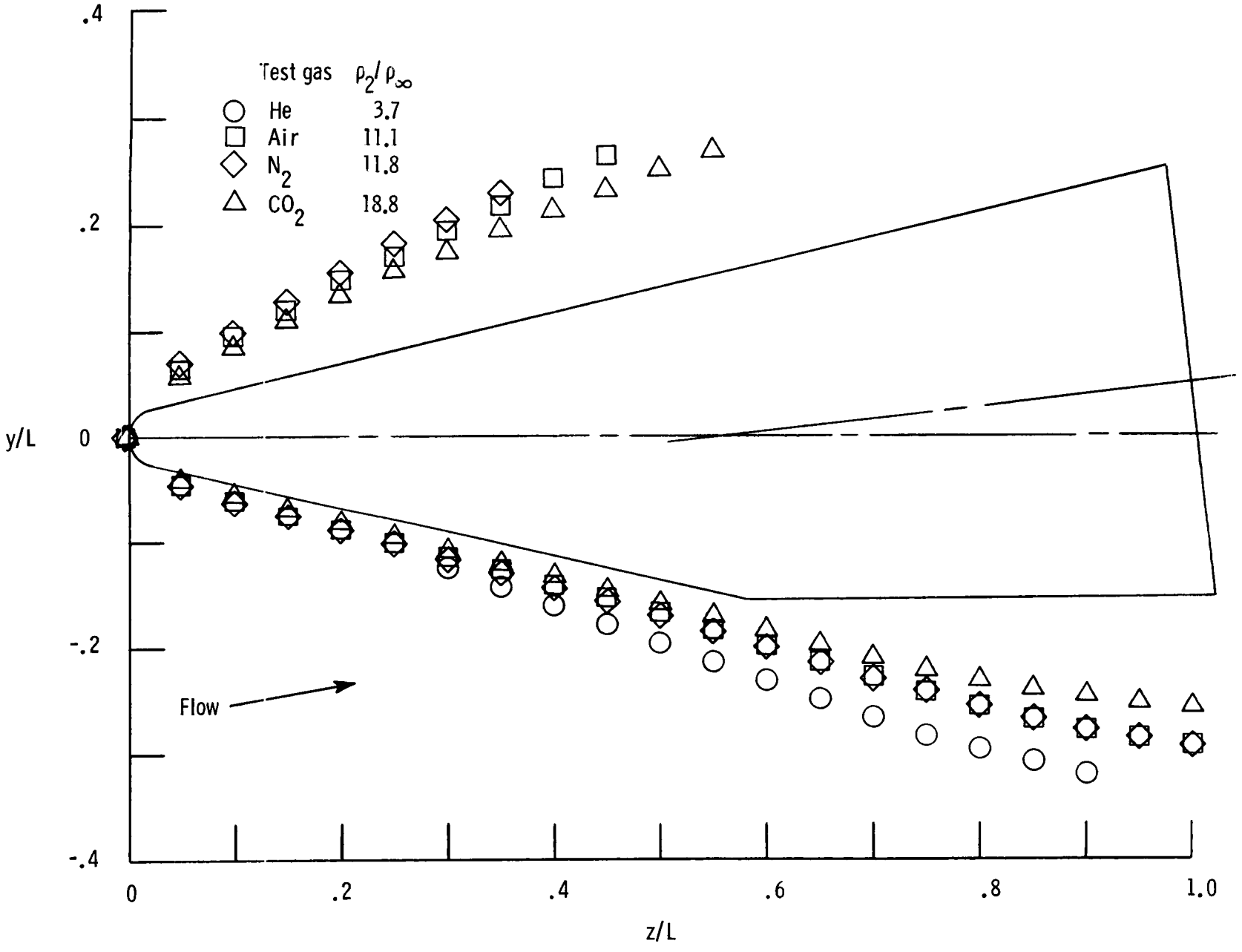

Figure 17.- Effect of normal-shock density ratio on shock shape for bent-nose biconic at $\alpha = 4°$.

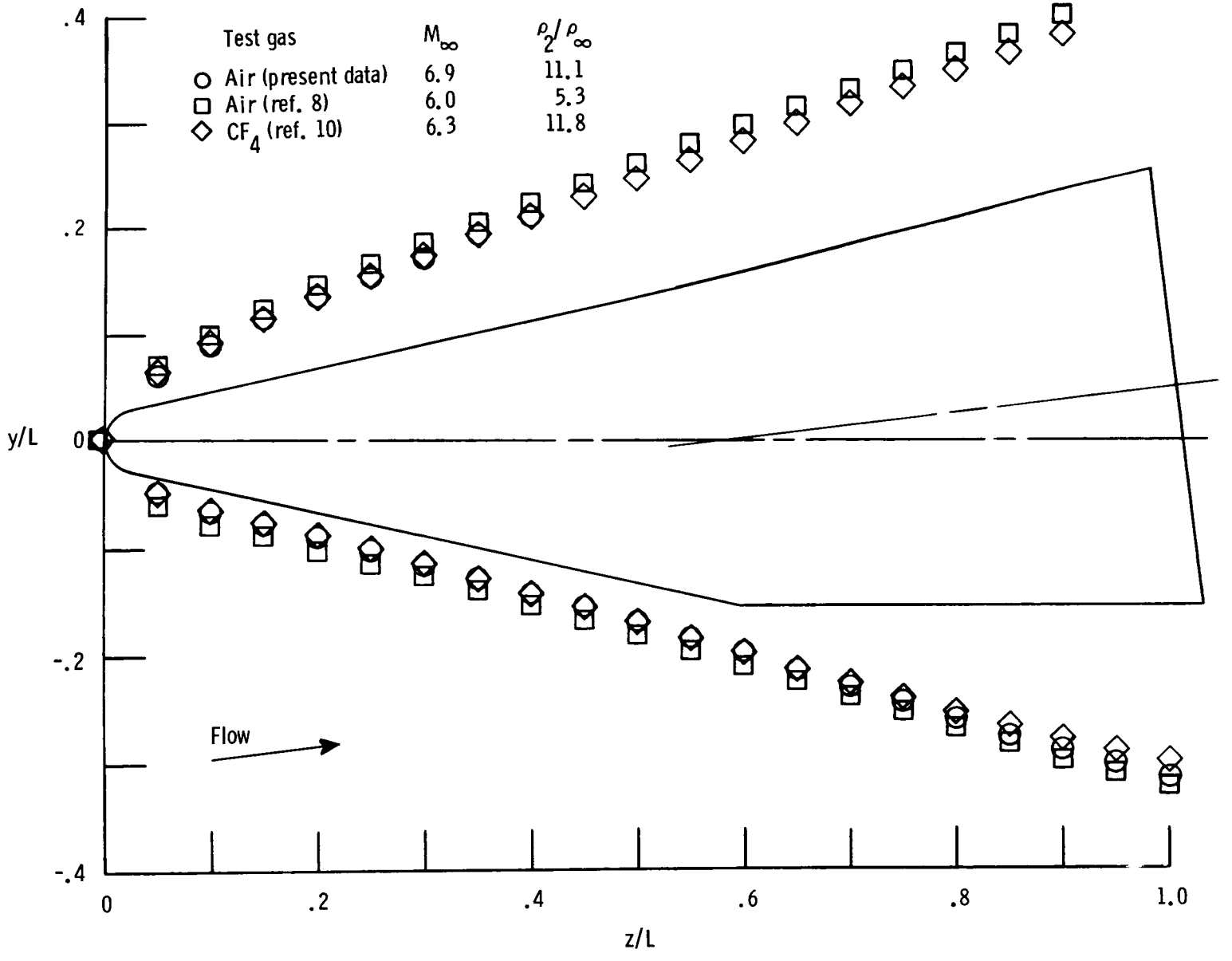

(a) $\alpha = 0°$.

Figure 18.- Comparison of shock shapes for bent-nose biconic in air with those measured in ideal air and in CF_4.

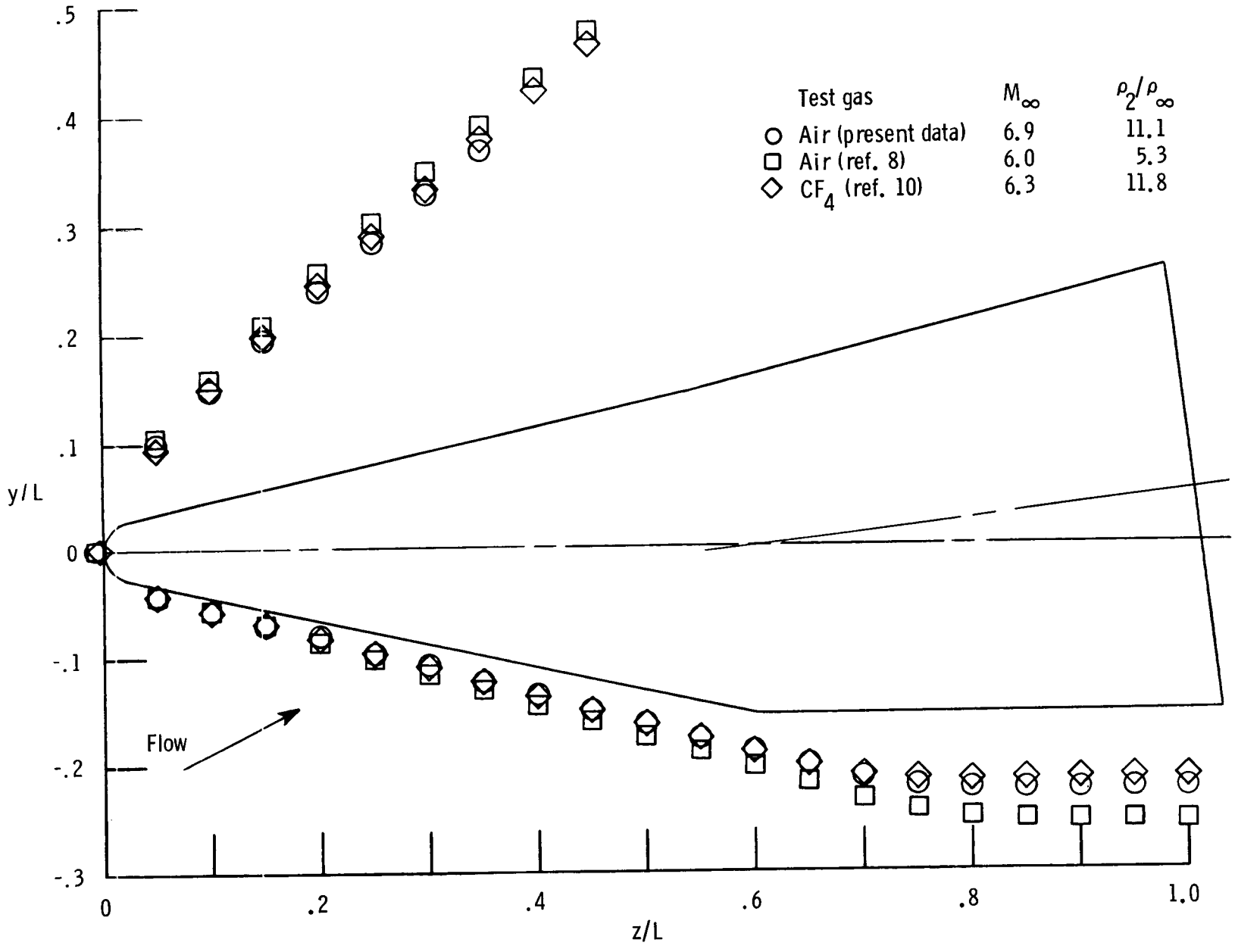

(b) $\alpha = 20°$.

Figure 18.- Concluded.

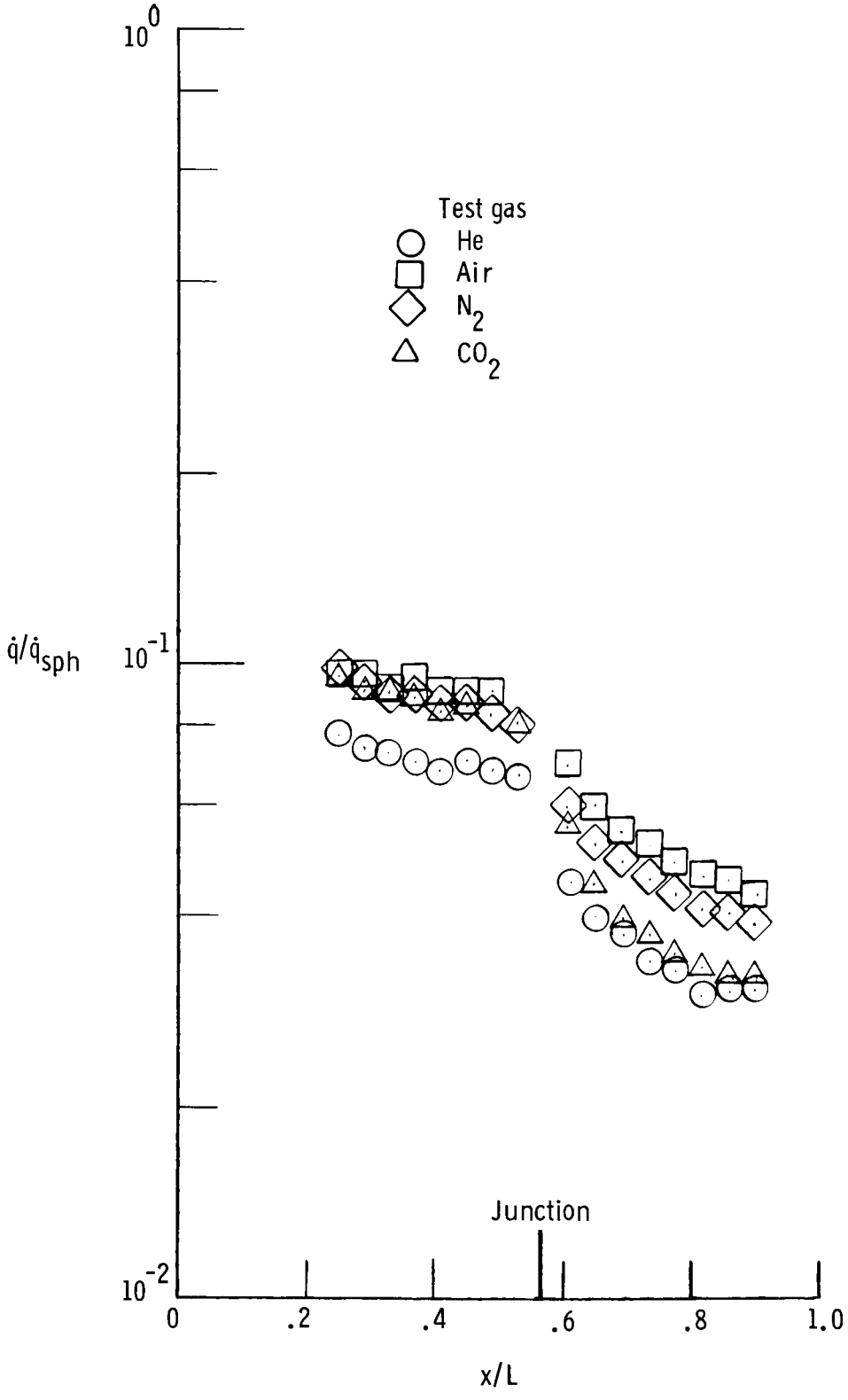

(a) $\alpha = 0°$.

Figure 19.- Heating distributions for straight biconic in present test gases.

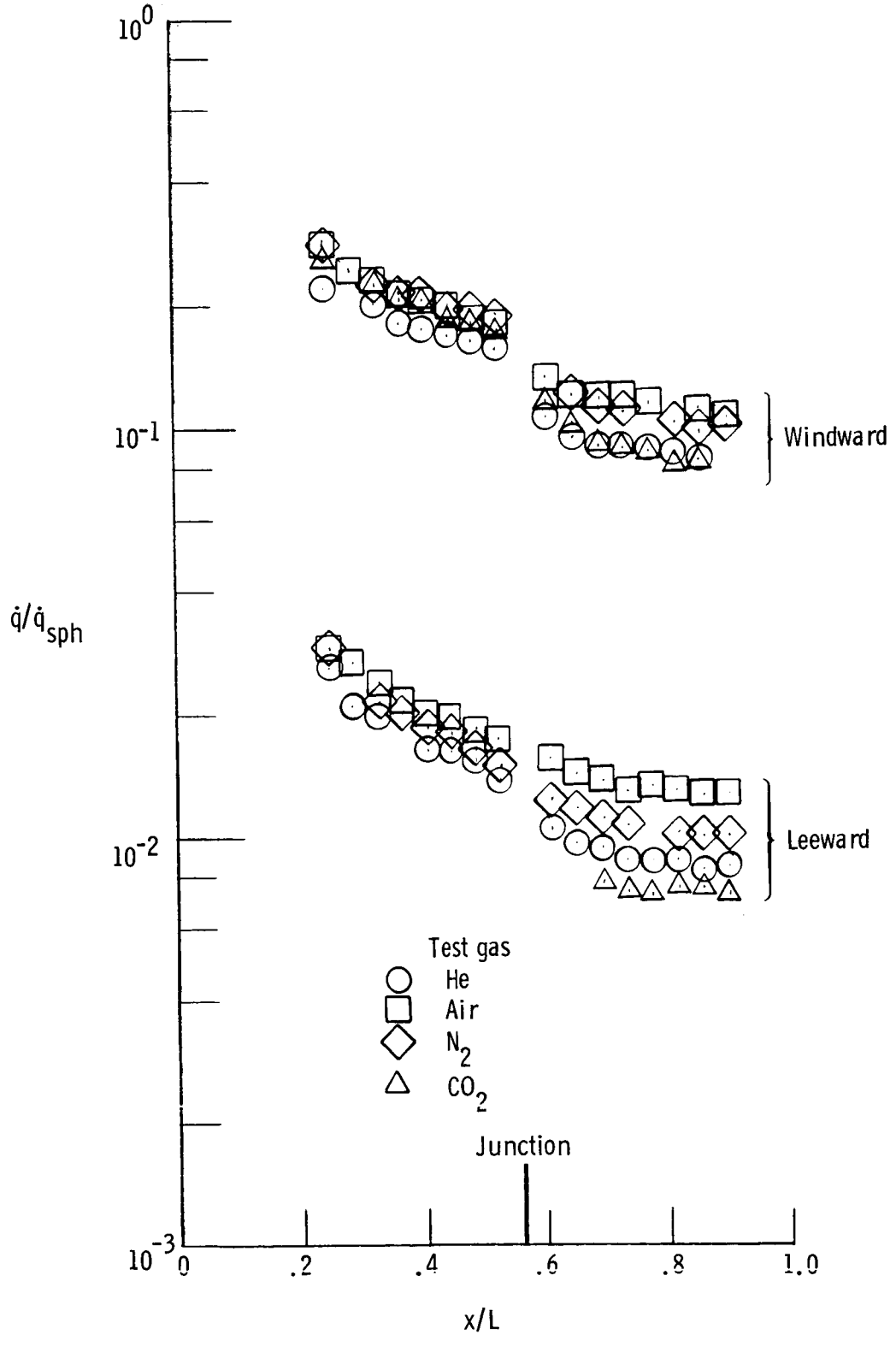

(b) $\alpha = 12°$.

Figure 19.- Continued.

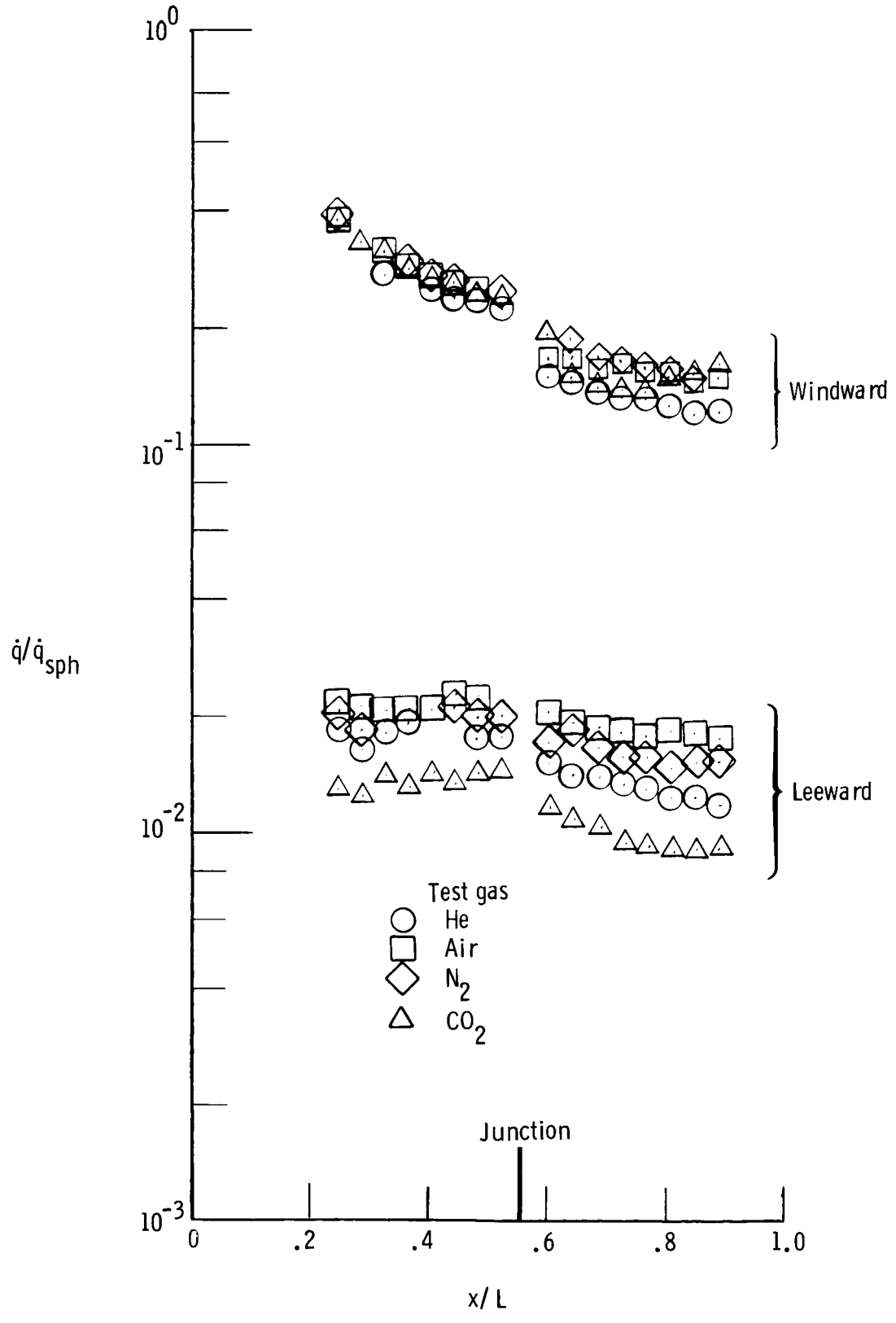

(c) $\alpha = 20°$.

Figure 19.- Concluded.

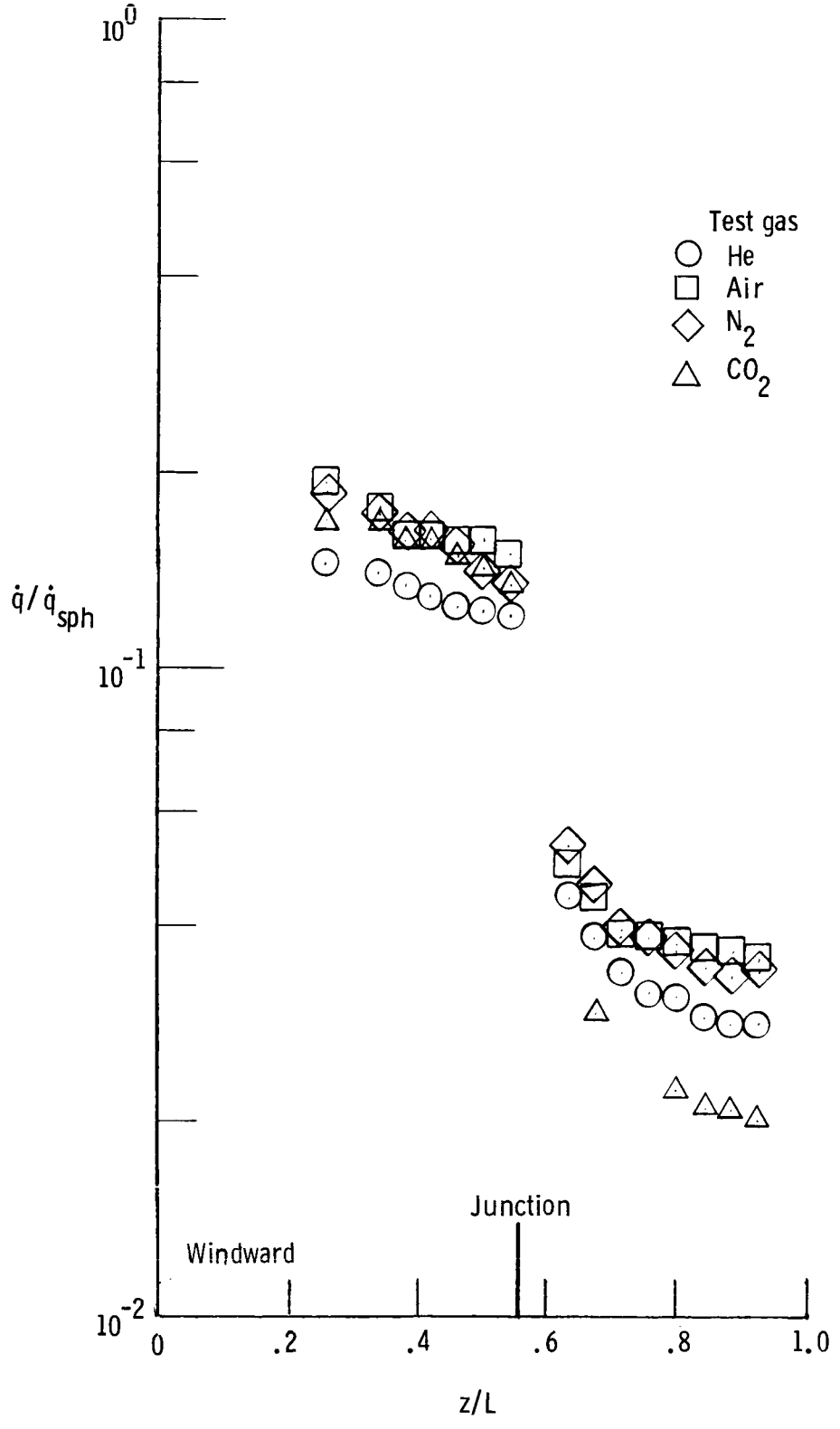

(a) $\alpha = 0°$.

Figure 20.- Heating distributions for bent-nose biconic in present test gases.

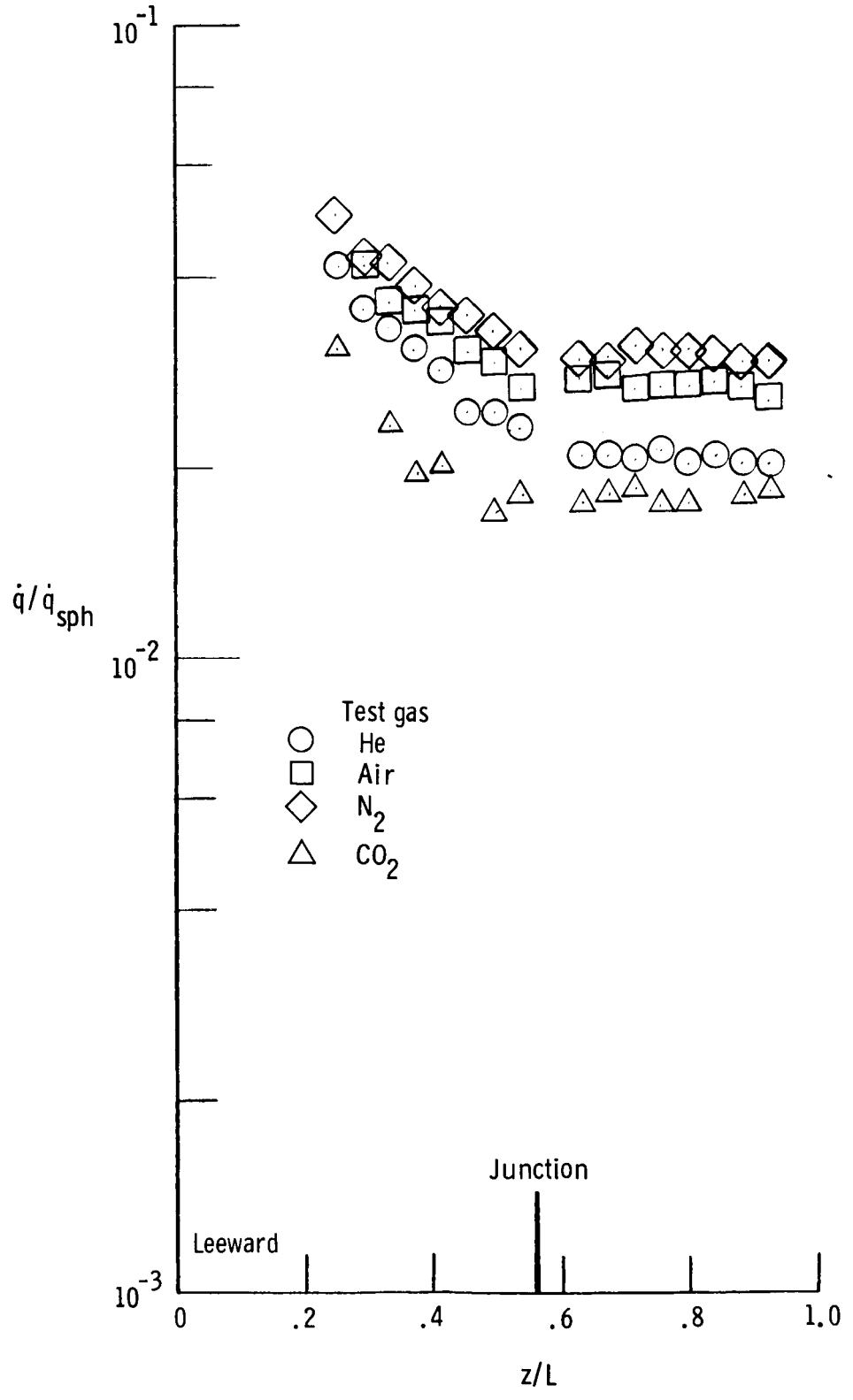

(a) $\alpha = 0°$.

Figure 20.- Continued.

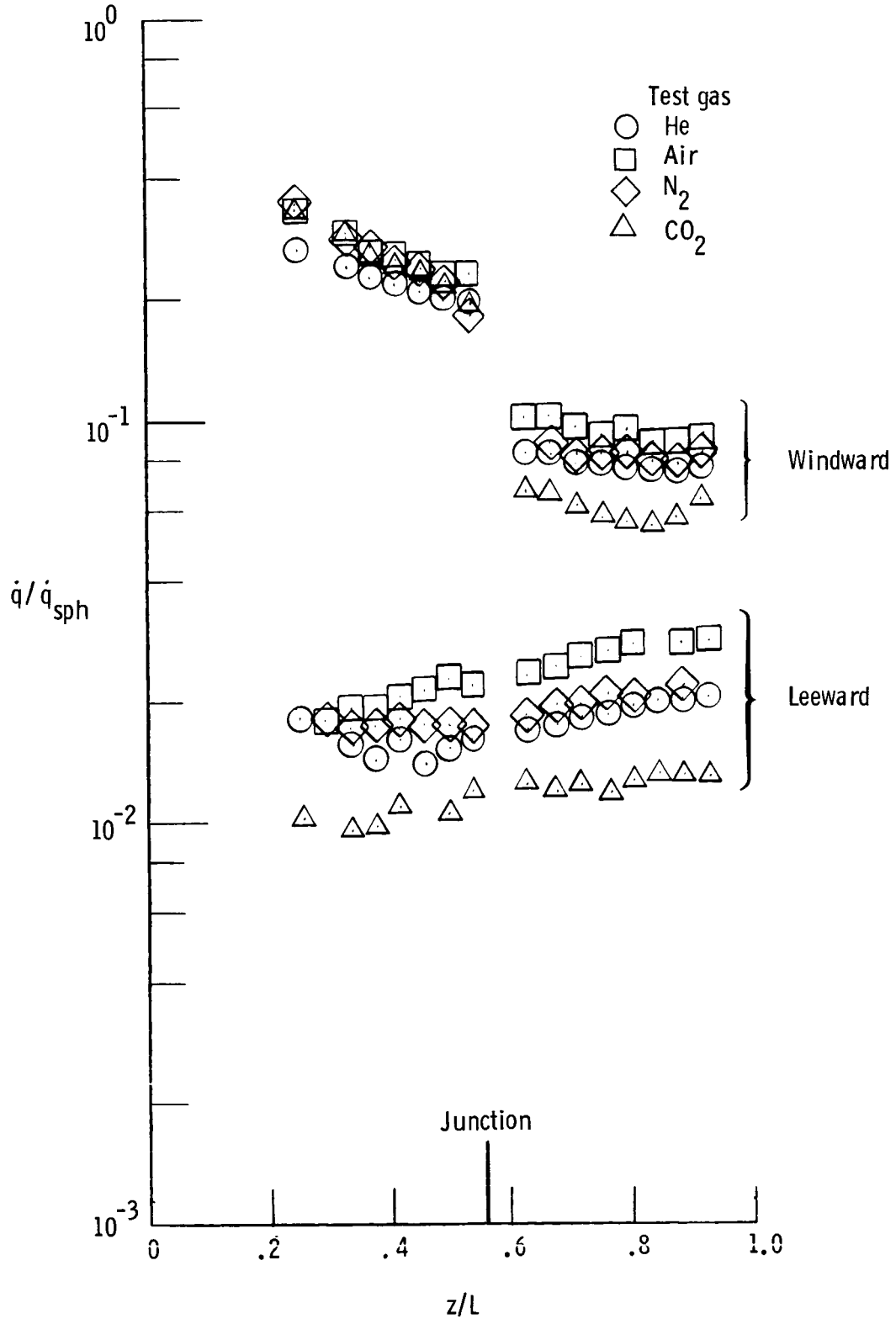

(b) $\alpha = 12°$.

Figure 20.- Continued.

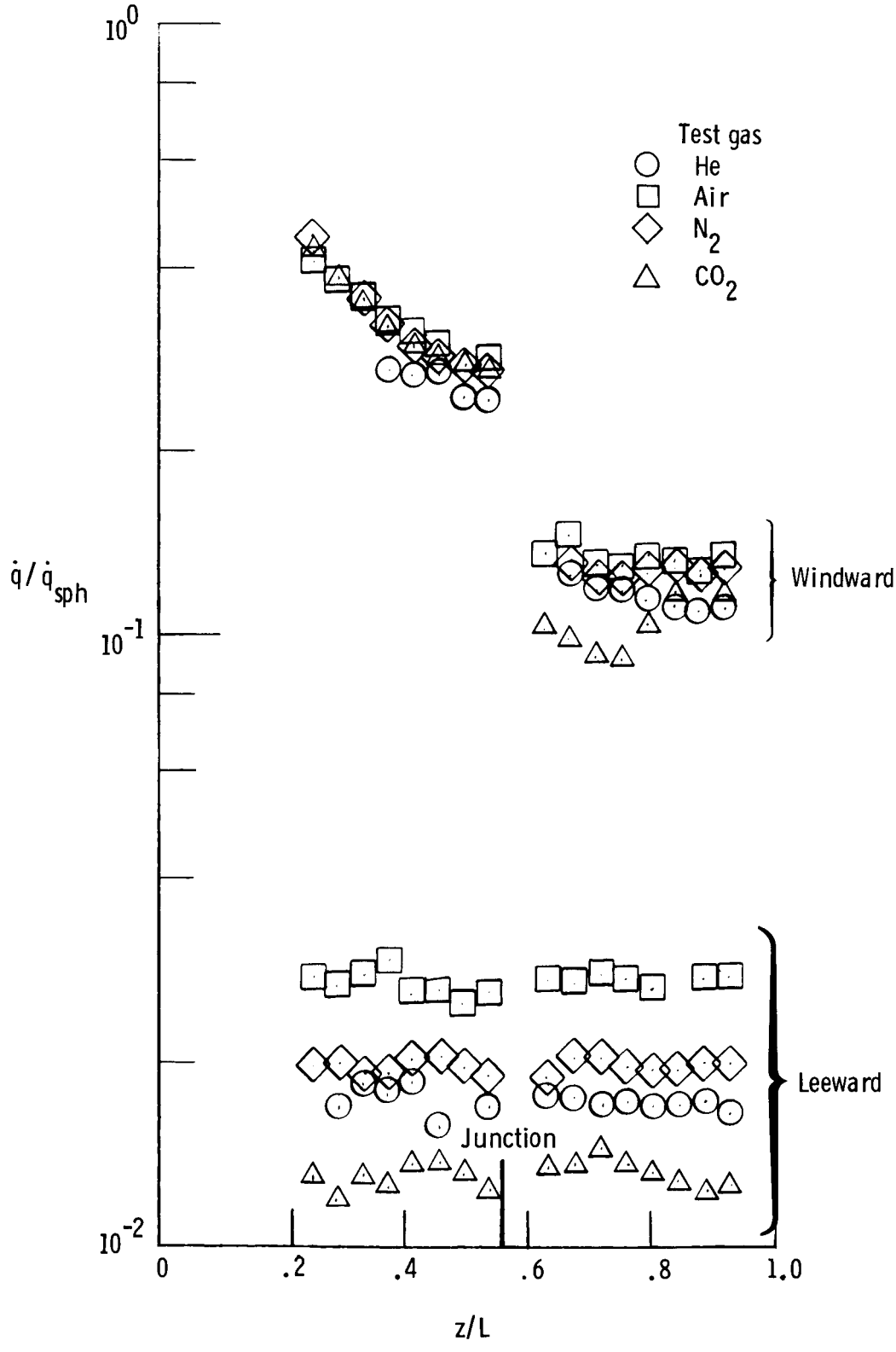

(c) $\alpha = 20°$.

Figure 20.- Concluded.

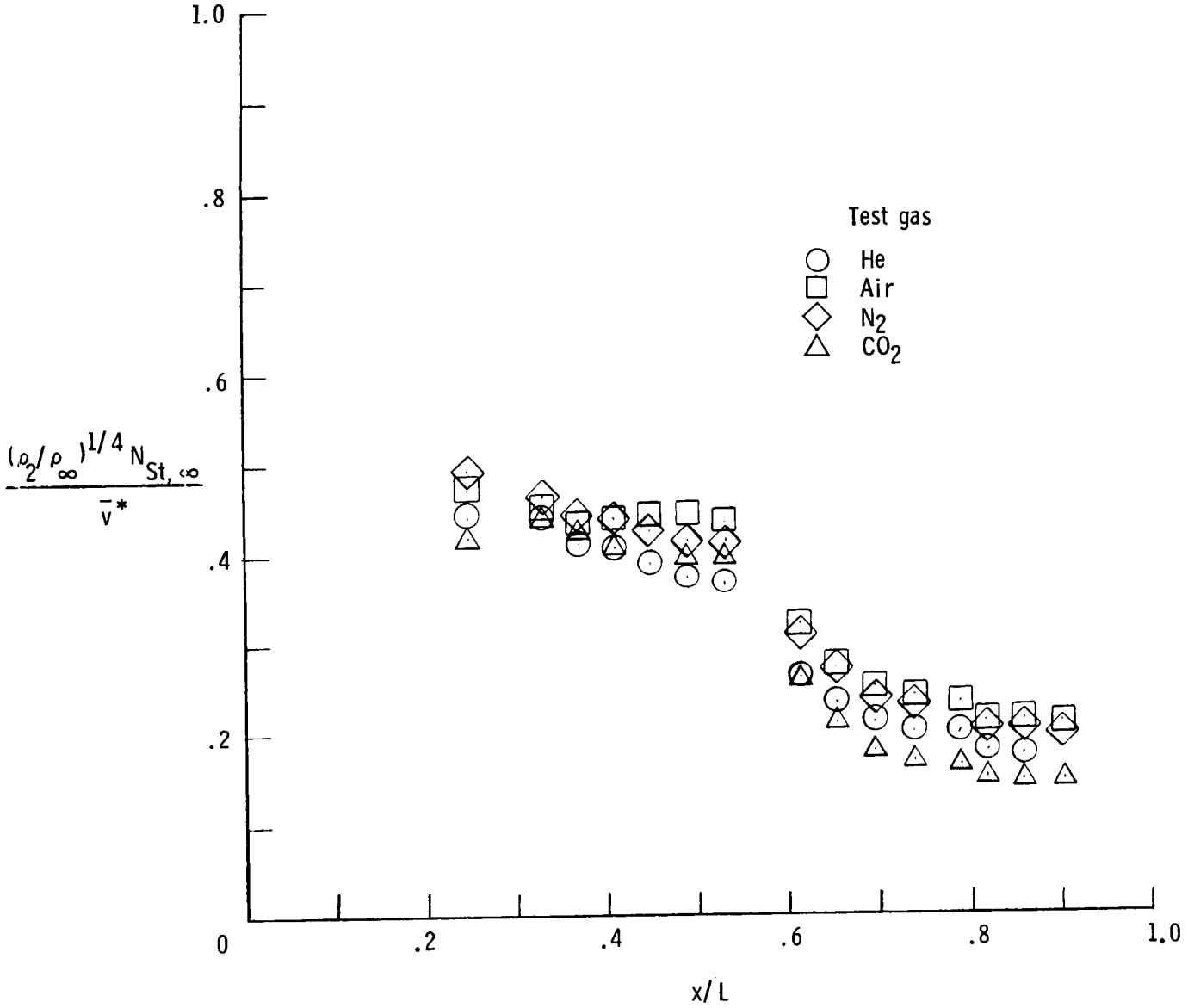

(a) $\alpha = 0°$.

Figure 21.- Windward heating distribution in terms of viscous interaction parameter and density ratio for straight biconic.

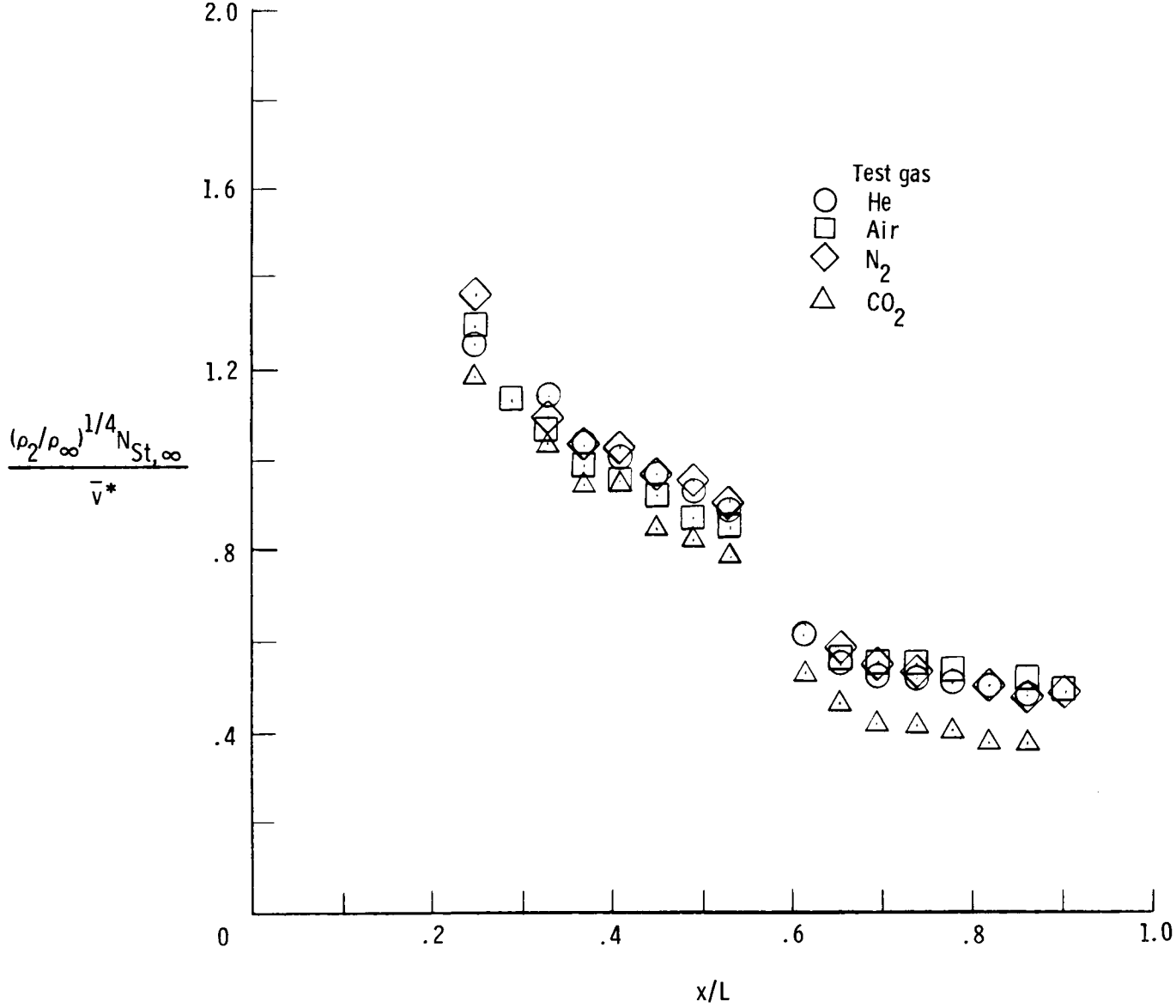

(b) $\alpha = 12°$.

Figure 21.- Continued.

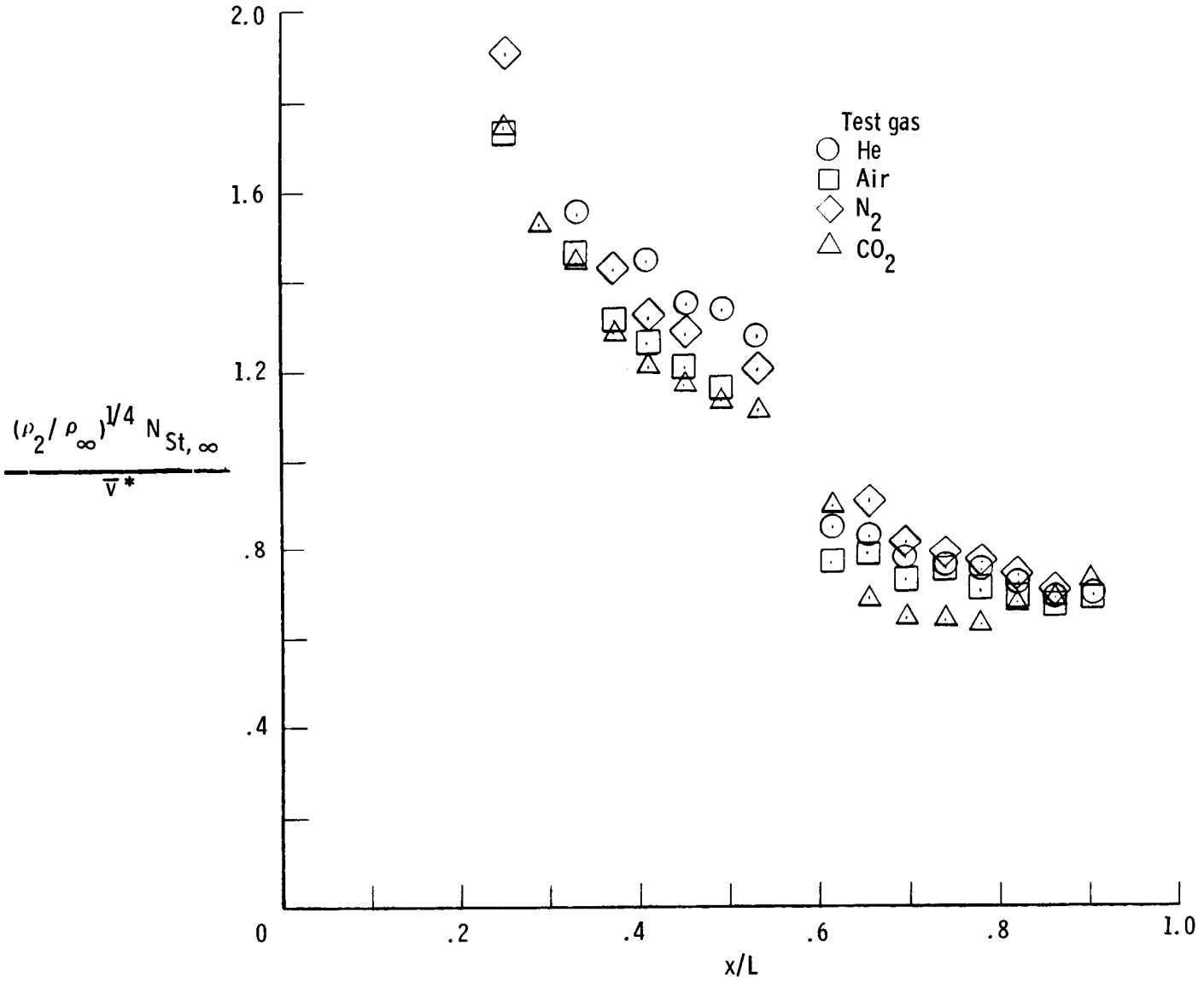

(c) $\alpha = 20°$.

Figure 21.- Concluded.

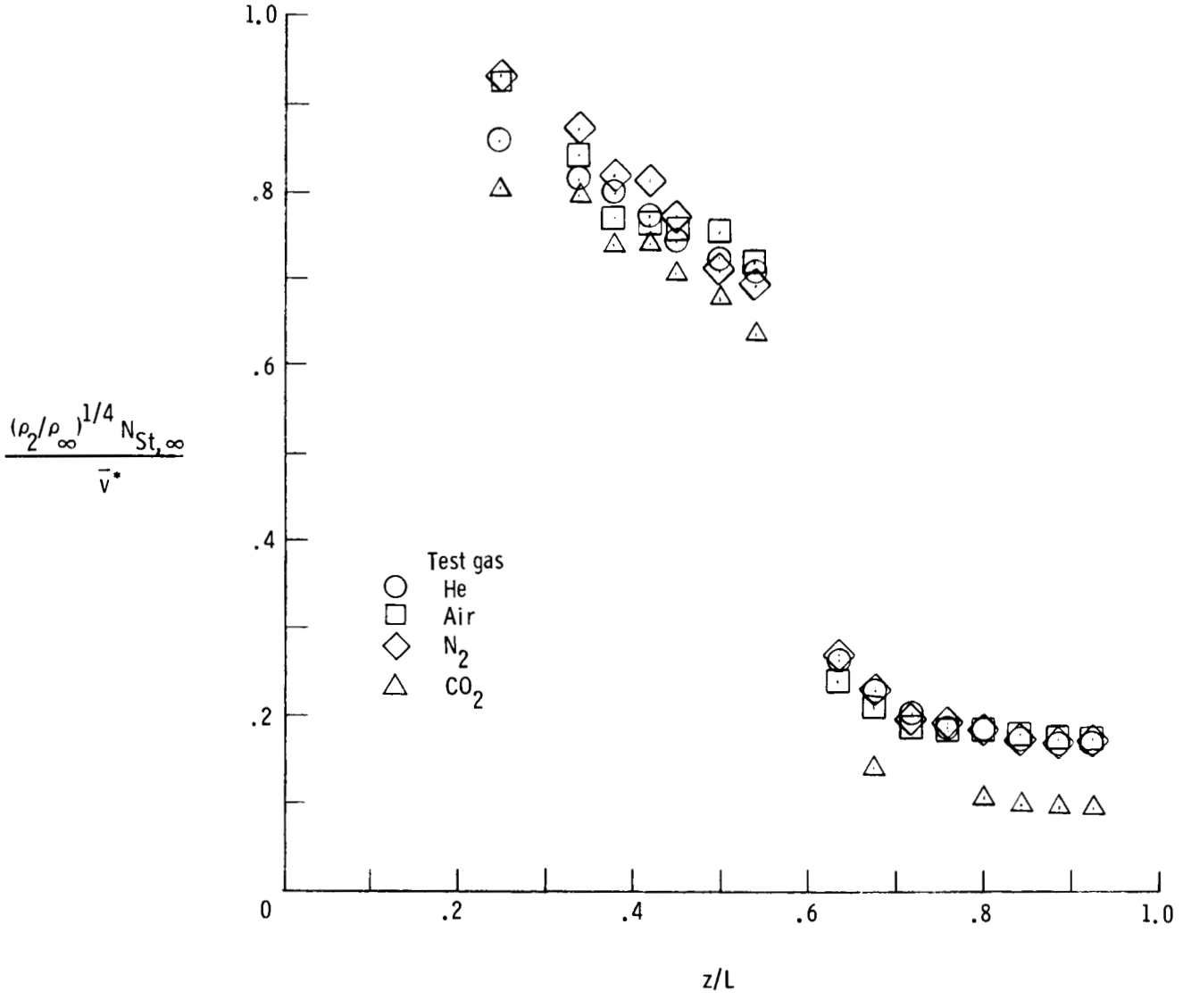

(a) $\alpha = 0°$.

Figure 22.- Windward heating distribution in terms of viscous interaction parameter and density ratio for bent-nose biconic.

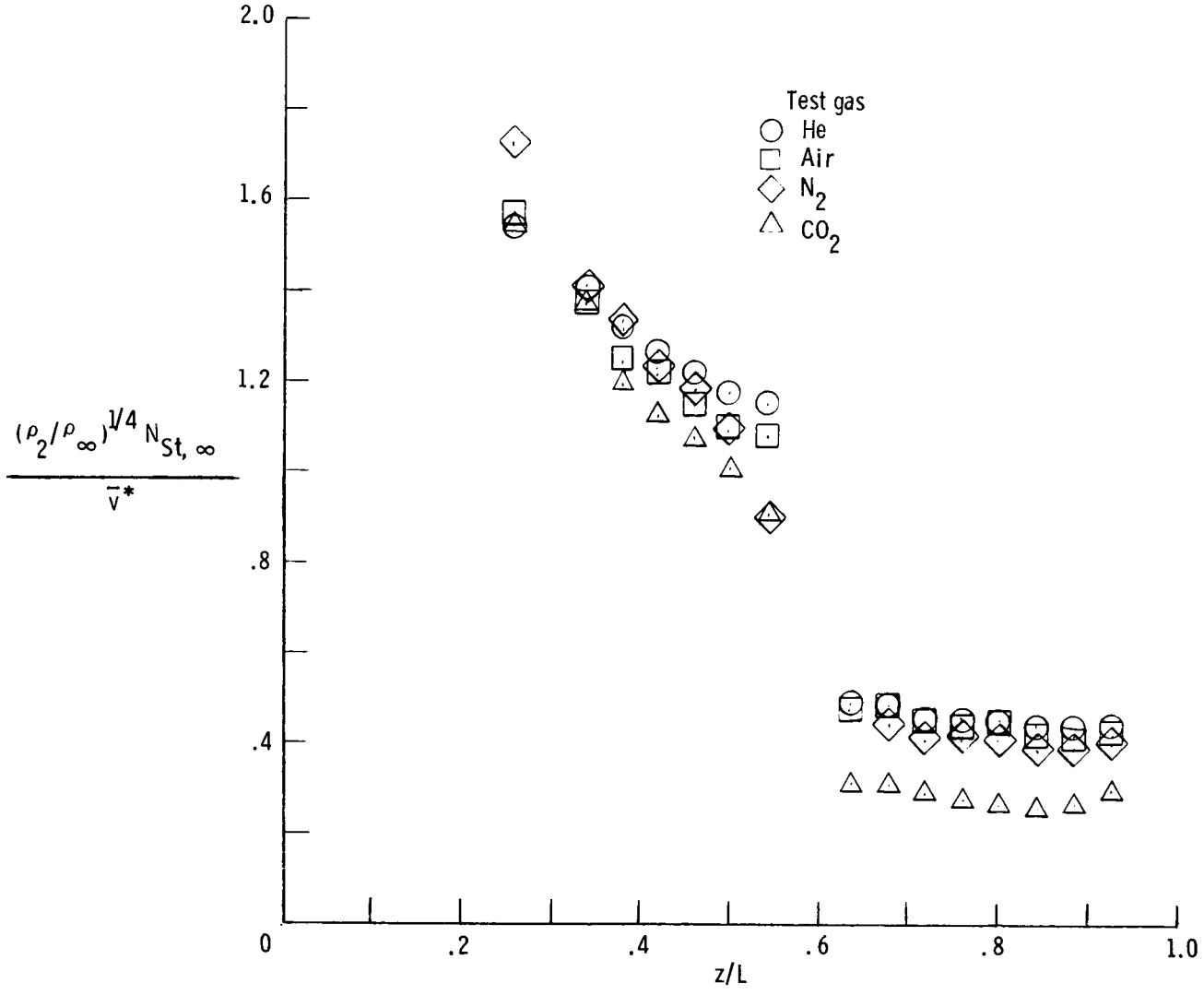

(b) $\alpha = 12°$.

Figure 22.- Continued.

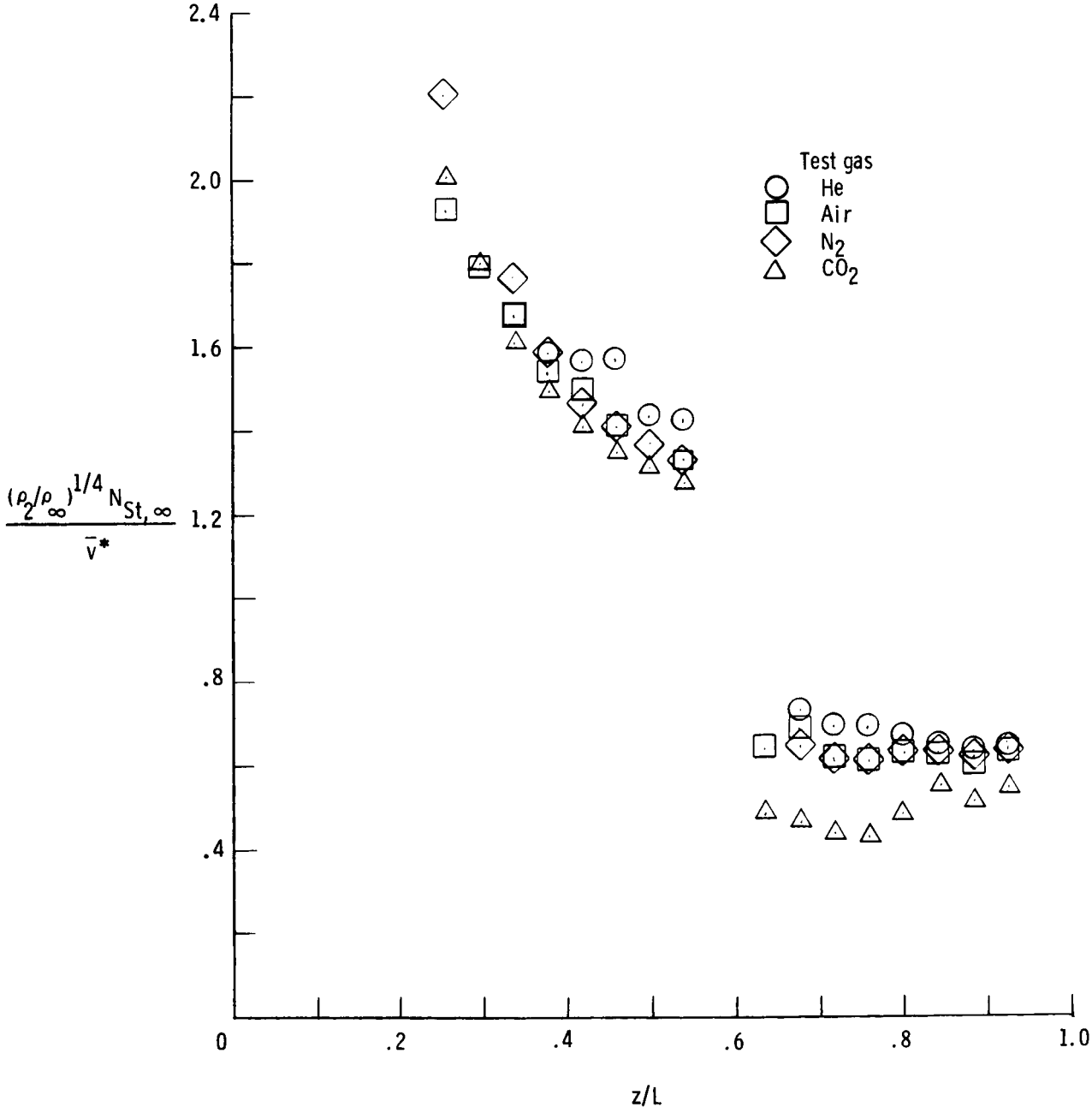

(c) $\alpha = 20°$.

Figure 22.- Concluded.

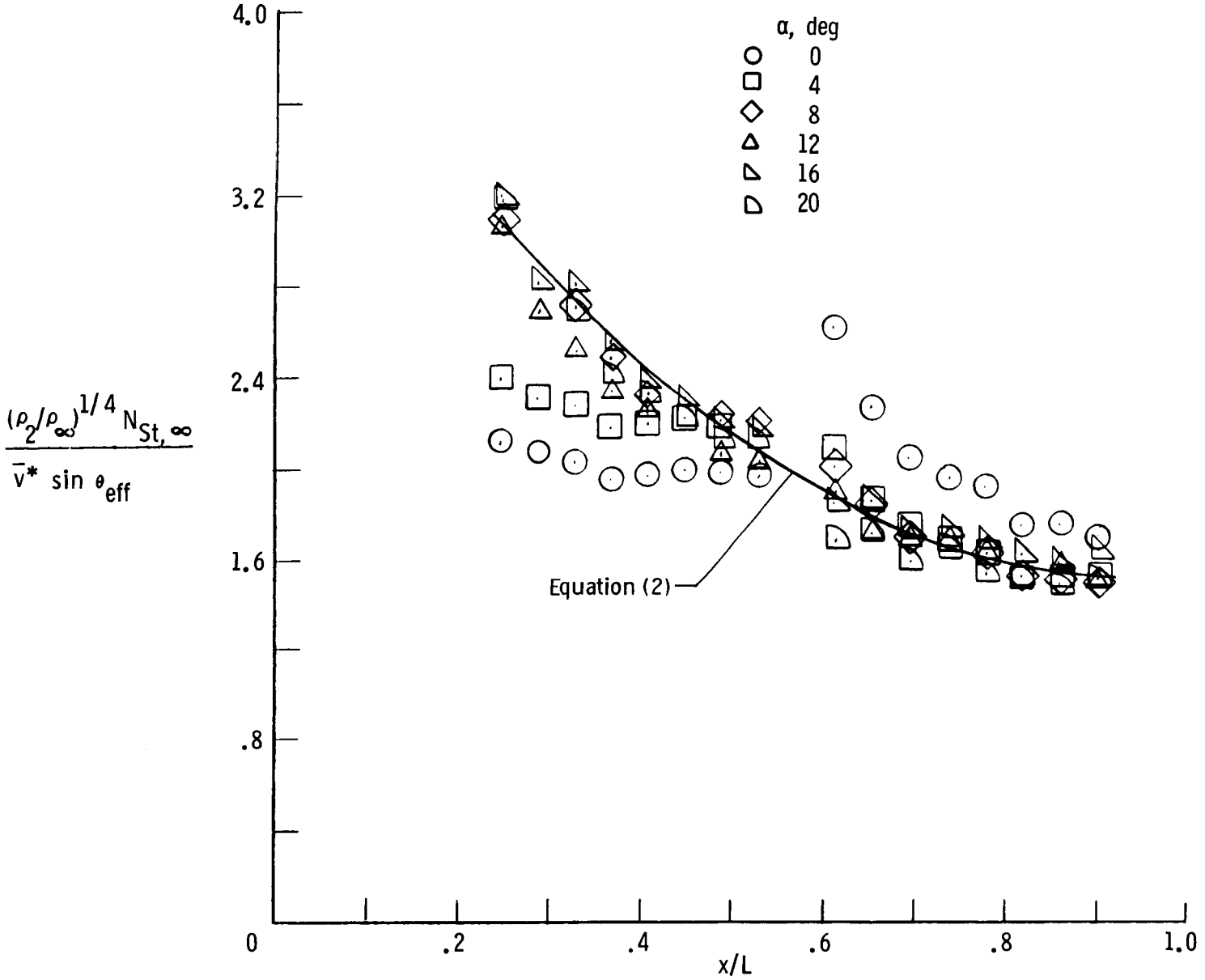

(a) Straight biconic.

Figure 23.- Windward heating distribution in terms of viscous interaction parameter, density ratio, and effective cone angle for air.

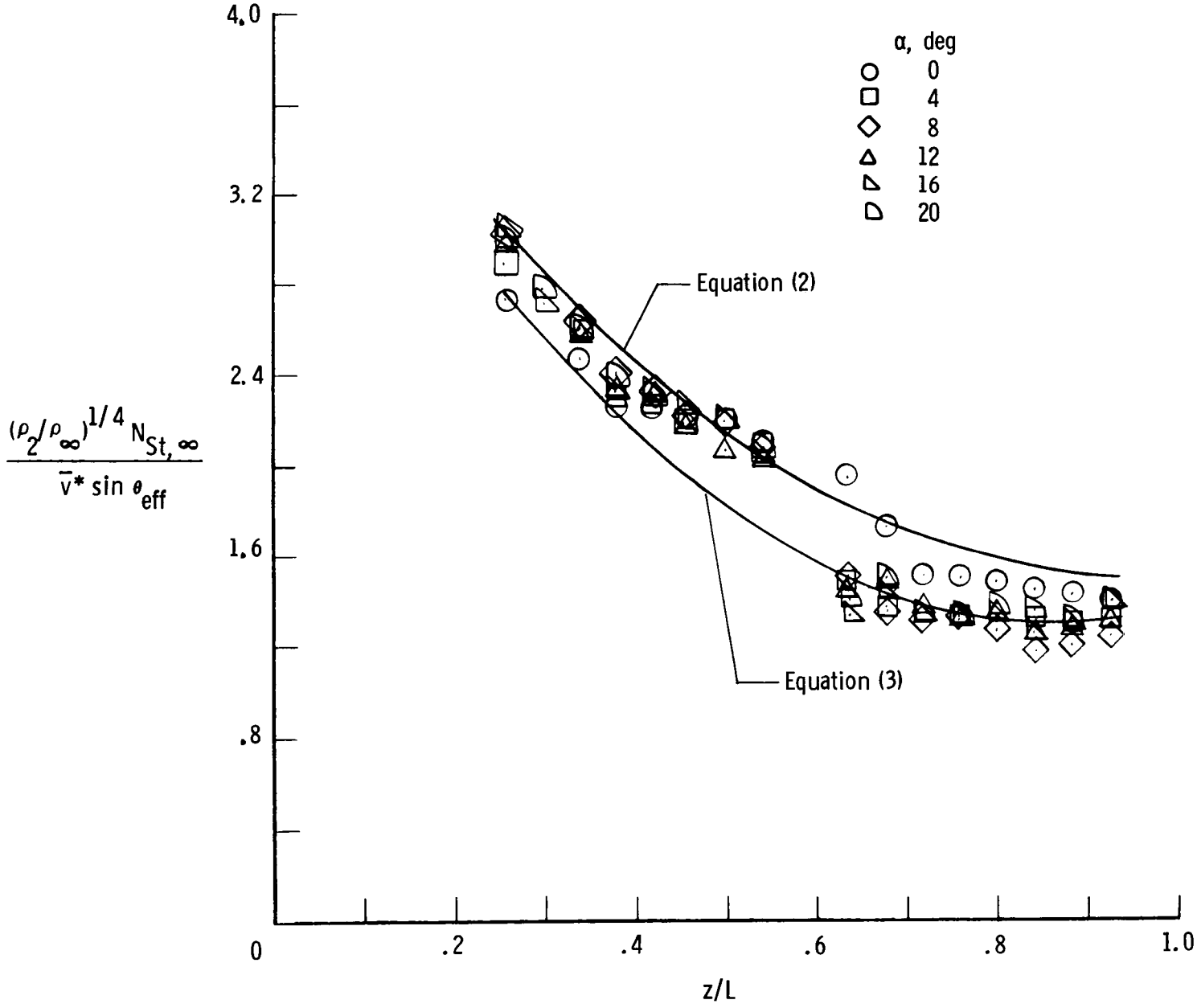

(b) Bent-nose biconic.

Figure 23.- Concluded.

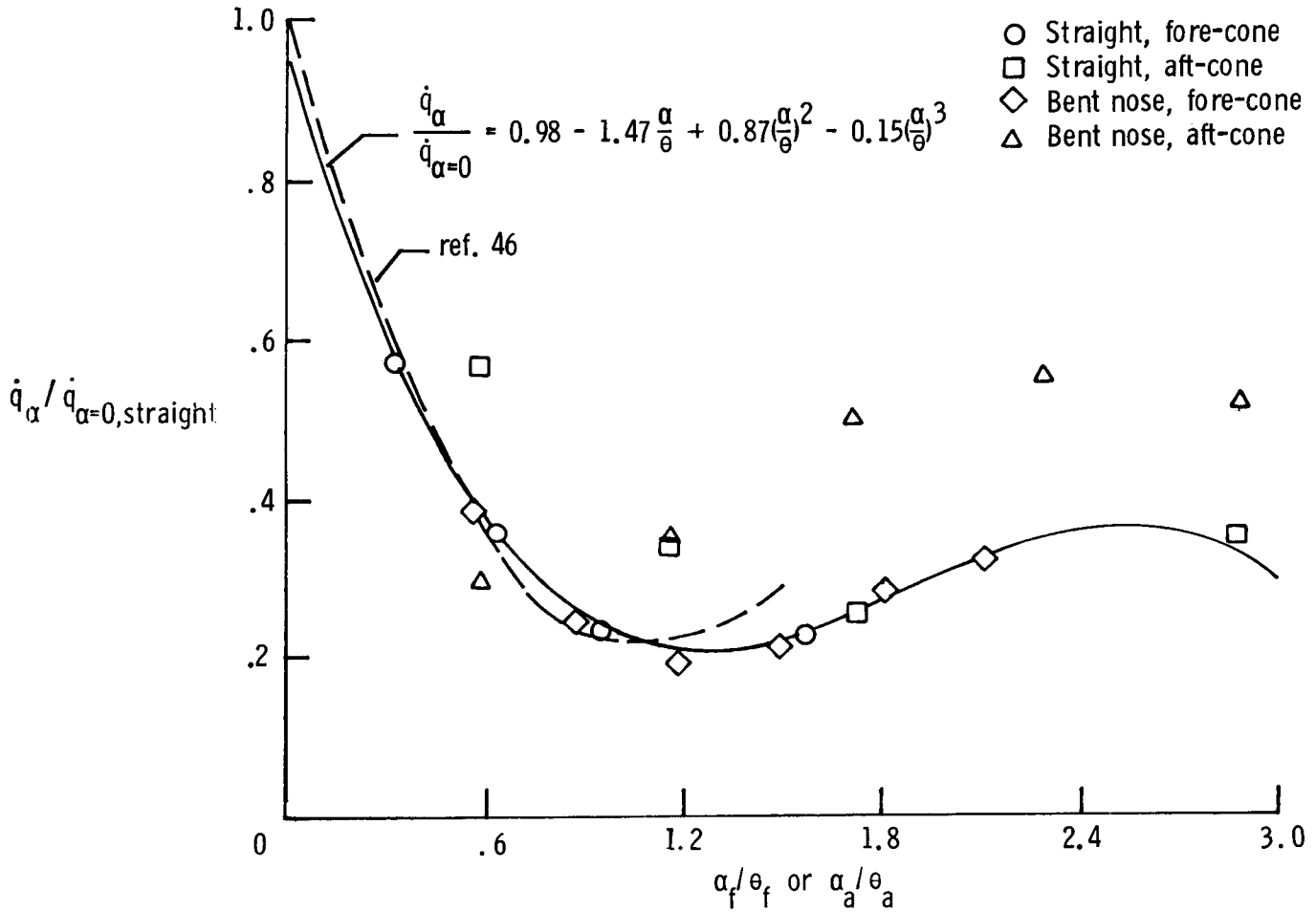

Figure 24.- Leeward heating for straight biconic and bent-nose biconic in air. Fore-cone data correspond to x/L or z/L = 0.37; aft-cone data correspond to x/L or z/L = 0.75.

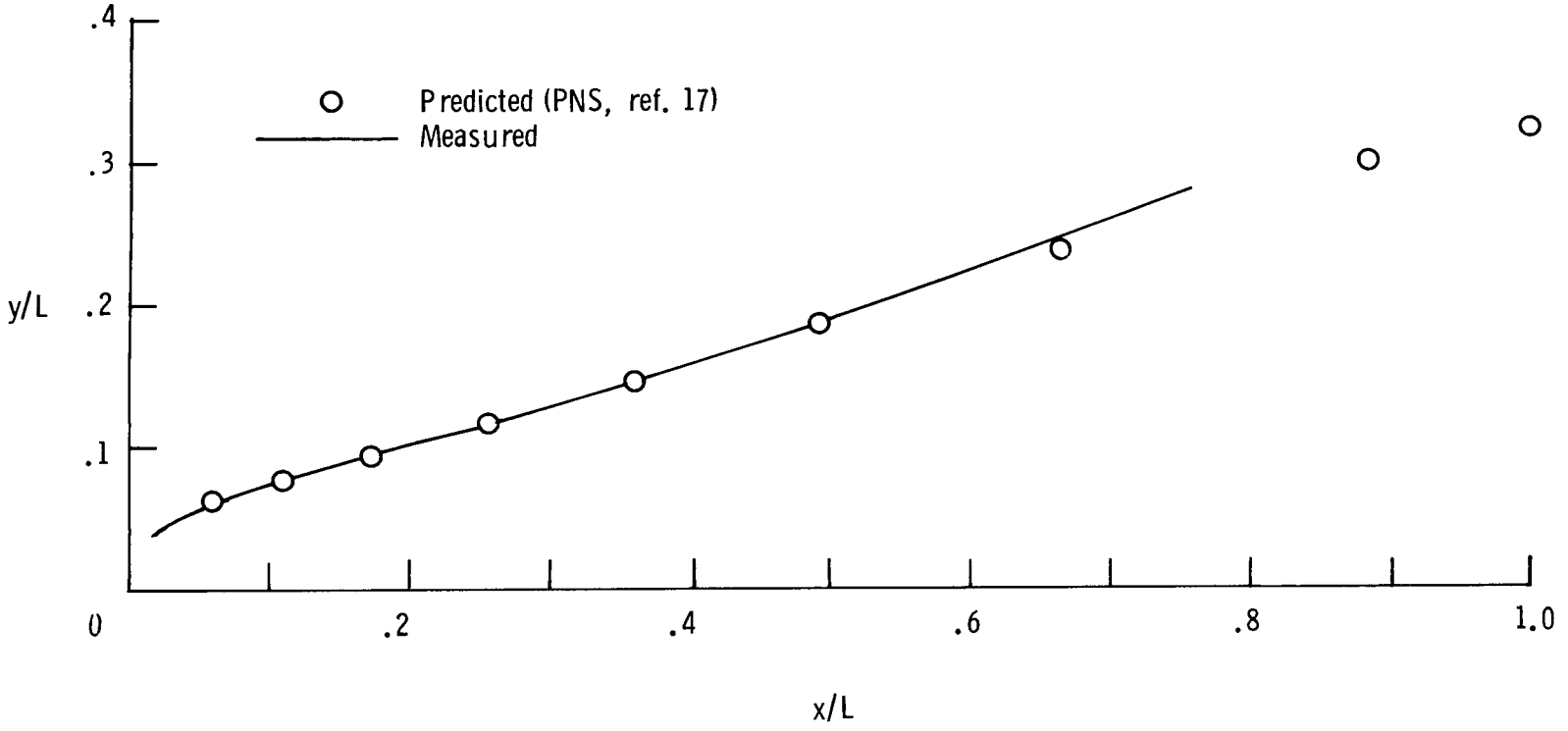

Figure 25.- Measured and predicted windward shock shape for straight biconic in He at $\alpha = 12°$.

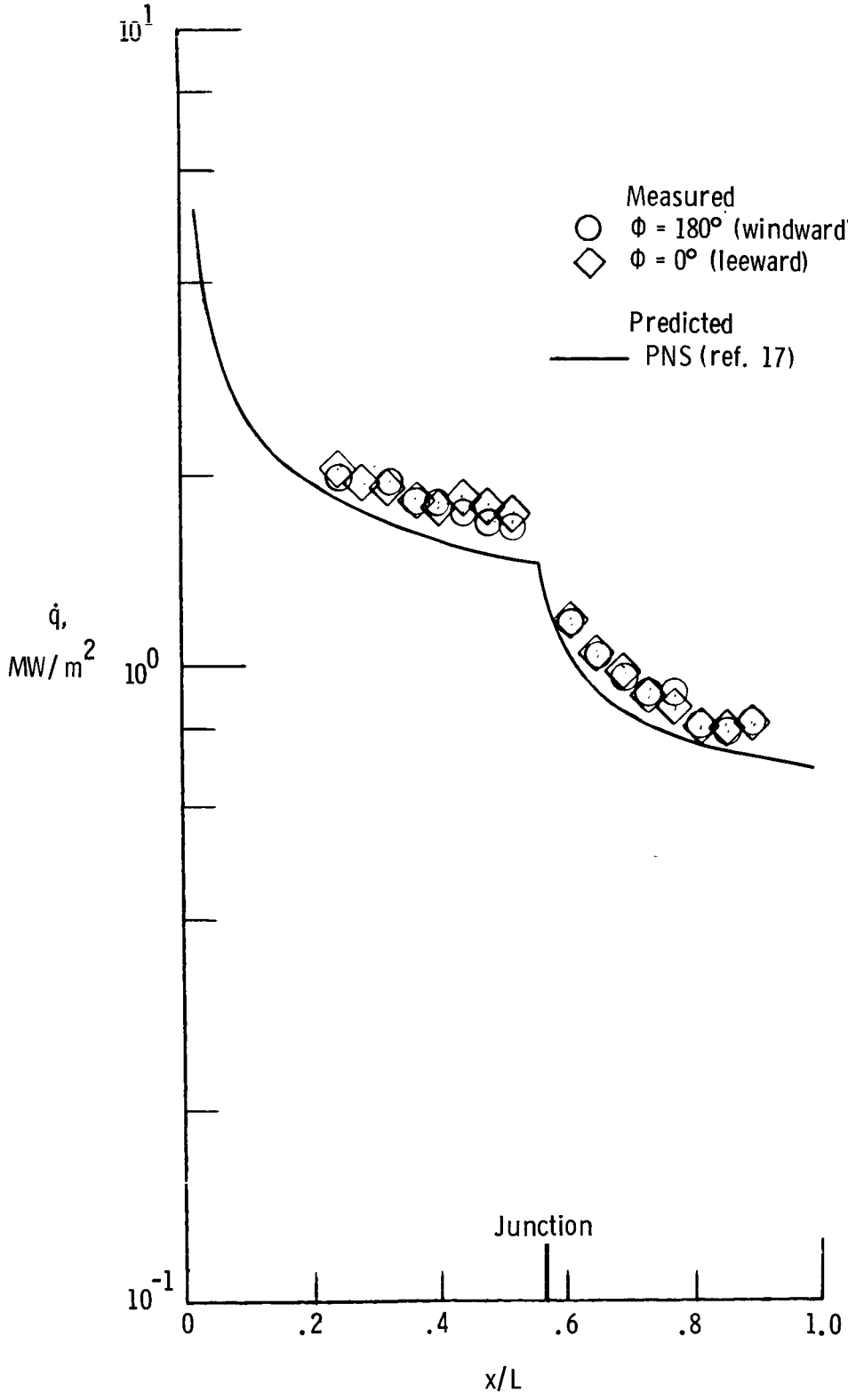

(a) $\alpha = 0°$.

Figure 26.- Measured and predicted heating for straight biconic in He.

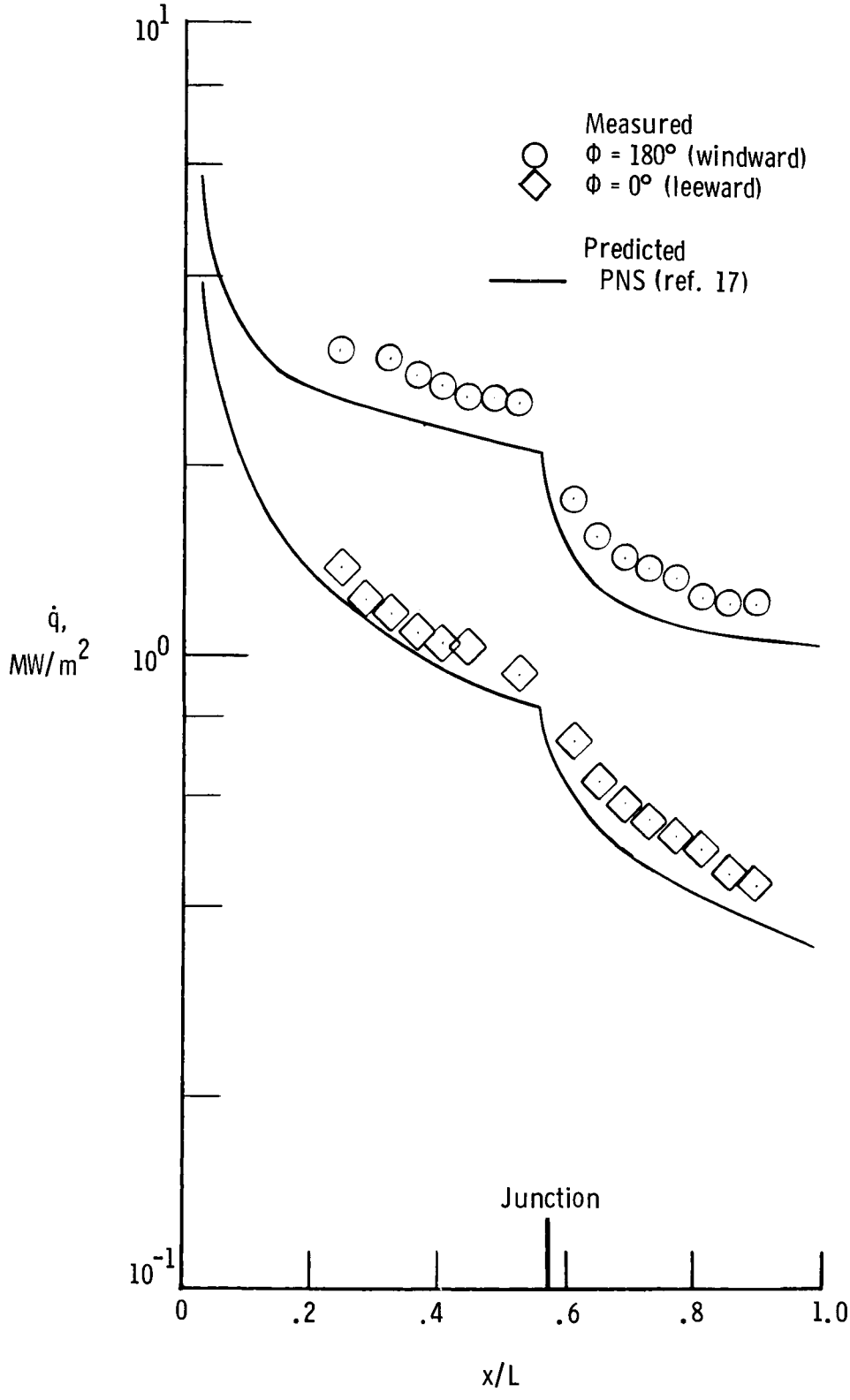

(b) $\alpha = 4°$.

Figure 26.- Continued.

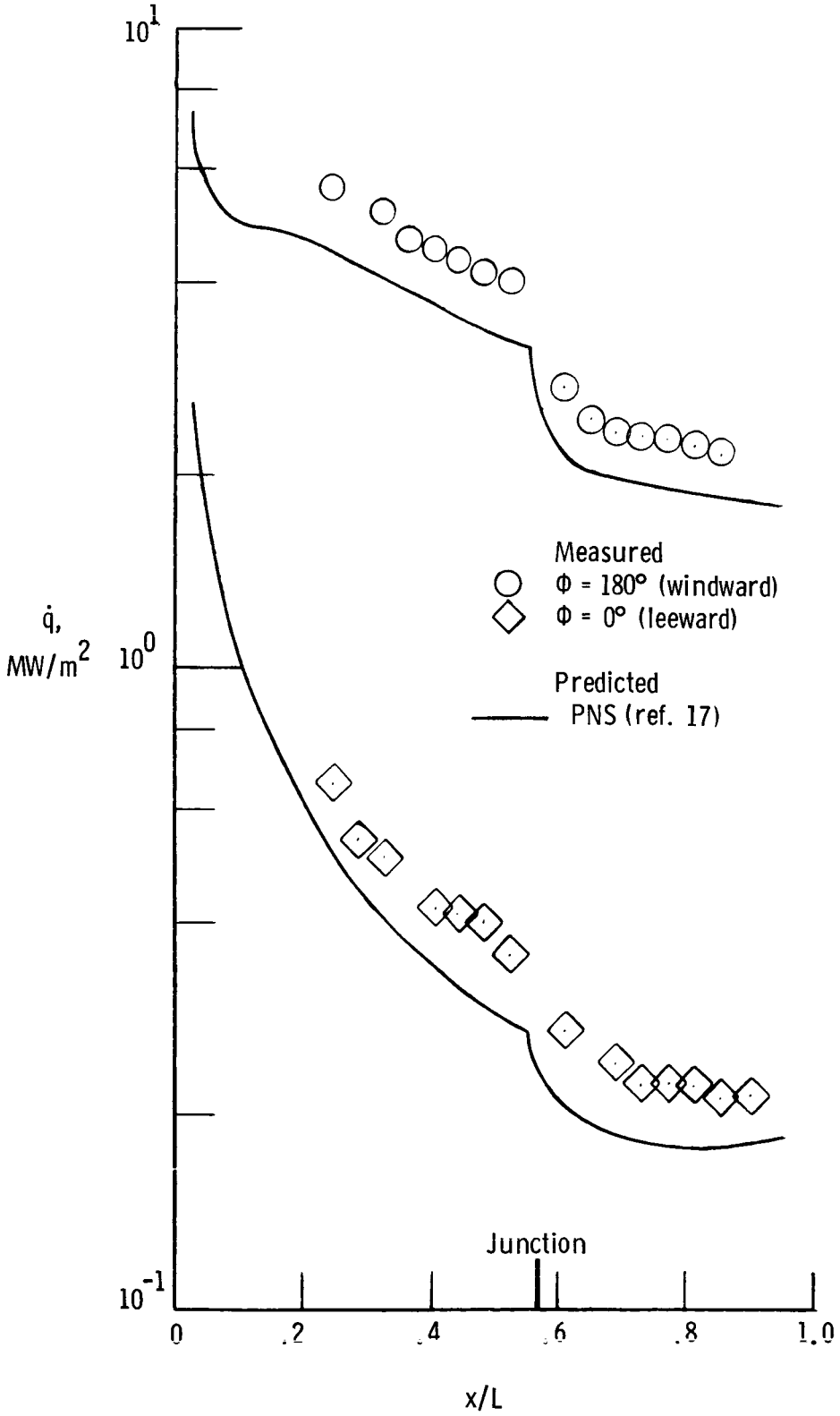

(c) $\alpha = 12°$.

Figure 26.- Continued.

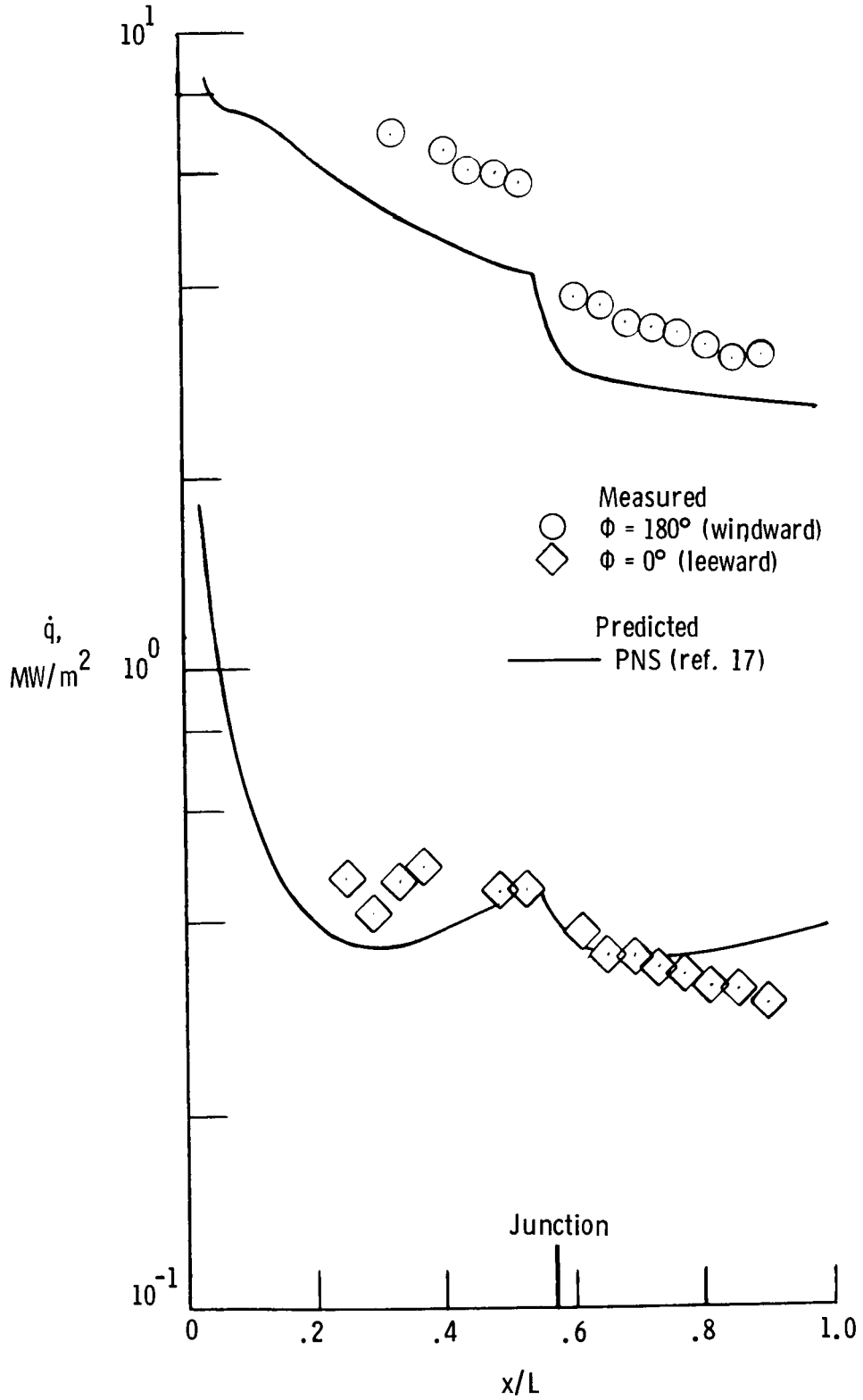

(d) $\alpha = 20°$.

Figure 26.- Concluded.

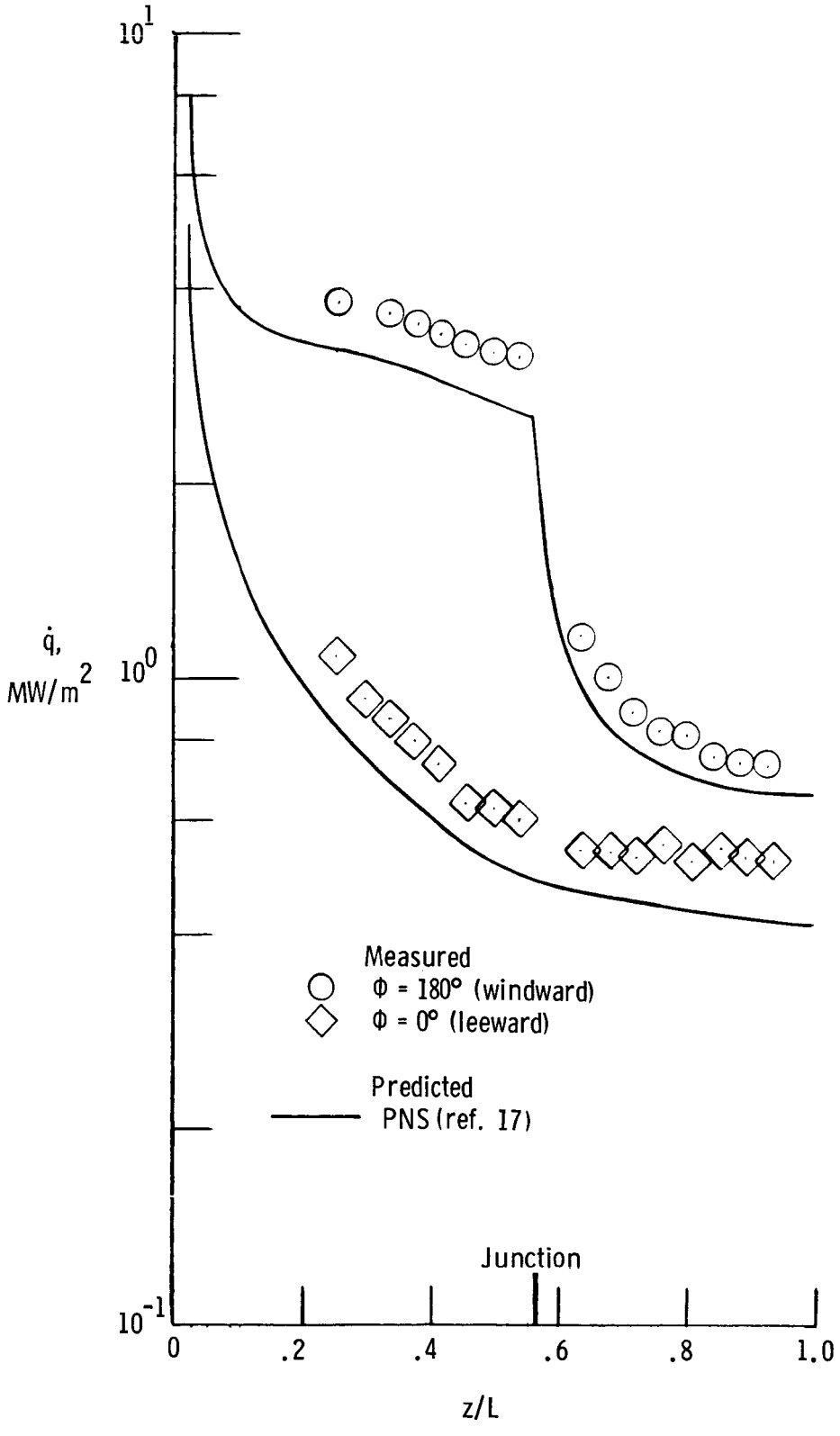

(a) $\alpha = 0°$.

Figure 27.- Measured and predicted heating for bent-nose biconic in He.

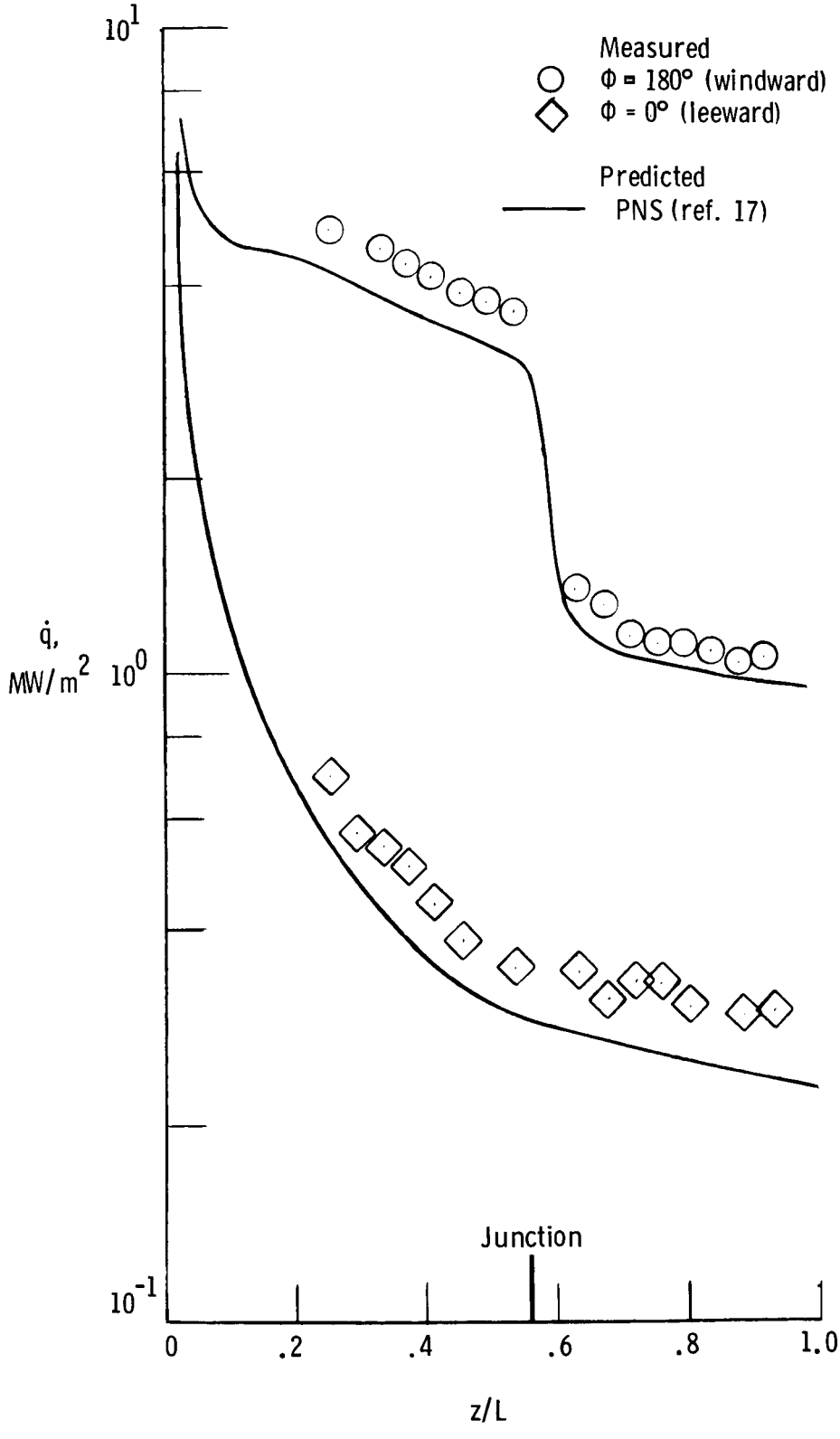

(b) $\alpha = 4°$.

Figure 27.- Continued.

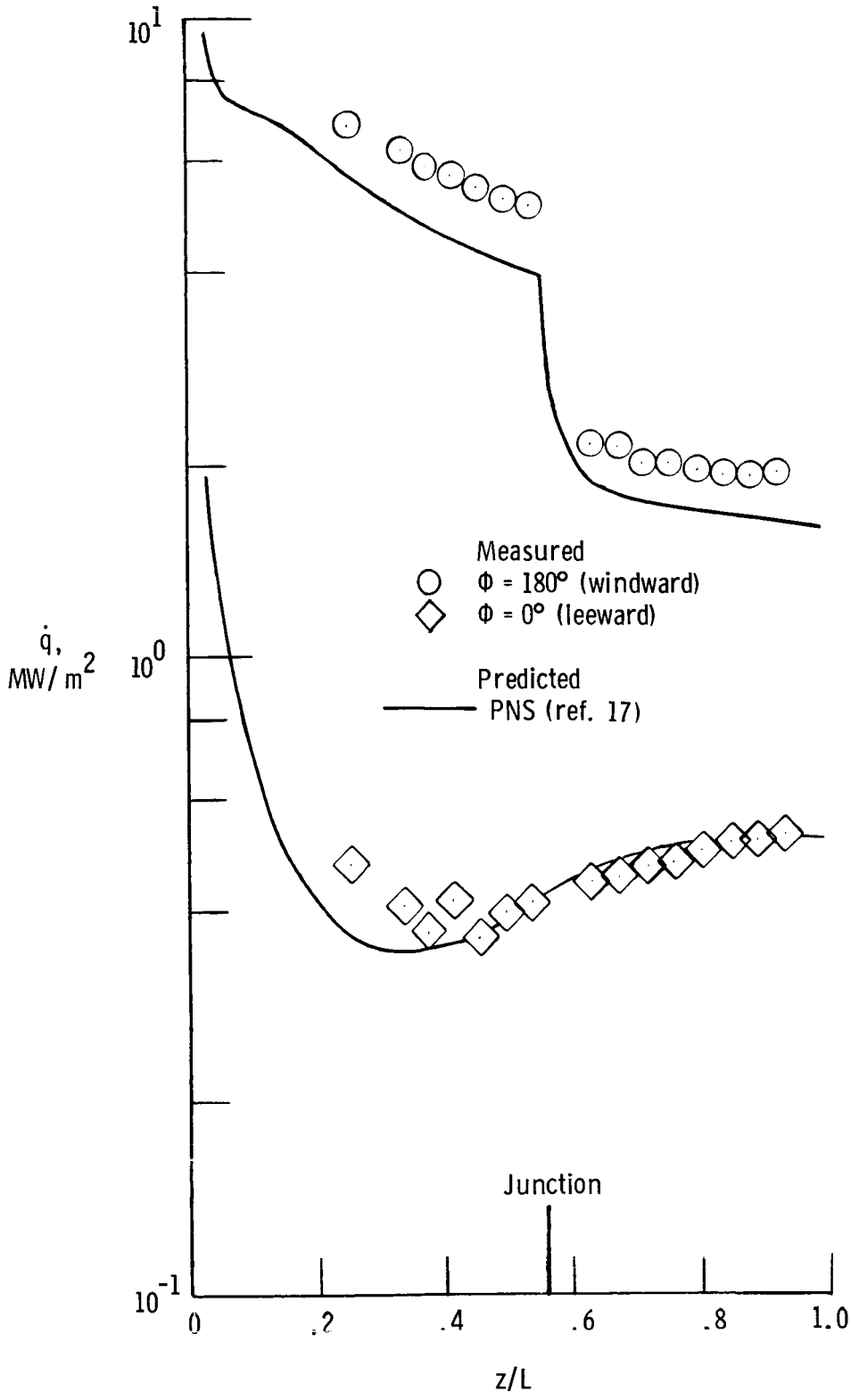

(c) $\alpha = 12°$.

Figure 27.- Concluded.

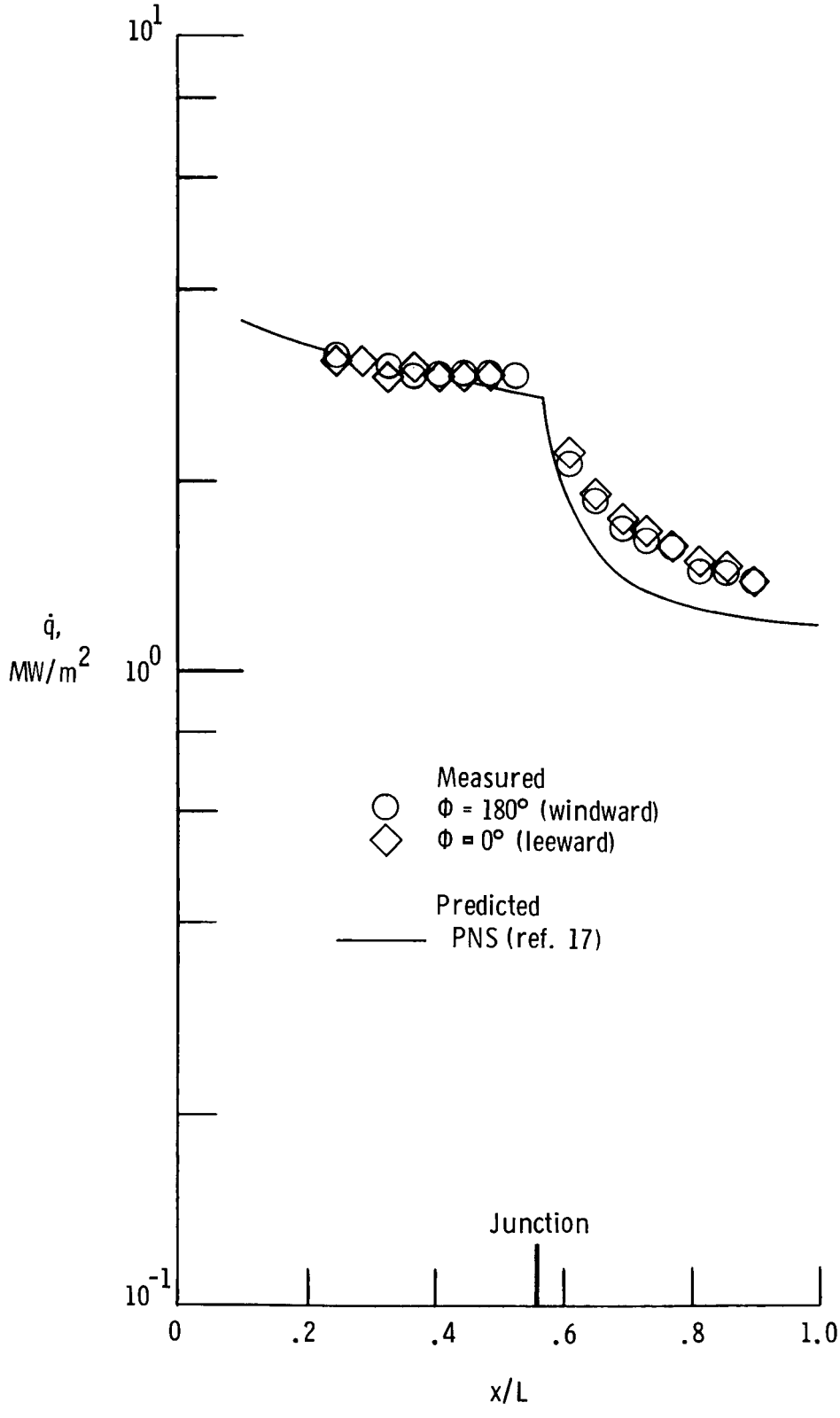

(a) $\alpha = 0°$.

Figure 28.- Measured and predicted heating for straight biconic in air.

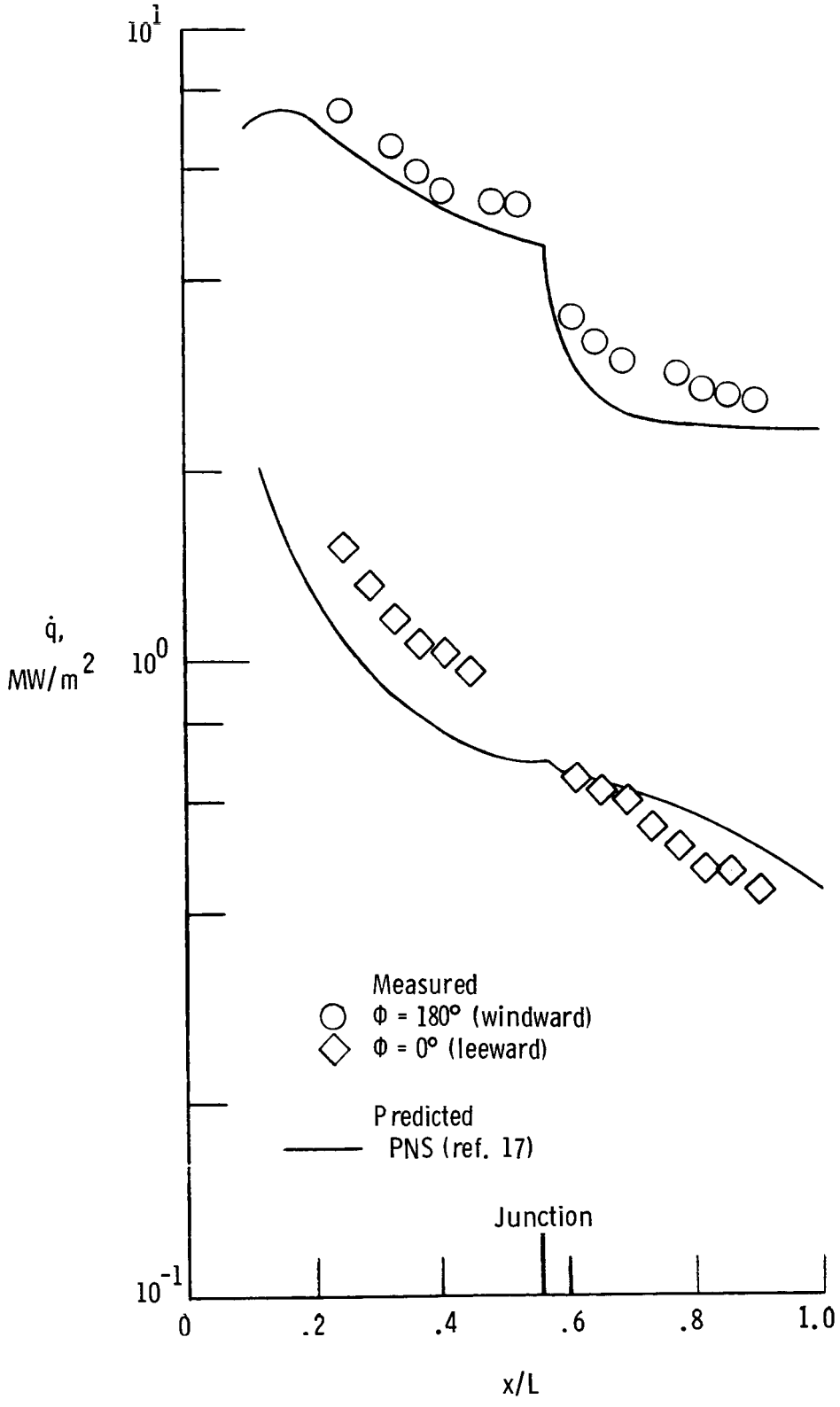

(b) $\alpha = 8°$.

Figure 28.- Continued.

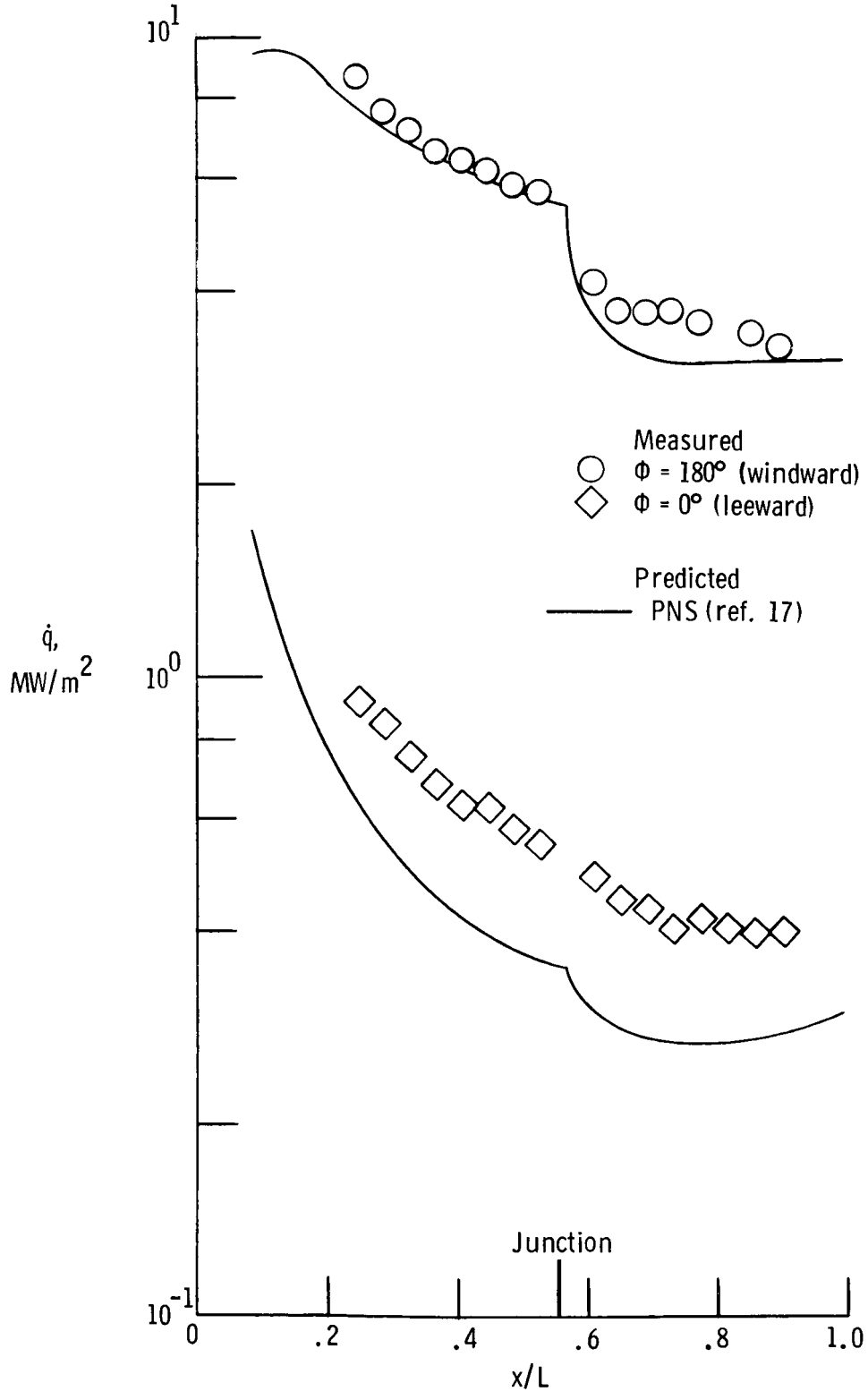

(c) $\alpha = 12°$.

Figure 28.- Continued.

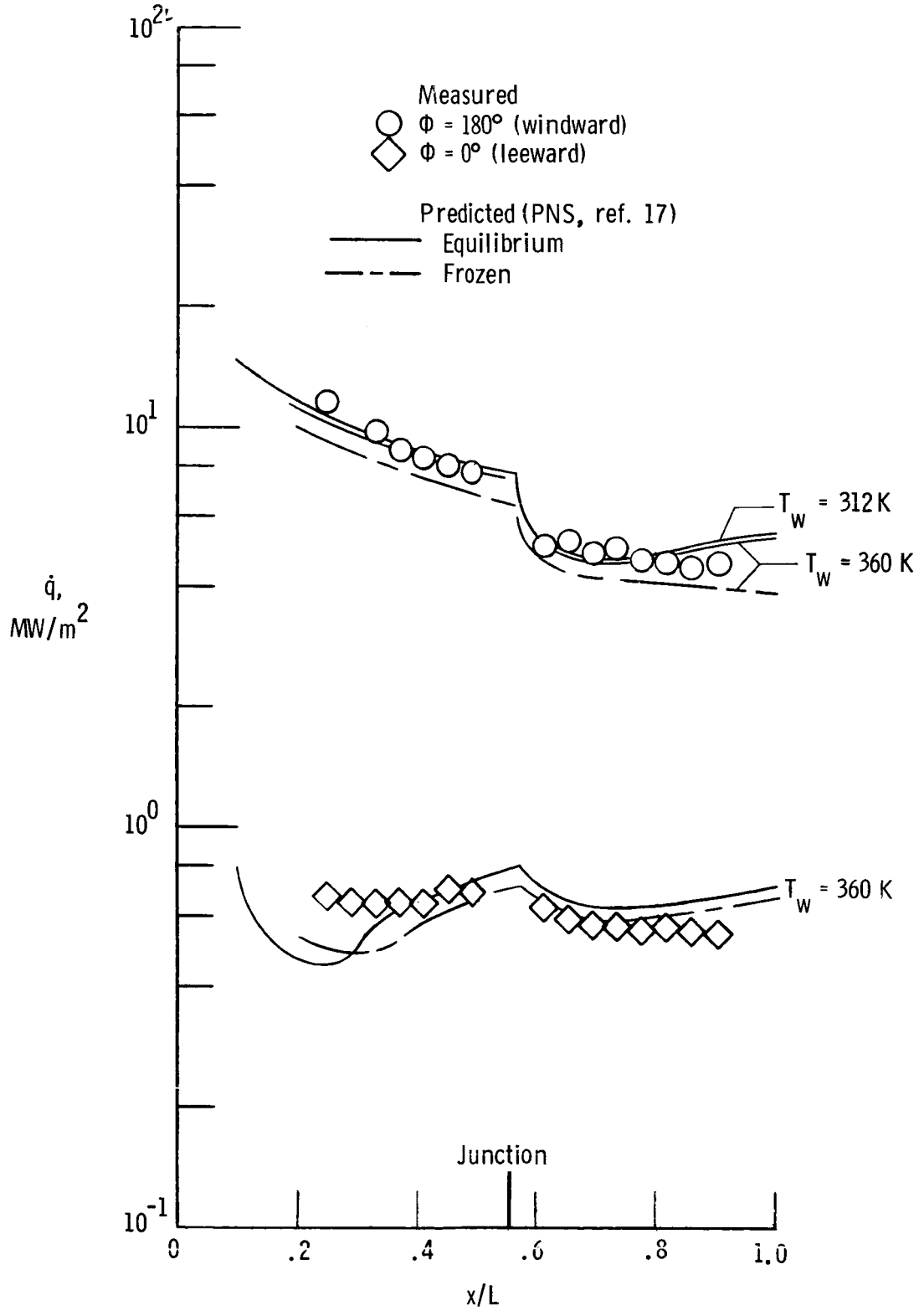

(d) $\alpha = 20°$.

Figure 28.- Concluded.

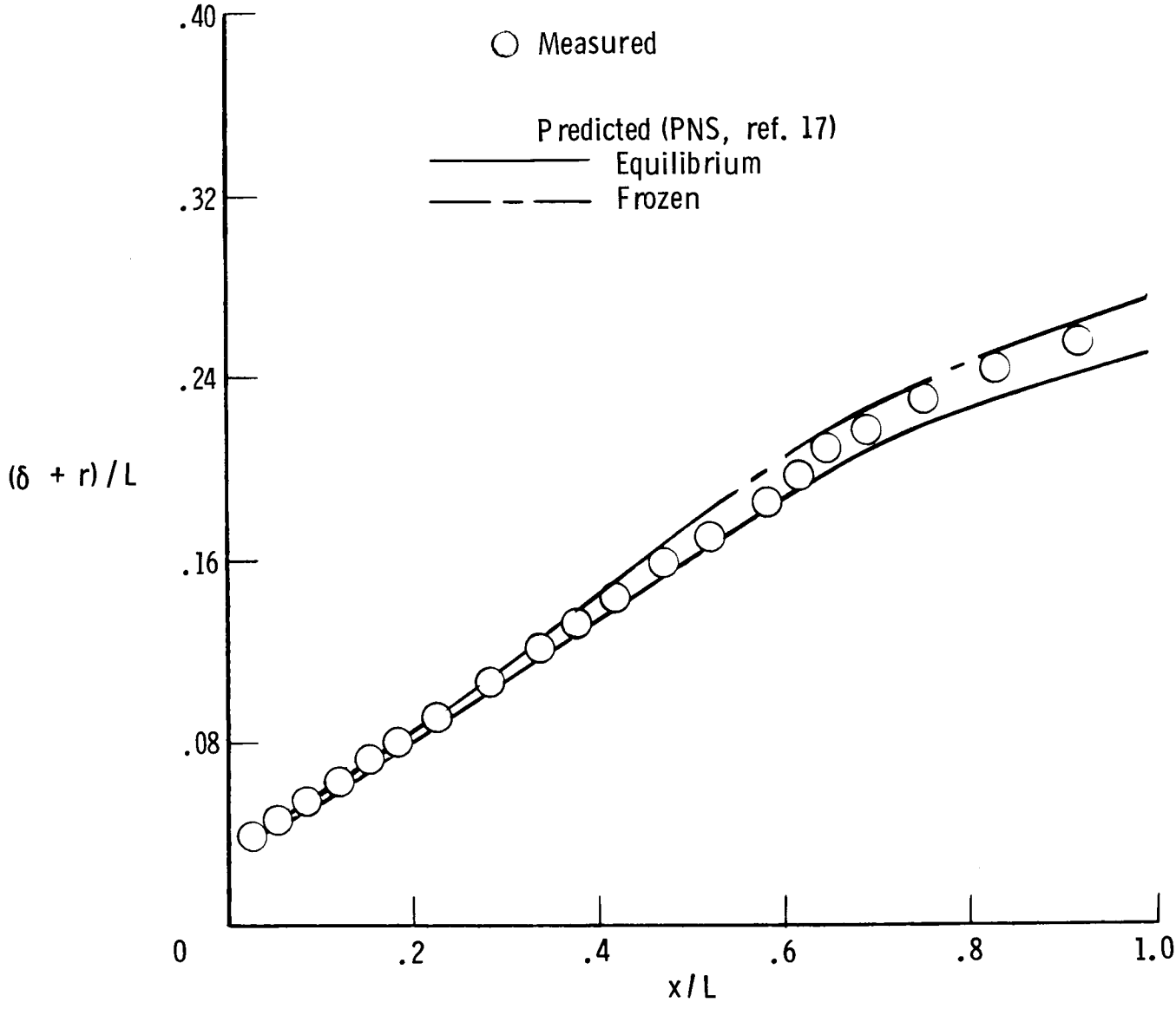

Figure 29.- Measured and predicted windward shock detachment distance for straight biconic and $\alpha = 20°$ in air.

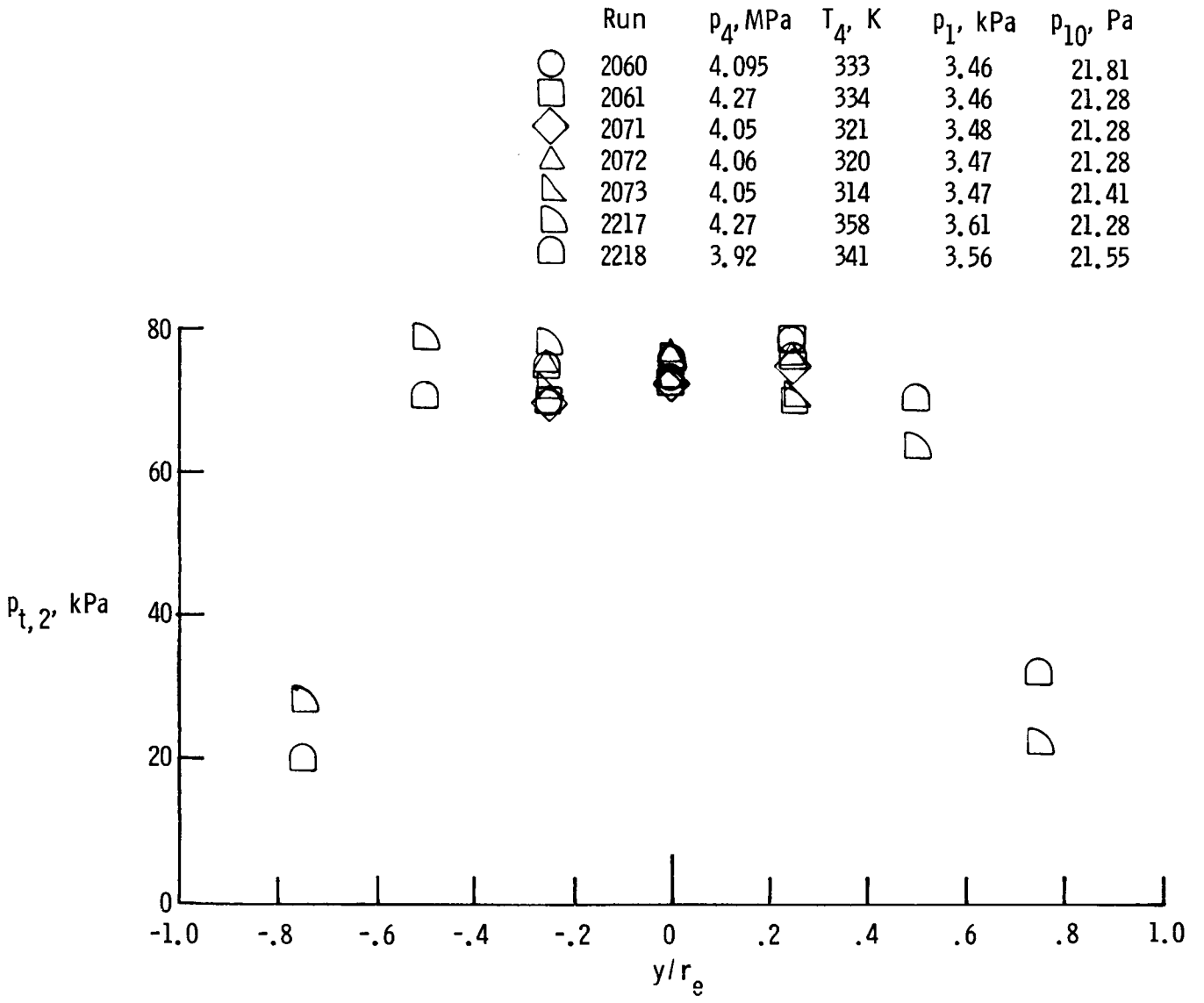

(a) Helium.

Figure 30.- Vertical pitot-pressure profiles for He, air, N_2, and CO_2. $\bar{x}$ = 5.6 cm; r_e = 7.6 cm; t = 200 μsec.

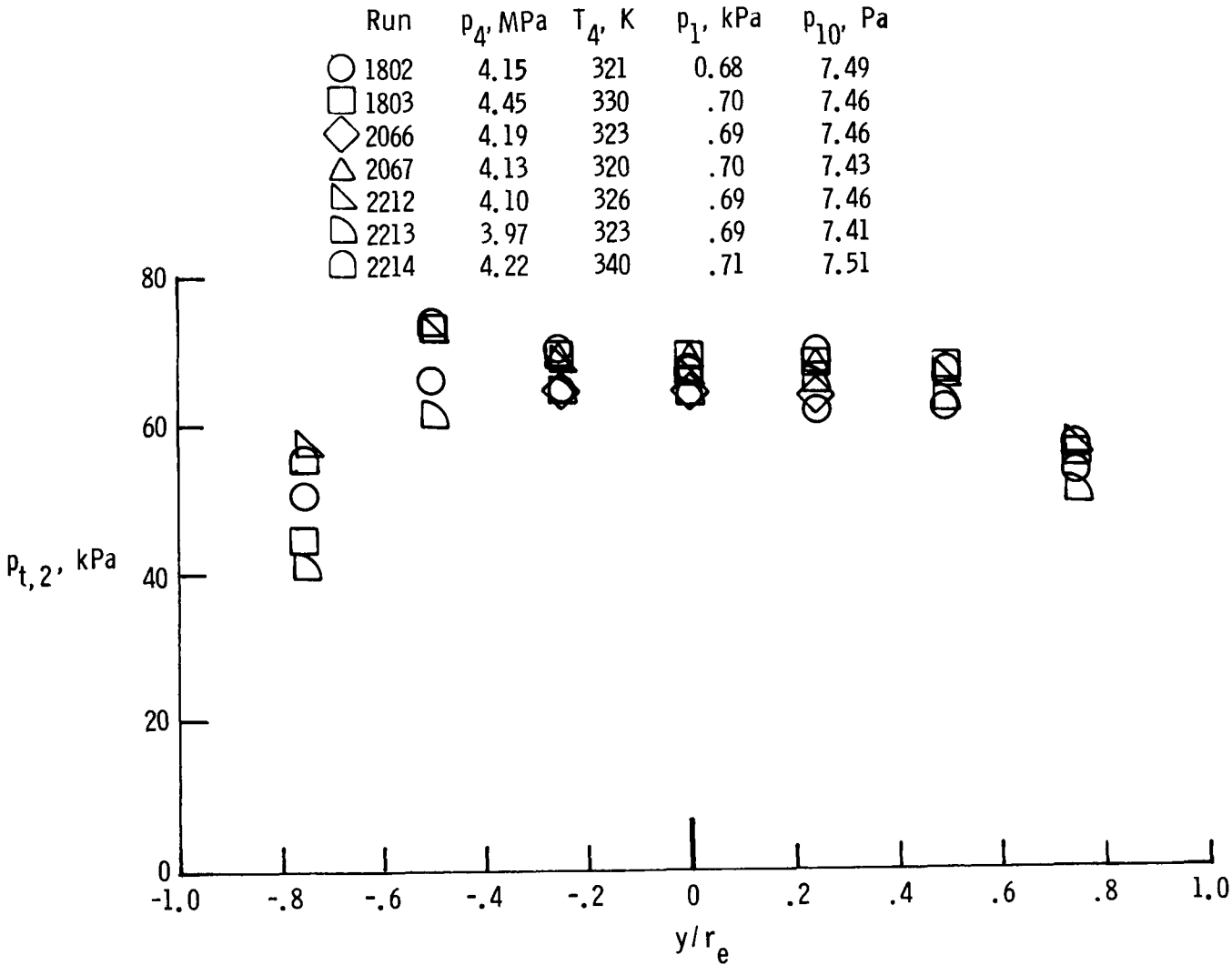

(b) Air.

Figure 30.- Continued.

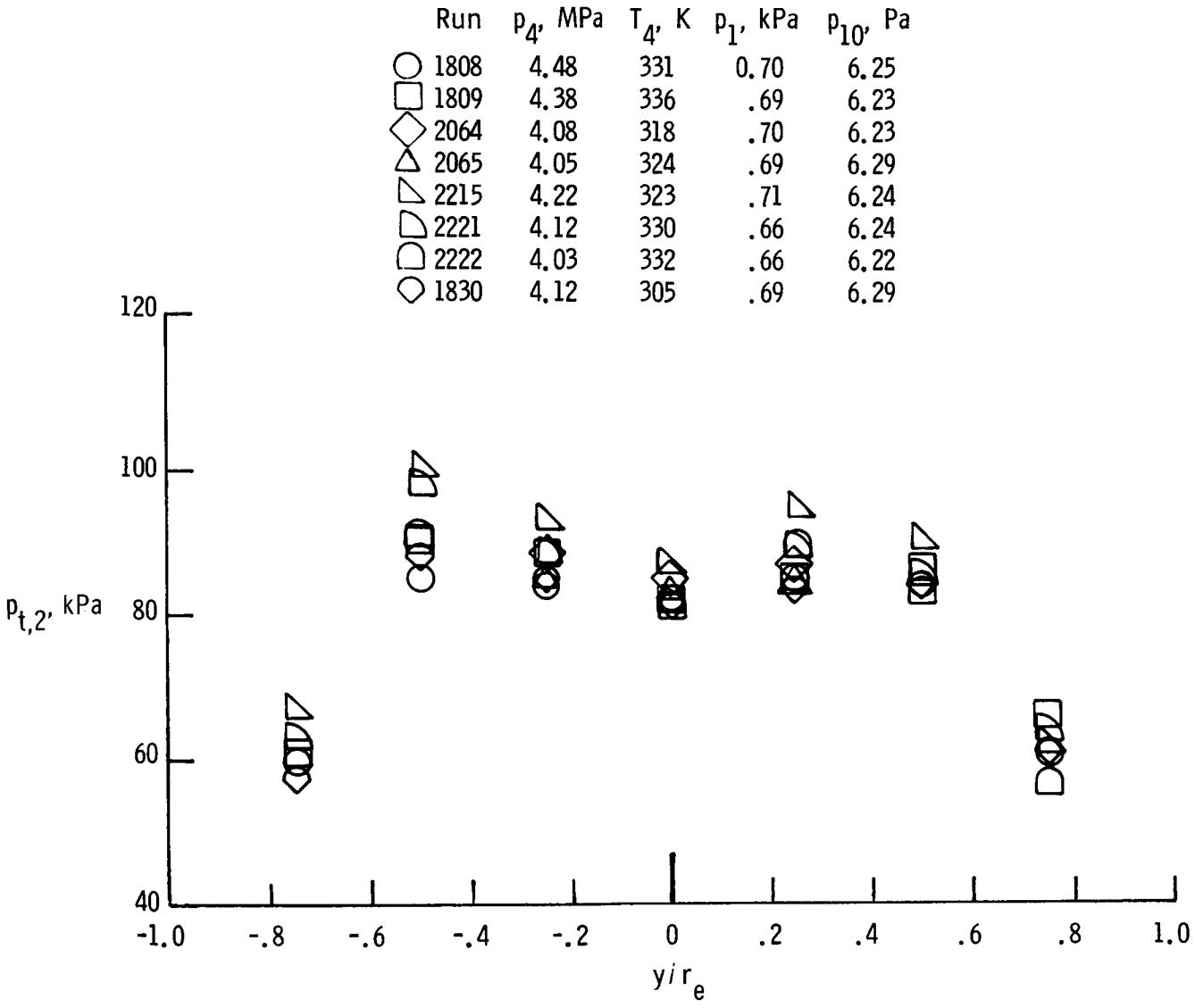

(c) Nitrogen.

Figure 30.- Continued.

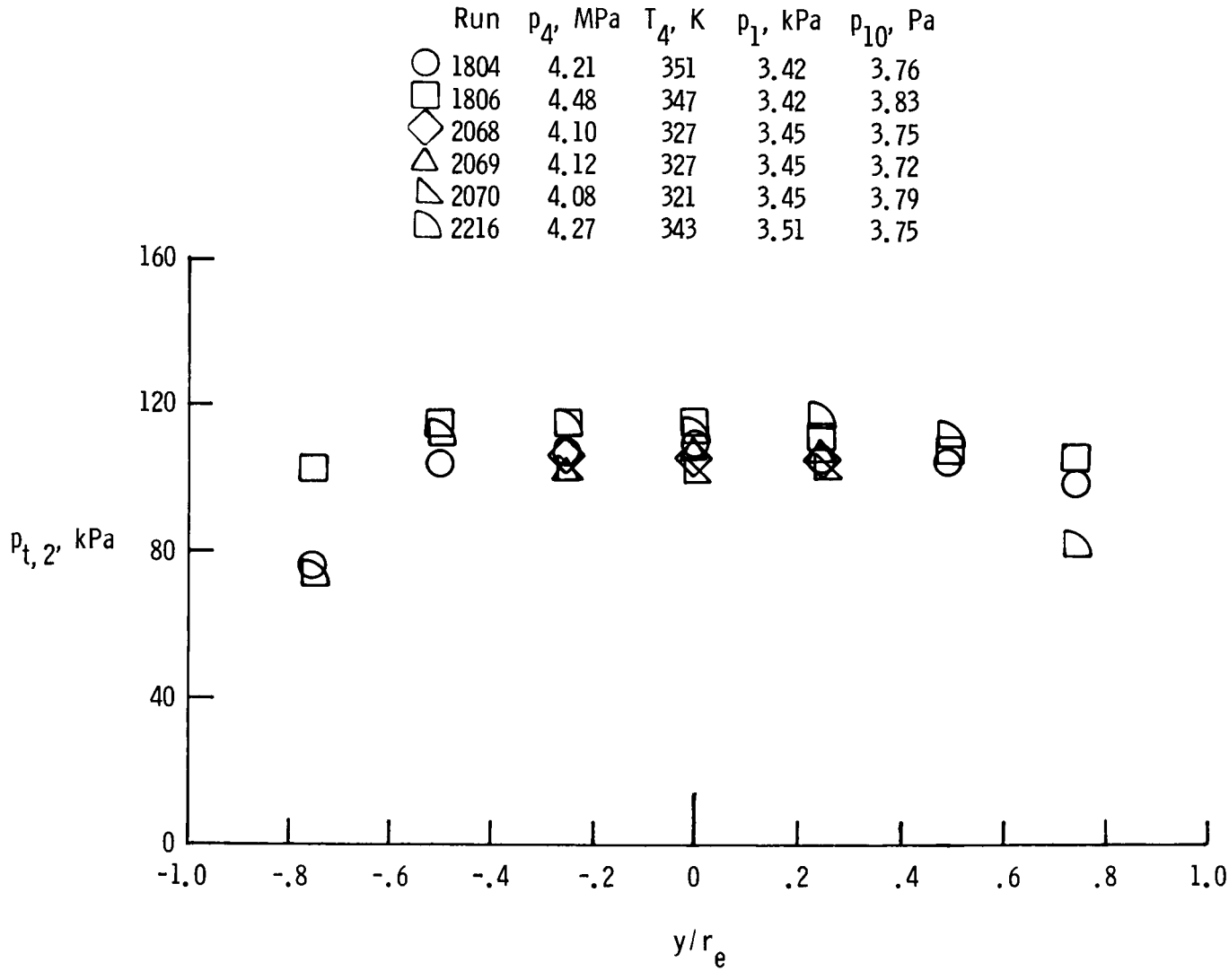

(d) CO_2.

Figure 30.- Concluded.

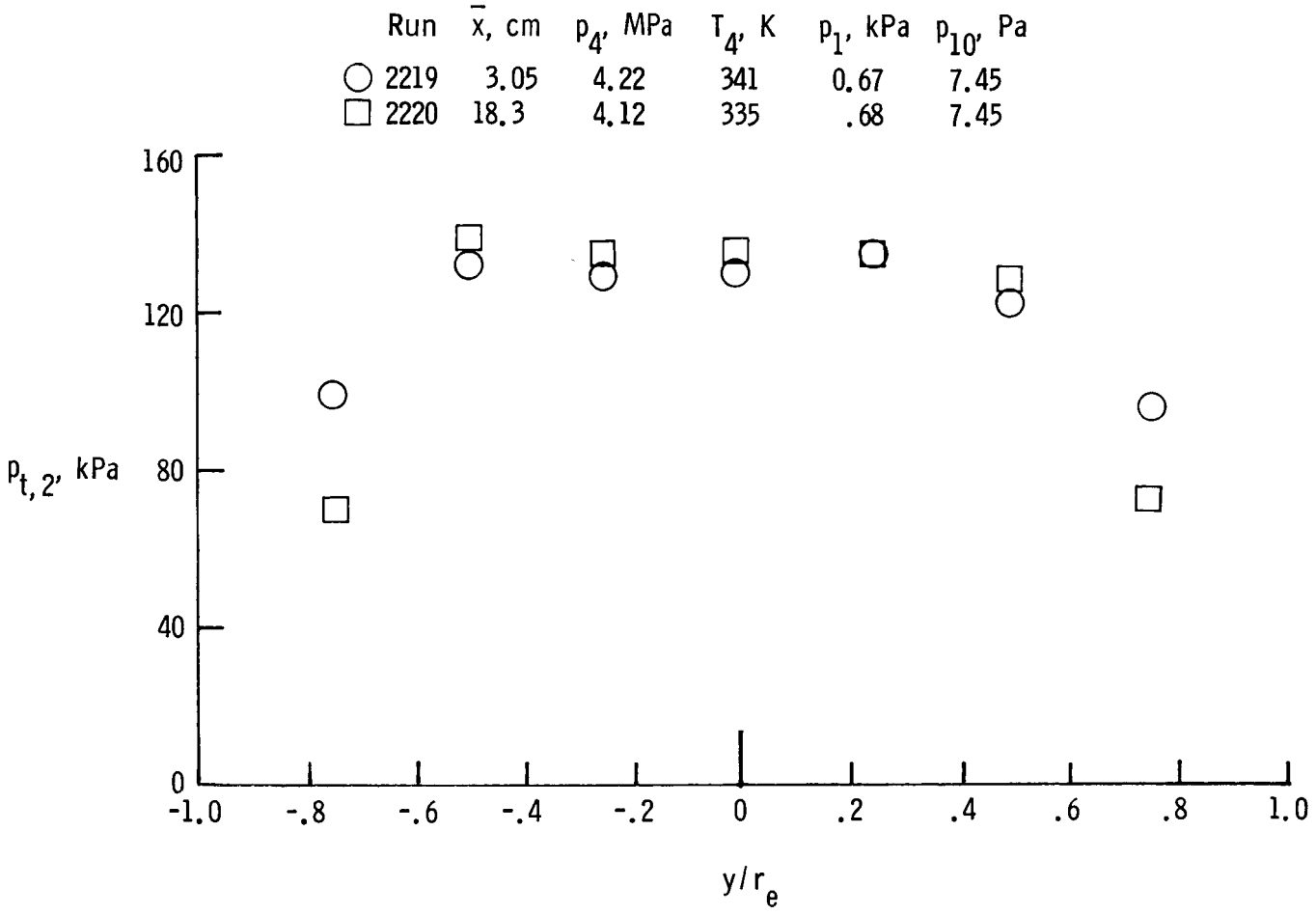

Figure 31.- Effect of axial station on pitot-pressure profile for air.
r_e = 7.62 cm; t = 200 μsec.

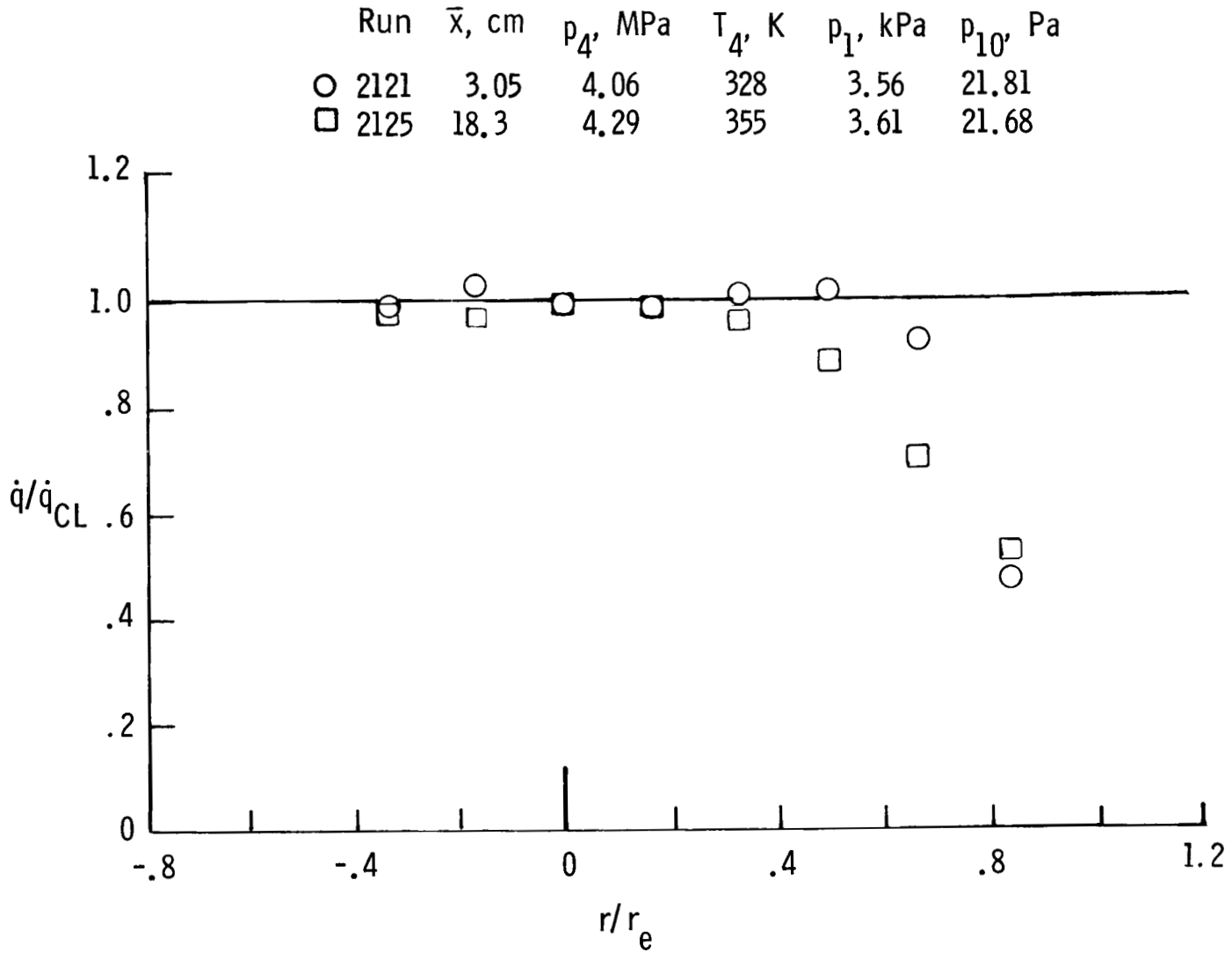

(a) Helium.

Figure 32.- Radial profiles of heat-transfer rate on 6.35-mm-diameter flat-faced cylinders for He, air, N_2, and CO_2 test gases. r_e = 7.62 cm, t = 200 μsec.

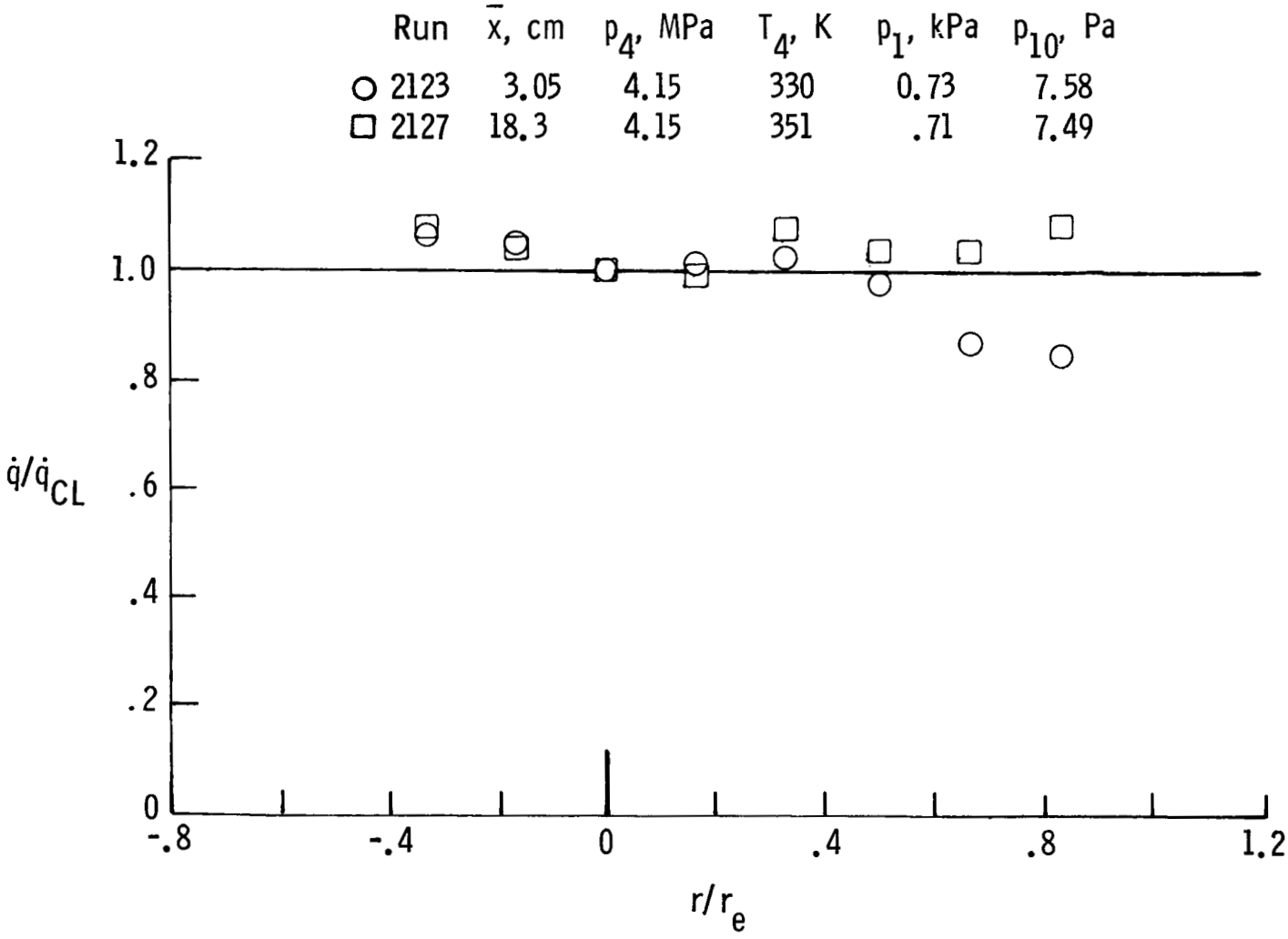

(b) Air.

Figure 32.- Continued.

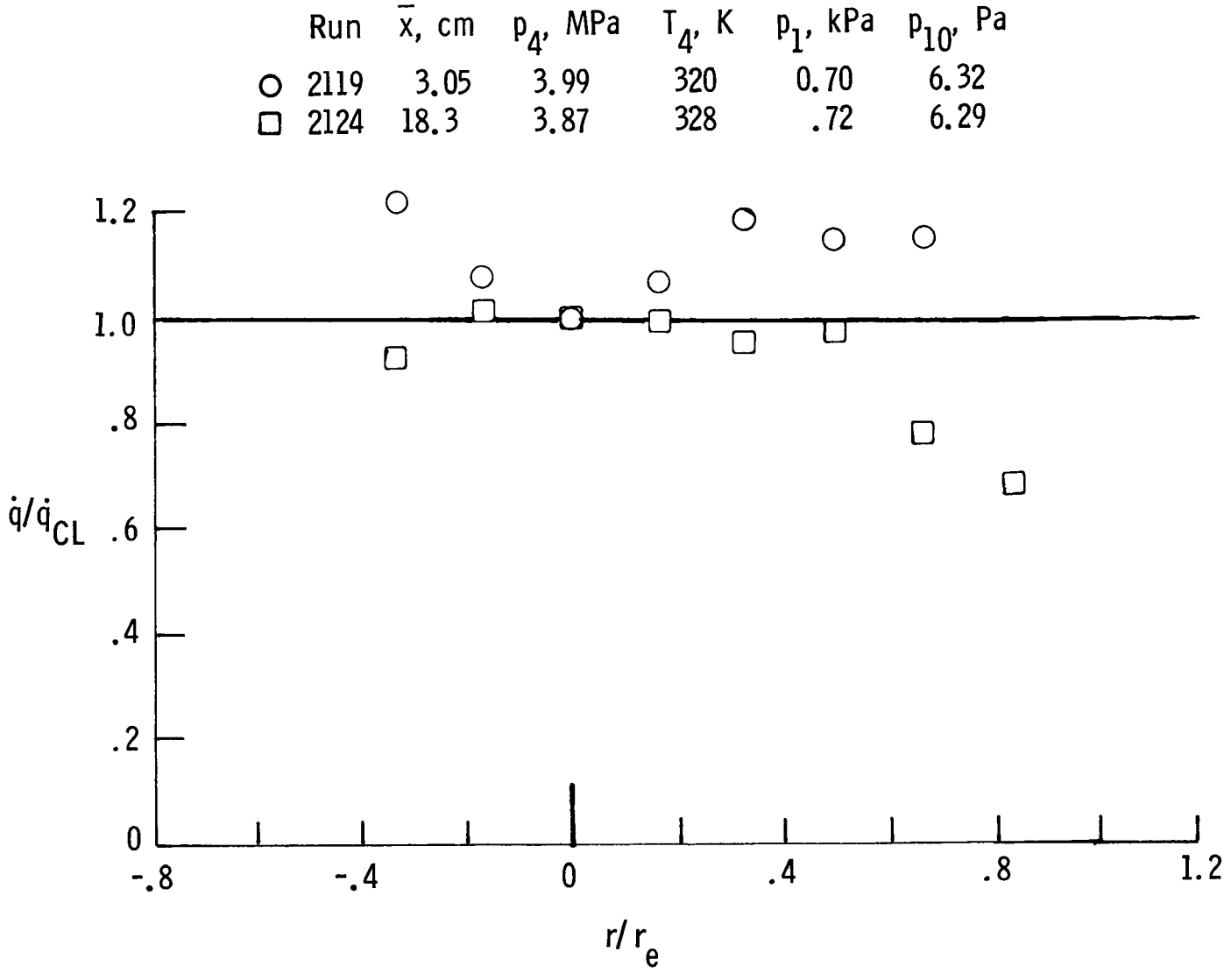

(c) Nitrogen.

Figure 32.- Continued.

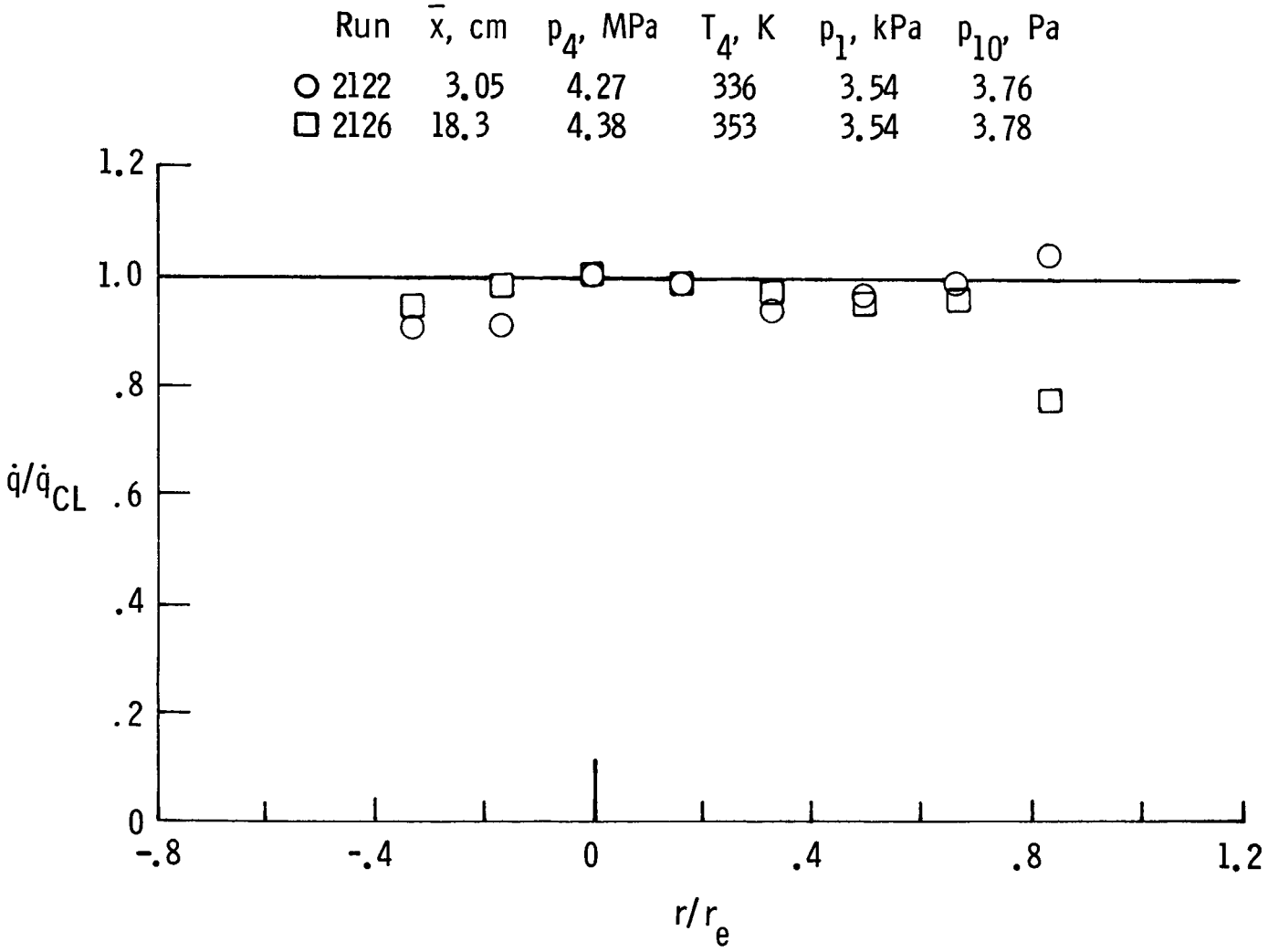

(d) CO_2.

Figure 32.- Concluded.

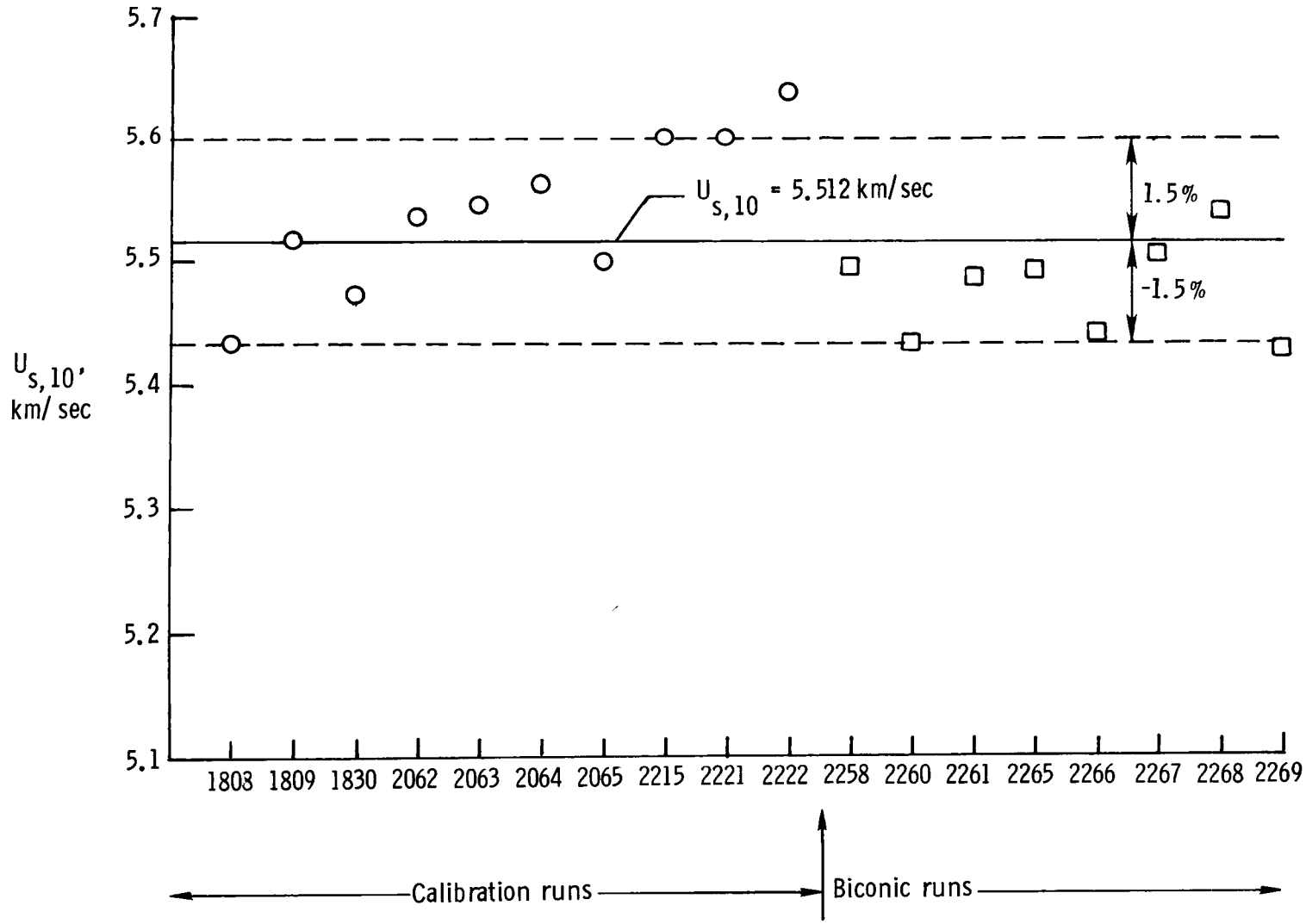

(a) Test-gas and acceleration-gas interface velocity.

Figure 33.- Variation of several measured flow quantities for expansion-tube runs with N_2 test gas.

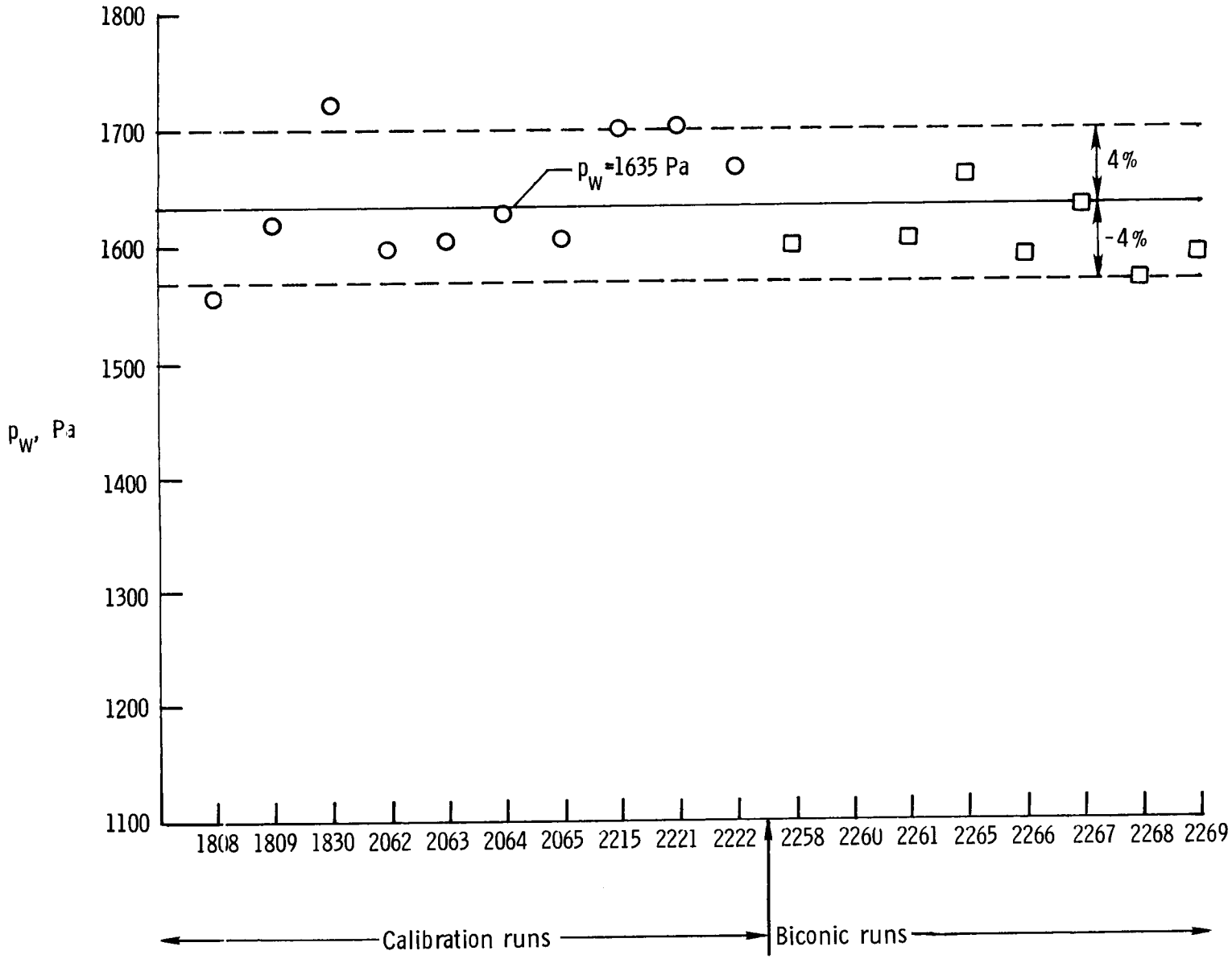

(b) Tube wall static pressure.

Figure 33.- Continued.

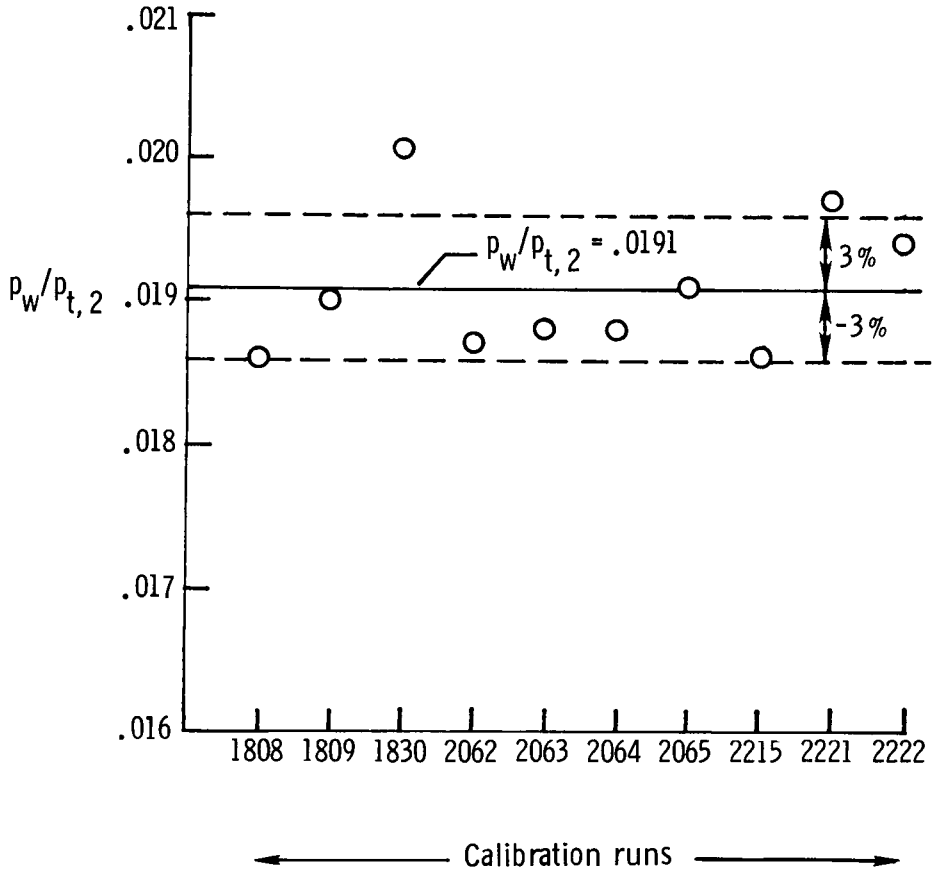

(c) Ratio of tube wall static pressure to pitot pressure.

Figure 33.- Concluded.

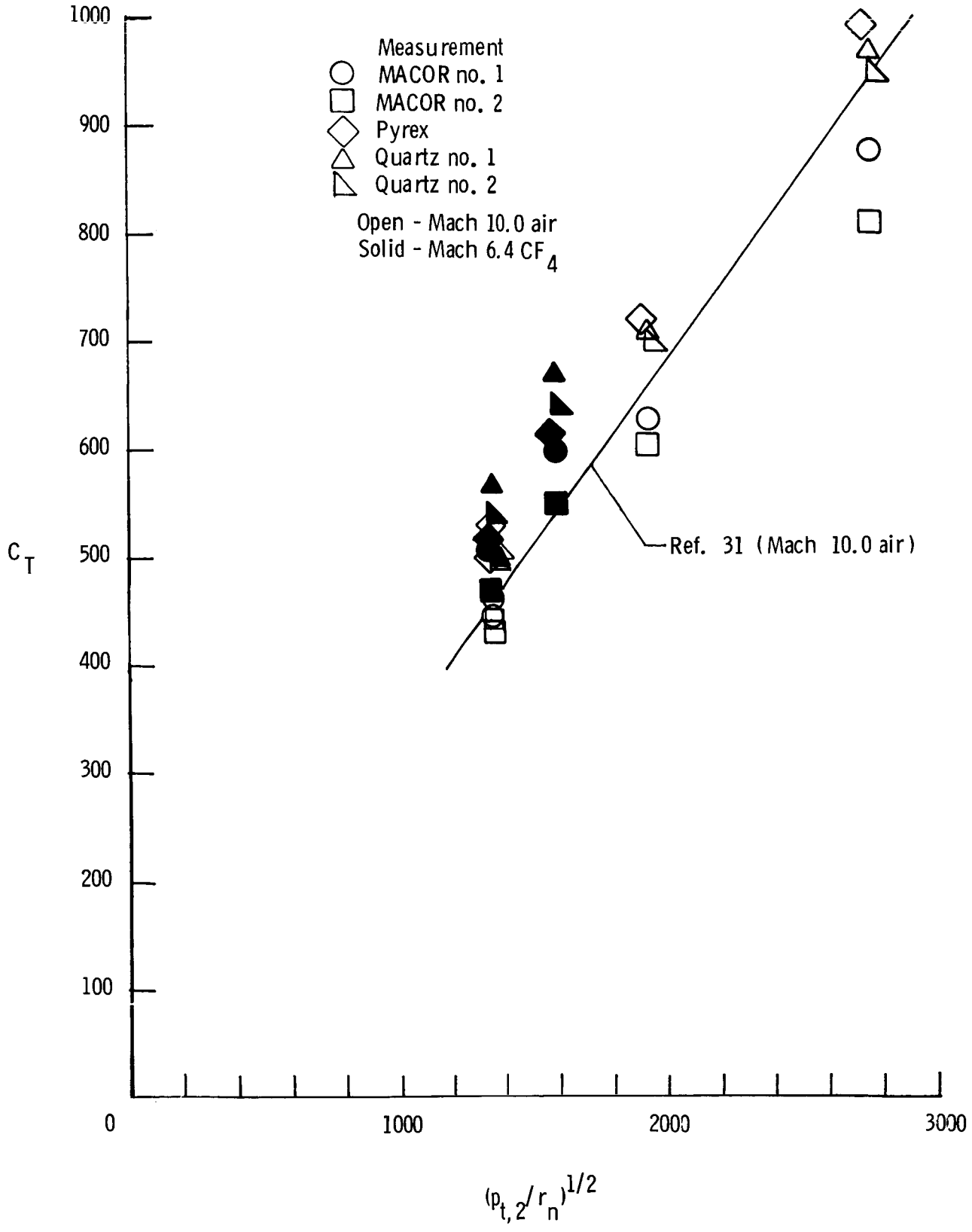

Figure 34.- Stagnation-point heat-transfer rate for a sphere as a function of velocity gradient.

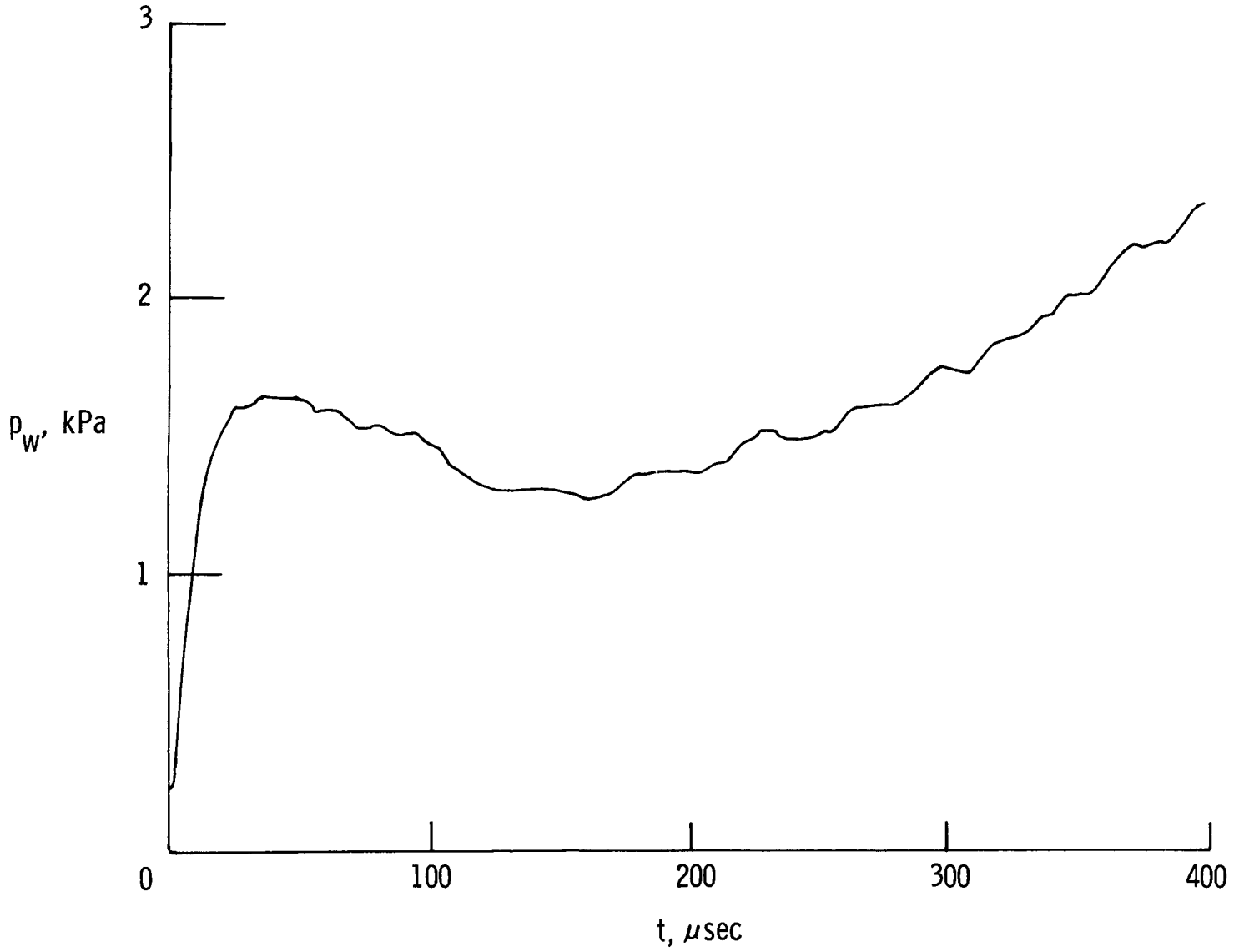

(a) Helium.

Figure 35.- Time histories of tube wall pressure measured 1.7 m upstream of tube exit for He and air test gases.

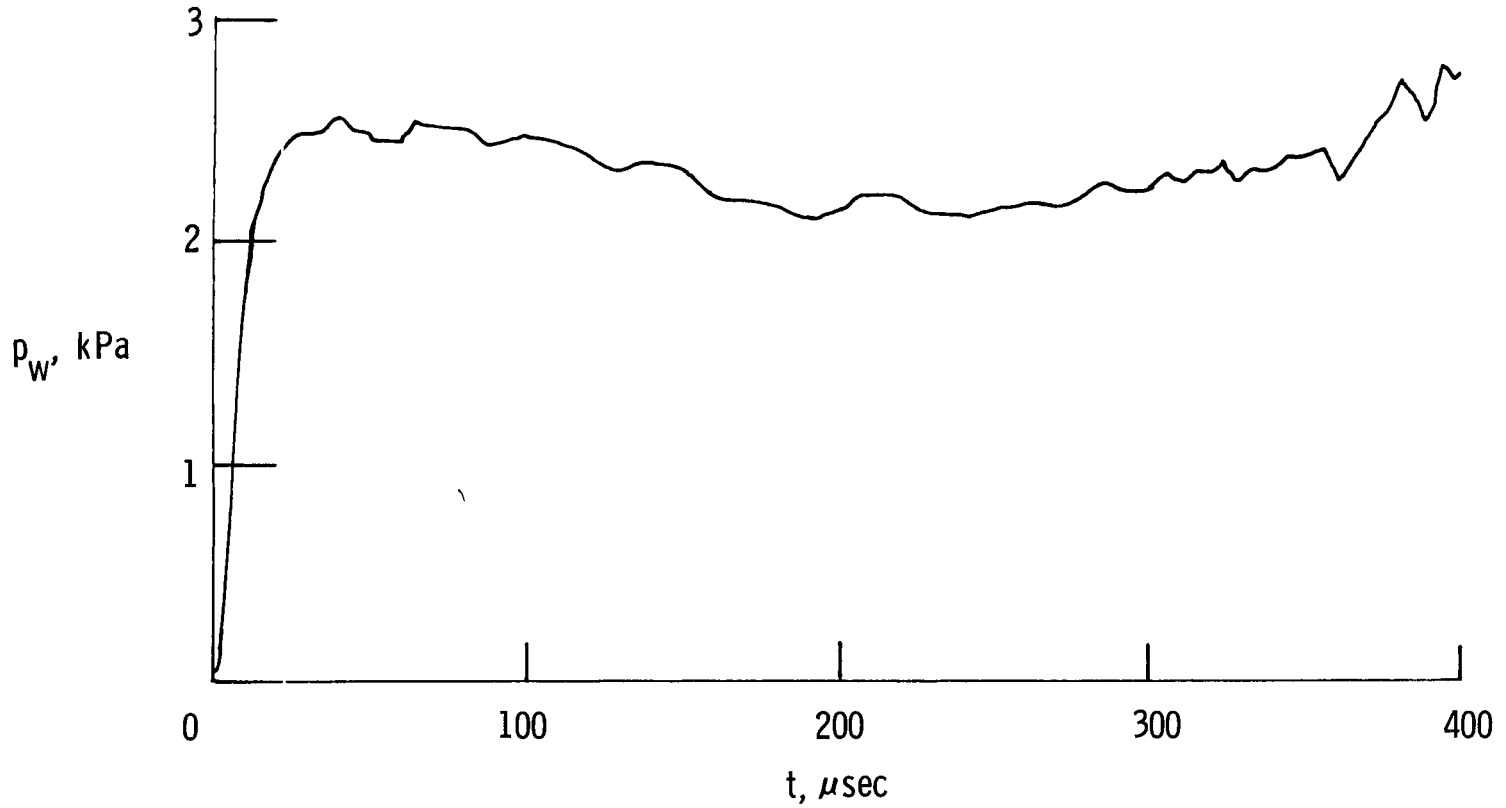

(b) Air.

Figure 35.- Concluded.

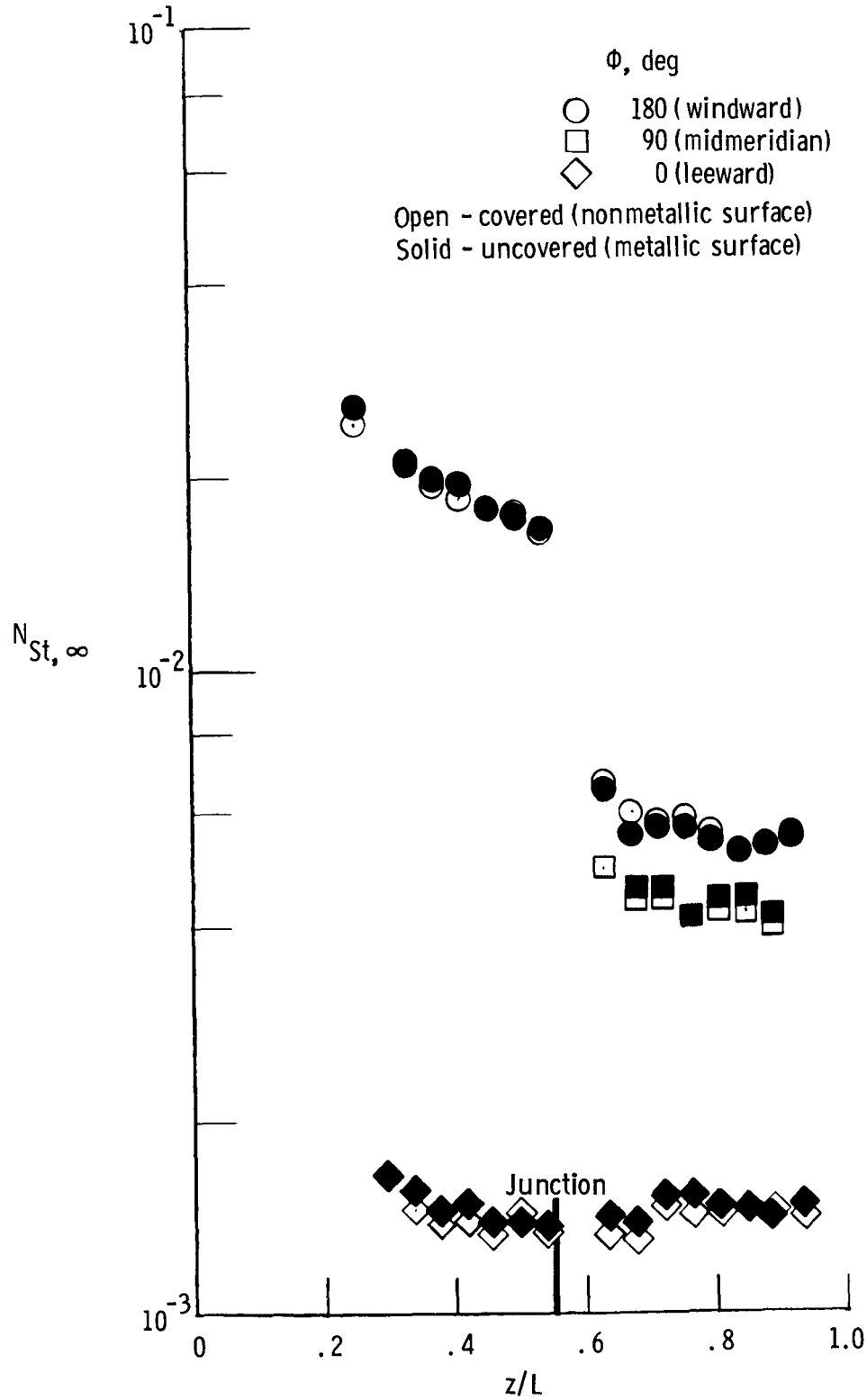

Figure 36.- Effect of model cover or coating on heating for bent-nose biconic in air at $\alpha = 8°$.

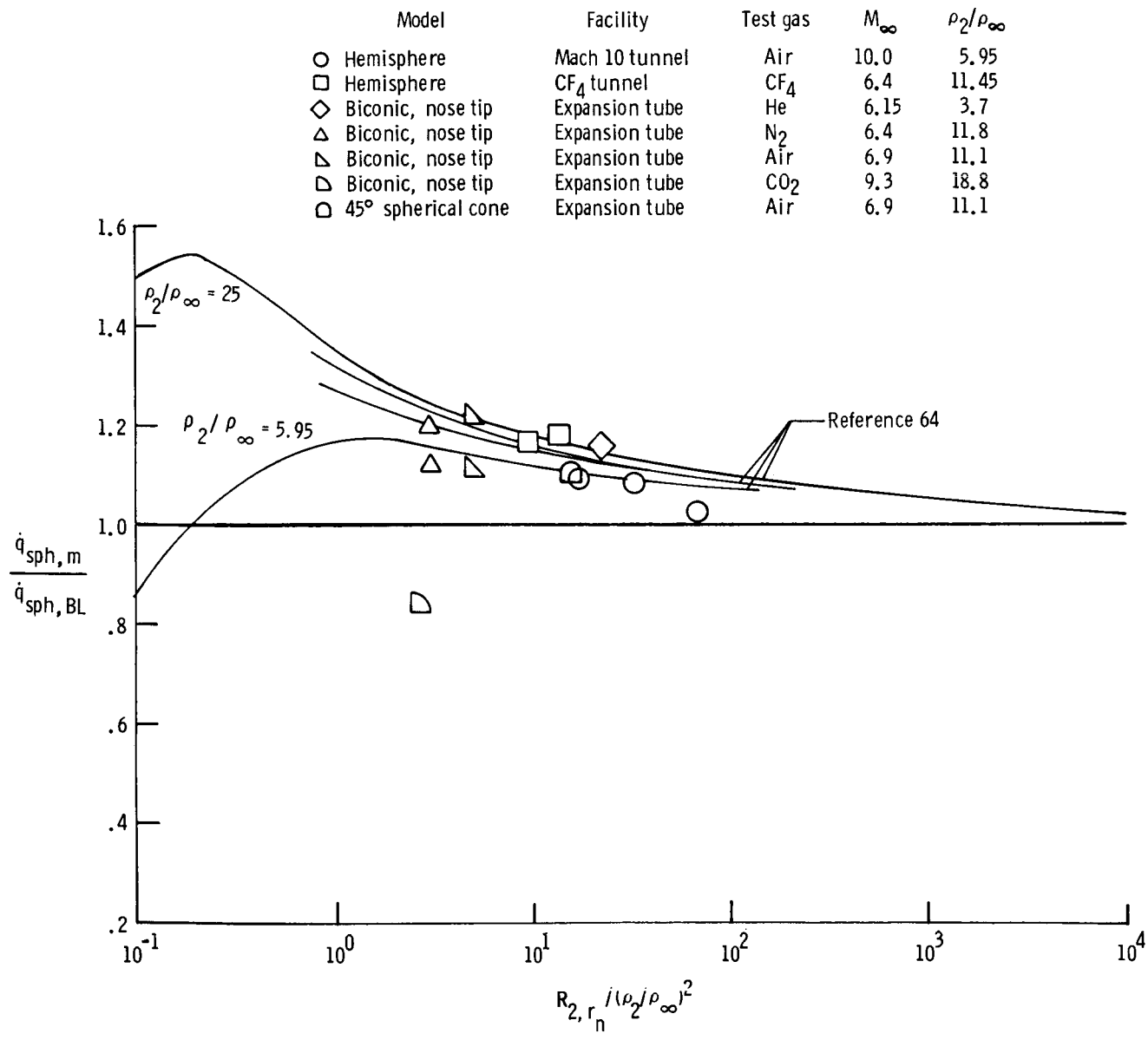

Figure 37.- Ratio of measured to predicted (with classic boundary-layer theory) stagnation-point heat-transfer rate of a sphere as a function of Reynolds number and density ratio.

1. Report No.	2. Government Accession No.	3. Recipient's Catalog No.
NASA TP-2213		

4. Title and Subtitle	5. Report Date
LAMINAR HEAT-TRANSFER DISTRIBUTIONS ON BICONICS AT INCIDENCE IN HYPERSONIC-HYPERVELOCITY FLOWS	January 1985
	6. Performing Organization Code 506-51-13-01

7. Author(s)	8. Performing Organization Report No.
Charles G. Miller III, John R. Micol, and Peter A. Gnoffo	L-15645
	10. Work Unit No.

9. Performing Organization Name and Address	11. Contract or Grant No.
NASA Langley Research Center Hampton, VA 23665	
	13. Type of Report and Period Covered Technical Paper

12. Sponsoring Agency Name and Address	14. Sponsoring Agency Code
National Aeronautics and Space Administration Washington, DC 20546	

15. Supplementary Notes

16. Abstract

Laminar heating distributions were measured at hypersonic-hypervelocity flow conditions on a 1.9-percent-scale model of an aeroassisted vehicle proposed for missions to a number of planets. This vehicle is a spherically blunted, 12.84°/7° biconic with the fore-cone axis bent upward 7° relative to the aft-cone axis to provide self-trim capability. Also tested was a straight biconic (i.e., without nose bend) with the same nose radius and half-angles as the bent-nose biconic. These measurements were made in the Langley Expansion Tube at free-stream velocities from 4.5 to 6.9 km/sec and Mach numbers from 6.0 to 9.0 with helium, nitrogen, air, and carbon dioxide test gases. The range of calculated thermochemical equilibrium normal-shock density ratios for these four test gases was 4 to 19. Angles of attack, referenced to the aft-cone, varied from 0° to 20°. Heating distributions predicted with a parabolized Navier-Stokes (PNS) code were compared with measurement for helium and air test gases. Measured windward and leeward heating levels were generally underpredicted by the PNS code for both test gases, and agreement was poorer on the leeward side than on the windward side.

17. Key Words (Suggested by Author(s))	18. Distribution Statement
Heat transfer Hypersonic Hypervelocity Biconics	Unclassified - Unlimited Subject Category 34

19. Security Classif. (of this report)	20. Security Classif. (of this page)	21. No. of Pages	22. Price
Unclassified	Unclassified	144	A07

For sale by the National Technical Information Service, Springfield, Virginia 22161